

2D Fourier Transform Spectroscopy Setup and Ultrafast Dynamics of Porphyrins

THÈSE N° 6849 (2015)

PRÉSENTÉE LE 30 NOVEMBRE 2015
À LA FACULTÉ DES SCIENCES DE BASE
LABORATOIRE DE SPECTROSCOPIE ULTRARAPIDE
PROGRAMME DOCTORAL EN PHOTONIQUE

ÉCOLE POLYTECHNIQUE FÉDÉRALE DE LAUSANNE

POUR L'OBTENTION DU GRADE DE DOCTEUR ÈS SCIENCES

PAR

Andre AL HADDAD

acceptée sur proposition du jury:

Prof. O. Martin, président du jury
Prof. M. Chergui, directeur de thèse
Prof. T. Feurer, rapporteur
Prof. J.-P. Wolf, rapporteur
Prof. A. Hagfeldt, rapporteur



ÉCOLE POLYTECHNIQUE
FÉDÉRALE DE LAUSANNE

Suisse
2015

Acknowledgements

I would like to thank all the people who supported me to reach this point. The LSU group offered the scientific and social support that was essential for the realization of this project. After all of these years, I'm leaving EPFL with a PhD degree, but more importantly with priceless experience and friendships that will stay with me for years to come.

All of this wouldn't have been possible without Prof. Majed Chergui, who accepted me as a part of his group and gave me the ability to grow as a scientist. His support and encouragement, his deep and profound knowledge in the field of optical spectroscopy and femtochemistry, have guided me through the different stages of my PhD work. But more importantly, during these five years he has sent in me the true spirit of science, and through his vast knowledge he triggered my love to learn about music, politics, and history. Majed, you've been an inspiration and a great role model to me, thank you.

I am thankful to the thesis committee members, Prof. Jean-Pierre Wolf, Prof. Thomas Feurer, and Prof. Anders Hagfeldt for accepting to evaluate this work, for their recognition and valuable comments during the exam. I would like to thank Prof. Olivier Martin for providing the excellent scientific framework within the Photonics doctoral school and for accepting to be the president of the thesis committee.

I am very grateful to Monique Bassin for taking care of many administrative and organizational issues during my PhD. Thank you for helping find an apartment in Lausanne and being the nicest person to give me advice about any issue that happens outside EPFL.

I am deeply grateful to Dr. Frank van Mourik, Dr. Gerald Aubick, Dr. Jakob Grilj, and Dr. Christopher Arrell, for the guidance and discussions about different issues in the lab. Frank guided me through learning about ultrafast laser systems and spectroscopy, and stood sometimes for hours in the lab with me aligning and cleaning the laser systems. Gerald assisted me in the first year of my thesis and was present to answer my questions. One of the most knowledgeable people in femtochemistry and spectroscopy I have met is Jakob. For the last year of my thesis, Jakob was always available for discussion, and every time we met, I have learned something new. I owe you a lot. Chris opened the opportunity that made my thesis much more valuable by offering me to use the hollow core fiber that he brought and installed in the lab. I'm thankful for all the discussions we had in the lab and all the help you offered during these years, which added a lot to my knowledge and experience. But there is one more important aspect than work and lasers, its chicken! The best way to finish a long day of work is to have some good Portuguese chicken and wine with Jakob, Lars, Jose, Frank and Chris.

During these years I worked with various people in the lab, doing measurements or building new experiments, where I learned from every one of them, and enjoyed their companionship. I had the perfect experience over these years, since it was never only work. Friendships were made over during years, and the working days were more of a pleasure than a burden. Notably, all the long days and nights of measurements with Dr. Roberto Monni, were nothing but two buddies trying to make the best of what they know and can, and it totally worked. Struggle is the path to success. These days created a friendship that I will keep for long years to come. It was a pleasure to work with Adrien as well, where he supported me through the toughest part of my thesis, and was always encouraging me. I admire Adrien's patience and profound view of the world. We had a lot of discussions about science, but also about

religion, politics, sociology, and so on. I enjoyed being around Adrien, and enjoyed meeting his family every once in a while, seeing Gabriel growing up. Lars Mewes and Fabio Santomauro brought another spirit to the lab, where the work was mainly laughter and enjoyment. This made the long working weekends and late evenings easy to get through. Working with Lars made me more addicted to the lab, and kept me anxious to be present and get to know how things are going. Lars, one more glass??? Fabio's stream of ideas is limitless, dazzling like the never ending story, but blinks of genius appear here and there. But Fabio's wildest fantasy was always the Kebab!

The rest of the LSU group members were nothing but perfect, creating a friendly atmosphere where we had great moments. Every one of you had a positive impact on my stay at EPFL, with all the beers we had, group retreats and great lunches. Sharing the office with Edoardo was a great experience. Edoardo is a very knowledgeable person with a great personality. You cannot speak with him longer than 10 minutes and not learn something new! Lume group members were always present in my daily life, where we met for lunch, dinners, weekends, and for beers. Little Italy especially dominated the group, with the loud voices and sparkling Italian personality; it was inevitable but I became friends with all of them. Luca, Francesco, Tom, and Andreas have become friends that I meet with when I want to get out of work mood. We had lots of great times having dinners and poker nights, and enjoying great Italian wine and food.

During all of this, I met someone who changed my life. Giulia gave me a reason to keep fighting to finish this PhD, especially in the hardest moments. She stood by me during the good and the bad. Giulia you changed me and made me the person I am now. I cannot be more grateful for all what you have done for me. Four years together, changed my perception of life; you took for my first ever holiday! You taught me that life is not all misery and fighting to survive, life is good and can be better. Thank you my love. Giulia's family was nothing but great to me, where I felt I had another family in Italy that cares for me and stands by me when in need. I was engulfed by their love and felt protected and welcomed. I'm a lucky guy to be part of this family, thank you.

I cannot finish but thank Majed again, Ahmad and Lina, and my family.

ماجد، بأصدق المشاعر أقدم لك شكري وامتناني على هذه الفرصة التي غيرت مجرى حياتي. في هذه السنين الخمسة لقد بعثت في روح العلم و محبة المعرفة عبر خبراتك ألامحدودة في العلوم والتاريخ. لقد أنعشت في حب حضارتنا الغنية و أعدت إيماني في مستقبل مشرق لبلادنا. أنت تعرف معنا المعلم في حضارتنا، فسببى فضلك علي مدا عمري. شكرا

أحمد، يا أخالم تلده أمي، شكرا على كل فجان قهوة تشاركناه في هذه السنين، شكرا على كل نصيحة أعطيتني، و كل صحن طعام جلبت لي. كنت سندا لي في أصعب الظروف و وقفت بجانبني. أختي لينا، شكرا على كل ما فعلتني من أجلي و شكرا على أطييب المأكولات التي أرجعتني بالذاكرة إلى طفولتي. الأهم من كل ذلك أنكم كنتم عائلة لي في لوزان ، حيث لم أشعر بالوحدة بل شعرت بدعمكم الدائم و محبتكم اللامتناهية

و أخيرا أشكر أهلي، أكرم و دلال، أبي و أمي. لولاكم لما وصلت إلى هنا. بابا، أنت رمز العطاء و رمز المحبة. كنت أول من علمني حب العلوم و الفيزياء، اخترنا كل شيء سويا. شكرا على عطائك و محبتك لي. أنت من كان صخرتنا ارتكز عليها و مثلا يحتذي به. ماما، انتى من علمني الكتابة و القراءة، من ضحى بعمره لكي أصل، من سهر الليالي بجانبني. لا شيء بالدنيا يضاهي حنانك و محبتك لي. لقد كنتم رمز التضحية بالذات و فعلتم المستحيل لكي أصل. أتمنى يوما أن أعطي عائلتي ذرة من ما أعطيتم. و كيف لي أن أنسى إخوتي روبرت و رودي. محبتي لكم ليس لها نهاية، و مساعدتكم الدائمة لي كانت مصدر إندفاع لكي أصل و أفتح الطريق لحياة جديدة. شكرا جزيلا لكم

Abstract

This thesis was devoted into two main goals, designing and implementing a two dimensional Fourier transform spectroscopy setup and studying the relaxation dynamics of porphyrin systems upon photo-excitation. The first chapter is a fast review of the basics of non-linear optical spectroscopy, followed by a presentation of the two-dimensional and transient absorption spectroscopy. Wavepacket dynamics and vibration cooling (intra- and inter-molecular) are discussed as well, where differentiation between Condon and non-Condon wavepackets is presented. Finally we discuss the sampling theory and Fourier transformation, due to their importance in 2D spectroscopy measurements and in the wavepacket analysis.

The second chapter discusses the development and implementation of a two dimensional Fourier transform spectroscopy setup, that permits the recording of electronic 2D spectra in the visible regime. A hollow core fiber was used to generate broadband pulses, compressed down to sub-15 fs, allowing high spectral and temporal resolution measurements. The design relies on basic optical components (no diffractive optics or liquid crystal display) with pairwise manipulation of the beams, which lead to reduction of the signal modulation to the difference between the transition frequency and the laser frequency. The required timing precision as well as the mechanical stability is reduced due to the used geometry. For testing the integrity of the setup, stability measurements over several hours are presented as well as measurements on rhodamine 101 dye and Pentacene thin films.

The photophysics of porphyrins has been widely investigated because of their importance in biology and their relevance in a wide range of applications such as light harvesting applications, molecular electronics, and gas sensors. The energy of the photon absorbed by these systems is converted into electronic and vibrational energy, eventually triggering photochemical processes such as charge transfer, energy transfer, and bond breaking. Deep understanding of the specific early relaxation mechanism and nuclear wavepacket motion occurring in this family of molecules is therefore fundamental for further comprehension of the role of porphyrins in nature and future application using porphyrin-based molecular devices.

In the third chapter we discuss the impulsive heating of free-base porphyrins and the electronic and vibrational relaxation dynamics upon photo-excitation. Transient absorption and fluoresce up-conversion spectroscopy techniques with high temporal resolution were utilized to investigate the relaxation processes, and the heating/cooling dynamics. Wavepacket dynamics of free-base porphyrins are discussed in the fourth chapter, where the phase and spectral intensity of the vibrational modes were extracted using Fourier transform spectroscopy. Based on the mode phase and spectral dependent intensity each mode is assigned to being in-plane or out-of-plane mode and to whether it exists in the excited or ground state.

In the last chapter, excited state dynamics of triply fused diporphyrins in toluene is investigated using transient absorption spectroscopy. These highly π -conjugated organic systems are receiving considerable attention because they incorporate ease of synthesis with tunable chemical structure that can be tailored for various applications, such as molecular wires, mimic light harvesting complexes, and saturable absorbers dyes. These porphyrin tapes can chelate different metal centers, changing their optical and electronic properties. In this chapter a comparison between free-base, Zn, and Pt based triply fused diporphyrins is done in order to understand the role of the metal in the relaxation dynamics of these systems. By further comparing these systems with earlier studies, the peripheral substituents effects are also discussed. In the end, we show that the high ISC yield, long triplet lifetime, and high cross-section of Pt-3DP makes it a perfect candidate to be used as NIR sensitizer for photochemical up-conversion *via* triplet-triplet annihilation.

Keywords: Photophysics, non-linear optical spectroscopy, two-dimensional spectroscopy, transient absorption spectroscopy, fluorescence up-conversion, pulse compression, hollow-core fiber, free-base porphyrins, triply fused diporphyrins, metallo-porphyrins, electronic and vibration relaxation, wave-packet dynamics.

Sommario

Lo scopo di questa tesi è duplice: descrivere la progettazione e l'implementazione di un esperimento di spettroscopia bi-dimensionale in trasformata di Fourier e discutere la dinamica di rilassamento di sistemi porfirinici a seguito di un processo di foto-eccitazione. Il primo capitolo riassume le basi di spettroscopia ottica non lineare, seguito dalla spettroscopia bi-dimensionale e dalla spettroscopia di assorbimento transiente. Inoltre, vengono discussi la dinamica dei pacchetti d'onda ed il raffreddamento vibrazionale (*intra* ed *inter*-molecolare), con particolare attenzione alla differenziazione tra pacchetti d'onda di tipo *Condon* e *non-Condon*. Infine vengono presentate le basi di teoria del campionamento e della trasformata di Fourier, data la loro importanza nelle misure di spettroscopia bi-dimensionale e nell'analisi dei pacchetti d'onda.

Il secondo capitolo tratta della progettazione e dell'implementazione di un apparato sperimentale di spettroscopia bi-dimensionale in trasformata di Fourier che consente di ottenere lo spettro elettronico bi-dimensionale di campioni d'interesse nella gamma della luce visibile. Una fibra cava viene utilizzata per generare impulsi a banda larga, che vengono poi compressi sotto i 15 femtosecondi, consentendo misure con alta risoluzione spettrale e temporale. La progettazione è fondata sull'utilizzo di elementi ottici base (senza componenti ottiche diffrattive o basate su tecnologia a cristalli liquidi) con manipolazione accoppiata dei fasci di luce, cosa che consente la riduzione nella modulazione del segnale alla differenza tra la frequenza di transizione e la frequenza del laser. I requisiti sia di precisione temporale che di stabilità meccanica sono molto meno restrittivi grazie all'adozione di questa geometria. Al fine di comprovare l'integrità dell'apparato sperimentale, sono state effettuate molteplici misure di stabilità lungo l'arco di svariate ore, e sono stati condotti esperimenti prova su campioni di Rodamina 101 e su film sottili di Pentacene.

La foto-fisica delle porfirine è stata ampiamente investigata a cause del loro rilievo in ambito biologico ed in un ampio spettro di applicazioni quali quelle relazionate alla raccolta della luce, in elettronica molecolare e come sensori di gas. L'energia di un fotone assorbito da parte di questi sistemi è convertita in energia elettronica e vibrazionale, e può a sua volta innescare processi fotochimici quali trasferimento di carica o di energia, oppure la semplice rottura di un legame chimico. Un'approfondita comprensione del meccanismo specifico di rilassamento e del movimento dei pacchetti d'onda nucleari in questa famiglia di molecole è pertanto essenziale per una migliore comprensione del ruolo rivestito dalle porfirine in natura e per applicazioni future, fondate sull'impiego di dispositivi molecolari basati su porfirine.

Nel terzo capitolo si tratta del riscaldamento impulsivo di porfirine a base libera e della dinamica di rilassamento elettronico e vibrazionale a seguito del processo di foto-eccitazione. Le tecniche spettroscopiche di assorbimento transiente e di conversione fluorescente con alta risoluzione temporale sono state impiegate al fine di investigare i processi di rilassamento e la dinamica di riscaldamento/raffreddamento. La dinamica dei pacchetti d'onda di una porfirina a base libera viene discussa nel quarto capitolo, ove la fase ed i modi vibrazionali sono stati

estratti attraverso la spettroscopia in trasformata di Fourier. Sulla base della fase del modo e della dipendenza spettrale dell'intensità, ciascun modo è stato assegnato (i) come modo "sul piano" o "fuori dal piano", e (ii) come appartenente ad uno stato di base o ad uno stato eccitato.

Nel capitolo finale, viene investigata la dinamica dello stato eccitato di bi-porfirine triplamente fuse in toluene, attraverso la tecniche di spettroscopia di assorbimento transiente. Questi sistemi altamente π -coniugati hanno ricevuto molta attenzione poichè incorporano i vantaggi di un processo sintetico relativamente semplice con una struttura chimica manipolabile su misura a seconda delle applicazioni desiderate, quali fili molecolari, complessi che riproducano la raccolta della luce di sistemi naturali, e assorbitori coloranti saturabili. Questi nastri porfirinici posso chelare svariati centri metallici, cambiando di conseguenza le loro proprietà ottiche ed elettroniche. In questo capitolo viene presentata una comparazione tra bi-porfirine triplamente fuse a base libera, chelanti Zn e chelanti Pt, al fine di comprendere il ruolo del centro metallico nella dinamica di rilassamento di questi sistemi. Attraverso poi il raffronto tra questi esperimenti e studi precedenti, vengono analizzati gli effetti dei sostituenti periferici. Infine si dimostra che il sistema Pt-3DP è un perfetto candidato che puo' essere impiegato come sensibilizzante NIR per conversione fotochimica attraverso un processo di annientamento tripletto-tripletto, data l'alta resa di ISC, il lungo tempo di vita dello stato tripletto, e l'alta sezione trasversale.

Parole chiave: Foto-fisica, spettroscopia ottica non lineare, spettroscopia bi-dimensionale, spettroscopia di assorbimento transiente, spettroscopia di conversione fluorescente, compressione degli impulsi, fibra cava, porfirine a base libera, bi-porfirine triplamente fuse, metallo-porfirine, rilassamento elettronico e vibrazionale, dinamica dei pacchetti d'onda.

Contents

1	Basic concepts.....	1
1.1	Introduction.....	1
1.2	Spectroscopic experiments: theoretical representation.....	1
1.2.1	Non-linear polarization.....	1
1.2.2	Density matrix formalism of a statistical ensemble.....	2
1.2.3	The response function formalism.....	3
1.2.4	Linear response and lineshape functions.....	4
1.2.5	Third order polarization time resolved spectroscopy.....	6
1.2.6	2D Fourier transform spectra.....	10
1.2.7	Transient absorption spectroscopy.....	11
1.3	Wavepacket dynamics.....	12
1.3.1	Types of Wavepackets.....	13
1.3.2	Vibrational relaxation in condensed phases.....	19
1.4	Discrete Fourier transform.....	20
1.4.1	Sampling theorem and aliasing.....	21
1.4.2	Zero-padding.....	23
1.5	Heterodyne detection using frequency domain spectral interferometry.....	24
2	Implementation of an Ultra-Broadband Multidimensional spectroscopy Setup.....	27
2.1	Introduction.....	27
2.2	2D FT spectroscopy.....	27
2.3	2D spectra.....	28
2.4	Challenges.....	29
2.5	Choice of geometry.....	31
2.5.1	Interferometric based setup with active phase stabilization.....	31
2.5.2	Pump-probe geometry based setup.....	31
2.5.3	Diffraction optics based passive phase stabilized setups.....	33
2.5.4	DO free passive phase stabilized setups.....	34
2.6	Light source.....	34
	Pulse compression and characterization.....	38
2.7	Setup.....	44
2.8	Inherent Phase stability.....	48
2.9	Delay calibration.....	50
2.10	Acquisition procedure.....	51
2.11	Data analysis.....	54
2.12	Primary results.....	57
2.13	Conclusion.....	61

3	Impulsive heating and vibrational relaxation in free-base porphyrins.....	63
3.1	Introduction	63
3.2	Experimental section	64
3.2.1	Fluorescence up-conversion measurements.....	64
3.2.2	Transient absorption measurements.....	65
3.2.3	Sample preparation	65
3.3	Results	67
3.3.1	Fluorescence Up-conversion measurements.....	67
3.3.2	Transient absorption measurements.....	70
3.4	Discussion	73
3.5	Summary	78
4	Wave-packet dynamics in free-base porphyrins	81
4.1	Introduction	81
4.2	Experimental section	82
4.3	Data analysis	83
4.4	Results	85
4.4.1	Ultrafast fluorescence studies	85
4.4.2	Transient absorption studies	86
4.5	Vibrational modes assignment	92
4.6	Discussion	98
4.7	Summary	100
5	Excited state relaxation dynamics of triply fused diporphyrins.....	103
5.1	I. Introduction.....	103
5.2	Material and methods	104
5.2.1	The setup.....	104
5.2.2	Sample preparation	105
5.2.3	Data treatment.....	105
5.3	Results	106
5.3.1	Steady state spectroscopy	106
5.3.2	Free base triply fused diporphyrins (H2-3DP):	108
5.3.3	Zn-Zn triply fused diporphyrins (Zn-3DP):.....	111
5.3.4	Pt-Pt triply fused diporphyrins (Pt-3DP):	112
5.4	Discussion:	116
5.4.1	Conclusion:	119
6	References.....	121
7	Published work.....	137
8	Curriculum Vitae	159

Basic concepts

1.1 Introduction

The aim of this chapter is to refresh the reader's memory of the basic theoretical concepts needed to understand the light-matter interaction, which can be extended into understanding time resolved experiments. Then we will discuss some topics that will be useful to further understand the coming chapters. We will start by presenting the non-linear light induced polarization, and afterwards, we will turn to time-resolved experiments, i.e. the third-order polarization. Here, we will see that by systematically varying a sequence of three excitation pulses 2D spectroscopy measures the complete third-order response function. Then we will discuss briefly the transient absorption spectroscopy since it will be used to correct 2D spectra, and used independently to study the relaxation dynamics of molecular systems.

We will also discuss briefly the wave packets dynamics, and how can we resolve them in TA measurements. For that we set the basis to be able to differentiate between Condon and non-Condon wavepackets, theoretically and experimentally. Finally, we introduce briefly Fourier transformations since it will be used in the 2D spectra analysis as well as the extraction of the vibrational coherences from the transient absorption spectra. We introduce the sampling theory as well, which is important to respect when measuring a signal or extracting oscillations out of spectra.

1.2 Spectroscopic experiments: theoretical representation

Spectroscopy is the study of light interaction with matter, where an external electromagnetic field leads to a light induced polarization in the material which in turn relaxes by a light field emitted from the sample. Therefore, understanding spectroscopic techniques requires the knowledge about the microscopic properties and the quantum mechanical dynamics of the system under investigation, as well as the light induced macroscopic polarization $P(\vec{r},t)$. The light induced polarization $P(\vec{r},t)$ will be presented first, followed by a brief introduction of its quantum mechanical description based on the density operator formalism. Then, using a perturbative approach, we expand the density operator in terms of the electric field resulting in the response function formalism. Using the basis of the response function formalism we will discuss time resolved experiments. We will show that by systematically varying a sequence of three excitation pulses, 2D FT spectroscopy is able to completely measure the third order response function. Finally we will show that transient absorption spectroscopy is also a third order technique, and discuss its limitations stemming from the use of single excitation pulse.

1.2.1 Non-linear polarization

When impinging a laser pulse on matter, the electric field of the laser pulse induces a polarization of the material that can be split into linear and non-linear contributions [5].

$$P = P^{(1)} + P^{NL} = P^{(1)} + P^{(2)} + P^{(3)} \dots \quad \mathbf{1-1}$$

A relation between the electric field and the induced polarization can be presented using Maxwell's equations, where the polarization is associated directly with the electric field as follows

$$\nabla^2 E(\vec{r}, t) - \frac{1}{c^2} \frac{\partial^2}{\partial t^2} E(\vec{r}, t) = \frac{4\pi}{c^2} \frac{\partial^2}{\partial t^2} P(\vec{r}, t) \quad \mathbf{1-2}$$

This relation contains information about the electric field as well as the material properties. The induced polarization, its time dependence and transfer to the signal field unveil information about electronic and nuclear degrees of freedom, as well as their relaxation dynamics. Since the system we are dealing with is a quantum mechanical system, the expectation value of the polarization would be a more relevant observable to deal with.

$$\langle P(\vec{r}, t) \rangle = Tr[V\rho(t)] \quad \mathbf{1-3}$$

which is the trace of the interaction operator V and the density matrix $\rho(t)$.

1.2.2 Density matrix formalism of a statistical ensemble

In condensed phase systems, we deal with statistical ensembles of molecules, rather than a quantum mechanical pure state. There is no way to describe a statistical ensemble by a wavefunction, but it can be represented by the density matrix formalism. For a starting point, a pure state can be described by a single wavefunction Ψ , in which the density matrix is $\rho = |\Psi\rangle\langle\Psi|$. Therefore in the case of a statistical ensemble, the density matrix is defined as in Eq. 1-4 and in a basis representation as in Eq. 1-5:

$$\rho = \sum_s p_s |\Psi_s\rangle\langle\Psi_s| \quad \mathbf{1-4}$$

$$\rho = \sum_s p_s c_m^{s*} c_n^s = \langle c_m^{s*} c_n^s \rangle \quad \mathbf{1-5}$$

Here p_s is the probability of a system being in a state $|\Psi_s\rangle$, with $p_s \geq 0$ and $\sum_s p_s = 1$. Since eq. 1-4 is linear, we can express the expectation value of an operator \hat{A} as follows

$$\langle \hat{A} \rangle = Tr(\hat{\rho}\hat{A}) = \langle \hat{\rho}\hat{A} \rangle \quad \mathbf{1-6}$$

keeping in mind that there is no wavefunction representation which would be able to represent such a coherent superposition of states.

The time dependence of the density matrix of a statistical average can then be represented as follows

$$\dot{\rho} = \sum_s \frac{dp_s}{dt} c_n^s c_m^{s*} + \sum_s p_s \left(\frac{dc_n^s}{dt} c_m^{s*} + c_n^s \frac{dc_m^{s*}}{dt} \right)$$

$$= \sum_s \frac{dp_s}{dt} c_n c_m^* - \frac{i}{\hbar} [\hat{H}, \rho]_{nm} \quad 1-7$$

Eq. 1-7 contains two terms; the first one is related to statistical mechanics, and describes the dephasing and population relaxation, and the second one is related to quantum mechanics and leads to the Liouville - von Neumann equation.

1.2.3 The response function formalism

After we introduced the time dependent density matrix of a statistical average, we are ready to describe mathematically the polarization induced by an external electric field in a spectroscopic experiment. For that we will start by solving the Liouville-von Neumann equation mentioned in Eq. 1-7, which is the mixed state equivalent to the Schrödinger equation for a Hamiltonian H that contains an external electric field $E(\vec{r},t)$ [5].

$$H = H_0 + H_{int}(t) = H_0 - E(\vec{r},t)V \quad 1-8$$

Switching to the Liouville space notation will facilitate the discussion by treating the density matrix as a vector. Then the Liouville-von Neumann relation can be presented as follow

$$\dot{\rho} = -\frac{i}{\hbar} L\rho - L_{int}(t)\rho \quad 1-9$$

The next step is the expansion of $\rho(t)$ in powers of the electric field, i.e. in the number of interactions with this field

$$\rho(t) = \rho^{(0)}(t) + \rho^{(1)}(t) + \rho^{(2)}(t) \dots \quad 1-10$$

By introducing the Green's function of the quantum mechanical system in the absence of an external field in Liouville space $G(t) \equiv \vartheta(t)\exp(-\frac{i}{\hbar}Lt)$ and interaction times τ_i , the n-th order term of the formal solution of Eq. 1-9 can be expressed as presented in the figure below:

$$\rho^{(n)}(t) = \left(-\frac{i}{\hbar}\right)^n \int_{t_0}^t d\tau_n \int_{t_0}^{\tau_n} d\tau_{n-1} \dots \int_{t_0}^{\tau_2} d\tau_1 \quad 1-11$$

$$\times G(t - \tau_n) L_{int}(\tau_n) G(\tau_n - \tau_{n-1}) L_{int}(\tau_{n-1}) \dots G(\tau_2 - \tau_1) L_{int}(\tau_1) G(\tau_1 - \tau_0) \rho(t_0)$$

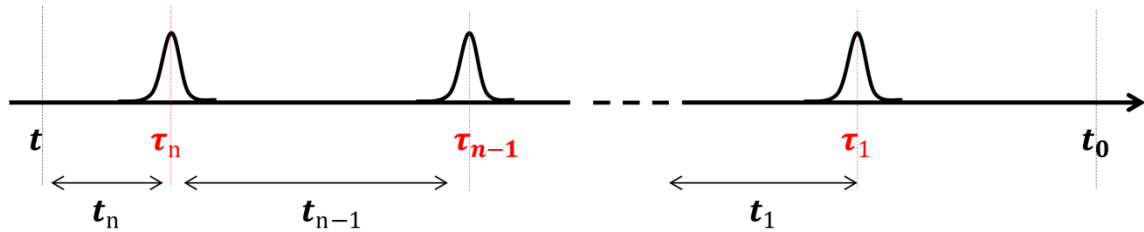


Figure 1-1 Time dependent density matrix with the time axis showing the sequential interaction of the system. Two time notations are presented, the interaction time τ , and the interval time t_x .

In the Eq. 1-11 introduced in the figure above, we could see that the starting point of the system is at $G(\tau_1 - t_0)\rho(t_0)$ where the system is initially at thermal equilibrium at t_0 . Each interaction comes separately in time, where the first interaction is at τ_1 , second is at τ_2 , and so on, where $t \geq \tau_n \geq \dots \tau_2 \geq \tau_1 \geq t_0$. After each interaction $L_{int}(\tau_1)$ with the system, the system is left to evolve according to the Green's function $G(\tau_n - \tau_{n-1})$. This sequence proceeds until the n-th interaction, where the system is left freely to evolve until t . Since our interactions with the system are through an electric field, we can express L as

$$L_{int}(\tau_n) = -E(t)V \quad \mathbf{1-12}$$

where V is the time-independent interaction operator in Liouville space. By changing the time variables from the interaction time to time intervals, and introducing the electric field into Eq. 1-11, we get:

$$\begin{aligned} \rho^{(n)}(t) = & \left(\frac{i}{\hbar}\right)^n \int_0^\infty dt_n \int_0^\infty dt_{n-1} \dots \int_0^\infty dt_1 G(t_n)VG(t_{n-1})V \dots G(t_1)V\rho(-\infty) \\ & \times E(\vec{r}, t - t_n)E(\vec{r}, t - t_n - t_{n-1}) \dots E(\vec{r}, t - t_n - t_{n-1} - \dots t_1) \end{aligned} \quad \mathbf{1-13}$$

Switching back to the interaction picture where V becomes time-dependent, and introducing it into Eq. 1-13. We can calculate the expectation value of the polarization as

$$\langle P(\vec{r}, t) \rangle = Tr\{V\rho(t)\} = \langle\langle V|\rho \rangle\rangle \quad \mathbf{1-14}$$

And now we can use Eq. 1-14 and write the n-th order polarization as

$$\begin{aligned} P^{(n)}(\vec{r}, t) = & \langle\langle V|\rho^{(n)} \rangle\rangle = \int_0^\infty dt_n \int_0^\infty dt_{n-1} \dots \int_0^\infty dt_1 S^{(n)}(t_n, t_{n-1}, \dots, t_1) \\ & \times E(\vec{r}, t - t_n)E(\vec{r}, t - t_n - t_{n-1}) \dots E(\vec{r}, t - t_n - t_{n-1} - \dots t_1) \end{aligned} \quad \mathbf{1-15}$$

where $S^n(t_n, t_{n-1}, \dots, t_1)$ is the n-th order response function, that is represented as

$$S^{(n)}(t_n, t_{n-1}, \dots, t_1) = \left(\frac{i}{\hbar}\right)^n \langle\langle V|G(t_n)VG(t_{n-1})V \dots G(t_1)V|\rho(-\infty) \rangle\rangle \quad \mathbf{1-16}$$

This response function contains complete microscopic information about the quantum mechanical system under investigation, since it includes the full time evolution of the density operator for a given interaction condition. This formalism is advantageous since it separates the treated quantum mechanical system $S^{(n)}$ and the classically treated external electric field.

1.2.4 Linear response and lineshape functions

It is important before we discuss the third order polarization to discuss the linear response function S. In the nonlinear formalism, we will deal with the system as multiple steps of linear perturbations that can be described by the linear response function. We will start by introducing the Liouville pathway

$$J(t_1) = Tr[V(t_1)V(0)\rho(-\infty)] \quad \mathbf{1-17}$$

with that the linear response would look like:

$$S^{(1)}(t_1) = \frac{i}{\hbar} \theta(t_1)(J(t_1) - J^*(t_1)) \quad \mathbf{1-18}$$

In the case of an isolated two level system with transition dipole moment μ , the time dependent interaction operator $V(t)$ can be considered

$$V(t) = U_0^\dagger(t)VU_0(t) \quad \mathbf{1-19}$$

Where $U_0(t)$ is

$$U_0(t) = \begin{pmatrix} \exp(-\frac{i}{\hbar}H_g t) & 0 \\ 0 & \exp(-\frac{i}{\hbar}H_e t) \end{pmatrix} \text{ and } V = \begin{pmatrix} \mu & 0 \\ 0 & \mu \end{pmatrix} \quad \mathbf{1-20}$$

Using Eq. 1-19 and 1-20, we can retrieve the linear response function $S^{(1)}$.

$$S^{(1)}(t_1) = -\frac{1}{\hbar} |\mu|^2 \sin(\omega_{eg} t) \quad \mathbf{1-21}$$

And the Liouville pathway

$$J(t) = |\mu|^2 \exp(-i\omega_{eg} t_1) \quad \mathbf{1-22}$$

introducing the energy gap frequency of a two level system $\omega_{eg} = \frac{(E_e - E_g)}{\hbar}$ into $S^{(1)}$ and $J(t)$. The response function oscillates at the transition frequency of the two-level system, which shows that the linear absorption in the time domain is nothing but two peaks at $\pm\omega_{eg}$ since we perform Fourier transformation. By that we can see that negative frequencies contribute since as well since $S^{(1)}(t)$ belongs to \mathbb{R} [5].

This representation works fine in an idealistic sample (diatomic molecule in vacuum), whenever we excite it will “forever” oscillate at the same frequency. However in the presence of a bath (such as the solvent for liquid samples), the surrounding will constantly affect the molecule leading to stochastic force on the molecule. To account for that, we have to consider an additional term to the Liouville pathway $J(t)$ that contains the line-shape function $g(t)$ [5].

$$J(t) = |\mu|^2 \exp(-i\omega_{eg} t_1) \exp(-g(t)) \quad \mathbf{1-23}$$

The lineshape function $g(t)$ is an integration over the frequency-frequency correlation function $C(t) = \langle \delta\omega(t)\delta\omega(0) \rangle$, where $g(t)$ is

$$g(t) = \int_0^t dt' C(t') \quad \mathbf{1-24}$$

$C(t)$ is constant in the case of purely inhomogeneously broadened system, i.e. ensemble of molecules with a static distribution of transition frequencies. In the case of Gaussian damping of the oscillatory response function ($g(t) \propto t^2$), the absorption line will have a Gaussian shape in the Fourier transform of $S^{(1)}$, While in a purely homogenous broadened distribution the absorption line shape will be a Lorentzian.

1.2.5 Third order polarization time resolved spectroscopy

The formalism described above, can be applied to all orders of nonlinear polarizations. The second order (lowest order) nonlinear polarization typically arises from a χ^2 nonlinearity which is limited to crystal materials with a non-centrosymmetric crystal structure, with the exception of nonlinearities happening at the surfaces, which are inherently non-symmetric. Therefore, a second order polarization would vanish in isotropic media [5]. The lowest polarization relevant to our multi-pulse experiments, two dimensional and TA spectroscopies, is the third order polarization $P^{(3)}(\vec{r}, t)$ presented as follows

$$P^{(n)}(\vec{r}, t) = \int_0^\infty d\tau_a \int_0^\infty d\tau_b \int_0^\infty d\tau_c S^{(3)}(\tau_a, \tau_b, \tau_c) \times \mathbf{E}(\vec{r}, t - \tau_a - \tau_b - \tau_c) \mathbf{E}(\vec{r}, t - \tau_b - \tau_c) \mathbf{E}(\vec{r}, t - \tau_c) \quad 1-25$$

The three electric fields are considered to be three δ -functions yielding a real-valued third order time-domain response function $S^{(3)}(\tau_a, \tau_b, \tau_c)$. The response function is nonzero only for τ_a , τ_b and τ_c being positive, to ensure causality [1]. Conforming with the previous literature of multidimensional spectroscopy, the waiting times between the first two pulses is named ‘‘coherence time τ ’’, and the between the second two pulses is ‘‘population time T’’, and the arrival time of the pulses is τ_n , as presented in Figure 1-2.

A triple inverse Fourier transform of the time-domain response function $S^{(3)}(\tau_a, \tau_b, \tau_c)$ with respect to τ_a , τ_b and τ_c yields the complex-valued third-order frequency-domain susceptibility $\chi^{(3)}(\omega_a, \omega_b, \omega_c)$ [2]. By varying the interaction times systematically an experimental determination of the susceptibility or the response function can be achieved. However, we need to consider that, since the time-domain electric fields are real valued, the frequency-domain electric fields are complex and will contribute to $\chi^{(3)}(\omega_a, \omega_b, \omega_c)$ with positive and negative frequencies [1, 2].

The emitted signal direction can vary depending on the combinations of the different signs of the frequencies contributing to the polarization. For example in a BOXCAR geometry (Figure 1-2 b), a contribution to the polarization with $\omega_c > 0$ and $\omega_b > 0$, and $\omega_a < 0$ will radiate along the vector $\vec{k}_s = -\vec{k}_a + \vec{k}_b + \vec{k}_c$, where \vec{k}_n is the wave vector of the excitation pulses. Since the BOXCAR geometry is fully non-collinear, the phase matching conditions will lead to the emission of the signal in the direction of \vec{k}_s , which is a completely different spatial direction of the three incoming pulses. Although the pulses are considered as δ -functions in formalism, in real experimental conditions these pulses still have a finite duration and the interaction can happen at any time within the pulse envelop, limiting the possibility to vary the waiting time τ_a, τ_b , and τ_c . Therefore the pulse centers at t_1 , t_2 , and t_3 must be moved. Note that envelop as well as the oscillatory phase terms should be shifted together (which is inherent in case of using mirrors) [1].

Typically in a 2D experiment the excitation fields used are identical pulses with complex amplitude $A(t) = \tilde{A}(t)e^{-i\phi(t)}$ centered at t_1 , t_2 , and t_3 in time, and centered at frequency ω_0 [1].

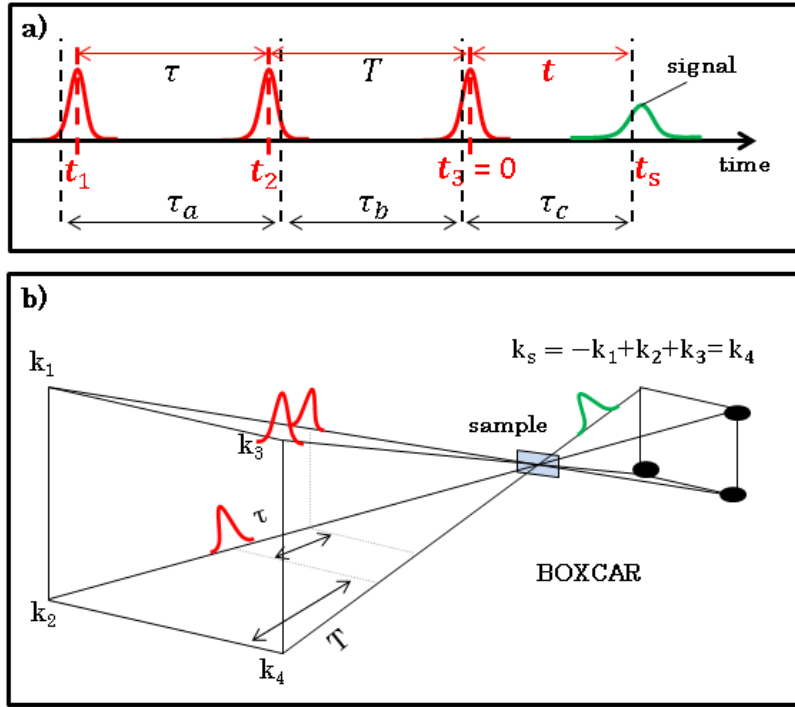


Figure 1-2 a) Definition of time variables. Time zero is defined at the center of the third excitation pulse. The first two pulses arrive at negative time $t_1 < 0$ and $t_2 < 0$, while the signal arrives at positive time delay $t_s > 0$. b) BOXCARS geometry showing the directions of the three excitation pulses and the emitted signal field.

$$\begin{aligned}
 E(t) = & \tilde{A}(t - t_1) \exp(-i\omega_0(t - t_1) + i\vec{k}_1\vec{r}) \\
 & + \tilde{A}(t - t_2) \exp(-i\omega_0(t - t_2) + i\vec{k}_2\vec{r}) \\
 & + \tilde{A}(t - t_3) \exp(-i\omega_0(t - t_3) + i\vec{k}_3\vec{r}) + c.c.
 \end{aligned} \tag{1-26}$$

As presented in Figure 1-2, time zero is chosen to be at the center of third excitation pulse. The waiting time between the pulses is customary called coherence time for $\tau = t_2 - t_1$, and population time $T = t_3 - t_2 = -t_2$. Substituting Eq. 1-26 into Eq. 1-25 yields $6 \times 6 \times 6 = 216$ terms as each field in the multiplication $E(\vec{r}, t - \tau_a - \tau_b - \tau_c)E(\vec{r}, t - \tau_b - \tau_c)E(\vec{r}, t - \tau_c)$ comprises 6 summands, since each term contains three envelope functions $\tilde{A}(t)$ or $\tilde{A}^*(t)$, and corresponding phase factors determining the directions and frequencies [1]. In other words, the polarization still contains contributions that arise from multiple interactions with the same pulse. In order to obtain contributions to the polarization that arise from exactly one interaction with each of the three excitation pulses, the non-collinear BOXCAR geometry can be used to detect the signal field emitted in the phase matching direction. This will limit the number of terms to only 6 out of 216, where all six of them share a common phase factor $\exp(-i\omega_0 t + i\omega_0 \tau)$ that is independent of the integration variables, and in addition they contain one of the phase factors that can be either of the following

$$\exp(i\omega_0(\tau_a + \tau_c)) \tag{1-27}$$

$$\exp(-i\omega_0(-\tau_a + \tau_c)) \tag{1-28}$$

$$\exp(i\omega_0(\tau_a + 2\tau_b + \tau_c)) \quad \mathbf{1-29}$$

And finally using the rotating wave approximation (RWA), considering only slowly oscillating terms and neglecting the fast ones in the calculation of the polarization, we can reach to the following equation [1, 6]

$$\begin{aligned} P_{rw}^{(3)}(\tau, T, t) = & e^{-i\omega_0 t + i\omega_0 \tau} \int_0^\infty d\tau_a \int_0^\infty d\tau_b \int_0^\infty d\tau_c \quad \mathbf{1-30} \\ & \times \left\{ S_{R,rw}^{(3)}(\tau_a, \tau_b, \tau_c) e^{-i\omega_0(-\tau_a + \tau_c)} \left[\tilde{A}^*(t - t_1 - \tau_a - \tau_b - \tau_c) \tilde{A}(t - t_2 - \tau_b - \tau_c) \tilde{A}(t - t_3 - \tau_c) \right. \right. \\ & \quad \left. \left. - \tilde{A}^*(t - t_1 - \tau_a - \tau_b - \tau_c) \tilde{A}(t - t_3 - \tau_b - \tau_c) \tilde{A}(t - t_2 - \tau_c) \right] \right. \\ & + S_{NR,rw}^{(3)}(\tau_a, \tau_b, \tau_c) e^{i\omega_0(\tau_a + \tau_c)} \left[\tilde{A}(t - t_2 - \tau_a - \tau_b - \tau_c) \tilde{A}^*(t - t_1 - \tau_b - \tau_c) \tilde{A}(t - t_3 - \tau_c) \right. \\ & \quad \left. + \tilde{A}(t - t_3 - \tau_a - \tau_b - \tau_c) \tilde{A}^*(t - t_1 - \tau_b - \tau_c) \tilde{A}(t - t_2 - \tau_c) \right] \\ & \left. + S_{DC,rw}^{(3)}(\tau_a, \tau_b, \tau_c) e^{i\omega_0(\tau_a + 2\tau_b + \tau_c)} \left[\tilde{A}(t - t_2 - \tau_a - \tau_b - \tau_c) \tilde{A}(t - t_3 - \tau_b - \tau_c) \tilde{A}^*(t - t_1 - \tau_c) \right. \right. \\ & \quad \left. \left. - \tilde{A}(t - t_3 - \tau_a - \tau_b - \tau_c) \tilde{A}(t - t_2 - \tau_b - \tau_c) \tilde{A}^*(t - t_1 - \tau_c) \right] \right\} \end{aligned}$$

where t_1 , t_2 , and t_3 are an abbreviation for $-\tau$, $-T$, and 0 to explicitly show that each pulse envelope \tilde{A} represents an envelope of the first, second, and third pulse, respectively. The response function was split into the summation of three Liouville pathways that survived the RWA rephasing $S_{R,rw}^{(3)}$, non-rephasing $S_{NR,rw}^{(3)}$, and double quantum coherence $S_{DC,rw}^{(3)}$. These pathways survive the RWA because they share a phase factor that cancels with the corresponding electric field factor. Each Liouville pathway has its own phase factor, as seen by the exponential factor in front of the integral, indicating that the polarization oscillates within a certain interval around ω_0 for the t coordinate and $-\omega_0$ for the τ coordinate [1]. In the rephasing Liouville pathway, the common phase factor is $e^{-i\omega_0(-\tau_a + \tau_c)}$, i.e. the phase acquired during τ_a is the complex conjugate of the one during τ_c . Therefore, the first interaction has to be with a negative wave vector \vec{k} , which is achieved only for $\tau > 0$. This will lead to the emission of a photon echo when the $P_R^{(3)}$ peaks at time τ femtoseconds after the third interaction. In contrast, in the non-rephasing pathways, the phase factor dictates that the first interaction is with a positive wave vector \vec{k} , this will be achieved for $\tau < 0$ and a free induction decay is observed. In this situation no rephasing will happen, leading to the absence of a photon echo. In the double quantum coherence pathway the system remains in coherence during the population time as well as the coherence time. In this pathway, the three pulses are required to be always close to each other in time and the first two interactions must occur with positive wave vector \vec{k} so the high lying coherence can be reached [7, 8].

An easy method to keep track of the changes in the density matrix caused by a sequence of interaction is using double sided Feynman diagrams. In these diagrams we keep track of the time of arrival of each pulse and its wave vector, which facilitate the process of finding which interactions are happening and the direction of the final emission. In Figure 1-3 we present the 16 double sided Feynman diagrams for resonant four-wave mixing with phase matching direction $-k_1 + k_2 + k_3$. In these diagrams, the ground state sublevels are labeled 0 or $0'$, singly excited sublevels are labeled 1 or $1'$, and double excited levels are labeled 2 , and the ket

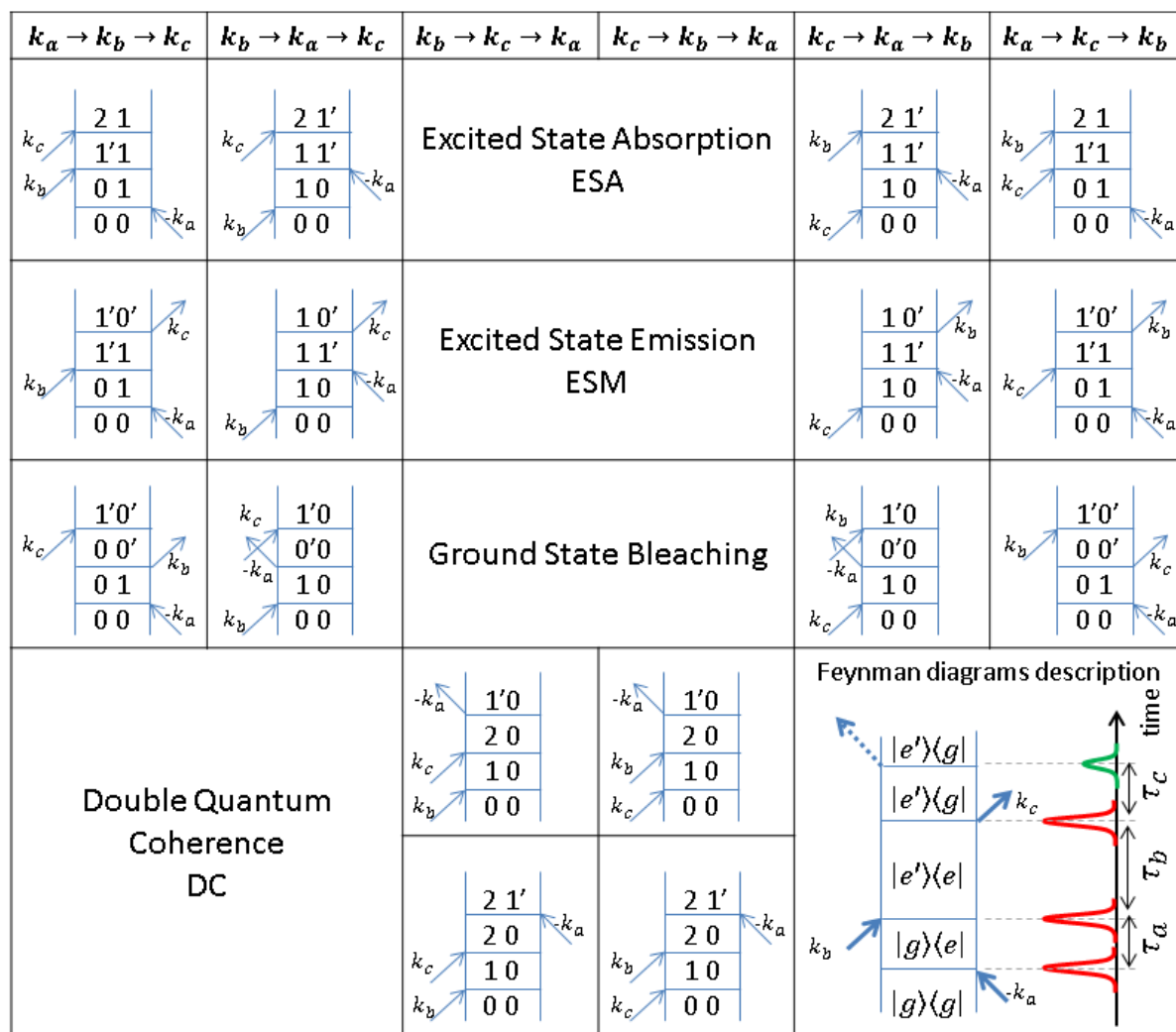


Figure 1-3 The 16 double sided Feynman diagrams for four wave mixing signals with phase matching direction $-k_1+k_2+k_3$. On top is the pulse sequence for each column, while each row present the type of process probed (ESA, ESM, GSB, and DC). In the right bottom side, is a small Feynman diagram representation showing the direction of the time axis and the time different between the pulses. Figure adapted from ref [2].

and bra are the left and right vertical line of the diagram. In the bottom of Figure 1-3 a small representation of the pulse sequence relation to the Feynman diagrams is presented. The arrows pointing towards the vertical lines on each side of the diagrams represent the excitation pulses and their time of interaction. Time increases from bottom to top along the vertical direction, which helps keeping track of the pulse sequence and relating it to certain processes. For each column the temporal pulse interaction order is given across the top.

In a two level system, pathways in which the system is in the excited state population after the second interaction, lead to stimulated emission (excited state emission), while the ground state bleach signal originate from molecules that are left in the ground state. This can be clearly seen in the diagrams in the second and third row. The second row represents the stimulated emission where the system is excited from $|0\rangle\langle 0|$ to $|0\rangle\langle 1|$ by the first pulse, and then to $|1\rangle\langle 1|$ with the second pulse. The system is left to evolve freely until the third pulse

arrives, taking the density matrix to the $|1\rangle\langle 0|$ level, stimulating the emission of a photon echo. In contrast, in the third row the first two pulses take the sample up to the excited state and back to the ground state, leaving the system to evolve in the ground state. Both pathways will lead to positive signals in the 2D spectra acquired. The first row represent the excited state pathways, where the system is excited left to evolve during the population time in the excited state, where the third pulse does not stimulate the emission, but instead excites it another time, creating a coherence with a second excited state $|2\rangle\langle 1|$ which is left to evolve and emits a photon echo. This ESA will contribute with a negative signal to our 2D spectra appearing at frequency depending on the energy gap ω_{12} [2, 5]. In the double quantum coherence case, the system is doubly excited with the first two pulses, and left at the end at the highest excited state to evolve. The DC will contribute negatively or positively to the signal depending on whether the system is left to emit from the highest $|2\rangle$ or first excited state $|1\rangle$.

1.2.6 2D Fourier transform spectra

After the calculation of the polarization $P_{rw}^{(3)}(\tau, T, t)$, a 2D frequency-frequency correlation spectrum can be obtained by performing Fourier transformation along the two time axis τ , and t , delivering a two dimensional spectrum corresponding to a population time T with frequency axis ω_τ and ω_t [5]. However, experimentally we do not detect the polarization directly but instead we detect the phase-matched signal field $E_s(\tau, T, t)$ [1]. The signal field is detected using a spectrometer, which automatically perform the first Fourier transformation over the t axis, so we really detect $E_s(\tau, T, \omega_t)$. The detected electric field can be directly related to the polarization using Maxwell's equations

$$E_s(\tau, T, \omega_t) = \frac{l}{2\epsilon_0 n(\omega_t) c} i\omega_t P^{(3)}(\tau, T, \omega_t) \quad 1-31$$

where l is the sample length, $n(\omega_t)$ is the linear refractive index, and c is the speed of light. Since the spectrograph already performed the first Fourier transform, one inverse Fourier transform is performed along the coherence time τ leading to the 2D frequency correlation spectrum at a specific population waiting time T

$$S_{2D}(\omega_\tau, T, \omega_t) = \int_{-\infty}^{\infty} iP^{(3)}(\tau, T, \omega_t) e^{-i\omega_\tau \tau} d\tau \quad 1-32$$

The obtained 2D spectrum is a complex quantity containing the absorptive information in the real part and the dispersive information in the imaginary part. In the equation of S_{2D} we notice that all the 2D spectra are additive, so that inhomogeneous broadening simply adds to 2D spectra [2]. This will appear as elongation of peaks along the diagonal only. Using the inhomogeneous lineshape we can track whether the homogeneous line shape depends on the excitation frequency.

For a measured 2D spectrum, the excitation and detection frequencies ω_t and ω_τ can be read directly off the double sided Feynman diagrams during τ_a and τ_c . The 2D FT superposes

signals from all the diagrams that contribute to the signal, yielding the total 2D photon echo signal. This can be a problem, since diagrams with negative transitions dipole product can cancel positive double resonances. This can be interpreted as femtosecond “freezing” of molecules [2], and can be solved by changing the pulse sequence and Fourier transforming with respect to different time variables, or techniques such as pulse shaping which enhances specific pathways over the others, and polarization dependent excitation [9].

1.2.7 Transient absorption spectroscopy

Transient absorption (TA) spectroscopy (also called pump-probe spectroscopy) is a technique that utilizes a two pulse sequence, where the first triggers a reaction or population and the second pulse follows after a certain time delay T to probe the system. TA probes the same third order non-linearity underlying signals as 2D spectroscopy, and the same formalism applies. To access the third order polarization we need three pulse interactions with the sample. Instead of using two excitation pulses as in the case of 2D spectroscopy, the first two interactions now occur within the same pump pulse with wave vector $\pm k_p$. Since the first two interactions happen simultaneously, we have no control on the coherence time anymore. As a consequence we can only access the spectrally resolved probe axis, while the excitation axis is lost. The two techniques are connected to each other by the projection slice theorem, where the projection of the real part of a 2D spectrum onto the probe frequency axis ω_t yields the TA signal at a specific population time T [2].

$$S_{TA}(T, \omega_t) = Re \left[\omega_t E_{pr}(\omega_t) \int \frac{S_{2D}(\omega_\tau, T, \omega_t)}{2\pi} d\omega_\tau \right] \quad 1-33$$

This projection slice theorem can be also used with multiple other techniques that also probe the third order nonlinearities such as transient grating.

The fact that the first two interactions with the system are made by the pump pulse, the phase matching conditions dictates that the emitted signal travels in the same direction of the probe $\vec{k}_s = -\vec{k}_{pu} + \vec{k}_{pu} + \vec{k}_{pr}$. The signal is therefore intrinsically heterodyned by the probe pulse, whose spectrum is measured in the absence of the pump pulse and accounted for during data evaluations. This reduces dramatically the requirements to perform pump-probe spectroscopy compared to multi-dimensional spectroscopy, which triggered some groups to implement 2D spectroscopy schemes using TA geometries, this will be discussed in the next chapter in details, and where introduce the advantages and disadvantages of such implementation.

The fact that the probe triggers the signal emission in its direction and is used to detect it at the same time results in an unambiguous measurement of the absolute signal phase. This can be of great value in the data analysis of the 2D spectra. To phase the data using the projection slice theorem, the real part of the projection of the 2D spectrum onto the probe axis is multiplied by a phase factor [1].

$$A_{2D}(T, \omega_t) = Re \left[\frac{\omega_t}{n(\omega_t)} \int S_{2D}(\omega_\tau, T, \omega_t) e^{i(\varphi_c + (\omega_t - \omega_0)t)} d\omega_\tau \right] \quad 1-34$$

This would yield in finding the absolute phase of a 2D spectrum acquired in BOXCAR geometry with an ambiguous phase between the signal and the local oscillator [1, 2]. Typically to achieve high accuracy on the phasing process, the TA must be measured using identical pulses to the ones used to measure the 2D spectra. This can be done by using two of the beams in the box geometry to perform the TA measurement.

In order to obtain the TA signal, we need to measure the probe spectrum passing through the sample in the case of pumped and un-pumped sample. In our case we use a shot-to-shot detection system, a very fast optical chopper is used to block the odd pump pulses and record the odd and even probe pulses. By employing a fast acquisition system using a fast CCD and DAQ cards triggered by the laser and the chopper, we can easily differentiate between the odd and even pulses. This allows us to measure the transmitted pulse of the pumped and un-pumped sample. The TA spectra are calculate as follow

$$\Delta OD = -\log_{10} \left(\frac{I_{pu}^{pr}}{I_0^{pr}} \right) \quad \text{1-35}$$

Where I_{pu}^{pr} and I_0^{pr} are the pumped and un-pumped probe intensity, respectively. The shot-to-shot measurement does not require a reference, since the laser spectrum will not change much between the single shots, and due to the high statistics. The phasing procedure will be discussed in the next chapter showing some examples.

1.3 Wavepacket dynamics

To understand chemical processes entirely, we need to access information about the nuclear motions during the course of the reaction with sufficient spatial resolution and temporal resolution. In this respect, the concept of vibrational wavepackets, known as coherent superpositions of vibrational eigenstates, has proven to be very useful [10]. The nuclear wave packets are well localized in space, and their time evolution is a quantum counterpart of the classical particle-like evolution of the system. When using an ultrafast laser pulse to monitor molecular dynamics, we are spatially selecting a significant portion of the ensemble [11]. This selected portion is transferred to a nonstationary state in the excited state (ES) potential (Franck-Condon (FC) transition from the ground state GS) after which the molecules start to move in phase, i.e. coherently [12, 13]. At the limit of exciting a molecular system with a pulse shorter than its vibrational period, a wavepacket can be treated in classical form, as long as the probability distribution is well localized and follows a classical trajectory over time [14].

In order to generate and observe WPs, several techniques can be used. In this thesis we utilize transient absorption spectroscopy, fluorescence up-conversion, and 2D FT spectroscopy techniques. In TA measurements we can visualize the WP dynamics by the induced change in the signal intensity (excited state absorption, stimulated emission and ground state bleach) observed at different time delays. By taking advantage of the broadband detection, we can resolve the spectral dependent phase and intensity of the WPs which enables the assignment of the WPs to a specific state and to conclude information about the shape and position of the

potential energy surface. For example, a breathing WP will appear in TA spectrum by changing its shape (spectrally) in time, therefore if single wavelength detection is employed, such information is lost. In contrast to TA, the detection of the fluorescence allows the selection of the WPs in only the excited state of the system. By detecting the fluorescence at different wavelength overtime, we can track the oscillation of the WP in the ES potential. The spectral dependence of the emission depends on the instantaneous inter-nuclear separation in addition to the information about the GS and ES potential energy surfaces.

In the next section we will present two types of WPs, the Condon type and the non-Condon type, where the FC approximation fails. Then we will show how to experimentally differentiate between them, and between WPs originating from different states (ES and GS). Finally we will present vibrational relaxation in condensed phase.

1.3.1 Types of Wavepackets

Using the Born-Oppenheimer approximation, the wave function of a molecular electronic state can be factorized into electronic and nuclear component in most molecular systems. Consequently, the transition dipole depends directly on the nuclear wave function overlap given by the Franck-Condon factor. As a result of WP formation either in the excited or ground state, time dependent FC overlap leads to modulation in the signal intensity on the same frequency of the WP movement. In such a case the Condon approximation is satisfied, and the WP is called Condon-type WP. The Condon approximation fails for non-allowed transitions and when mixing between the electronic and vibrational wave functions happens as in the case of porphyrins, where the Q band is known to originate from the Herzberg-Teller type transition [15], which causes the electronic transition probability to be exchanged [16]. This violates the Condon approximation when the WP motions directly cause structural deformation of the molecule and as a consequence modification of the corresponding electronic energies of the states. The change in the electronic transition energies of the states is experimentally observed by time dependent modified absorption intensity [16]. Thorough experimental and theoretical works on non-Condon WP motion in various samples (e.g. Porphyrin J-aggregates, and Thiophene derivatives) have been performed by Kobayashi et al., introducing the Dynamic Intensity Borrowing (DIB) concept in case of strong Herzberg-Teller transitions [17-19]. In this section, a basis for assignment of the different vibrational modes will be given under different criterion, whether it's a Condon or non-Condon mode, the PES that the WP is moving on (ground or excited state), and a differentiation between displacement and/or curvature modification of the PES due to the WP motion.

1.3.1.1 Condon type WP

The main difference between the Condon type and non-Condon type WP is expressed by the time dependent transition dipole moment between two vibronic states. Setting a basis for discussion, we need to start by presenting the Condon type WP, and then consider the more complex case of the non-Condon type. Under the Born-Oppenheimer approximation the wave function of a molecular system can be factorized into the electronic part and nuclear part as

presented in Eq. **1-36**, where q and Q represents the electron and nuclear coordinates, respectively.

$$\Psi(q, Q) = \Phi(q, Q) \chi(Q) \quad \mathbf{1-36}$$

The electronic transition dipole moment $\mu(q) = eq$ between an initial and final vibronic state (e.g. ground and excited states in case of WP moving on the excited state PES), presented by $\Psi_1(q, Q)$ and $\Psi_2(q, Q)$, respectively, is given in Eq. **1-37** based on Condon approximation as follows [19, 20].

$$\begin{aligned} \langle \Psi_1(q, Q) | \mu | \Psi_2(q, Q) \rangle &= \langle \Phi_1(q, Q) | \langle \chi_1(Q) | \mu | \Phi_2(q, Q) \rangle \mu | \chi_2(Q) \rangle \\ &= \langle \Phi_1(q, Q) | \mu | \Phi_2(q, Q) \rangle \langle \chi_1(Q) | \chi_2(Q) \rangle \\ &= \langle \mu \rangle F \end{aligned} \quad \mathbf{1-37}$$

Where F is the Franck-Condon factor, which is the overlap integral between the vibrational wave functions of the ground and excited states. Stressing again, that such a formalism holds only in case the transition between the two states is allowed. In this situation, the transition dipole does not depend on the configuration change induced by the vibrations. On the other side, the FC factor is directly related to the motion of the WP on the PES along a certain normal coordinate [16, 21]. As a consequence, the change in transition probability depends solely on the time dependent FC factor. This time dependent FC factor is expressed in equation **1-38** [16].

$$F = \sum_l \sum_m c_l^* c_m \langle \tilde{\chi}_l^i(Q) | \tilde{\chi}_m^f(Q) \rangle = \sum_l \sum_m c_l^* c_m \langle \chi_l^i(Q) | \chi_m^f(Q) \rangle e^{i(l-m)\omega_v t} \quad \mathbf{1-38}$$

The nuclear wave function with a vibrational quantum number of l or m is presented in **1-38** as $|\tilde{\chi}_a(Q)\rangle = |\chi_a(Q)\rangle e^{ia\omega_v t}$, where ω_v is the molecular vibrational frequency relevant to the vibronic coupling. The pump laser spectrum and the cross section of the ground state absorption are represented by $c_l^* c_m$. The oscillatory part of the relation is multiplied by the FC factor depending on the vibrational quantum number l and m , and the initial and final state. Therefore, a linear combination of the overlap between the wave functions in the ground state and the vibrational levels populated by the pump pulse in the excited state lead to the time dependent FC overlap, where the oscillator strength is conserved.

1.3.1.2 Non-Condon type WP

In the previous part, the transition dipole moment was considered to be independent of the nuclear coordinates change. Here, this premise does not hold any more, the transition dipole can be expanded using Herzberg-Teller expansion of the states to account for vibronic coupling. Therefore, in this case a three level system composed of S_0 , S_1 and S_2 , with vibronic coupling between S_1 and S_2 is considered. According to the work of Eyring et al. the transition dipole moment operator can be expanded to be expressed in terms of the displacement of nuclear coordinates from the equilibrium configuration, in order to describe the vibronic coupling effect [19, 22]. This situation is analogous to the case of free base porphyrins, where the Q states are forbidden due to the symmetry of the electronic structure.

It becomes allowed and gains intensity through the mixing of the electronic properties with the B state by the configuration interaction and the vibronic coupling [15]. The following wave functions are considered for the three levels, taking into account the vibronic coupling between S_1 and S_2 [16, 19].

$$|S_0(q, Q)\rangle = |\phi_0(q, Q)\rangle |\chi_n^0(Q)\rangle \quad \mathbf{1-39}$$

$$|S_1(q, Q)\rangle = \left(|\phi_1(q, Q)\rangle + \frac{H_{\text{vib}}}{\Delta E_{21}} Q |\phi_2(q, Q)\rangle \right) |\chi_m^1(Q)\rangle \quad \mathbf{1-40}$$

$$|S_2(q, Q)\rangle = \left(|\phi_2(q, Q)\rangle - \frac{H_{\text{vib}}}{\Delta E_{21}} Q |\phi_2(q, Q)\rangle \right) |\chi_l^2(Q)\rangle \quad \mathbf{1-41}$$

The electronic and nuclear wave functions of each state S_0 , S_1 , and S_2 are represented by $|\phi_x(q, Q)\rangle$ and $|\chi_k^x(Q)\rangle$, respectively for $x = 0, 1$, and 2 . In the nuclear wave function $|\chi_k^x(Q)\rangle$, the vibrational quantum number is denoted by $k = n, m$, and l . Since we considered the vibronic coupling happening between S_1 and S_2 , then both wave functions are interacting between each other through the mixing of the electronic configuration. S_1 and S_2 are not bound to be the first and second excited state, but can be any two states that interact together. In the porphyrin's case, we can consider S_1 to be the Q state, and S_2 to be the B state. Where we have intensity borrowing from the B state to the Q state, denoted here by the addition of the $|\phi_2(q, Q)\rangle$ to the S_1 , and subtraction from the S_2 wave function. The strength of the interaction is given by the difference in energy between the two bands ΔE_{21} and the interaction Hamiltonian H_{vib} . Finally, the transition dipole can be calculated, which will not have constant strength; instead it will vary depending on the vibrational motion of the mode and the consequent configuration interaction of the two electronic states. The effective electronic wave functions will be expressed by the original electronic wave function and the additional mixing with the other state as presented in Eq. **1-42**, considering $|\phi_Q(q, Q)\rangle = |\phi_1(q, Q)\rangle$ for the Q state, $|\phi_B(q, Q)\rangle = |\phi_2(q, Q)\rangle$ for the B state, and α represents the degree of mixing.

$$|\phi_Q(q, Q)\rangle = |\phi_Q^0(q, Q)\rangle + \alpha |\phi_B(q, Q)\rangle \quad \mathbf{1-42}$$

The transition probability is given as follows [16, 18, 19]:

$$\begin{aligned} & \langle S_1(q, Q) | \mu(Q) | S_0(q, Q) \rangle \\ &= \langle \chi_m^1(Q) | \left(\langle \phi_1(q) | + \frac{H_{\text{vib}}}{\Delta E_{21}} \langle \phi_2(q) | Q \right) \mu | \phi_0(q) \rangle \chi_n^0(Q) \rangle \\ &= \langle \phi_1(q) | \mu | \phi_0(q) \rangle \langle \chi_m^1(Q) | \chi_n^0(Q) \rangle \\ & \quad + \alpha \langle \phi_2(q) | \mu | \phi_0(q) \rangle \langle \chi_m^1(Q) | \chi_n^0(Q) \rangle \\ & \quad + \frac{H_{\text{vib}}}{\Delta E_{21}} \langle \phi_2(q) | \mu | \phi_0(q) \rangle \langle \chi_m^1(Q) | Q | \chi_n^0(Q) \rangle \\ &= F_1 + F_2 + F_3 \end{aligned} \quad \mathbf{1-43}$$

$$F_1 \equiv \mu_{10}^0 \langle \chi_m^1(Q) | \chi_n^0(Q) \rangle \quad \mathbf{1-44}$$

$$F_2 \equiv \alpha \mu_{20} \langle \chi_m^1(Q) | \chi_n^0(Q) \rangle \quad \mathbf{1-45}$$

$$F_3 \equiv \beta \mu_{20} Q_{mn} \quad \mathbf{1-46}$$

Where β , μ_{10} , and μ_{20} are:

$$\beta = \frac{H_{\text{vib}}}{\Delta E_{21}} \quad \mu_{20} = \langle \phi_2(q) | \mu | \phi_0(q) \rangle \quad \mu_{10} = \langle \phi_1(q) | \mu | \phi_0(q) \rangle$$

The transition dipole moment presented in Eq. **1-43** is divided into three parts. The first part is F_1 which is the ordinary FC factor without any non-Condon effects, which is identical to the one presented in Eq. **1-37** [19]. F_2 is a term for static intensity borrowing by the electron correlation mechanism [19]. Although the F_1 , F_2 , and F_3 are calculated for the transition probability from S_0 to S_1 , the factorized variables F_2 and F_3 contain the transition dipole moment between S_0 and S_2 . F_3 is a dynamic intensity borrowing (DIB) [16, 18] by the vibronic coupling. In the case of porphyrins, we can roughly consider that the FC factor is nearly unity and the vibrational excitation is mainly caused by the DIB presented in Eq. **1-46**. Assuming an impulsive limit, the time dependent wave function can be expressed as follow [18]:

$$|\Psi(t)\rangle \equiv e^{\frac{iHt}{\hbar}} \mu(q) |S_0(q, Q)\rangle \propto |\alpha|^2 \mu_{20} |\phi_2 \chi_0^0\rangle + \beta \mu_{20} \sum_{m \neq 0} Q_{m0} e^{-im\omega_v t} |\phi_2 \chi_m^0\rangle \quad \mathbf{1-47}$$

Using equation Eq. **1-47**, the transition between the ground state and the excited state WP can be presented as follow:

$$\langle S_0(q, Q) | \mu | \Psi(t) \rangle = |\alpha|^4 \mu_{20}^4 + |\beta|^2 \mu_{20}^2 \sum_{m \neq 0} |Q_{m0}|^2 e^{-im\omega_v t} \quad \mathbf{1-48}$$

In the case of free base porphyrins, μ_{20} is replaced by the transition dipole between the ground and B state μ_{BG} , and $S_0(q, Q)$ is considered the ground state wave function. The square of Eq. **1-48** represents the difference absorption signal measured. Therefore the DIB corresponds to a real time observation of the vibronic coupling between the Q and B bands, which is manifested by the coefficient Q_{m0} [18]. In other words, this model allows the transition dipole moment to be modulated as a function of the WP motion, leading to non-conserved oscillator strength. Such a WP will synchronously modulate both the BL/SE and ESA signals, which will be reflected in a constant phase across the bands, and only π phase jumps appear between the two processes. Therefore, in the case of DIB, the integrated signal intensity across the Q band should not be constant, and the modulation should persist.

1.3.1.3 Wavepacket motion of the ground state PES

Differentiation between WP in motion on the ground state or excited state PES can be directly related to the initial phase of the oscillation and its spectral dependence over the absorption band. Wavepackets in the ground state are generated through impulsive stimulated Raman scattering. As presented in Figure 1-4 a, the WP is generated in the ground state at

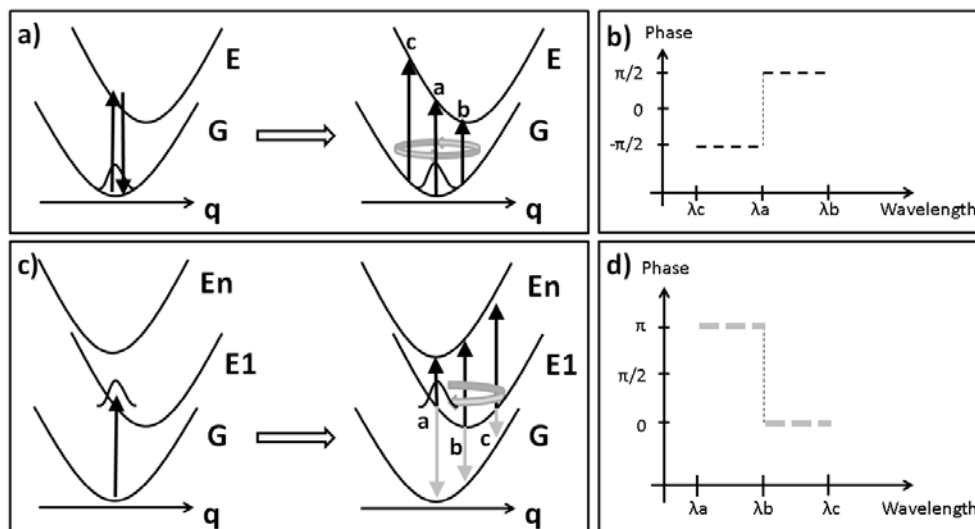


Figure 1-4 a) Wavepacket motion on the ground state PES. b) Wavepacket motion on the ground state PES.

point **a** located in the bottom of the PES. This WP can oscillate both ways along the vibration coordinate q , starting from $\mathbf{a} \rightarrow \mathbf{b} \rightarrow \mathbf{a} \rightarrow \mathbf{c}$ or from $\mathbf{a} \rightarrow \mathbf{c} \rightarrow \mathbf{a} \rightarrow \mathbf{b}$. The presence of the WP at a certain point along the vibrational coordinate leads to decrease in the absorption intensity at the probe energy (let's call it λ_a) corresponding to the vertical energy transition from the ground state to the excited state, as demonstrated by arrows upwards. When the WP moves away from point **a**, the absorption intensity at wavelength λ_a will increase. As a consequence, the oscillation of the WP along the vibration coordinate leads to modulation of the difference absorption spectra at λ_a at the same frequency of the vibrational mode.

When the WP moves from $\mathbf{a} \rightarrow \mathbf{b}$, the absorption intensity at λ_b will decrease and at the same time, the absorption intensity at point λ_a will increase. Therefore the oscillation appearing at in the time traces at wavelength λ_a will have a $\Phi_a = 0$, while at while at λ_b the oscillation will be shifted by half an oscillation, which is $\Phi_b = \pi/2$. As a consequence, the WP at point **c** will arrive after a half cycle, which will be shifted by π , therefore the oscillations will appear in the time trace at λ_c with a phase of $\Phi_c = -\pi/2$, as depicted in Figure 1-4 b. If the WP moves along the opposite direction, the phase will be reverse between **b** and **c**, yielding $\Phi_b = -\pi/2$ and $\Phi_c = \pi/2$. Therefore the oscillations on the time traces appearing due to a WP prepared in the ground state is always represented by a sine function [20, 23, 24].

1.3.1.4 Wavepacket motion of the excited state PES

The oscillation of the WP on the excited state PES modulates the signal of the probe at the same frequency of the WP movements from $\mathbf{a} \rightarrow \mathbf{b} \rightarrow \mathbf{c} \rightarrow \mathbf{b} \rightarrow \mathbf{a}$, considering that the WP was initially prepared at point **a**. Figure 1-4 c and show the movement of the WP and the phase corresponding to its position. The modulations due to the WP will appear in both the ESA (black) and GSB/SI (gray). In the SI region, the phases of the oscillation are 0, $\pi/2$, and π , for points **a**, **b**, and **c**, respectively. Based on the phase of these oscillations, a WP on the excited state PES is always represented by a cosine function [20, 23, 24]. In the ESA region, the

oscillations will appear at the same frequency but with a π phase difference. Assuming comparable ESA and GSB/SI contribution to the signal, a π phase difference must show in the oscillations between $E_{\text{probe}} = E_{\text{abs}}$ and $E_{\text{probe}} = E_{\text{abs}} - 2 \times E_{\text{stokes}}$, where E_{abs} and E_{stokes} are the peak photon energies of the absorption and the shift of the maximum of the fluorescence spectra from E_{abs} , respectively [17, 18]. This π phase change signifies the region where the signal dominance is changing between SI and ESA. This phase flip can be washed out in the case of ESA dominated signal.

In both the cases of WP on the excited or ground state PES, the integrated signal intensity (I.S.I.) of the spectral region of the band should not be modulated. These WP models are based on the simultaneous photoexcitation of the multi-vibrational quantum states depending on the Franck-Condon factor while conserving the transition dipole moment, and assumes that transition from the ground state to the excited state is allowed. Therefore, these models are the typical WP motion where the Condon approximation is still valid.

The cases where the initial phase differ from 0, $\pm\pi$, or $\pm\pi/2$, the WP motion is considered to be a mixed contribution of the WP motion on the ground and excited state. This can happen when the frequency of the mode in both excited and ground state are close to each other, if both the PESs have comparable shapes. This is highly expected in porphyrins since in the excited state the molecule does not undergo geometrical reorganization keeping the PES nearly identical. This makes it harder for resonant Raman studies to identify modes happening in the ground or excited state due to loss of phase.

1.3.1.5 Curvature and displacement of the PES

Both Condon and non-Condon type WP motion can induce effects on the displacement and curvature of the PES of the involved states. In the case of a shift of the PES of the final state with respect to the initial state, the spectral change will resemble the first derivative of the absorption spectrum. Typically this situation happens when very large geometrical relaxation occurs upon photoexcitation [16]. A π phase jump should be present at the peak wavelength of the absorption band [16, 20]. In contrast with the displacement case, when the PESs of both states are perfectly overlapped (very small stokes shift), the oscillations usually happen due to the breathing of the WP instead of moving between two turning points. The WP will appear due to the second order difference between the involved states, which is given by the breathing of the WP in time. In cases of small geometrical changes, the curvature of the PES of the initial and final states is nearly identical. Accordingly, the spectral change due to a breathing WP is determined by the second derivative of the involved transitions. In the case of ground state WP, the spectral intensity of the oscillation will resemble the second derivative of the static absorption spectrum, while a WP motion on excited state PES will resemble more the second derivative of the SI/GSB and ESA spectrum [16, 19]. The zeroth order is always present in the case of the non-Condon modes, in addition to the first or second derivative contribution, to fulfill the non-conserved integrated transition probability [16]. Therefore, if the spectral dependent amplitude of a certain mode contains a contribution of the zeroth order, it can be safely considered to be caused by a non-Condon type WP motion.

1.3.2 Vibrational relaxation in condensed phases

Whenever we speak about chemical reactions or biological process, we cannot dismiss the effect of the surrounding environment, which in most cases are the solvent molecules. These solvent molecules play a crucial role in enhancing, driving and selecting the channels of the reaction. Their impact on vibrational relaxation stems from the fact that the solvent molecules can couple to the vibrational motion of the molecules; in the case of strong interaction, this will lead to alternating of the PESs of the solute. Such alteration of the PESs would give the solvated molecules different properties than the isolated ones, thereby permitting processes that were not possible in the latter case. Therefore, to be able to describe the reaction dynamics in solutions we need to understand the solvent-induced vibrational relaxation processes.

Two relaxation routes are typically considered in the solute-solvent interaction. The first relaxation route is the intramolecular vibrational energy redistribution (IVR) [25] to other modes of lower frequency in the solute itself without the assistance of the solvent. The second would be through external vibrational relaxation (EVR) [26] through vibrationally elastic collisions between the solvent and the solute involving the continuous adiabatic fluctuations in the energy levels of the solute molecules, which is known as pure dephasing. The harmonicity of the vibrational modes of the solute can be affected as well by the pure dephasing.

Vibrational relaxation times in liquid phase can vary vastly from fs to ps depending on the solute-solvent interaction. The IVR and EVR processes are typically competing processes. In the case of simple diatomic molecules in solution, these molecules are practically an isolated vibrational mode that has no possibility to couple to other intramolecular modes, leaving the IVR process practically non-existent. Because of this, diatomic molecules make the ideal system to study solute-solvent EVR by eliminating the interference from the competing IVR [13, 27]. Such experiments have the EVR happening in the range of picoseconds. When increasing the molecular complexity (organic molecules with more than 30 atoms such as porphyrins), the density of vibrational states increases and anharmonic coupling between the internal modes provide a competing channel to the EVR. If the coupling of these internal modes is sufficient, the vibrational energy deposited in a certain mode would equilibrate among the many other modes (IVR) in the time range of 10s to 100s of fs. Such a fast IVR relaxation would be by orders of magnitude faster than dissipation through energy transfer to the solvent through collisions (EVR) reducing its contribution [28].

Typically electronic and vibrational relaxations are described by making use of the approximations of the optical Bloch equations. In case of a two-level system, the total coherence decay rate in the optical Bloch picture using a statistical treatment of the stochastic, weakly-coupled solute-solvent interactions, is given by [29, 30]

$$\frac{1}{T_2} = \frac{1}{2} \left(\frac{1}{T_{1a}} + \frac{1}{T_{1b}} \right) + \frac{1}{T_2^*} \quad \mathbf{1-49}$$

$$\frac{1}{T_2} = \frac{1}{2T_1} + \frac{1}{T_2^*} \quad \mathbf{1-50}$$

where the second equation represents the case where the lower level is infinitely long lived (e.g. for the $v = 1 \rightarrow v = 0$ transition). T_{1a} and T_{1b} are the population life times of vibronic levels a and b and T_2^* is the pure dephasing time. In Eq. 1-50, T_1 is the lifetime of the upper level and T_2 can never exceed $2T_1$. For the general two-level system, the coherence decay time is limited by [29]

$$T_2 \leq \frac{2T_{1a}T_{1b}}{T_{1a} + T_{1b}} \quad \mathbf{1-51}$$

which implies that T_2 cannot exceed T_1 if $T_{1a} = T_{1b} = T_1$. These equations show that the optical Bloch picture only include dissipative terms that correspond to transitions between the system levels (T_1) and random fluctuations of system energy levels T_2 .

Based on the previous equations, we can conclude a relation between the slow rate of vibrational energy relaxation and the observation of vibrational WPs. This conclusion cannot be generalized since the optical Bloch treatments do not include coupling between populations and coherences as well as transfer of coherences between pairs of levels. In some rare cases, the EVR happens faster or on the same time scale as the loss of the phase coherence in the system i.e. $T_1 < T_2$, which can be accounted for by using the Redfield theory [29]. Such cases can be a result of very efficient coherence transfer between different levels.

1.4 Discrete Fourier transform

Fourier Transform is a linear integral transform that connects reciprocal spaces, such as time and frequency domain. A FT of a function of time is a complex-valued function of frequency, whose absolute value represents the amplitude of the various frequencies present in the original function, and whose complex arguments is the phase offset of the cosine of these frequencies [31]. Transformation from time to frequency domain of function $f(t)$ is represented as

$$F(\omega) = FT[f(t)] = \frac{1}{\sqrt{2\pi}} \int_{-\infty}^{\infty} f(t)e^{i\omega t} dt \quad \mathbf{1-52}$$

And the inverse Fourier transform FT^{-1} , from frequency to time of the function $F(\omega)$ is represented as

$$f(t) = FT^{-1}[F(\omega)] = \frac{1}{\sqrt{2\pi}} \int_{-\infty}^{\infty} F(\omega)e^{-i\omega t} d\omega \quad \mathbf{1-53}$$

This presentation considers a continuous integral transform, which is not the case in a real life experiment where we get a finite number of data points. This limitation arise from several

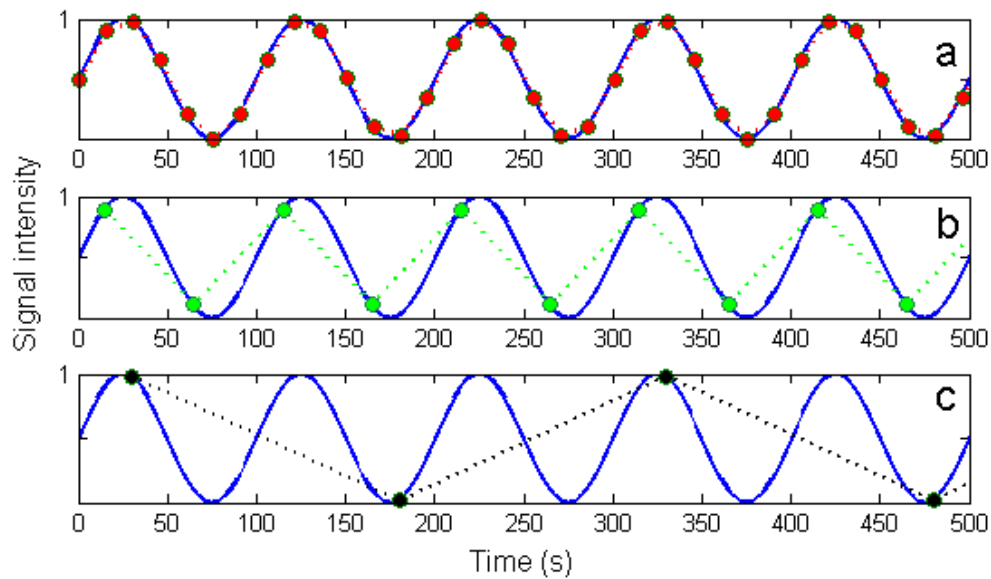


Figure 1-5 Illustration of the consequences of improper sampling. Panels (a), (b), and (c) show the sampling of identical continuous sin wave with different sampling rates. In (a) the sampling rate is high enough to capture the full details of the original signal. (b) the sampling used is at the Nyquist frequency. c) under sampling of the signal causes aliasing.

experimental aspects, such as the finite number of pixels of the CCD to sample the wavelength axis, or the finite number of points used to scan the coherence time to contract a 2D spectrum. The number of data intervals and ranges has to be wisely chosen to avoid under sampling and signal aliasing. For that reason we will introduce briefly the sampling theorem, the effects of under sampling and finally the effect of timing errors on the FT.

1.4.1 Sampling theorem and aliasing

The sampling theorem is the fundamental bridge connecting the analog signals (continuous) to the digital signals (discrete). This theorem describes the sufficient conditions for a sampling rate such that a discrete sequence of samples acquires all the information from a continuous time signal of finite bandwidth. In other words, a continuous function can be measured by a sequence of discrete samples, where these sampling points can be used to reconstruct the original function. The fidelity of the reconstructed signal depends on the density of the sampling points. This theorem is valid for a class of mathematical functions having a Fourier transform that is zero outside of a finite region of frequencies. In other words, for a function $x(t)$ that contains no frequencies higher than F_m , it can be confidently determined by sampling it at a frequency of $2F_m$, or at time interval of $1/2F_m$. If the sampling frequency is lower than the bandlimit, imperfection known as aliasing will appear in the reconstruction. The frequency threshold $F_m/2$ and sampling rate $1/2F_m$, are called Nyquist frequency and Nyquist rate, respectively [32].

In Figure 1-5, we present a continuous signal over 500 seconds of sinusoidal function of frequency of 100 s equivalent to 0.01 Hz. This continuous signal (solid blue) is sampled with three different sampling rate of 15 s (0.06), 50 s (0.02), and 150 s (0.006).

Basic Concepts

The sampling frequency used in Figure 1-5 is six times higher than the continuous sin wave frequency. This represents 6 samples taken over each complete cycle, leading to the ability to fully reconstruct the analog signal with high confidence. When going to the Nyquist sampling rate limit, sampling frequency being double the analog frequency, we can see that the frequency of the original wave can be still retrieved, and according to our criterion this can be still considered as proper sampling. In the last scenario, the sampling frequency is well below the recommended Nyquist sampling rate, which leads to a complete loss of the analog signal, and measuring a much lower frequency compared to the analog one. This phenomenon of changing frequency during sampling is called aliasing. This third example is what can be considered as improper sampling.

Now that we presented an example of proper and improper sampling, it is time to discuss aliasing and its effects of the integrity of the retrieved data. Let's consider $x(t)$ an analog continuous function with a Fourier transform $X(f)$

$$X(f) = \int_{-\infty}^{\infty} x(t)e^{-i2\pi ft} dt \quad \mathbf{1-54}$$

The Poisson summation formula indicates that the samples, $x(nT)$, of $x(t)$ are sufficient to create a periodic summation of $X(f)$ with a sampling frequency f_s . The result is

$$X_s(f) = \sum_{k=-\infty}^{\infty} X(f - kf_s) = \sum_{k=-\infty}^{\infty} T \cdot x(nT)e^{-i2\pi nTf} \quad \mathbf{1-55}$$

Which is a periodic function and its equivalent representation as a Fourier series, whose coefficients are $T \cdot x(nT)$. This function is also known as the discrete-time Fourier transform (DTFT) of the sequence $T \cdot x(nT)$ for integers n [33]. This is depicted in the figure below showing replicas of the $X(f)$ shifted by multiples of f_s and combined by addition.

When considering a bandlimited function ($X(f) = 0$ for all $|f| \geq F_m$), the sampling frequency should be chosen to be sufficient enough for the replicas to remain distinct from each other. If the Nyquist frequency is not satisfied, adjacent copies overlap, and it would not be possible to distinguish an unambiguous $X(f)$. All the frequencies above $f_s/2$ will be indistinguishable from the lower-frequency component. In such a case, the interpolation would produce the alias, instead of the original component.

Up to now, we have considered the sampling frequency for a finite temporal resolution which led to constraints for the minimum sampling frequency for a spectrum of maximum frequency F_m . Now we will take into account the finite number of points N that we acquire from an experiment. The discrete Fourier transform $Y = [Y_0, Y_1 \dots Y_{N-1}]$ of a time domain $y = [y_0, y_1 \dots y_{N-1}]$ can be defined as

$$Y_k = \frac{1}{\sqrt{N}} \sum_{m=0}^{N-1} y_m e^{i2\pi km/N} \text{ for } k = 0, 1 \dots N-1 \quad \mathbf{1-56}$$

The element $k = 0$ corresponds to DC term, which is a simple sum over all the elements of y , and the resolution in the frequency domain is given by

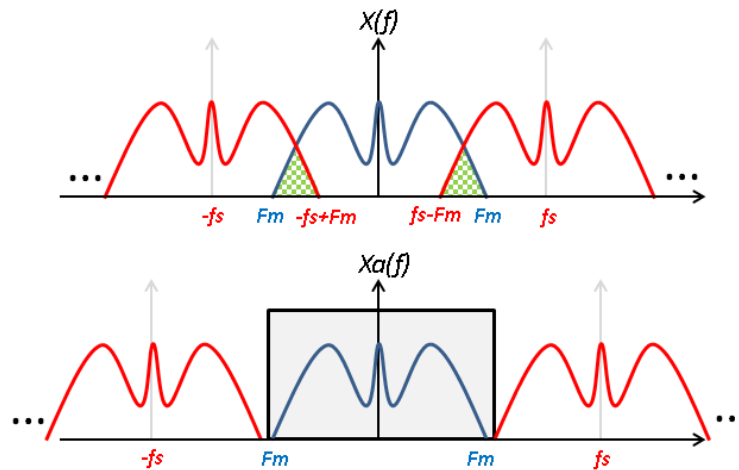


Figure 1-6 Spectrum $X(f)$ is the continuous Fourier transform of $x(t)$ with different sampling frequency f_s . In the upper plot, when the sampling frequency is lower than the Nyquist frequency, with overlapping copies of the Fourier transform. In the bottom plot, the sampling frequency is higher increasing the gap between the replicas with no more overlap

$$\Delta f = \frac{f_0}{N} = \frac{1}{T_s N} \quad 1-57$$

Therefore, when performing a 2D FT spectroscopy experiment, for a photon echo of limited time duration of t_L , it is sufficient to achieve a frequency resolution of $\Delta f = 1/t_L$. That puts some boundaries on the number of sampling points N and the number time window scanned T_s . For achieving high frequency resolution, we can always increase the number of sampling points. But due to practical reasons, long scan duration and phase instabilities, it would be always better to limit the number of sampling points to minimum.

1.4.2 Zero-padding

An effective method of increasing the number of points in the time domain is zero-padding. It has been shown in NMR spectroscopy that zero-padding is a safe method to increase the frequency resolution without altering the data measured [34]. When we measure a 2D spectrum, we typically take into account that no response will be present outside the measurement window. Therefore adding a block of zeros surrounding the data for longer time scales will increase the measurement window and number of points, which is reflected in an increase in the number of frequency points. This method will not add any extra information to the frequency data, but it can be used to increase the number of points in the frequency axis leading to more pronounced features and more “esthetic” spectra.

In TA data, when analyzing wave-packet dynamics in transient spectra the same frequency time limitations are available. The sampling frequency and the time window used define the frequency resolution of which we can resolve the frequency modes. Applying zero padding also increases the resolution of the Fourier transform without adding any extra information.

1.5 Heterodyne detection using frequency domain spectral interferometry

Frequency domain spectral interferometry (SI) is a technique that can measure the intensity profile and spectral phase of an ultrashort pulse [35, 36]. SI will be used in different situations in our experiments, starting by the delay stages calibration and more importantly to characterize the weak signal field in the 2D spectroscopy experiment [37-40]. In SI, the pulse under investigation $\tilde{E}_s(\omega)$ and a reference pulse $\tilde{E}_r(\omega) \exp(i\omega\tau)$ are temporally shifted by τ from each other and spatially superimposed into a spectrometer measuring their combined spectral intensity $S(\omega)$. The measured spectral intensity $S(\omega)$ for a constant τ would look like:

$$S(\omega) = |\tilde{E}_s(\omega) + \tilde{E}_r(\omega)e^{i\omega\tau}|^2 \quad 1-58$$

$$= E_s(\omega)E_s^*(\omega) + E_r(\omega)E_r^*(\omega) + \tilde{E}_s^*(\omega)\tilde{E}_r(\omega)e^{i\omega\tau + i\Delta\Phi(\omega)} + c. c. \quad 1-59$$

$$= I_s(\omega) + I_r(\omega) + \sqrt{I_s(\omega)I_r(\omega)}e^{i\omega(\tau) + i\Delta\Phi(\omega)} + c. c. \quad 1-60$$

$$= I_s(\omega) + I_r(\omega) + f(\omega)e^{i\omega(\tau) + i\Delta\Phi(\omega)} + c. c. \quad 1-61$$

where $I_x(\omega) = |\tilde{E}_x(\omega)|^2$, $\Delta\Phi(\omega) = \varphi_r(\omega) - \varphi_s(\omega)$, and $f(\omega) = \sqrt{I_s(\omega)I_r(\omega)}$. As one could notice, the first two terms are static, while the other two contain high frequency oscillatory components. The oscillatory term with its complex conjugate can be written as $2|f(\omega)|\cos(\Delta\Phi(\omega) + \omega\tau)$, resulting in interference fringes that are inversely proportional to the time delay between the two pulses τ , and the phase of the fringe pattern is directly connected to the relative spectral phase $\Delta\Phi(\omega)$ [36].

Figure 1-7 show the steps followed to isolated the spectral intensity and phase of the pulse under investigation. The first step is taking the inverse Fourier transform of the measured spectrum giving:

$$FT^{-1}[S](t) = E_s^*(-t) \times E_s(t) + E_r^*(-t) \times E_r(t) + f(t - \tau) + f(-t - \tau)^* \quad 1-62$$

The first two terms correspond to the field autocorrelation functions of the individual pulses ($FT^{-1}[I_s(\omega)] = E_s^*(-t) \times E_s(t)$) and are centered at $t = 0$ as seen from Figure 1-7b. The third term $f(t-\tau)$ is the correlation function shifted by τ , while the fourth is shifted by $-\tau$. The time difference τ should be chosen to be large enough such that $f(t-\tau)$ does not overlap with the peak around zero, which makes it possible to extract the signal by applying a numerical filter. The numerical filter (rectangular filter) is presented by the dashed blue lines setting the signals along the entire time axis to zero except the peak around $+\tau$. Finally by applying a Fourier transform to the filtered part we can go back to the frequency domain where the $f(\omega)e^{i\omega\tau + i\Delta\Phi(\omega)}$ is extracted. Figure 1-7d show the plot of $f(\omega)$, and the linear and non-linear relative phase between the two pulses. The dashed line shows the phase caused by the time difference between the two pulses, while the solid one contains the non-linear phase as well.

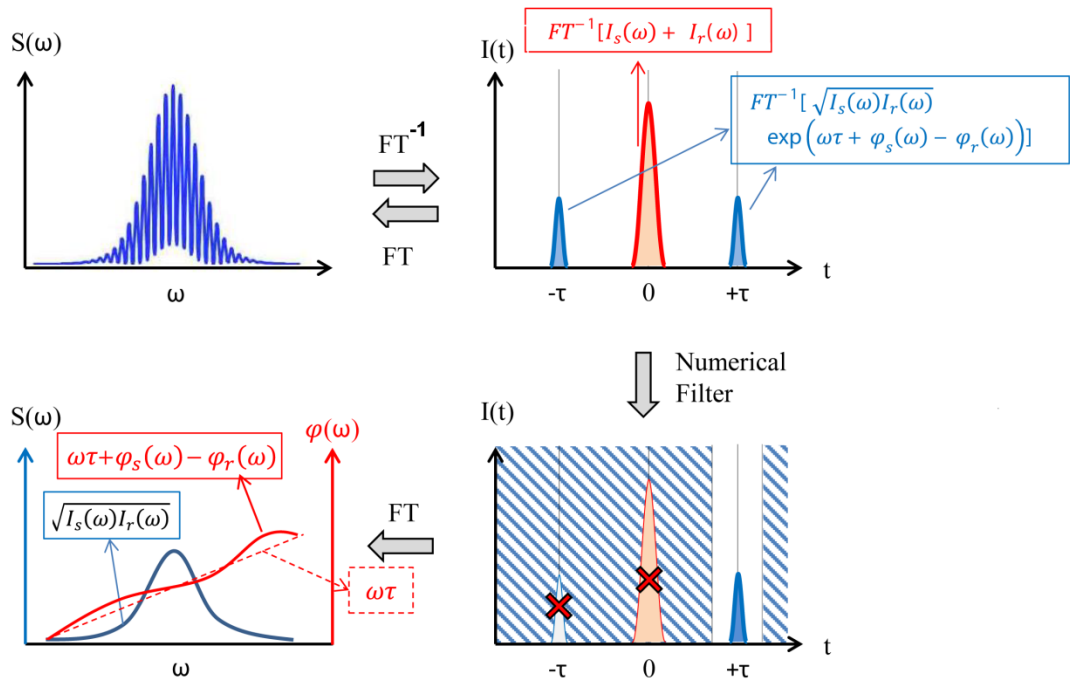


Figure 1-7 The four steps starting from the spectral fringes to the extraction of the spectral phase and intensity (figure adapted from www.fastlite.com).

Recalling Eq. 1-60, the first two factors of the static autocorrelation contributions are canceled by the numerical filtering and what we are left with is $\sqrt{I_s(\omega)I_r(\omega)} \exp(i\omega\tau + i(\Phi_r(\omega) - \Phi_s(\omega)))$. At this point, by using a well characterized reference beam knowing its spectral phase $\Phi_r(\omega)$ with a well-defined time delay τ between itself and the pulse under investigation, we can retrieve the spectrally dependent phase $\Phi_s(\omega)$ and amplitude $I_s(\omega)$.

Heterodyne detection is based on spectral interferometry. By sending a well characterized pulse called Local oscillator in the same direction of the emitted signal field, the phase and amplitude of the signal field can be well characterized. Heterodyne detection also offers amplification of the weak signal field as well, due to its multiplication with the local oscillator field.

Spectral interferometry is also used in the delay stage calibration process, where the single mode fiber is set in the sample position, and the spectral interference of each two beams is recorded for each step, where a relation between the travel of the delay stage and the time delay difference can be calculated.

Implementation of an Ultra-Broadband Multidimensional spectroscopy Setup

2.1 Introduction

After establishing the theoretical background of time-resolved spectroscopy in the first chapter, we will now present the experimental implementation of a 2D ES setup. We start with a discussion about the challenges facing such implementations, and a comparison between partially collinear and different types of non-collinear geometries showing their advantages and drawbacks.

After presenting the motif to choosing a fully non-collinear geometry, we start by introducing the light source used to generate broadband pulses in the visible regime and the pulse compression and characterization techniques used. This is followed by the detailed explanation of the experimental setup and phase stability achieved by the pairwise beam manipulation. We will also discuss the measurement procedure and the data analysis. After all we will show two primary measurements performed on rhodamine dye and pentacene films.

2.2 2D FT spectroscopy

Since the first pump-probe optical spectroscopy measurement realization in the middle of the past century [41, 42], a wealth of optical spectroscopy techniques have been developed. Techniques are being pushed to obtain the greatest possible spectral information with the highest temporal resolution [5]. Multidimensional spectroscopy is one of the techniques that combines the high time resolution while maintaining high spectral resolution and has been utilized to address many fundamental questions in condensed phase dynamics [2, 43]. The concept of multidimensional Fourier transform spectroscopy is an optical analog to the 2D NMR experiments known as COSY (Correlation Spectroscopy) [2]. During these years, multidimensional spectroscopy has been implemented in different frequency domains starting from terahertz frequencies [44, 45], mid-IR [46-49], visible frequencies [50-56], and the UV [57-62].

Most of these experiments are restricted to spectrally narrow excitation and probe pulses limiting the studies to one or a small number of transitions found in a narrow range within UV-visible or mid-IR ranges. The beauty of multidimensional spectroscopy is studying the correlation between multiple distant transitions revealing a wealth of information about diverse chromophores and environments. For that reason, the future of multidimensional spectroscopy would be going to much broader pulses where multiple transitions would be excited simultaneously. The recent advancement of light sources generating continua in inert gases [3, 63] allows for the realization of ultra-broadband 2D setups in the visible regime covering spectral ranges between 480 nm and 900 nm.

2D Spectroscopy

A 2D Fourier transform spectrum has several clear advantages over traditional one dimensional spectroscopy or non-Fourier transform 2D spectroscopy such as the well-known pump-probe spectroscopy. First of all, in case of congested spectra the signal of different transitions that are not well separated will end overlapping and leading to loss of information about different possible processes. On the other hand, 2D FT spectroscopy spreads the probed data along the extra dimension of the excitation spectrum; this leads to the disentanglement of the overlapping signals where cross peaks can reveal interactions between the different transitions. Second, the 2D FT gives the absorptive and refractive parts of the non-linear signal, whereas refractive part is completely lost in other techniques. Third, 2D FT spectroscopy offers high temporal-spectral resolution with no trade off. While in pump-probe spectroscopy the temporal-spectral resolution are coupled to each other due to the time-bandwidth product, in 2D FT spectroscopy the spectral resolution is only dependent on the maximum time delay during the scan between the excitation pulses. This enables the use of ultra-broadband pulses with sub-10 fs temporal resolution in 2D FT spectroscopy, without compromising the spectral resolution. This powerful combination makes 2D Fourier transform spectroscopy the ideal tool for unraveling couplings and coherences among diverse resonances and dynamics in complex systems without any compromise on the temporal or spectral resolution [2, 64].

2.3 2D spectra

A 2D spectrum is a spectrum with two frequency axes, the probe frequencies and excitation frequencies. It is constructed at a specific waiting time delay T , where the time difference between the excitation pulses 1 and 2 is scanned and Fourier transformed, obtaining the excitation frequency axis. The detection frequency axis is obtained directly by a spectrograph. In Figure 2-1 we present a cartoon of 2D spectrum at $T = 0$ and $T > 0$ of a two transitions under investigation. Along the diagonal, two main peaks appear at the absorption frequencies of each transition, while interaction between these transitions is represented by cross-diagonal peaks (CP). At early waiting times ($T = 0$), valuable information can be extracted about the fundamental line shapes of the transitions, where inhomogeneous (IB) and homogeneous (HB) broadening can be estimated by measuring the elasticity of the bands, where the major and minor axis represent IB and HB, respectively [2]. The excitonic coupling between the two transitions is visible as cross peak in the 2D correlation spectrum.

The evolution of the peak positions and shape is a reflection of various changes in the system itself and its surrounding (the solvent in case of liquid samples). The correlation spectrum at $T > 0$, show a broadening in the peaks along the anti-diagonal axis, and a shift of the diagonal peaks to slightly lower detection frequencies, as well as change in the shape of the excitonic cross peak. The diagonal peaks shifting from the diagonal are signature of the dynamic stokes shift [65]. While the diagonal peak shape evolution over time show the loss of the IB elongation with the increase of HB, which is typically due to the memory loss due to spectral diffusion. This can be used as a direct access to measure the time dependent bath dynamics and solvation [66]. For the cross peaks, the growth in the cross peaks shapes is a sign of

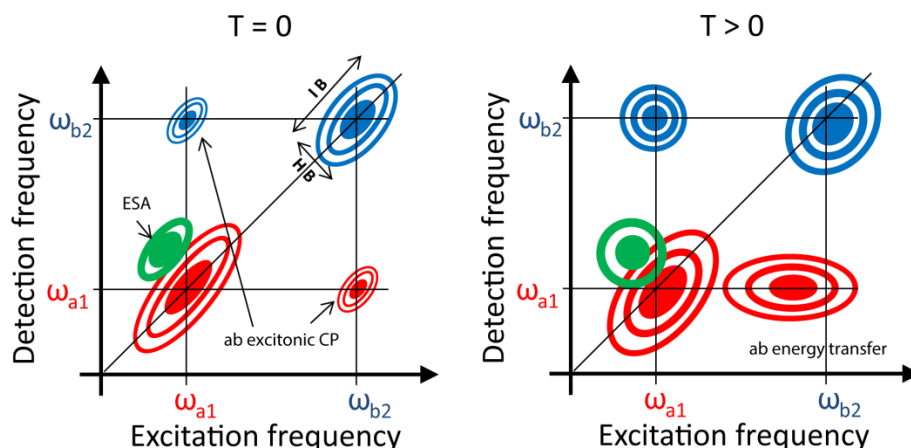


Figure 2-1 Schematic illustration of an absorptive 2D correlation spectrum of two transitions a and b, at waiting time $T = 0$, and $T > 0$. For $T = 0$, information about the homogeneous (HB) and inhomogeneous (IB) line width, excited state absorption (green), and excitonic coupling, can be revealed. For $T > 0$, information about the spectral diffusion, Stokes shift, and energy transfer can be extracted.

electronic coupling and energy transport [67]. Finally, time-dependent oscillations of the diagonal and cross peaks reveal vibrational, vibronic, and electronic coherences [68-70].

2.4 Challenges

When implementing 2D FT ES experiment, one of the major technical challenges is creating and delivering the appropriate pulse sequence with variable delay between them, yet with high phase stability. The phase stability can be expressed as the relative variation of the phase between two optical pulses at a given time delay. The timing jitter between the pulses directly impacts the phase stability, where the relevant timescale is directly dependent on the oscillation period of the optical field (proportional to wavelength) [2, 54]. Such a requirement can be easily achieved for long wavelengths (IR) using ordinary delay stages to create the interferometer and control the timing between the pulses [71, 72]. The shorter the wavelengths (Visible, and UV) used the more demanding the instrumentation will be to achieve high interferometric stability. If the phase stability requirement is not achieved, artifacts can appear in the 2D spectra after the Fourier transformation, leading to mixing between the real and imaginary information [2]. This issue has been tackled with various techniques and geometries that are implemented to circumvent such a problem [54].

Applying Fourier transformation over the two time delays τ and t require high phase stability and precise timing. During these time intervals the system is in a coherence state between the excited and ground state. During the second time delay T , the system is in a population state, where the changes are slow and timing errors are not as critical. If Fourier transformation is applied on the population waiting time delay T , a 3D FT spectrum will be obtained revealing the waiting time coherence frequencies due to coherences between vibrational, vibronic, or electronic excited and ground states. Those frequencies are orders of magnitude lower than optical frequencies and do not require high phase stability compared to the optical coherence frequencies observed in τ and t [2, 73].

2D Spectroscopy

For an accurate retrieval of the excitation frequency axis, interferometric precision of $\lambda/60$ is required for the τ delay times, which correspond to timing errors of 0.03 fs (path lengths error of 9 nm) at 550 nm [2]. In the IR, such phase stability ($\lambda/60$) can be achieved by normal optics using beams splitters and a delay stage for each beam where the required stability is on the range of 0.27 fs at 5 μm wavelength. In typical interferometers with no active or passive phase stabilization, mechanical instabilities and optical path length fluctuations can introduce RMS value of 0.1 fs of timing errors. 2D FT IR experiment implemented by Hamm et al. [48] using only delay stages and beam splitters demonstrated that even at long wavelengths (5 μm) the quality of the 2D spectra deteriorates due to the phase instabilities, compared to actively stabilized system. This illustrates the importance of using actively or passively phase stabilized geometry for shorter wavelengths.

To access the components real (absorptive contribution) and imaginary (refractive contribution) parts of the complex-valued entities of the 2D spectra, heterodyne detection is employed to calculate the phase of the emitted signal. Heterodyne detection is performed by spectral interferometry between the signal field and a reference beam typically called local oscillator (LO) and resolved using a spectrograph. And this technique is explained in details in section 1.5. By fully characterizing the spectral phase and intensity of the LO, and knowing the time of arrival into the spectrograph relative to pulse 3, the complex signal field can be extracted (phase and intensity). Therefore, a stable relative time delay t and phase between pulse 3 and the LO is required such that an inverse FT can be performed in the extraction process.

Resolving small 2D signals in non-collinear geometries brings another challenge, since the signal must be isolated from the background noise created by scattering from the pumping beams and non-desired signals. When using BOXCAR geometry, the signal is emitted in the direction of the fourth vertex as a consequence of the phase matching conditions, leading to a background free signal. This is not completely true, since the scattering from the three pumping beams can be in some cases much higher in intensity compared to the signal and needed to be removed. For that recording the scattering of each pulse and the combination of pairs can be used to subtract the scattering contribution. In the case of linear geometries, the signal is emitted in the direction of the probe pulse, and two techniques have been proposed to solve this problem, that were utilized separately or together [74, 75]; amplitude modulation, phase modulation (cycling).

In case of choosing a fully non-collinear geometry, phasing of the 2D spectra becomes a requirement. As mentioned earlier, by using heterodyne detection, the complex signal can be measured allowing the separation between the absorptive and dispersive components of the 2D spectrum. Due to the sensitivity to the absolute timing between the local oscillator and the signal, the detected signal might be phase shifted from the purely absorptive or dispersive signal by a polynomial function of the frequency [2, 54, 76]. By performing a spectrally resolved pump-probe or transient grating experiment complimentary to the 2D experiment, the phase function can be calculated by invoking the projection slice theorem [2, 77, 78]. The spectrally resolved transient spectrum at specific time delay in a pump-probe experiment represents the real part of the third order signal. It is possible to find a frequency dependent

phase function that connects the pp-spectrum and the projection of the absolute retrieved 2D spectrum at the same time delay. Other techniques have been also employed to solve the phasing problem, based on balanced detection schemes, or even without the projection slice theorem using only optical methods [78-81].

In the next sections we will give details on the choice of the geometry and its advantages and disadvantages, the light source used, the experimental setup, the delay stage calibration, data acquisition and noise subtraction, phasing, and finally primary results obtained.

2.5 Choice of geometry

Various experimental implementations have been proposed for multidimensional spectroscopy to tackle the problems discussed earlier. Each geometry and implementation has its own advantages and disadvantages, some are ideal for obtaining high phase stability but are inherently limited to narrow excitation pulses and vice versa, while other geometries such as pump-probe geometry can achieve ideal phase stabilization but have higher noise and are limited to narrow excitation bandwidth but with continuum probe. The aim of our experimental setup is to perform ultra-broad band excitation/detection in the visible range as well as in the UV in the near future. Therefore the geometry chosen should be considered with care considering all the possible limitations.

2.5.1 Interferometric based setup with active phase stabilization

The first 2D FT experimental implementations were using excitation pulses in the IR centered at around 800 nm and employed an interferometer to create the pulse sequence needed [76, 82]. In the work of Joffre et al. [82], the non-linear response of a nonlinear crystal (type II KDP) was mapped out and spectral interferometry between a reference pulse and the other excitation pulses and signal separately was utilized to determine the full complex field in two dimensions. In the work of Jonas et al. [76], the third order 2D ES measurements were performed using a fully non-collinear beam geometry generated by interferometers. A tracer beam was utilized to calibrate the stages. These techniques were sufficient to achieve acceptable phase stability due to the long wavelength used. An actively phase stabilized approach was developed primarily by Cundiff et al. [64] where interferometers were used. The mirrors were mounted on piezo transducers locked the relative phase of the interferograms while the relative path lengths were monitored by a continuous wave laser (He-Ne laser). Actively phase stabilized approach enables broadband measurements at shorter wavelengths with high phase stability. Such experimental implementations require sophisticated instruments for motion control, electronics, and a real time optical measurement.

2.5.2 Pump-probe geometry based setup

In pump-probe geometry, the first two excitation pulses are collinear ($k_1 = k_2$) while the probe pulse comes with a small angle as presented in Figure 2-2. The rephasing and non-rephasing signals are both emitted in the direction of the probe pulse and are heterodyned with the

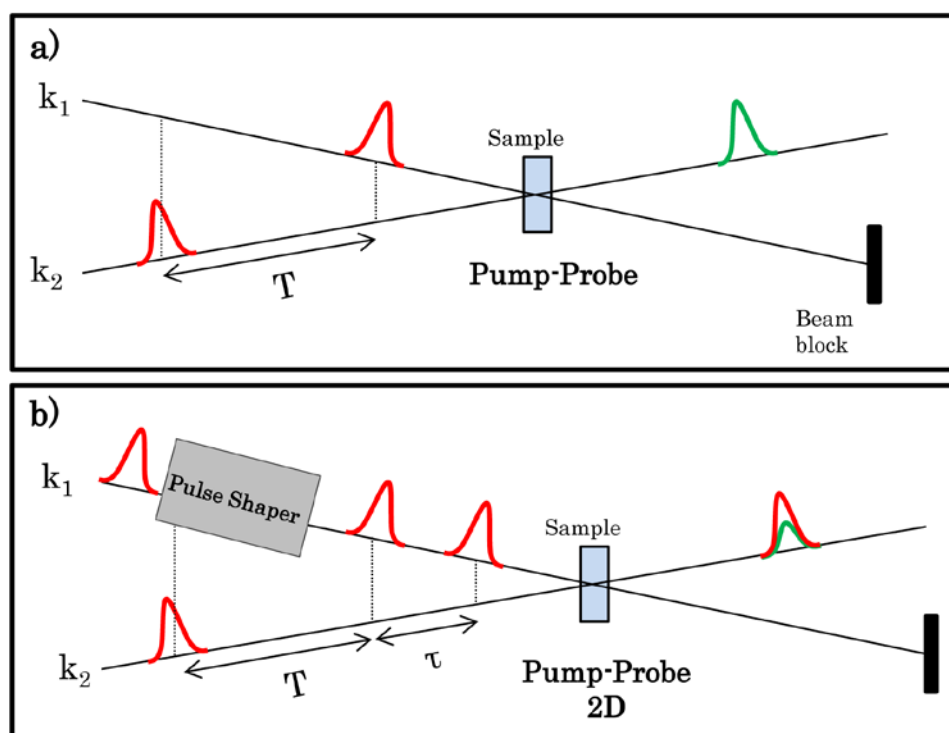


Figure 2-2 a) Typical pump-probe geometry. b) A pulse shaper is inserted in the pump path to create the pulse sequence needed to perform 2D spectroscopy experiments. The signal is emitted in the same direction for the probe beam due to phase matching conditions.

probe. This excludes any errors stemming from the different scans to obtain both rephasing and non-rephasing signals and the signal has well established zero-phase between itself and the probe. The coherence time between the excitation pulses (1 and 2) is created by a pulse shaper, where in the Fourier plane to yield a $4f$ setup a liquid crystal display (LCD) imprints a fringe pattern onto the pulse spectrum that is translated in the time domain after spectral recombination to yield a pulse sequence. Since the collected signal is not background free, phase cycling is required to extract the clean complex 2D spectra. This implementation has been demonstrated with high signal to noise ratio in the visible and NIR [53, 83]. One of the main advantages of this geometry is the ability of performing a two color experiments where the probe can be chosen to be different from the excitation pulses. For that very often the probe pulse is a white light continuum generated by filamentation in a non-linear medium (water, CaF_2). These setups are usually fast in signal collection due to the absence of any moving stages and the fast change in the pulse shaper configuration.

One of the main drawbacks of this implementation is the limitation in the bandwidth of the excitation pulses, where it becomes harder to achieve long time delays for very broad pulses unless a very large pulse shaper is used. Also the chirp of the pulses must be compensated carefully since this technique can suffer from distortions of the 2D spectra due to the different linear chirp added to the pulses (relative between the excitation and probe) [84].

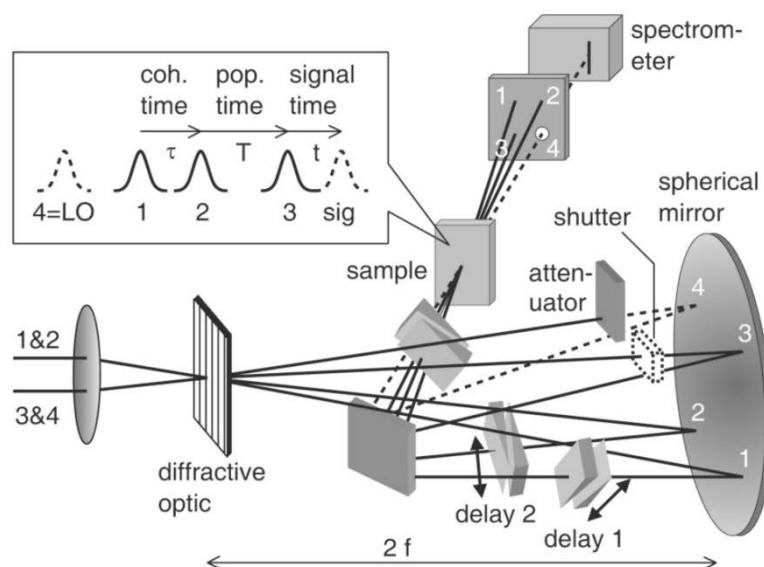


Figure 2-3 Diffractive optics based 2D spectroscopy setup with glass wedges to scan the timing between the pulses. Figure taken from reference [1]

2.5.3 Diffractive optics based passive phase stabilized setups

Passively phase stabilized implementations require only optical elements where the phase stability is achieved through using common optical components for beam pairs such that mechanical and timing jitters would cancel out. The first passive phase stabilized systems were developed for TG spectroscopy with heterodyne detection employing diffractive optics (DO) to generate the pulse sequence and utilized common optical components for all four beams to keep the relevant phase as stable as possible, imaging the DO-generated beam onto the sample (presented in Figure 2-3) [38, 77]. By adding the ability to control the timing between the pulses, these setups were able to perform 2D spectroscopy with high phase stability. The time delays between the pulses are tuned by inserting rotating glass slides [85] or translation of wedges in the beam path [85, 86]. These setups are fully non-collinear and allow the ability to do polarization dependent measurements.

Other experimental configurations were proposed using coupled retroreflectors instead of refractive elements, where broadband excitation was proved to be possible and pulse shaping of the first two excitation pulses to coherently control population transfer in rhodamine 101 [87, 88].

Utilizing DO imposes a limitation on the spectral bandwidth to an octave due to overlapping diffraction orders produced by the DO. And due to the use of variable thickness refractive elements to produce the time delays also poses a problem for large bandwidth, especially in the UV. Such refractive elements will lead to a variable broadening which was estimated about 6% for 10 fs pulse at 600 nm in case of delay of 300fs. This would be more dramatic in case of broader pulses or UV.

2.5.4 DO free passive phase stabilized setups

Several groups have demonstrated all reflective BOXCARS setups that use beam splitters rather than DO, excluding any bandwidth limitation. Same as the in the DO based setups, this technique make use of the concept of correlated pulse pairs to achieve passive phase stability [50, 89]. Other configurations were presented that use spatial masks or 2D pulse shapers to generate the four beams in the BOXCARS geometry, where beams hit common optics and the time delays are tuned by a spatial light modulator or piezo controlled mirrors all mounted on the same stage [90, 91]. Engel et al. [55] also presented an all reflective setup operating with 10 fs compressed pulses ranging between 550 nm and 680 nm. Beam splitters were used to generate the pulse sequence in BOXCARS geometry and they employed independent mirrors mounted to slightly angled stages to perform fine time delay steps with a phase stability of $\lambda/75$ at 800 nm.

All reflective setups with correlated pulse pairs show no limitation on the excitation bandwidth and proved to achieve high phase stability with a limited effort (no need for beam tracers and active corrections). In case of use of broadband compatible optics, tunability between the visible and the deep UV should be trivial.

By comparing all of these different implementations, the all reflective setup would be the most suitable for our demands, due to its high tunability and its ability to utilize broadband pulses with the only limitation of finding beam splitters that can support the bandwidth. Therefore we embraced this technique and combined it with an ultra-broadband source that has the ability to generate octave spanning pulses centered at 700 nm. In the following part we will introduce the light source and the pulse shaper used to compress the pulses and future improvements utilizing chirped mirrors to achieve dispersion free experiments with sub-10 fs pulses.

2.6 Light source

Optical parametric amplifiers (OPA) are widely used in electronic spectroscopy experiments (pump probe, fluorescence up-conversion, and multidimensional spectroscopy) due to their ease of tunability over wide spectral range (480 nm – 1300 nm). Various groups over the years demonstrated the possibility of generating ultra-broadband pulses with sub-10 fs pulse duration by amplification of tilted pulse fronts eliminating the pulse front mismatch due to the non-collinear geometry [92-95]. OPA systems have their limitations concerning the pulse energy output that is limited to the damage threshold of the amplification medium (Barium Borate BBO crystal) and their non-uniform beam profiles that show a spatial chirp. The intensity throughput limitation can be averted by amplification of temporally chirped pulses and compressing them afterwards. But still the highest pulse energies achieved are in the range of multiple μJ only.

In our experiments we are aiming to utilize visible broadband pulses (up to 200 nm) that are compressed to near-Fourier limit to avoid errors in the 2D spectra due to dispersion of the pulses. Accordingly, a deformable mirror based pulse compressor as well as a set of chirped

mirrors is used to manipulate the phase in the Fourier plane achieving a compressed pulse at the point of the sample. During this procedure, energy losses are unavoidable due to the use of gratings and the non-planar surface of the deformable mirror. Extra losses should be also considered in the multidimensional setups, since we use beam splitters and compensation plates to create our pulse sequence (discussed in details section 2.7). Therefore it would be wise to choose a light source that can generate more energetic pulses with a broad spectrum covering the spectral region of interest (500 nm - 700 nm). The unavoidable spatial chirp in NOPA systems can create aberrations in the multidimensional spectra due to the non-homogeneous excitation of the three pulses. Hollow core fibers are considered as a good replacement of the NOPA systems due to their superiority in throughput energy and the ideal EH₁₁ mode generated at the fiber exit.

Hollow core fibers are glass fibers filled with a noble gas acting as a dielectric waveguide for the light. In this technique, intense laser pulses are spectrally broadened upon passage through the gas medium (non-linear medium) through self-phase modulation (SPM) generating pulses that can be compressed to be shorter than the input pulse using the suitable optical dispersive elements [3, 96]. The waveguide traps the intense laser pulse allowing significantly longer laser-medium interaction length leading to increase in spectral broadening [3]. Spatially uniform broadening and EH₁₁ spatial profile are inherent from the transverse profile of the fiber, giving a dramatically better beam profile compared to NOPA systems [97]. SPM in hollow core fibers is becoming a standard technique in generating few-cycle infrared or visible pulses with hundreds of μJ of pulse energy, e.g. utilized in production of attosecond pulses via high harmonic generation [98, 99]. Pulses in the UV are also possible to generate by performing sum frequency generation between a 400 nm and a white-light spectrum inside the fiber [100, 101].

In this section we will discuss briefly the SPM process and some technical details of the fiber, showing the capabilities and boundaries of this technique. Starting with the SPM process, the frequency bandwidth attained from SPM in the fiber, considering a Gaussian pulse in the absence of dispersion, can be approximated as follows [3]:

$$\Delta\omega = \frac{0.86}{T_0} \int_0^L \gamma(z)P(z)dz \quad 2-1$$

where z is the distance along the fiber, T_0 is the 1/e term of the temporal full width of the input pulse, L is the length of the fiber, $P(z)$ is the peak laser power given by $P(z) = P_0\zeta e^{-\alpha z}$, where P_0 is the peak incident power, ζ is the coupling efficiency and α is the attenuation coefficient of the fiber, and $\gamma(z) = \eta_2 p(z)\omega_0/cA_{\text{eff}}$, where η_2 is the nonlinear response of the medium, $p(z)$ is the gas pressure along the fiber, ω_0 is the laser central frequency, and A_{eff} is the effective mode area of the fiber [3]. Therefore for a fixed fiber length, the bandwidth generated is directly dependent on the input pulse duration and intensity, and the gas pressure along the fiber.

In our laboratory we are using a 1.1 m long hollow core fiber with 260 μm diameter purchased from Imperial Consultants pumped by a cryogenically cooled Ti:Al₂O₃

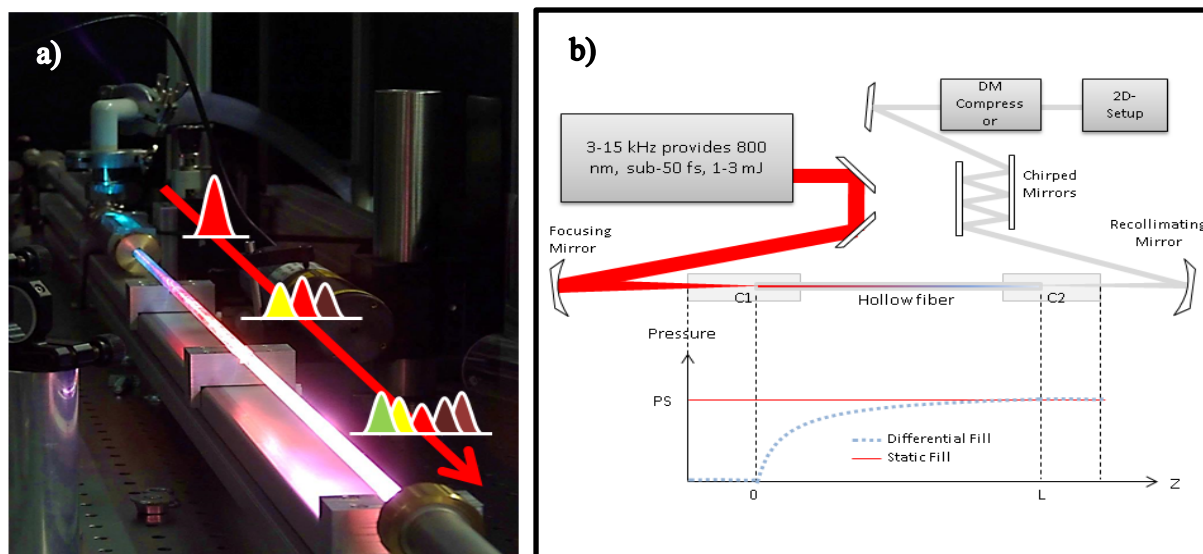


Figure 2-4 a) picture of the 1.1 m fiber in the laboratory. **b)** the schematic of the experimental setup, including the Laser system that is used to pump the hollow core fiber, the chambers used to put the fiber in two different modes: under static pressure or differential pressure. After recollimation, the beam is sent into a set of chirped mirrors and a deformable based compressor to compensate for the temporal chirp.

regenerative amplifier at 6 kHz rep rate providing sub-50 fs centered at 800 nm. To maximize the energy throughput, we need to match the focal spot of the laser to the guided mode of the fiber. The amplified laser output has a Gaussian beam profile that can be best coupled into the EH_{11} mode when $1/e^2$ radius of the beam is equal to $0.325d$ ($84 \mu\text{m}$), where d is the inner diameter of the fiber [3, 96]. The beam is coupled into the fiber using a 75 cm concave mirror, set on a motorized mount. By inserting a thin fused silica window in the input path of the beam (between the focusing mirror and the fiber chamber) we can track the focal spot of a CCD in real-time and compensate for slow beam pointing fluctuations. This ensures higher long term stability and avoids damaging the fiber input in case of misalignment.

The fiber is supported by two aluminum chambers with 0.2 mm thick glass windows (no coating) that can support the gas pressure inside (up to 3 bars). Figure 2-4 shows a picture of the fiber in the lab, a schematic of the fiber including the chambers C1 and C2, and a graph depicting the gas pressure along the chambers and the fiber in both static and differential pumping (DP). In the static pumping, both chambers are exposed to equal pressure of gas, leading to a homogeneous fill along the fiber depicted by the red line in the graph. In the case of DP, C2 is exposed to a static gas pressure (PS) while C1 side is blocked from the gas input and connected to a scroll pump to vent the chamber reaching a gas pressure of $\approx 10^{-2}$ bars. As a consequence, an increasing gradient of pressure will be formed along the fiber changing between 0 bars and the static pressure PS of C2 [102], with a pressure distribution following

$$p(x) = \sqrt{\left(p_0^2 + \frac{x}{L}(PS^2 + p_0^2)\right)}$$
, where p_0 is the pressure in C1 and PS is static pressure applied in C2.

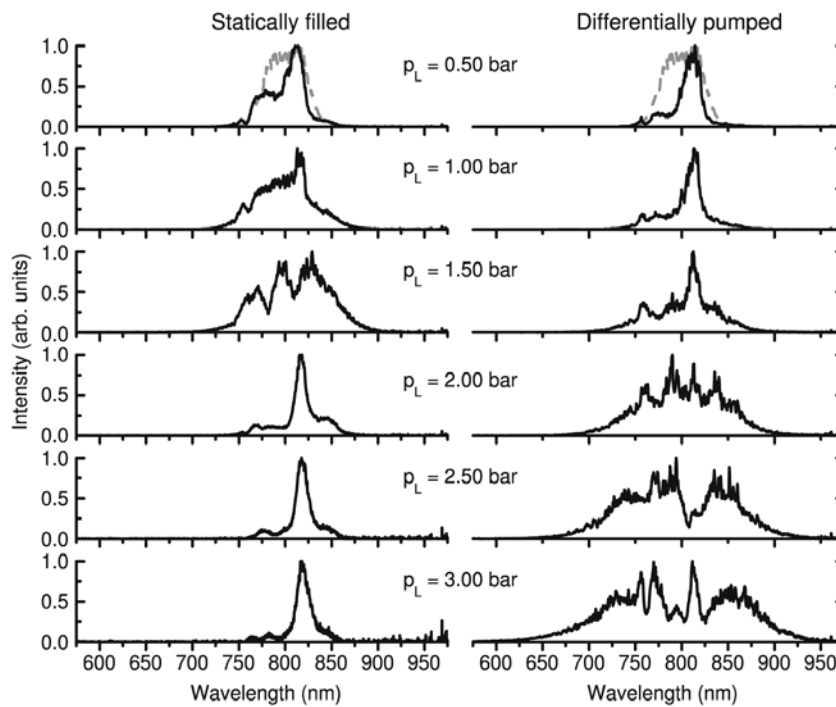


Figure 2-5 This figure is from the work of Robinson et al [3] showing the normalized spectra acquired after broadening in a hollow core fiber for both SP (left) and DP (right) cases. The spectrum of the input pulse is included as a grey line.

For both modes DP or SP, aligning the fiber is usually done with very low power ($\approx 8\mu\text{J}$) at 0 bars in both chambers. The fiber position and the focusing mirror are adjusted to obtain the highest transmission ($\approx 50\%$) and the cleanest mode. Then the laser intensity is raised gradually reaching pulse energies of $\approx 280\mu\text{J}$. The gas pressure is also gradually increased while tracking the transmitted spectrum and mode shape until reaching the needed broadening. In case of SP, the energy transmission is constant with the pressure increase up to the point where the gas starts to ionize, causing defocusing at the fiber entrance due to change in the focal spot size and beam direction, leading to reduced coupling efficiency and higher noise. This does not happen in the DP mode since the entrance of the fiber has very low gas pressure, leading to a stable energy transmission with the increase of the laser intensity, enabling higher energy operation. This has been shown by various groups theoretically [103] and experimentally [3, 102]. It is also reported that smoother spectral shapes are obtained when using DP. The systematic study done by Robinson et al. [3], demonstrated that using DP operation mode of the fiber, they could use higher pulse energies as input, leading to spectrally broader and temporally shorter pulses while avoiding noise and instabilities caused by the gas ionization. This result is depicted in Figure 2-5 is taken from reference [3].

Since we are aiming to use broad and stable light source, the obvious choice is using the fiber in the DP mode. Furthermore, to achieve spectral broadening going down to 500 nm, Argon gas was used instead of Neon due to its higher non-linearity and dispersion. Finally, fine tuning of the input pulse duration and phase can lead to broader output pulses where typically

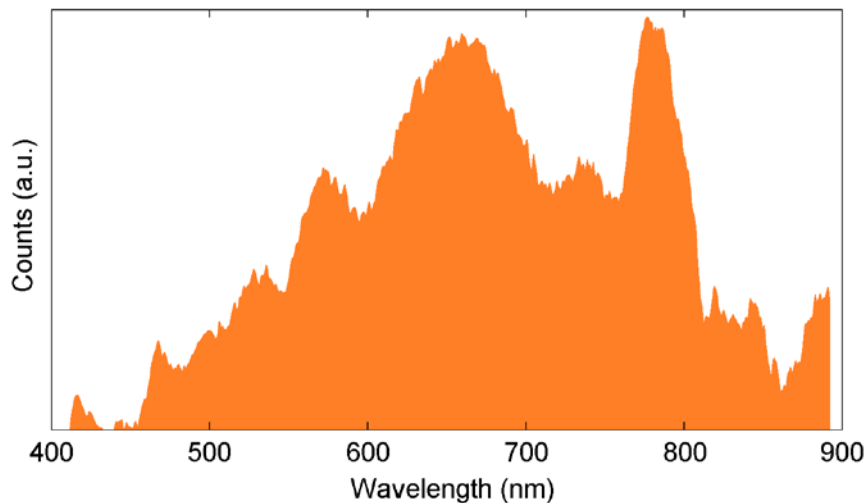


Figure 2-6 The spectrum of the spectrally broadened pulses to over an octave using a hollow fiber pulse compressor.

positively chirped pulses are most suitable. Figure 2-6 shows the spectrum of the output pulse covering the whole visible spectral region between 450 nm and 900 nm with pulse energies of $\approx 140 \mu\text{J}$. For utilizing only part of the spectrum, 100 μm thick short pass Schott filters were purchased with variable cutoff frequencies to tune the red side of the spectrum between 600 nm and 750 nm. The filters were chosen to be 100 μm thick to reduce GVD added by the glass of the filter. The blue side is tuned by varying changing the gas pressure in the fiber leading to decrease or increase in the broadening, where wavelength down to 450 nm can be achieved.

Shot-to-shot noise measurements were performed at the exit of the fiber by acquiring the signal intensity using a fast photo-diode that records the intensity of the fiber output at the same rate of the laser frequency. The RMS energy fluctuations were found to be $\sim 3.6\%$ compared to the input pulse noise of $\sim 3\%$. In DP mode, the stability was not affected when changing the input power or gas pressure, except when going with very high power where we start ionizing the gas. Measurements of the shot noise were also performed on narrow bands of the bandwidth by isolating them with a diffraction grating, where we found that the noise at the wings of the spectrum (< 550 nm) possess higher noise than the central frequencies. The noise was estimated $\sim 5\%$.

Pulse compression and characterization

To achieve our aim of obtain Fourier limited pulses at the position of the sample in the 2D setup, we need to compensate for the GVD added by the fiber and all the optical components present before and in the 2D setup (i.e. filters, beam splitters, compensation plates, GDD added by mirrors, and air). A home built deformable mirror (DM) based pulse shaper is used to compress the pulses to near Fourier limit using the geometry proposed by Vdovin et al. [104]. A 3.3 cm long DM (OKO tech) is positioned in the Fourier plane of a folded 4f negative dispersion stretcher. The stretcher consist of a 300 grooves/mm grating blazed for

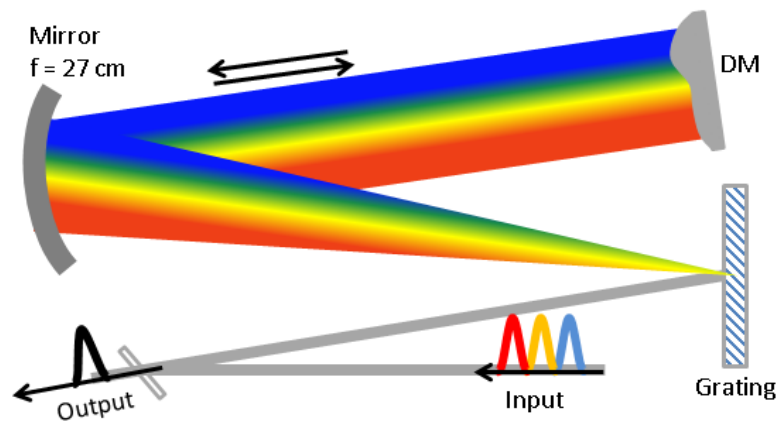


Figure 2-7 Compression stage using a 4f compressor with a deformable mirror in the Fourier plane.

550 nm and a 27 cm focal length mirror allowing to use of the whole DM surface with a spectral range of about 200 nm visible light (presented Figure 2-7).

The DM used in this setup is coated with bare Silver to support broadband operation in the visible optical regime and has 19 piezoelectric actuators to control the surface. These actuators are connected to a voltage amplifier controlled via a digital to analog converter card. Using a He-Ne laser as a light source for an interferogram with the DM in one arm, the surface of the DM can be mapped out in high accuracy. Figure 2-8 shows the changes in the DM surface in nm showing a maximum stroke of 9 μm . This allows for group delay to be corrected in the range of 60 fs, where the phase shift of individual frequencies is estimated by $\Delta\varphi(x) = 2 \frac{2\pi}{\lambda(x)} \delta z(x)$, where δz is the membrane displacement in the position x relative to the wavelength $\lambda(x)$. The fact the surface of the mirror is rigid; fully activating one actuator will impact the whole surface, leading to a smooth deformation as presented in the central plot in Figure 2-8.

First step in the pulse compression procedure is the alignment of the compressor. By putting the surface of the DM flat (acting as a normal flat mirror) this setup can be considered as a telescopic grating disperser that can account to linear dispersion as a typical folded grating compressor. But also if miss aligned it can lead to sever pulse chirps and pulse tilts that the DM cannot compensate for. The dispersion can be tuned from positive to negative by varying the reflection of the collimating mirror and the distance between the mirror and the grating [16]. The process of the alignment is tracked by checking the FROG trace at the point of the sample for every step of the alignment achieving the highest temporal resolution, compensating for the chirp added by the fiber and all the optics in the path reaching the sample point. This process contributes to the compensation of the linear chirp.

The nonlinear chirp cannot be corrected by a prism or grating compressor and this is where the DM comes into action. Tuning the surface of the DM such that it matches the non-linear phase of the pulse leads to this compression of the pulse. This process can be done by measuring precisely the phase of the pulse using FROG analysis and imprinting the shape into the DM. Such a process requires high measurement accuracy of the phase, and very

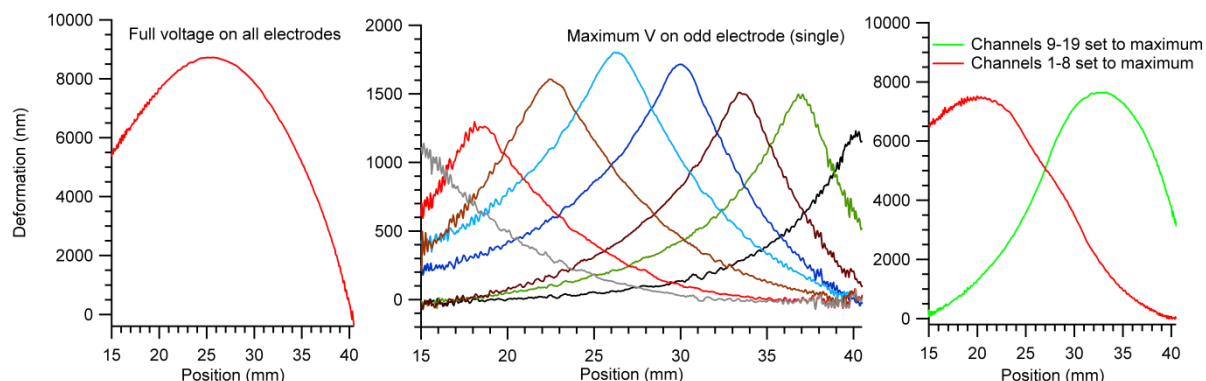


Figure 2-8 Deformable mirror calibration showing the change in the surface of the deformable mirror under various conditions by setting the maximum voltage of 255 V, first on all the actuators, second on the odd actuators (one at a time), and finally on half of them at a time.

precise manipulation of the DM surface. As mentioned earlier, the shape of the DM is not linear with the voltage applied, leading to a complicated procedure to precisely manipulate the surface. Therefore another method was used to perform such manipulation.

In order to eliminate the need to fully characterize the absolute phase of the pulse and the DM surface, a genetic algorithm (GA) with a closed feedback loop was used to find the best configuration [105, 106]. Spectrally resolved frequency doubling of the pulses is used as a feedback for the GA. The GA is a population based search technique that maintains populations of potential solutions during the search. A population of 25 potential solutions is created randomly; each consists of 19 variables varying between 0 and 255. Each potential solution is evaluated by measuring the yielded SHG signal (reward or fitness value) at the position of the sample. On the basis of these evaluations, some genetic operations (crossover, mutation, and reproduction) are employed to generate the next generation. The procedure of

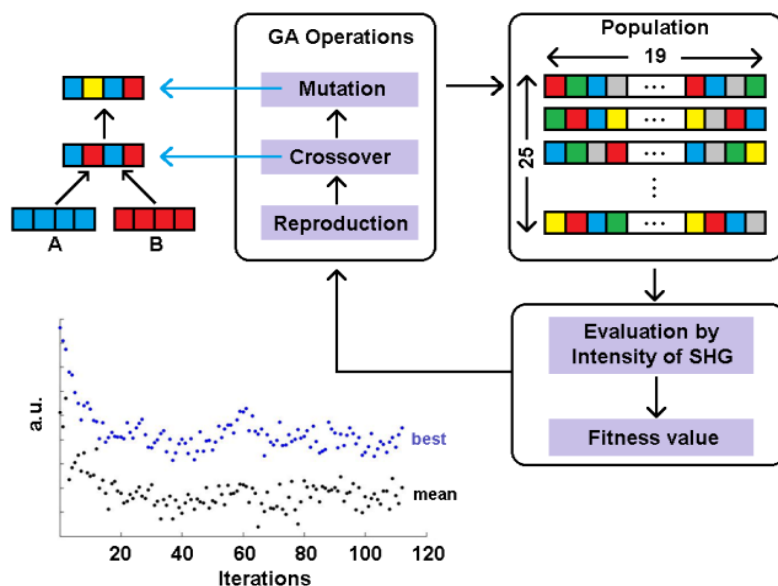


Figure 2-9 Genetic evolution work flow showing the processes included in each iteration and the convergence towards an acceptable answer after 120 iterations.

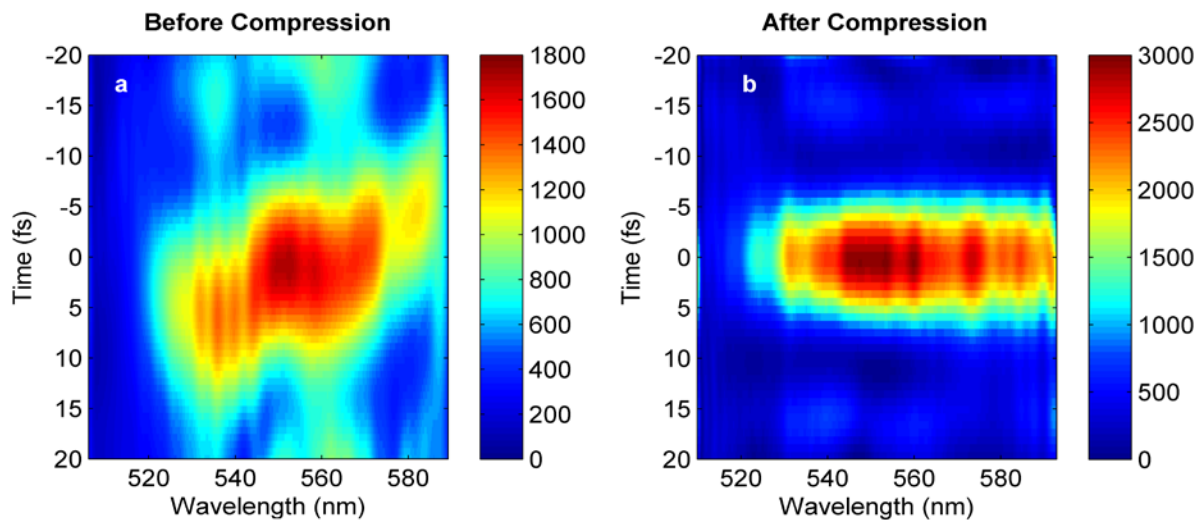


Figure 2-10 FROG traces of a pulse before and after compression, showing a strong change in the spectral phase and the pulse duration. The pulse duration is compressed down to 8.3 fs FWHM where it was estimated to be 25 fs before compression.

evaluation and generation are iteratively performed until the optimal solution is found or the max iterations allowed is reached [107, 108]. The process is depicted in Figure 2-9, showing the steps of the closed loop.

Frequency resolved optical gating (FROG) is used to measure the pulse characteristics (temporal and spectral phase and intensity). FROG traces of pulses before and after compression are presented in Figure 2-10 showing strong difference. The pulses before compression show a strong spectral phase change between the individual frequencies leading to a chirped pulse spanning around 25 fs. After 10 minutes and 200 iterations of the GA, a suitable population was found. The FROG trace of the corrected pulse show a flat spectral phase with pulses that are very close to the Fourier limit, and a reasonable increase in intensity. Analyzing the FROG traces by a commercial FROG analysis program (Femtosoft FROG 3.2.4), the temporal intensity was estimated by 8.3 fs FWHM, while the Fourier limit is around 6 fs. The FROG technique is discussed in the coming part.

Considering that the only feedback for the GA is the SHG signal, the whole process is very sensitive to which frequencies are contributing to the signal. Therefore, the GA will be blind to frequencies that do not contribute due to low spectral intensity or being out of phase matching conditions. This leads to strongly chirped pulses since the phase of blind frequencies will be randomly manipulated by the mirror. The first step to solve the problem is using a non-linear medium that can phase-match a broad pulse up to 200 nm. This was achieved by purchasing a 10 μm thick BBO type I cut at 40° optimized for 600 nm purchased from Eksma optics. By reducing the thickness of the BBO, the efficiency of the SHG process will be reduced, but the phase matching of broader pulses will be easier. The SHG tuning curve is presented in the figure below showing a fairly sharp change in the region below 550 nm, which explains the fast drop in phase matching conditions for wavelengths below 550 nm compared to higher wavelengths.

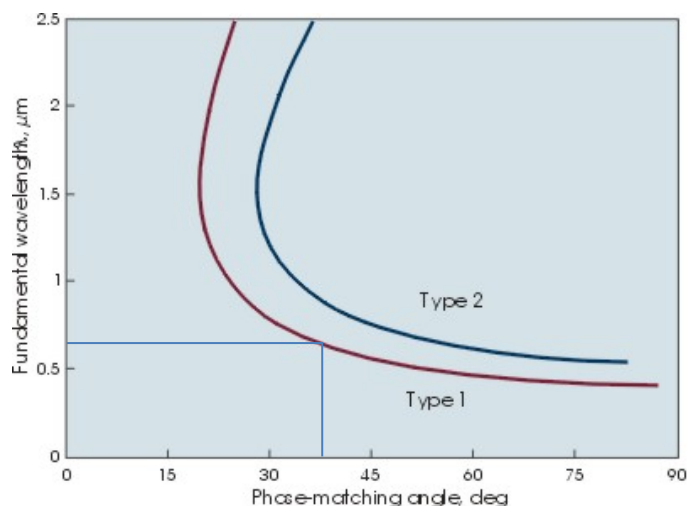


Figure 2-11 Second harmonic generation tuning curve (figure taken from Eksma optics)

As a consequence, the phase matching conditions will favor frequencies between 550 nm and 700 nm and reduced contribution from the other frequencies. To overcome this limitation, the SHG signal is spectrally resolved and multiplied by a wavelength dependent digital filter function (inverse of the phase match curve) before integration in order to optimize for all doubled frequencies with equal weight. This allows the compression of broader pulses. In Figure 2-12, a selected visible spectrum ranging between 480 nm and 670 nm is presented (black) along with the SHG spectrum after compression with (purple) and without (dotted red) the addition of the digital filter (dotted green). The one compressed with the digital filter show a broader spectrum spanning around 60 nm in the UV instead of 30 nm.

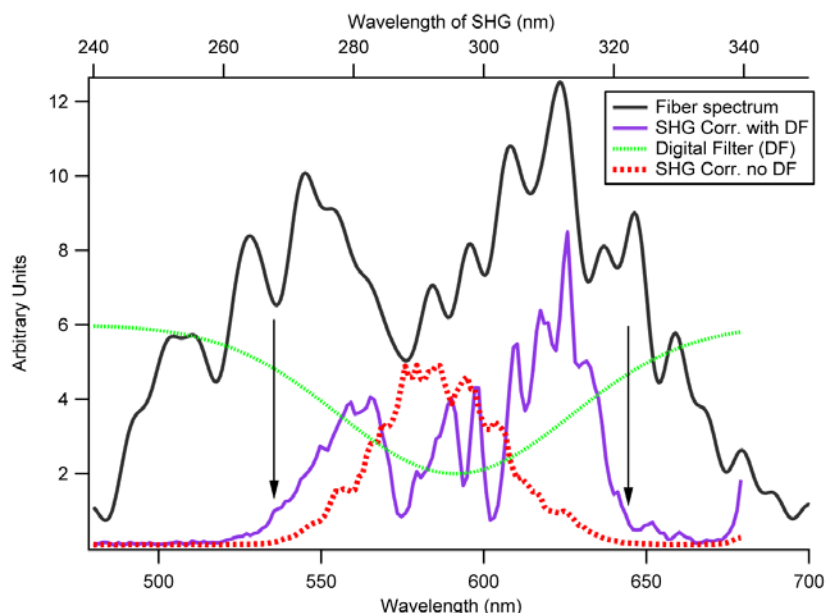


Figure 2-12 The pulse spectrum of a pulse spanning between 480 nm and 670 nm (black) is presented along with the SHG signal generated after compression with (purple) and without (dotted red) the use of the digital filter (dotted green).

After the pulse compression we need to verify the pulse duration and check for linear and high order chirp that will affect the 2D measurements, strongly mixing the real and the imaginary spectra. Therefore, the pulse characterization is a crucial step, where we need to measure not only the pulse duration but the spectrally dependent phase as well. FROG is a great technique that can be implemented in different geometries allowing the retrieval of the pulse duration and the spectrally dependent phase. Various FROG geometries have been developed, each suitable for certain requirements [109]. Considering the BOXCARS geometry of our setup and the need of investigating the pulses at the sample position, the most obvious geometry would be the Transient-Grating FROG (TG-FROG). This technique uses two pulses to produce a momentary refractive index grating on an optical Kerr medium such as a fused silica plate, where a third pulse with variable delay diffracts off the grating into a fourth direction [110, 111]. The signal field generated in this technique is mathematically equivalent to the one of Self-Diffracted FROG or Polarization-Gating FROG depending on the chosen variable pulse. In the case of pulse 2 is variably delayed, while fixing the time difference between pulses 1 and 3 to zero, the signal pulse is expressed as follow:

$$I_{FROG}^{TG2}(\omega, t) = \left| \int_{-\infty}^{\infty} E_1(t)E_2^*(t - \tau)E_3(t) \exp(-i\omega t) dt \right|^2 \quad 2-2$$

Considering that all the pulses are identical this becomes:

$$I_{FROG}^{TG2}(\omega, t) = \left| \int_{-\infty}^{\infty} E^2(t)E^*(t - \tau) \exp(-i\omega t) dt \right|^2 \quad 2-3$$

TG-FROG has several advantages over the two beam geometries. Compared to PG-FROG, in TG-FROG no polarizers are needed that may distort ultrafast pulses and it can be used in the deep UV. Since it can use all parallel polarization, this techniques yields higher signal strength because the diagonal elements of the susceptibility tensor are a factor of three larger than the off-diagonal elements used in PG-FROG. It also has number of advantages over the SD-FROG, giving high signal strength and low noise due to the background free detection. Since TG-FROG is phase matched, long interaction lengths in the non-linear medium may be used, enhancing the signal strength due to the length squared dependence of the signal.

In our setup we use a 0.1 mm microscope slide as a Kerr medium in the position of the sample and perform the TG-FROG by setting the beams 1 and 3 to overlap temporally and scanning the beam 2. Figure 2-13 shows a TG-FROG scan of a pulse spanning between 520 nm and 680 nm compressed down to 9 fs. Traces were analyzed using FROG ver. 3.2.4 (Femtosoft Technologies) to calculate the temporal and spectral phase as well as the pulse duration.

As mentioned earlier, the frequencies that are at the wings of the spectrum are not phase matched as the central ones, leading to lower sensitivity in the phase correction. This is observed in the spectral phase of the pulse that show a fairly flat phase in the center of the pulse (550-650 nm) and increases up to 0.2 radians around the edges. After all, the pulse duration estimated by the Femtosoft software is around 9.6 fs. In summary, we managed to

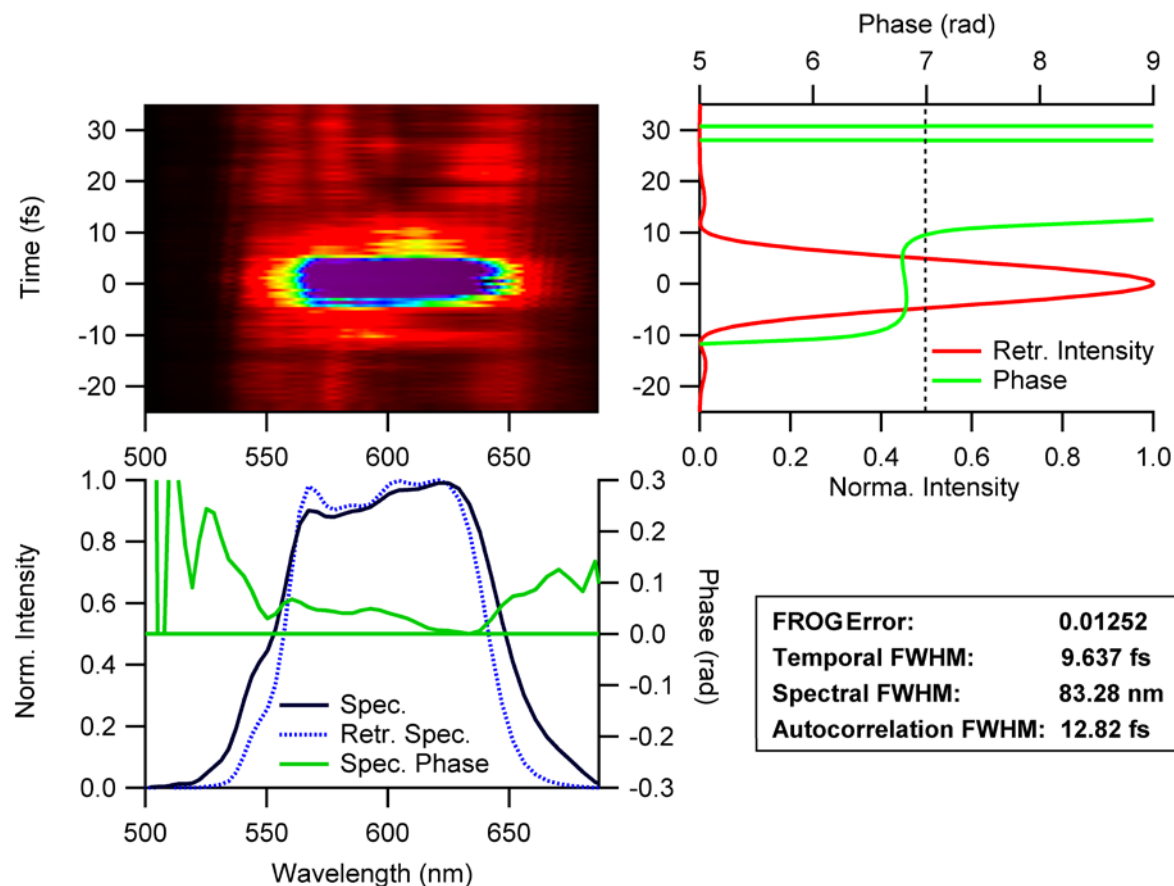


Figure 2-13 a) Measured PG-FROG trace of a 160 nm pulse centered around 600 nm, showing strong signal in the center and weak signal at the wings. b) Retrieved intensity (red) and phase (green) vs time. c) Retrieved spectrum (dashed blue), measured spectrum (solid blue), and phase vs wavelength (nm).

achieve acceptably compressed broadband pulses using a deformable mirror based compressor and characterized the pulses using TG-FROG. Compression of pulses broader than 180 nm in the visible would be easier if a set of chirped mirrors are used to compensate for most of the quadratic chirp before the pulse shaper. Chirped mirrors that support spectra between 500 and 900 nm with 60 fs^2 per bounce are already purchased (Ultrafast Innovations PC70), but due to the lack of time are not implemented yet. These mirrors can account for most of the linear and quadratic chirp reaching sub-5fs at the point of the sample, where there will be no limitation to using a broad spectrum spanning from 780 nm down to 500 nm.

2.7 Setup

After the pulse compression stage, the beam is sent into the 2D spectrometer, where the pulses are split into 4 identical pulses using beam splitters. For achieving high phase stability, the setup was built to be as compact as possible and uses pairwise geometry. The compact geometry is presented in Figure 2-15, showing a side and top view.

The beam going into the setup is sent upwards using a polarization preserving periscope that lifts the beam to a height of about 30 cm above the table. This beam is translated horizontally

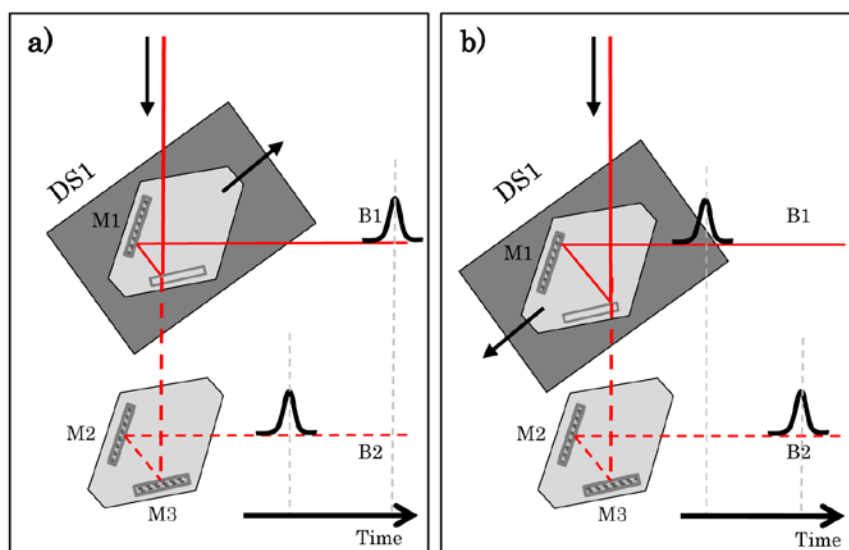


Figure 2-14 The change in time delay between the two beams B1 and B2 when moving the delay stage 1. The travel distance of the transmitted beam is constant, while the travel distance of the reflected beam B1 is variable. A) Delay stage moved to the top \rightarrow B1 arrives earlier than B2 in time. b) Delay stage moved to the bottom \rightarrow B1 arrives later in time relative to B2.

and sent back down towards the optical table into the first beams splitter (BS) creating the first beam pair. The beam splitter is mounted at an angle in respect to the table, such that the reflected beam is directed onto a metallic mirror that directs the beam parallel to the table again, this can be seen by the side view of the setup in Figure 2-14. The transmitted beam goes into two fixed mirrors, mounted in a very similar geometry as the combination of BS and M just described. The two beams B1 and B2 propagate parallel to each other and vertically displaced by 3 cm. The BS and M1 are mounted on a precision delay stage (PI 25 mm travel distance) that travels with a 45° angle with respect to the table Figure 2-14. By moving the delay stage upwards or downwards, the travel distance for the reflected beam B1 is decreased or increased, respectively. Since the beam path of the transmitted beam B2 is stable, the time difference between the two pulses can be varied by moving the delay stage, we call its travel distance $\Delta DS1$.

After we created the first beam pair B1 and B2, we will split each of them into two other, where B1 and B2 will become beam pairs 1/2 and 3/4, respectively, as shown in Figure 2-16 b. Therefore the manipulation of the time between these two beam pairs is equivalent to pairwise manipulation (correlated manipulation). The splitting of the beams is done using another set of BSs (BS2) mounted on a single metallic mount, vertically displaced by 3 cm such that B1 and B2 will impinge on each BS as shown in Figure 2-15a/b. The beams reflected off the BSs impinges onto two mirrors M4 attached to the same metallic mount, reflecting the beams in a perpendicular direction relative to the incoming direction, creating the first half of the BOXCAR geometry. On the other hand, the transmitted beams will reach a set of mirrors, M4 and M6, mounted on a single metallic mount that will direct the beams into the other two corners of the square of the BOXCAR geometry. The metallic mount of these mirrors is fixed on a piezo delay stage (PI) that has a travel distance of $500 \mu\text{m}$ only, creating the time difference between pulses 1/2, and 3/4 that is proportional to its travel

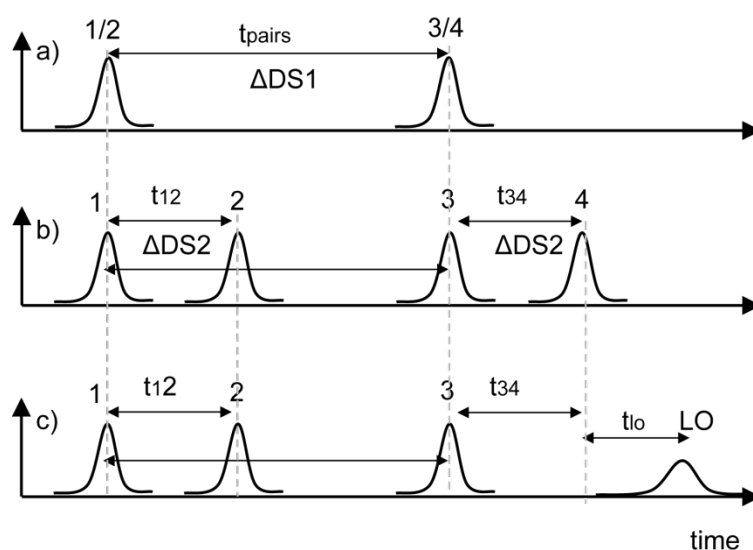


Figure 2-16 Pairwise beam manipulation. a) The first beam pair 1/2 and 3/4 created by DS1. b) DS2 splits each beam into two identical pulses 1 and 2, and 3 and 4, with identical time difference between them. c) The fourth pulse, the local oscillator LO, is shifted in time and decreased in intensity because of the variable density filter in its path.

distance $\Delta DS2$ as presented in Figure 2-16 b. Pairwise manipulation, in this case correlated manipulation of beams 1/2, and 3/4, is achieved by the using the single long metallic mounts. Details of the inherent phase stability are discussed in the next section.

All the BS and mirrors are especially chosen to support broadband pulses, where the mirrors are bare aluminum mirrors that have high reflectivity covering the spectral range between 200 nm to the IR. The beam splitters used are 1 mm thin silver coated fused silica substrate

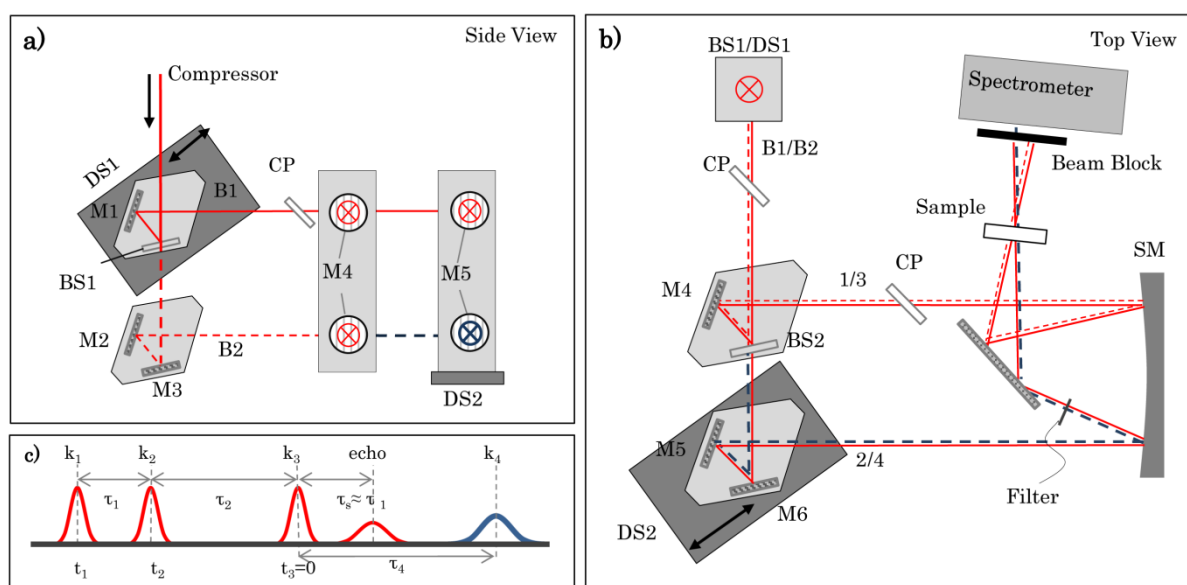


Figure 2-15 Schematic drawing of the setup. a) Side view showing the metallic holders and the spitting of the incoming pulse into beam 1 and 2. b) Top view of the setup showing the second stage and the path of the 4 beams through the sample and into the spectrometer. c) Generated pulse sequence.

suitable for broadband use between 450 nm and 750 nm, yielding 50/50 ratio.

A standard spherical mirror ($f = 40$ cm) focusses the four beams onto the sample via a folding mirror and with a focal spot of $80\ \mu\text{m}$ in diameter. This eliminates the need of an off-axis parabolic mirror that is typically harder to align. As we discussed earlier, the signal in this geometry will be emitted in the phase matched direction, which will be co-propagating with the fourth beam (local oscillator LO). For that reason, we spatially block the three excitation pulses, and only let through the signal and the local oscillator thus reducing the amount of scattered light that reaches the detector. Then the signal and the LO are both focused onto a single mode fiber using a 10 mm focal length achromatic doublet lens, which images a small volume of the focal spot at the sample. This helps to reduce scattering effects and select a homogeneously excited and probed area of the sample, thus reducing spatial effects on the third order signal. This is not a major issue in our setup, due to the highly homogeneous mode of the hollow core fiber, where in the case of NOPAs this might be an issue. The single mode fiber is coupled to a 0.5 m imaging spectrograph (Shamrock 303) and a cooled 400×1600 CCD camera (Andor newton 971). In case of very weak signals, measurements were performed without the use of single mode fiber, where the signal and LO were sent directly into the spectrograph, this way the entire generated signal was collected instead of a spatially chosen volume.

As mentioned earlier, distortions in 2D spectra due to chirped pulses are significant when the pulses used have different amounts of chirp [2, 112]. In our geometry, pulses that pass through the beam splitters will contain different chirp from the ones reflected, and the timing between the two will be slightly off. The chirp and time difference can be compensated for by using compensation plates that are the bare substrate of the BS. The compensation plates (CP) are set at a specific angle, chosen to obtain the minimum relative spectral phase between the three pulses. The angle of the CP is adjusted to minimize the spectral phase difference between the three beams, which is measured by spectral interferometry. Spectral interferometry is performed between pulse pairs minimizing the non-linear phase down to sub radian level along the whole spectral range. By that we make sure that all the pulses arriving at the sample position share the same spectral phase, and temporal width.

A thick variable density filter is placed in the path of the local oscillator to attenuate its intensity, and delay its arrival relative to the other three pulses and the photon echo signal. The fringe spacing observed from the spectral interferogram between the signal and LO directly depends on the time delay between them. Therefore choosing the thickness of the variable density filter inserted in the path of the LO is crucial to be able to resolve the fringe pattern well above the Nyquist frequency. When using the spectrograph to resolve a 90 nm spectral width, a filter thickness of 2 mm is used to delay the LO by 3.2 ps, leading to high fringe density, where we can record about 5 pixels for each oscillation well above the Nyquist frequency. When moving to broader spectral window of 250 nm, the spectral resolution will be reduced by about 3 times which gets us close to the Nyquist frequency. At this point, a 1 mm thick filter is used to reduce the timing between the signal and LO down to ~ 1.6 ps leading to larger fringes, allowing for a good sampling rate.

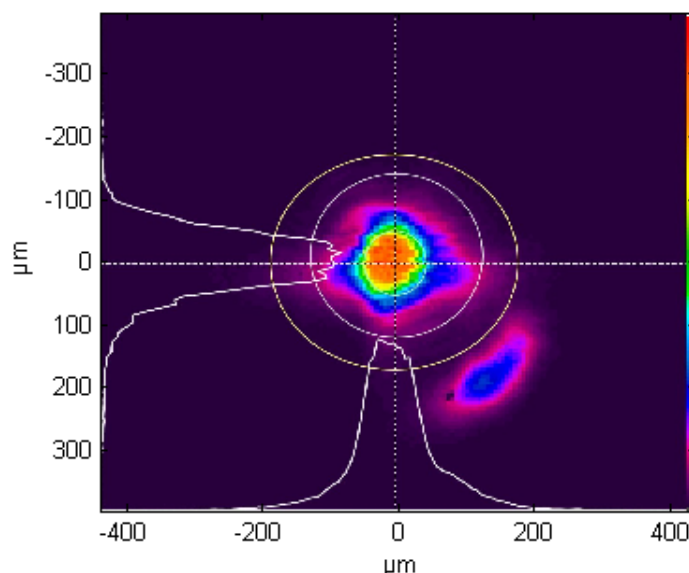


Figure 2-17 Beam profile of the focal spot of the three pulses, with the LO out of the focal spot

The filter is positioned between the spherical mirror and the sample, in a tilted position, to displace the focal spot on the sample, thus avoiding overlap with pulses 1 to 3, while the beam remains parallel to its original path. In Figure 2-17 we see the 80 μm focal spot of the pulses 1-3, and the LO shifted out of the focus by the tilted glass filter. This is required to prevent the local oscillator from getting contaminated by undesired pump-probe signals [1]. Finally, automatic beam blocks are introduced in the path of the three excitation pulses that will be used during the data acquisition to record the scattering contribution.

2.8 Inherent Phase stability

As discussed in Section 1.2.6, in order to resolve the excitation frequency dependence of the system, we detect the signal modulation with $\omega_{\text{eg}} \sim \omega_0$ (ω_0 is the central frequency of the laser) as a function of the coherence time τ . To resolve such frequencies, the timing control of the excitation pulses should be on the order a fraction of the oscillation period. The time scan along the coherence time is done with steps smaller than half the minimum oscillation period (higher than the Nyquist frequency) in order to avoid under-sampling which leads to aliasing of the resolved frequencies. Another important aspect that can impact the measurements is the phase stability of the laser pulses that generate and measure the third order signal. This phase stability is one of the most challenging experimental requirements that we face when implementing such a setup. Phase drifts can be directly related to optical path lengths variation due to mechanical vibrations, thermal drifts, and even air currents. To achieve high phase stability, we need these path length variations to be much smaller than the excitation wavelength $\lambda_0 = \frac{2\pi c}{\omega_0}$. To give a feeling of such vibrations, when using an excitation wavelength of 500 nm, we require phase stability, and thus the mechanical movement, to be below 8 nm.

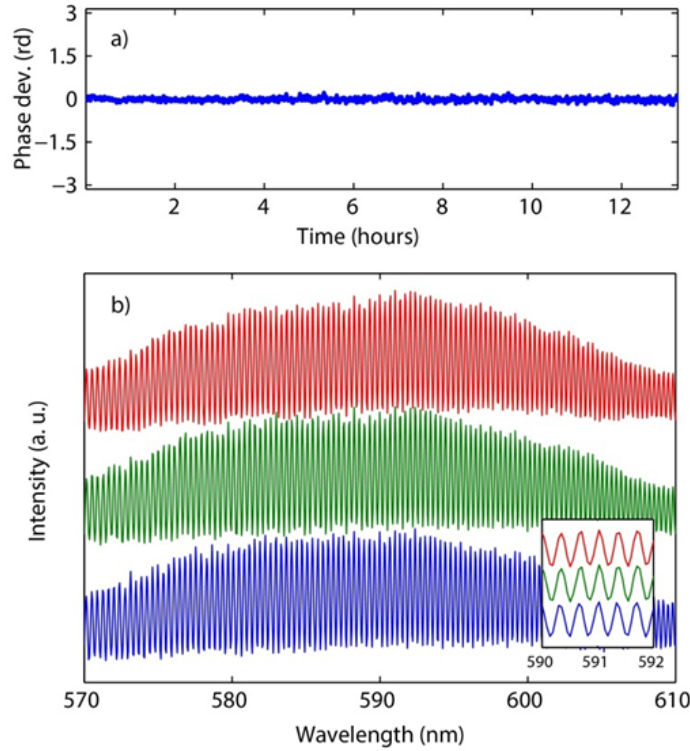


Figure 2-18 Phase stability measurements. (a) Phase deviation calculated from the spectral interference between third order nonlinear signal generated by a thin glass plate and the local oscillator was recorded every second over 12 hours. (b) Cuts from different 2d spectra taken over multiple 2d scans (6 hours apart) showing stability of the fringes and reproducibility of the general shape.

The phase effects on the third order polarization were discussed in Section 1.2.6, where we found that the third order polarization depends directly on the arrival time of the three excitation pulses, which can be seen in the phase factor $e^{i\omega_0(-t_1+t_2+t_3)}$. An additional phase factor is included when utilizing the heterodyne detection scheme using a fourth pulse as the LO. At the end, the experimentally measured absolute phase is the signal phase relative to the LO phase $\varphi_{\text{measured}} = i\omega_0(-t_1 + t_2 + t_3 - t_{\text{LO}})$.

In an idealistic environment, we could say that the arrival time of each pulse can be perfectly known and is stable, and the final measured phase will be stable. But this is not the case; vibrations down to nm scale affect our experiment. Looking into the relation of the phase in details, one could see the opportunity to use a trick to achieve phase stability without stabilizing individual pulses. The whole phase relation can be zero if the timing of opposite signs can maintain equal movements.

From the geometry of our setup in Figure 2-15, the pulses 1 and 3, and 2 and 4 share the same optical components, leading to a coupled phase between each other. Any path variation of beams 1 or 2 causing a change in its arrival time Δt_1 or Δt_2 , will cause an opposite variation to its pair 3 or 4, respectively, changing the arrival time by $-\Delta t_3 = \Delta t_1$ or $-\Delta t_{\text{LO}} = \Delta t_2$. Therefore, as total phase variation of the four beams we get

$$\varphi_{\text{measured}} = i\omega_0(-\Delta t_1 + \Delta t_2 + \Delta t_3 - \Delta t_{\text{LO}}) = 0 \quad \text{2-4}$$

2D Spectroscopy

Our geometry utilizes the same concept implemented by Selig et al. [50] with variation of the implementation method, where we used a more compact geometry and a different folding scheme leading to better long term phase stability. Such implementations can achieve high phase stability up to $\lambda/85$ at 800 nm.

In order to assess the stability of the setup, a photon echo signal is generated by placing a 100- μm glass plate in the sample position and setting the coherence and population time to zero. Spectral interference between the nonlinear signal and LO is recorded every second for more than 13 hours. The mean phase deviation was calculated using an inverse Fourier transform. Figure 2-18 a shows that over the 13 hours of measurements, we obtain a shot-to-shot (0.2 sec accumulation per shot) stability of $\lambda/60$ at 540 nm while there was no noticeable long term drift. This long term stability allows for the systematic phasing correction of the 2D spectra taken over multiple hours.

To check if the phase stability is still high even when the delay stages are moving for a long time, 2D measurements over 20 hours were performed. In Figure 2-18 b, we show three spectral inference fringe patterns between the photon echo signal of rhodamine dye and the local oscillator 6 hours apart. The absolute phase and timing between the pulses is highly stable.

The short term stability (over several minutes) is important to perform 2D measurements, while the long term stability (over hours) is an additional advantage. The long term stability makes the tedious phasing procedure (finding the absolute phase between the LO and signal for every 2D scan) easier, since all the scans share the same timing between the pulses. Therefore the phasing procedure is usually done for one scan, and applied to the rest.

The short term phase stability is attributed to the pairwise beam manipulation scheme utilized and the compact geometry of the setup. While the long term stability can depend on the setup and on the light source. For this, we warm up the setup for a while before performing any measurements, leading to stable temperature of the delay stages and mirror mounts. And the light source is highly stable since the pointing of the light source depends not on the laser itself, but on the fiber output which is mechanically fixed.

2.9 Delay calibration

The time delays relevant to our experiments require subwavelength accuracy and need to be equidistant to facilitate the Fourier analysis without artifacts. For this we use high precision delay stages with a precision down to sub-5 nm steps. The calibration of these stages is of high importance. Any errors in the calibration of the stages will lead to errors in the Fourier transforms and consequently to spectral distortions.

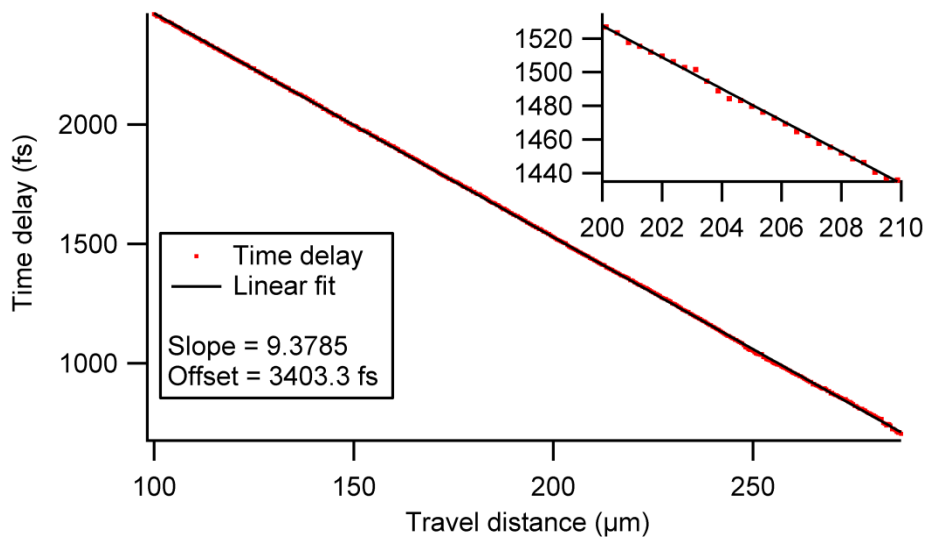


Figure 2-19 Time delay vs delay stage travel distance showing a linear relationship. In the inset is a zoom of a small region of the line to show the errors in timing between the pulses.

For the calibration procedure, the sample is replaced by a single mode fiber coupling the four beams into the spectrograph. To calibrate the delays stage DS1, we block the beams 2 and 4, and we record the spectral interferogram of the pulses 1 and 3. Spectral interferograms are recorded for 0.9 μm steps over the full travel distance of the stages. By fitting the spectral phase retrieved with a linear function, we can estimate the effective time delay between the two pulses at every step. From that we can precisely measure the effective time delay made by the stage down to sub-fs resolution. The same procedure is performed for the other delay stage. Figure 2-19 shows the measured delay time in fs vs the travel distance of the delay stage in μm . A linear relationship between the travel distance ΔDS and the time delay can be found.

In the inset of Figure 2-19, a zoom in on the travel distance between 200 and 210 μm show that fluctuations of sub-5 fs appear in the trace. Since the phase stability is achieved by pairwise manipulations, such timing fluctuations will be balanced by exactly opposite ones between the other two beams, leading to the overall cancelation of their effects.

2.10 Acquisition procedure

The procedure to measure a 2D spectrum involves several steps that include collecting some information about the pulses used, and their temporal overlap, that will be used in the correction process before the data evaluation. The whole measurement procedure is presented sequentially in the Figure 2-20. The first step would be finding accurately the temporal overlap between the three excitation pulses. In particular, the temporal overlap of pulses 1 and 2 is very critical since it defines the time zero for the coherence time τ . Therefore, we perform a similar procedure to the delay stage calibration by putting a single mode fiber in the focal point (sample position) and recording spectral interferograms, until we find the temporal overlap $t_1 = t_2 = t_3 = 0$.

Since the LO is delayed relative to the other three pulses by inserting a variable density filter, the temporal overlap found earlier will not include the timing of the LO. In the SI procedure to extract the complex signal information, the LO should be accurately characterized, including its time delay from time zero and its non-linear spectral phase. For that we use again SI between itself and the other three pulses, where we obtain the time and relative high order spectral phase. Further refinements of these values are performed later during the data analysis.

Now we are ready to perform the scanning procedure. In Figure 2-15 we established the time ordering needed, and the pulse timing $t_1 < t_2 < t_3 = 0$, where the population time T is defined by the shortest time difference between pulse 3 and the pulses 1 or 2.

$$T = \begin{cases} t_3 - t_2 & \text{if } t_1 \leq t_2 \\ t_3 - t_1 & \text{if } t_1 > t_2 \end{cases} \quad 2-5$$

The time difference between the first two pulses (1 and 2) has been already defined as the coherence time τ . In our measurements we scan the coherence time from negative to positive, swapping the time ordering of pulses 1 and 2 in the process. When measuring the rephasing signal, pulse 1 arrives first to sample followed by the other pulses 2 and 3, the population time in this case, is described by the time difference between pulses 2 and 3. When measuring the non-rephasing spectra, the time ordering is swapped, leading to the population time being measured between pulses 1 and 3. Both situations are considered in Eq. 2-3.

Due to the pairwise beam manipulation, each stage moves the time difference of a pulse pair, not single pulses. In agreement with naming convention established in Figure 2-16, the deliberate time shift created by each stage is called ΔDS_x , where x is the number of the delay stage. DS1 shifts the pulses 1 and 2 by a time $\Delta DS1$, and leaves 3 and 4 unaltered. During the movement of DS1, t_{12} and t_{34} are constant. DS2 shifts pulses 2 and 4 by a time dependent on $\Delta DS2$, but leaves pulses 1 and 3 untouched. During the movement of DS2, t_{24} and t_{13} are constant. Therefore, the arrival times of all pulses are

$$\begin{aligned} t_1 &= \Delta DS1 \\ t_2 &= \Delta DS1 + \Delta DS2 \\ t_3 &= 0 \\ t_4 &= \Delta DS1 + t_{40} \end{aligned} \quad 2-6$$

where t_{40} is the extra time delay added to the LO by the insertion of the filter. As a result, we can express the coherence and population time in relation to the combined delay stage movement, and vice versa, as follow

$$\begin{aligned} \tau &= \Delta DS2 \\ T &= \begin{cases} \Delta DS1 & \text{if } \tau \geq 0 \\ \Delta DS1 - \Delta DS2 & \text{if } \tau < 0 \end{cases} \quad \Leftrightarrow \quad \begin{aligned} \Delta DS1 &= \begin{cases} T & \text{if } \tau \geq 0 \\ T - \tau & \text{if } \tau < 0 \end{cases} \\ \Delta DS2 &= \tau \end{aligned} \end{aligned} \quad 2-7$$

After establishing the relationship between the movement of the delay stages and the time delays, we can discuss the procedure of measuring a 2D spectrum. To measure a 2D spectrum

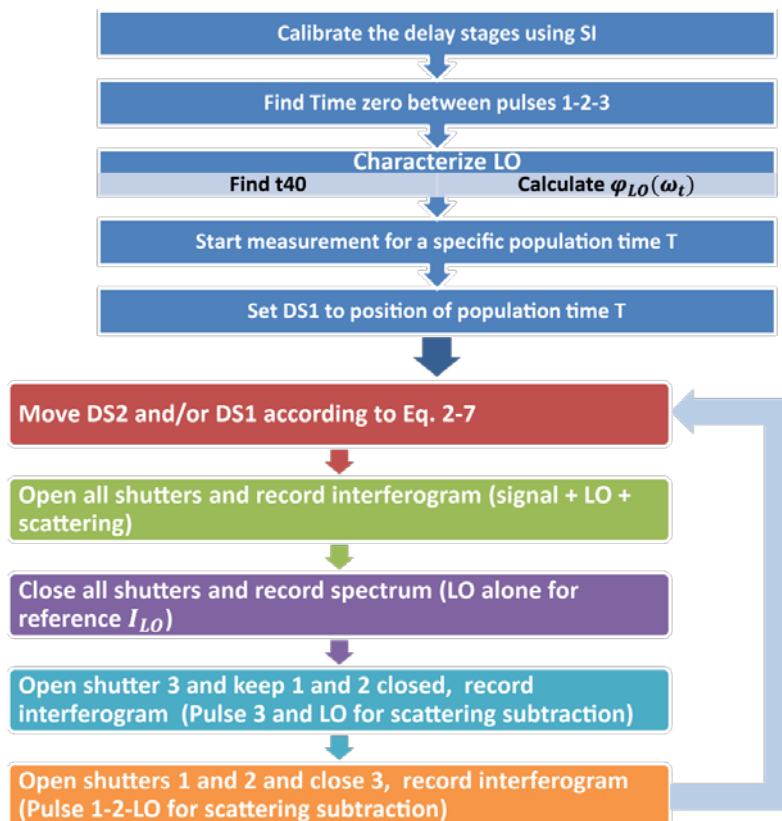


Figure 2-20 Flow chart of the measurement procedure, and the sequence of each time step in one 2D scan

at a specific population time delay T , we start by moving DS1 to the respective position, while the coherence time is kept zero. Then, DS2 is moved to the most positive coherence time required τ_{\max} in the scan. Now we need to scan along the coherence time in a continuous manner, such that we can obtain equidistant sequential time steps facilitating the Fourier transform. Typically the coherence time is scanned with sub-2 fs steps over a range of ± 80 fs. The choice of these numbers depends on the excitation spectrum. The fine steps of the coherence time are chosen such that the Fourier transform along $\tau \rightarrow \omega\tau$ is broader than the excitation spectrum. The scan keeps moving DS2 only until it reaches time zero, where excitation pulses temporally overlap. After that point if DS2 keeps moving on its own, the time difference between pulses 1 and 2 will keep changing where $\tau < 0$, and the population time will be considered between pulses 1 and 3 which will be decreasing gradually with the increase of the coherence time. Therefore, at the point of temporal overlap, DS1 starts moving together with DS2, to maintain a stable population time. For this motion to happen fluently and without timing errors, the calibration of the delay stages and the temporal overlap are critical.

Since we perform pairwise pulse manipulation, the delay time between the LO and the third excitation pulse is inherently equal to the coherence time plus the extra time added by the glass filter.

$$\Delta t_{LO} = t_4 - t_3 = t_{40} + \tau \quad 2-8$$

The signal is emitted after the interaction of the third pulse with the system by a time comparable to the coherence time τ . Therefore the signal field is shifted from the LO by a time difference dependent on the glass plate of only t_{40} . In other words, for all scanning of the delay stages the time difference between the signal field and the LO is stable at a time difference t_{40} .

Scanning both the coherence and population times, we record at every step the spectral interferogram of the signal field with the LO. Although we are measuring using BOXCAR geometry where the signal is background free, contamination of the signal might happen due to scattering from the three excitation pulses. At every time step, the SI of the signal field and the LO is measured, and the scattering contribution of pulses 3 and LO, and 1, 2, and LO are measured by the aid of the automated beam shutters. The acquisition software combines all of the acquired data in 3 matrixes, one for the data and two for the scattering.

2.11 Data analysis

The data analysis of individual 2D spectra comprises multiple steps before obtaining the reconstructed absorptive and refractive information. In this section we will show the processes performed to reconstruct a 2D spectrum at a specific population time T .

During the measurements, light scattering at the sample might contribute to the signal field if the scattered light happens to propagate in the same direction as the signal and the LO. This would lead to distortions in the reconstructed 2D spectra [1, 2]. Therefore, on the detector of the spectrograph we will not only detect the third order signal E_s and the LO, E_4 , but we will also be recording the light contribution of the three pulses E_1 , E_2 , and E_3 . Each of these recorded fields will have its own intensity I_a , phase φ_a and arrival time t_a . The total measured spectral intensity when all four incoming beams are present would be as follow

$$\begin{aligned} I_{total} &= |E_1 + E_2 + E_3 + E_4 + E_s|^2 \\ &= (E_1 + E_2)^* E_3 + (E_1 + E_2) E_3^* + |E_1 + E_2|^2 + |E_s|^2 \\ &\quad + (E_1 + E_2)^* E_s + (E_1 + E_2) E_s^* + E_3^* E_s + E_3 E_s^* \\ &\quad + (E_1 + E_2)^* E_4 + (E_1 + E_2) E_4^* + |E_3 + E_4|^2 \\ &\quad + E_4^* E_s + E_4 E_s^* \end{aligned} \quad 2-9$$

Where each complex electric field E_a is of the form

$$E_a = \sqrt{I_a(\omega)} e^{i\varphi_a(\omega) + i\omega t_a} \quad 2-10$$

In an ideal scenario without scattering, only the last two terms of Eq. 2-9 would be obtained. However, the detected signal contain all of these terms. During the SI evaluation, the Fourier transformation of I_{total} is computed leading to splitting of each contribution over the time axis. When applying the windowing function, we can get rid of any contribution that has a time delay difference from the one of $t_4 - t_3$. At this point the only surviving terms are the last two lines in Eq. 2-8, which are the spectral interference between pulses 3 and 4, and pulses 1-2

and 4. As mentioned in the experimental section, these terms are measured separately at every step during the scan by closing/opening shutter sequence. To obtain the scattering effects due to pulse 3-4, we close shutters 1 and 2, and for the pulses 1-2-4 we close shutter 4. The recorded spectral of I_{34} and I_{124} are as follow

$$\begin{aligned} I_{34} &= |E_3 + E_4|^2 \\ I_{124} &= |E_1 + E_2 + E_4|^2 \\ &= (E_1 + E_2)^* E_4 + (E_1 + E_2) E_4^* + |E_1 + E_2|^2 + |E_4|^2 \end{aligned} \quad \text{2-11}$$

The I_{total} can now be corrected from the scattering contributions by simply subtracting them $I_{\text{corrected}} = I_{\text{total}} - I_{34} - I_{124}$, which cancels the terms in the second last line of Eq. 2-8, leaving the desired signal terms remain in the Fourier window of the SI evaluation. Since we subtracted an extra $|E_4|^2$, we add it again to the corrected data leaving us with

$$I_{\text{corrected}} = I_{1234} - I_{34} - I_{124} + I_4 \quad \text{2-12}$$

After the scattering correction, we are left with only the spectral interferogram between the signal and the LO. This can be expressed as

$$I_{\text{corrected}} = \sqrt{I_s(\omega_t) I_4(\omega_t)} \exp(i[\varphi_s(\omega_t) - \varphi_4(\omega_t) - \omega_t t_{40}]) \quad \text{2-13}$$

where both the signal intensity $I_s(\omega_t)$ and the signal phase $\varphi_s(\omega_t)$ can be recovered. This can be done only if we know the spectral phase $\varphi_4(\omega_t)$ and intensity $I_4(\omega_t)$ of our local oscillator, and the time difference between the two fields. An extra measurements is performed at every step (individual coherence time point) by closing the shutters and recording the spectrum of the LO only. Therefore, we can divide the $I_{\text{corrected}}$ by the square root of the measured intensity $\sqrt{I_4(\omega_t)}$, and this way we get access to the electric field of the signal.

In the experimental procedure, we mentioned that we measure the timing between the pulses precisely before the measurements using SI. With that we have a very close estimate to the time difference between the LO and signal. The spectral phase of the LO can be measured using SI also when measuring the time, or can be estimated by perform a heterodyned TG-FROG measurement. This is done by simply performing a TG-FROG measurement while letting the LO pass and interfere with the TG signal. Such a measurement will enable us to resolve the relative phase between the excitation pulses and the LO precisely at the point of the sample. In case of solid samples deposited on a substrate, the substrate can be used as the Kerr medium to perform the TG-FROG and resolve the LO phase and timing in an environment similar to measurements. In case of a liquid sample, we can perform the TG measurement on the solvent (if it is transparent at the excitation wavelength used).

2D Spectroscopy

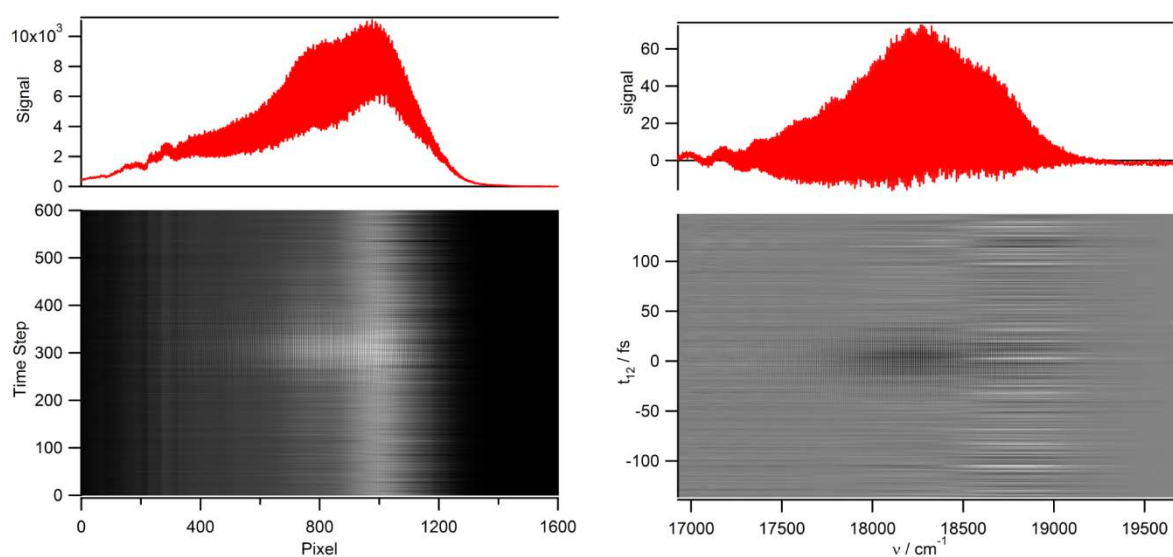


Figure 2-21 Background subtraction and interpolation over the frequency axis. The time axis is set according to the calibrated time zero instead of time steps.

After we have all the pre-requisites, we can start the analysis of the data to reconstruct the absorptive and dispersive 2D spectra. After the cleaning procedure explained above, the first step is to interpolate the data along the detection frequency axis. Since we detect the interferograms using a spectrograph, the spectra are equally spaced in the wavelength range (pixels), but we need them to be equally spaced in the frequency domain.

The second step is to perform an inverse Fourier transformation along the detection axis, which changes the frequency axis into time axis. Here we can apply a square filter to remove the scattering signals that were not accounted for by the subtraction. During this filtering, we can account to the extra scattering terms that we did not subtract.

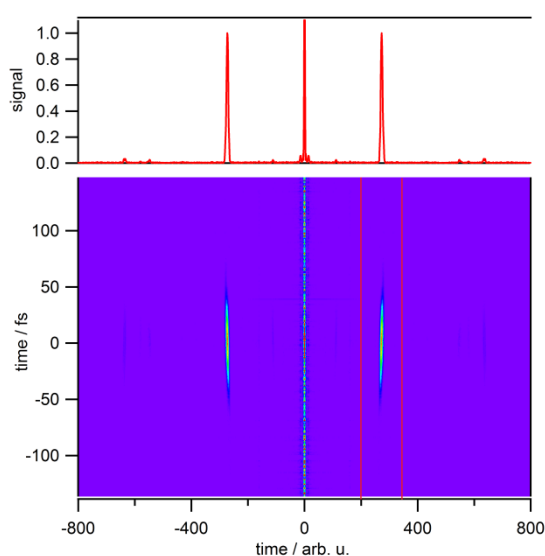


Figure 2-22 Fourier windowing applied over the time-time trace, setting everything but the signal to zero.

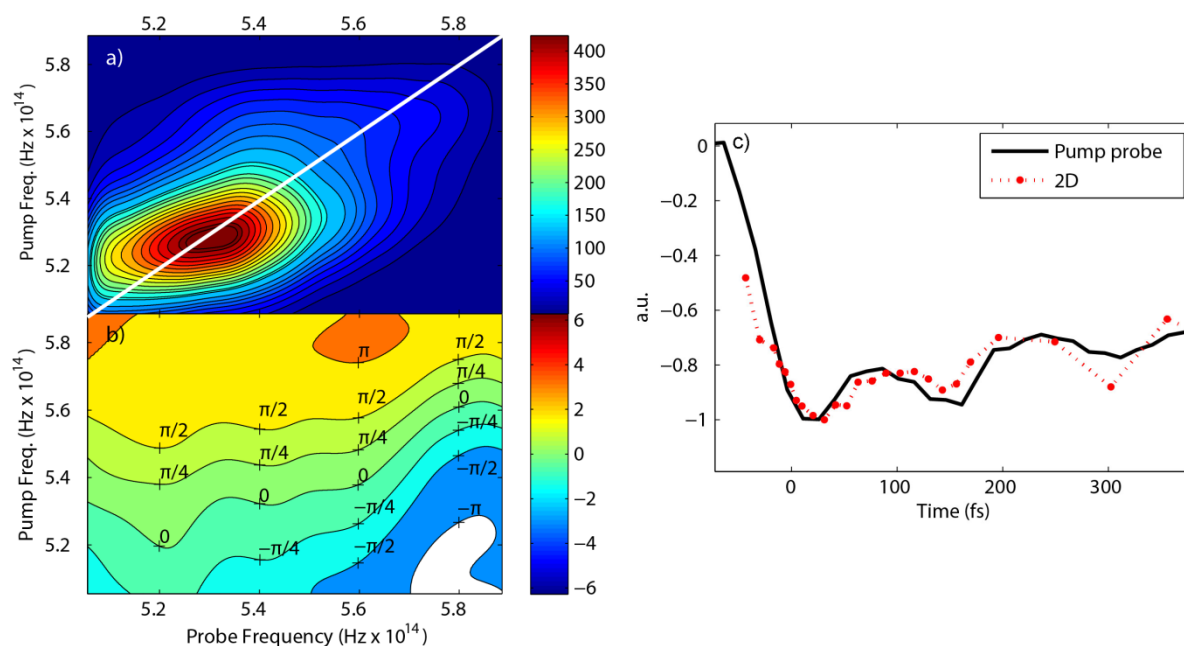


Figure 2-23 Absolute 2D spectrum of Rhodamine 101 at $T = 100$ fs showing the diagonal peaks. b) Contour plot of the phase showing a stable phase along the diagonal peaks. c) Oscillations detected in the pump probe data and 2D spectra showing 150 fs period.

After applying the Fourier filter, Fourier transformation along the detection axis is used to bring the 2D spectrum back to the time-frequency domain. A second FT along the coherence time axis yields a frequency-frequency complex-valued 2D spectrum. Using the absolute time and spectral phase of the LO obtained earlier, the phasing process can be performed, and the real and imaginary 2D spectra can be obtained.

2.12 Primary results

To test the accuracy of the setup, 2D measurements were performed on a test system, Rhodamine 101 in ethanol in a 0.1 mm flow cell, which has been intensely studied previously and is known to exhibit vibrational coherences that can be triggered by short pulses [9, 88]. Pulses with 90 nm bandwidth centered at 550 nm were compressed to 7 fs and used to perform 2D measurements, as well as TA measurements. Interferograms were taken at a specific time delay from every 2D-scan and compared to each other (as presented in Figure 2-18). The phase was highly stable even though the stages were repeatedly moving for several hours. An example of a 2D spectrum at 100 fs population time is shown in Figure 2-23 a) and b).

The signal is a positive peak along the diagonal axis caused by ground state bleach, with a pronounced elongation indicative of spectral inhomogeneity. Analysis of the 2D spectra and integrating over a 10 nm window around the peak ($570 \text{ nm} \cong 5.25 \times 10^{14}$) shows an oscillation of 150 fs period decaying within the first picosecond. The same oscillations were also observed in the pump-probe measurements performed on the 2D setup and on an independent setup using sub-30 fs pump pulses centered at 580 nm Figure 2-23 c).

We performed measurements on Pentacene films using laser pulses with spectrum between

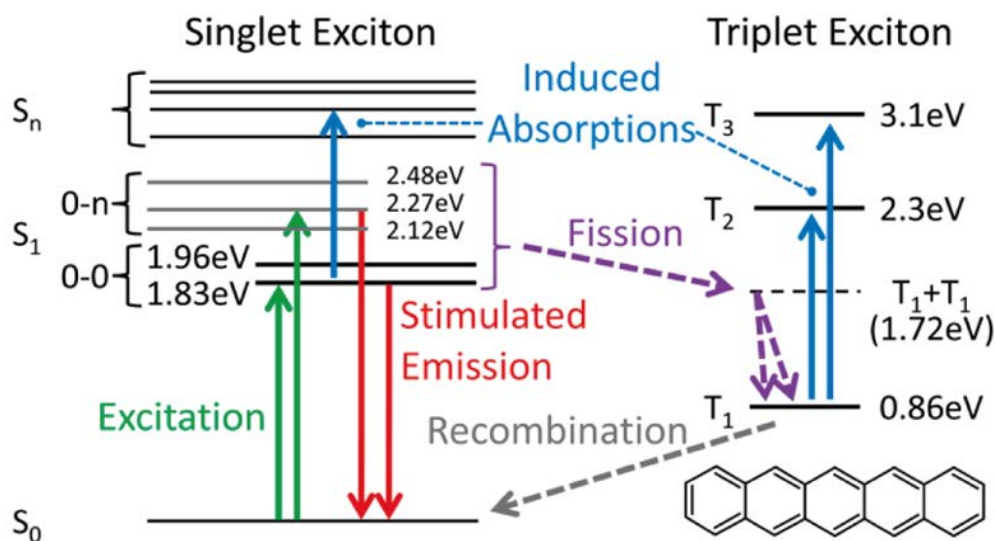


Figure 2-24 Energy level scheme of the pentacene film. The S_1 exciton is represented by two levels of the Davydov doublet. The population transfer from $S_1 \rightarrow {}^1(TT) \rightarrow 2T_1$ and the recombination are represented by dashed arrows, while optical transitions caused by the excitation pump or probe pulses are depicted by the solid lines. this figure is taken the work of Wilson et al.[4]

680 nm and 560 nm to demonstrate the ability to perform broadband visible 2D spectroscopy. Pentacene amorphous thin films are considered as model systems for ultrafast singlet fission, which is a result of its single-triplet energy levels ratio ($E_S > 2 E_T$) [4]. Singlet exciton fission produces two electron-hole pairs for every absorbed photon via the creation of a multi-excitonic intermediate state ${}^1(TT)$. This state will separate and generate two uncorrelated triplet states leading to the generation of two electron-hole pairs for every absorbed photon. Pentacene is potentially useful for solar cell efficiency beyond the Shockley-Queisser limit.



For such a process to be viable, the system should fulfill an important requirement, the energy of the singlet $E(S_1)$ should be at least double or more than the energy of the triplet $E(T_1)$. Pentacene fulfill this requirement by having $E(S_1) - 2 E(T_1) = 0.11$ eV, which permits the transition without the need for any thermal activation [113]. The energy diagram of the system is presented in Figure 2-24. In this diagram the S_1 is depicted by two transitions at 1.83 eV and 1.97 eV, which correspond to the Davydov splitting due to the different polarization of the two molecules in each unit cell relative to the b crystal axis.

The transfer process between S_1 and the multi-excitonic intermediate ${}^1(TT)$ happens on a sub-100 fs timescale. This multi-excitonic state is the main step in the fission process. Such a state is optically dark and has a very short life time, making it hard to detect using standard TA spectroscopy experiments. In TA experiments exciting the S_1 Davidoff state, the excitonic coupling between these S_1 states will not be visible, due to their short life time (sub-90 fs). What we could see in such an experiment is the ESA and SE of the S_1 which can give

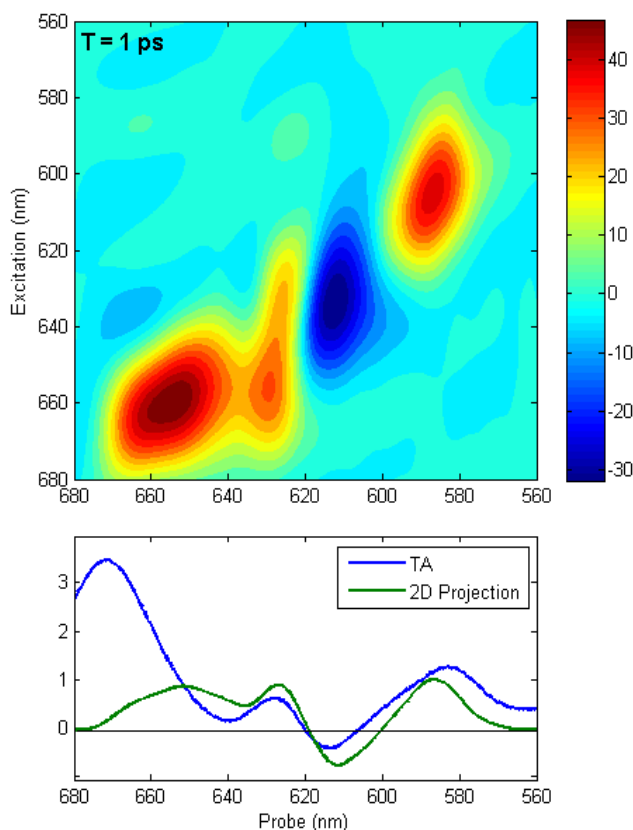


Figure 2-25 In the upper panel we present the real part of a 2D spectrum at $T = 1$ ps. The phasing procedure

us information about its relaxation dynamics. Concerning the multi-excitonic state, its lifetime is extremely short such that it was never detected. In addition the $S_0 \rightarrow T_1$ transition is optically forbidden, making the generation of $^1(TT)$ through doubly exciting the molecules impossible.

In that respect, we started to investigate this sample using 2D FT broadband spectroscopy. Using 2D spectroscopy we can retrieve information about the $^1(TT)$ state and the underlying vibrational and electronic dynamics involved in the fission process. We can take advantage of the broad spectral range to have a full picture of the system in one single measurement and employ high temporal resolution to observe the transitions in real time.

A primary measurement was performed using a spectral window between 680 nm (1.82 eV) and 560 nm (2.21 eV) covering the absorption bands of S_1 and S_n states as well as the ESA from the T_1 state. A 2D spectrum at 1 ps population time is presented in Figure 2-25, showing 3 positive peaks at 660 nm, 630 nm, and 580 nm representing the GSB of the S_1 (lower Davidoff state), S_1' (upper Davidoff state), and S_n states, respectively. The ESA from the T_1 state is present as a negative peak at 610 nm.

The phasing of this 2D spectrum is presented in the same figure, showing a fairly acceptable agreement between the TA data and projection of the 2D data into the detection frequency axis. The reason it is not a perfect match, is that the TA data were taken on a different setup

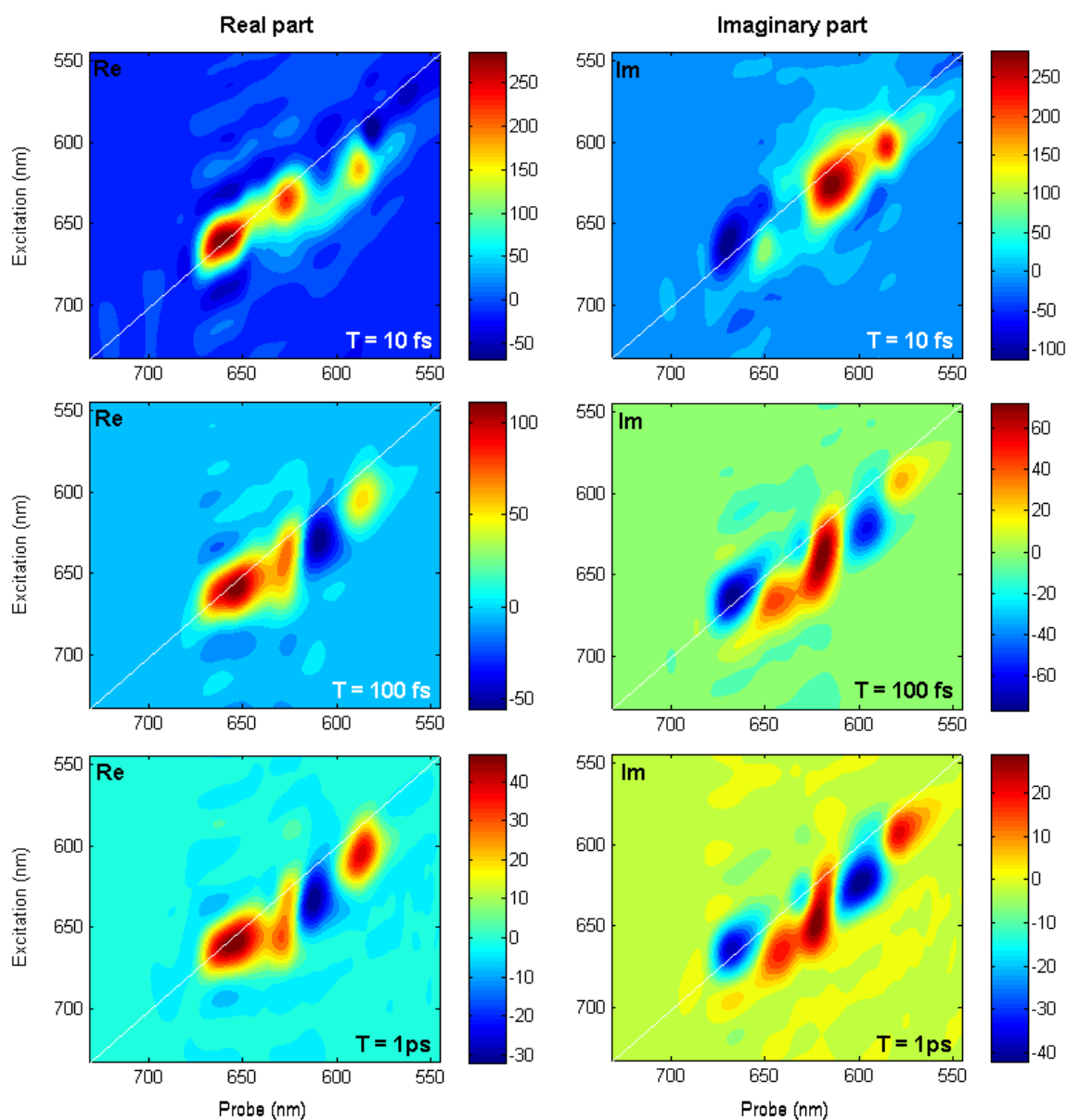


Figure 2-26 Absorption and diffractive 2D spectral of Pentacene films (100 nm) deposited on a 100 μm glass plate. The spectra are at population time 10 fs, 100 fs, and 1 ps, with a excitation and probe window between 730 nm and 545 nm.

using narrow band excitation pulses. The probe spectrum of the TA data was much broader since it was a white-light continuum between 750 nm and 500 nm. On the other side, the excitation spectra for the 2D measurements were low in intensity between 680 nm and 660 nm leading to the reduced peak intensity around 570 nm.

In Figure 2-26 we present the 2D absorptive and dispersive spectra at three different population times, $T = 10$ fs, 100 fs, and 1 ps. Evolution of the shape and intensity of the bands can be clearly seen. For $T = 10$ fs we observe that only positive features appear in the spectrum. These positive features correspond to the GSB of the singlet states. The lack of the negative feature at 610 nm shows that the T1 state is not populated yet.

A strong negative feature at 610 nm probe wavelength appears at 100 fs population time. This can be assigned to the ESA of the T1 state. Therefore, with this peak we can see the timescale of which the triplet state is being populated. The spectra of 100 fs and 1 ps do not show strong differences except for the reduced intensity. This behavior is expected since the triplet state is formed with the first 100 fs, and after that it lives for much longer than 1 ps.

Future measurements will be performed with broader pulses, covering up to 780 nm where we can visualize the multi-excitonic state or at least the transition to the triplet state. The population time will be sampled with fine steps such that we can record any vibration/vibronic oscillations happening within the split singlet states or the $S_1^{-1}(TT)$ state.

2.13 Conclusion

We presented the implementation of a broadband 2D FT spectrometer in the visible regime, which can access spectral range between 500 nm and 780 nm, with a broad spectral window of about 180 nm. The geometry chosen is a fully non-collinear geometry that employs the pairwise beam manipulation concept by steering the four beams in pairs. We proved that such geometry can achieve very high phase stability on both the long and short time scales, i.e. single measurement to several hours of measurements.

One of the important aspects of our work is the employment of self-phase modulation in a 1.1 m hollow core fiber to generate broadband pulses that were compressed by a deformable mirror base pulse shaper down to sub-10 fs. This ensures high temporal resolution in our experiments, and more importantly broad spectral windows allowing us to access coherences happening between distant chromophores.

We finally present primary measurements performed on Rhodamine 101 dye where we manage to observe the wavepacket dynamics of 220 cm^{-1} . Other measurements performed on pentacene films are also presented showing the spectral evolution of the bands over time.

Impulsive heating and vibrational relaxation in free-base porphyrins

3.1 Introduction

The photophysics of porphyrins has been widely investigated because of their importance in biology and their relevance in a wide range of applications [114-116]. The energy of the photon absorbed by these systems is converted into electronic and vibrational energy, eventually triggering photochemical processes such as charge transfer and bond breaking [117-121]. Deep understanding of the specific early relaxation mechanism and nuclear wavepacket motion occurring in this family of molecules is therefore fundamental for further comprehension of the role of porphyrins in nature and future application using porphyrin-based molecular devices. Here we focus on studying the relaxation dynamics of free-base porphyrins with substituents variation: tetraphenyl-porphyrin (H_2TPP) and octaethyl-porphyrin (H_2OEP).

The spectra of all porphyrins are characterized by an intense and narrow band around 400 nm (Soret band) with almost unitary oscillator strength corresponding to the $S_2 \leftarrow S_0$ transition and a dipole-forbidden but vibronically-induced transition in the 500-650 nm region (Q band) corresponding to $S_1 \leftarrow S_0$. The $\pi \rightarrow \pi^*$ transitions underlying this general absorption profile are described in the framework of Gouterman's Four-Orbital Model [122-124]. Since the Q bands are vibronically induced transitions, small changes in the molecular structure and active vibrational modes distorting the mixing of the electronic properties of the B state with the Q states, will lead to change in their properties such as intensity, spectral features and lifetime.

Over the years, free base porphyrins have been under intense investigation by a wide range of techniques in an attempt to elucidate the ultrafast electronic and vibrational relaxation processes occurring upon photo excitation, using femtosecond fluorescence up-conversion (FU) and transient absorption (TA) measurements. One of the first femtosecond FU measurements of a free-base porphyrin (H_2P) were performed by Akimoto et al. [125] with monochromatic detection, who reported a $Q_y \rightarrow Q_x$ internal conversion (IC) in 90 fs and intramolecular vibrational redistribution (IVR) within Q_x in 15 ps. Additional femtosecond time resolved FU and TA studies supported this picture of a sequentially cascading electronic and vibrational relaxation, where the dynamics after the internal conversion is exclusively happening in the Q_x state [126-128]. The fluorescence experiments were all based on monochromatic detection, making it hard to fully visualize the emission band profile, prohibited the possibility of observing band broadening and spectral shifts. Recently, Bialkowski et al. addressed this issue by means of broadband FU on H_2TPP in tetrahydrofuran excited at 3 different wavelengths within the Q bands with higher time resolution compared to earlier studies [129]. They proposed that while the Q_y and Q_x state are

instantaneously populated, there is an ultrafast inter-conversion between the two corresponding states, such that they can probe the relaxation of Q_x via the decay of Q_y emission. Finally, a study by Yeon et al., presented the first experimental observation of the Soret life time of H_2TPP which was reported to be $68 \text{ fs} \pm 15 \text{ fs}$ [130]. All of these studies adapted a cascading electronic relaxation scheme, where the depopulation of high energy states feeds the lower energy ones.

Very little is understood about the intramolecular vibrational energy redistribution (IVR) in porphyrins; where only the work of Holten et al. presented an interpretation of the thermal expansion of the macrocycle upon photoexcitation of metal and free-base porphyrins, showing that photoexcitation of the macrocycle leads to a lower HOMO-LUMO energy gap that recovers in the subsequent 10-20 ps [131]. Here, we investigate the ultrafast electronic relaxation dynamics using broadband FU and TA spectroscopy on both H_2TPP and H_2OEP . With the help of the broadband detection, we can track the changes in the HOMO-LUMO gap in both absorption and fluorescence from 50 fs to ps. We show that these molecules undergo an impulsive ($< 60 \text{ fs}$) expansion of the macrocycle, followed by longer IVR process on the 2 ps timescale, all contemporary with strong vibrational modes assisting the process. The ultrafast $Q_y \rightarrow Q_x$ IC is resolved for both systems for the first time, as a result of the high time resolution. We also shed light on the electronic relaxation of the Soret through various pathways.

3.2 Experimental section

3.2.1 Fluorescence up-conversion measurements

The set-up is as described in details elsewhere, [132, 133]. The sample was excited by 400 nm pulses with typical width 70 fs, power 80 nJ/pulse, focal spot 30 μm FWHM, and at a repetition rate of 250 Hz. The luminescence, collected in forward-scattering geometry, was up-converted in a 250-mm thick β -barium borate (BBO) crystal by mixing with an 800 nm gate pulse. The up-converted signal was spatially filtered and detected with a spectrograph and a liquid- N_2 -cooled charge-coupled device (CCD) camera in polychromatic mode. Appropriate Schott filters (Schott Glass Technologies) were used to attenuate the remaining excitation light. This greatly improved the signal-to-noise ratio but limited the detectable spectral range to a region from 40 nm red of the excitation wavelength to 700 nm. The temporal and spectral response of 110 fs and 15 nm respectively, were determined by a measurement of the Raman response from the solvent (data not shown). Measurements were performed at magic angle, placing a lambda half wave plate in front of the excitation beam.

The data were analysed by performing a multi-exponential fit of the kinetic vectors basis obtained from the singular value decomposition (SVD) of each 2-dimensional time-wavelength plot using a minimal number of decay components. The data of the fluorescence measurements in the 430-470 nm range were neglected during the analysis because of distortion by the Raman peak. The results were verified by performing a global

fitting procedure on kinetic traces taken across the total emission range. For both analyses, we obtained the same Decay Associated Spectra (DAS) and corresponding time constants.

3.2.2 Transient absorption measurements

The transient absorption measurements were carried on a 20 kHz laser system described in details elsewhere [134]. A commercial optical parametric amplifier (TOPAS-White) was used to generate the pump pulses at 505 nm, 40 fs width, 200 nJ/pulse power for H₂TPP (100 nJ for H₂OEP), that were focused on the sample (150 μm FWHM). The pulses were compressed by controlling the chirp of the white light used in the NOPA generation process and a pair of glass wedges leading to near-Fourier limit pulses at the position of the sample. The probe pulses were generated by focusing part of the 800 nm beam on a CaF₂ crystal to generate the super-continuum. The compensation for the chirp was done afterwards during the data analysis by applying Group Velocity Dispersion (GVD) correction on the data and setting all the traces back to time Zero, eliminating the effect of the chirp. TA measurements of the solvent under the same conditions in order to collect information about the GVD of the probe pulse and to estimate the instrumental response function (IRF). The IRF was estimated to be 57 fs ± 5 fs. Measurements were performed at magic angle by placing a lambda half wave plate in front of the probe beam, to avoid anisotropy effect of the reorientation.

3.2.3 Sample preparation

The porphyrins were purchased from Sigma Aldrich and dissolved in toluene. For the fluorescence measurements, a concentration corresponding to an optical density of ~0.3 at 400 nm was used in the 0.2-mm-thick fused silica flow-cell. For the transient absorption measurements, a concentration corresponding to ~ 0.2 O.D. for the Q_y(1,0) band was used in the 0.2-mm fused silica flow-cell (thin window).

As shown in Figure 3-1, just as all porphyrins, the spectra of the H₂TPP and H₂OEP share general features such as the Soret (B) and Q bands. The Soret B band is an intense and narrow band around 400 nm with almost unitary oscillator strength corresponding to the S₀→S₂ transition. Although the Q state S₀→S₁ (475-650 nm region) is a dipole forbidden state because of the symmetry of the electronic structure (D_{2h}), but it becomes allowed due to the mixing of the electronic property with the B state with the Q state by the configuration interaction and vibronic coupling explained by the Herzberg-Teller effect [122-124, 135, 136] The Q band is split into orthogonally polarized Q_x and Q_y electronic transitions, where *x* refers to the H-H axis [124].

The Soret band of H₂TPP peaks at 416 nm (410'000 cm⁻¹M⁻¹) is narrow and has a shoulder at 400 nm, whereas that of H₂OEP is at 399 nm (with a shoulder at 375 nm), and it is substantially broader and lower in intensity (160'000 cm⁻¹M⁻¹). The Soret-Q bands energy splitting is weakly affected by the peripheral group. Contrary to the Soret band, the Q bands of H₂OEP are narrower than those of H₂TPP. In both absorption and fluorescence spectra, the progression strongly deviate from a Poisson distribution because of the forbidden nature of

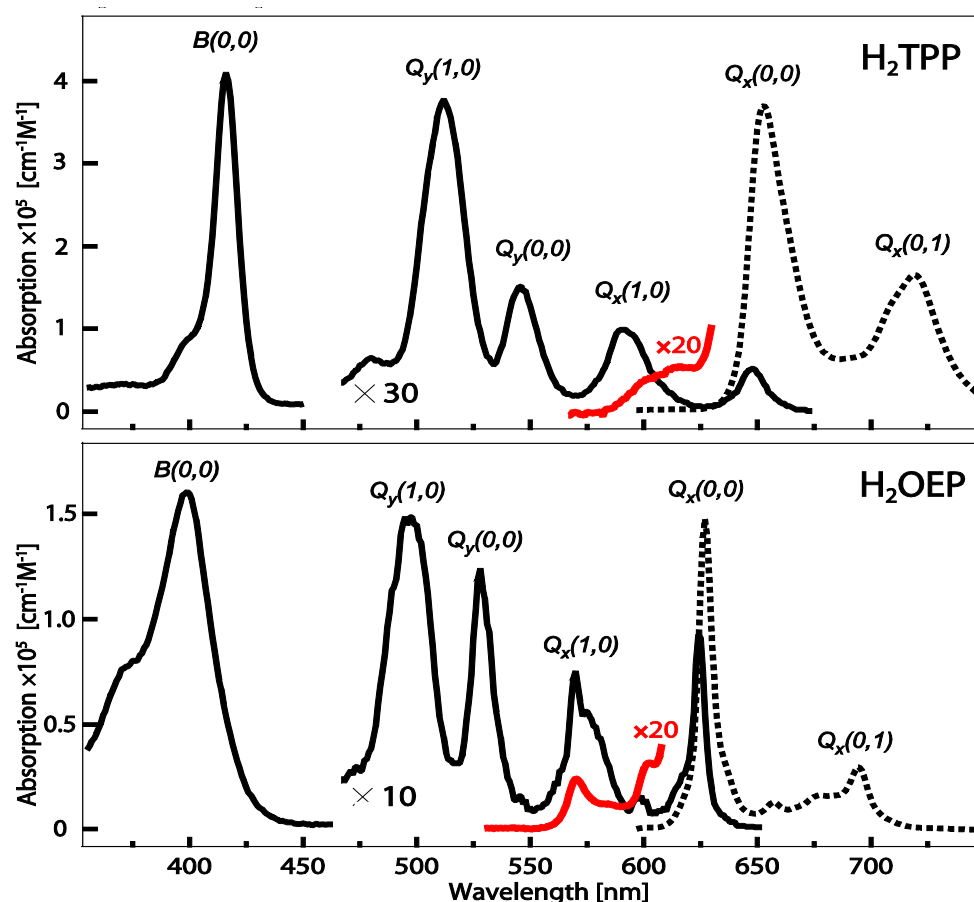


Figure 3-1 Steady state absorption (continuous traces) and emission (dashed traces) of H₂TPP (top) and H₂OEP (bottom) in toluene. The Q band region (470 to 670 nm) has been multiplied by a factor of 30 and 10 for H₂TPP and H₂OEP, respectively. The red traces are the blue-most region of the emission spectrum multiplied by 20.

the Q bands. Indeed while the (0-0) transition is orbitally forbidden, the first replica (0-1) is vibronically induced and gains intensity through the Herzberg-Teller effect [135-137]. The ratio between the first vibronic band and the 0-0 band is indicative of how much the transition is allowed [138], showing that the H₂OEP Q-band has a more allowed character than that of H₂TPP.

The fluorescence quantum yield of these complexes is ~ 0.1 , reflected in ~ 10 ns intersystem crossing to the triplet state T₁, which itself decays on the millisecond timescale [139, 140]. The very small Stokes shift of both molecules is evidence of negligible structural rearrangement and/or solvation. The frequency spacing between 0-0 and 0-1 lines of ~ 1600 cm⁻¹ corresponds to the C=C stretch mode in the pyrrole rings. In the static fluorescence spectrum (Figure 3-1), a weak shoulder is observed at ~ 610 nm for H₂TPP (red trace) and a peak at 570 nm for H₂OEP (red trace) with amplitude $< 1\%$ of that of the Q_x(0,0) band. This feature, disappearing at low temperature [141], is thermally populated and has been attributed to a hot band.

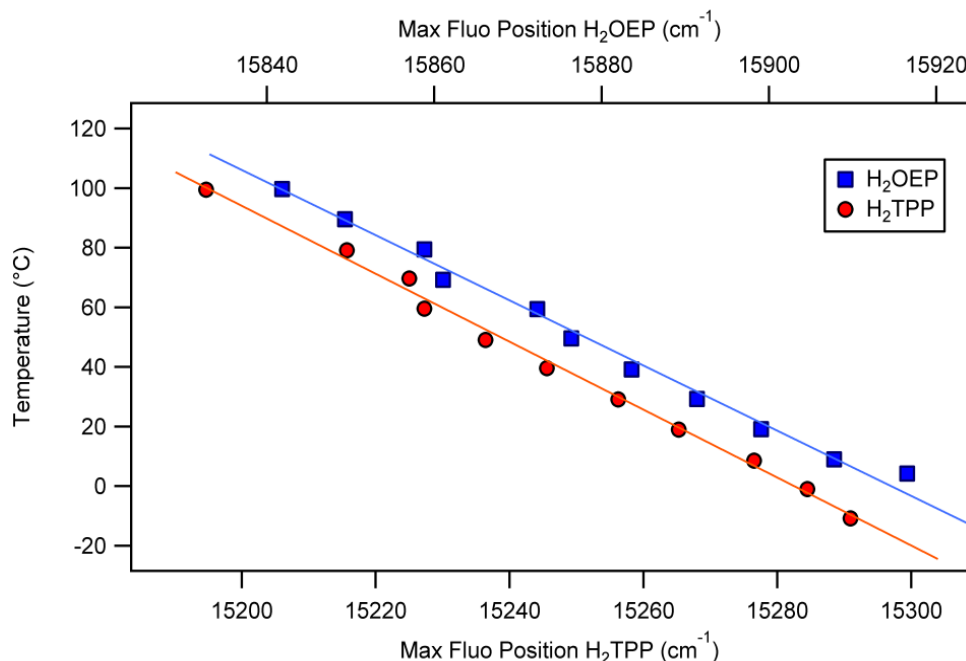


Figure 3-2 Temperature dependence of the stationary $Q_x(0,0)$ fluorescence maximum of H_2TPP and H_2OEP in toluene, along with their linear fits.

Temperature dependent fluorescence spectra were recorded for each sample, using a static fluorimeter. The fluorescence spectra were measured at a various temperatures between 120°C and -15°C. The peak of the fluorescence of the $Q_x(0,0)$ show a linear dependence on the temperature, as can be seen in Figure 3-2. This will be used later to estimate the local temperature upon photoexcitation by tracking the fluorescence spectra in time.

3.3 Results

3.3.1 Fluorescence Up-conversion measurements

Figure 3-3 shows a selection of kinetic traces (top) and transient fluorescence spectra (bottom) of H_2TPP and H_2OEP in toluene upon excitation at 400 nm at low (solid lines) and high fluence (dashed lines). The strong peak at 455 nm corresponds to the 3000 cm^{-1} Raman peak of toluene.

At time zero, the emission covers the entire detection range within our instrumental response, as seen from the kinetic traces of Figure 3-3 (the rise reflects the instrumental response function). The weak and large band below 480 nm (blue arrow), which vanishes within 300 fs and 200 fs for H_2TPP and H_2OEP respectively, is ascribable to the Soret emission based on its near-mirror image character with respect to the Soret absorption band, bearing in mind the strong reabsorption of the sample, which reduces the blue wing [126, 142, 143]. Above 480 nm, a broad emission with three clear bands appears promptly (black, green, orange and red arrows). The selection of kinetic traces shows that the two blue bands (550 and 600 nm for H_2TPP and 530 and 575 nm for H_2OEP) decay bi-exponentially within a few picoseconds.

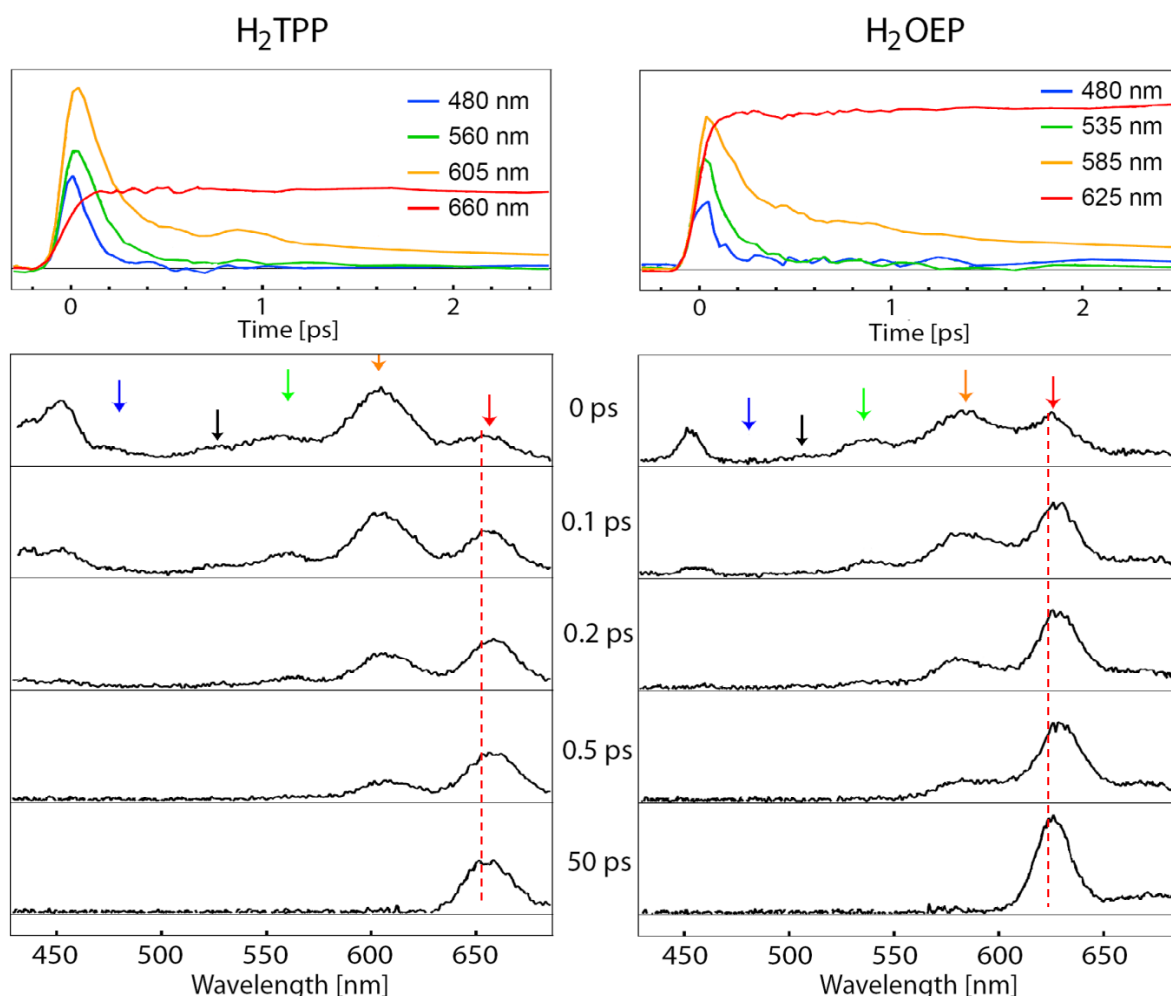


Figure 3-3 Representative selection of kinetic traces (top) and transient fluorescence spectra (bottom) of H₂TPP (left) and H₂OEP (right) in toluene excited at 400 nm. The strong peak at ~455 nm is the Raman response of the solvent (~3000 cm⁻¹). The transient spectra were selected from the 2D plots normalized at long time delay (50 ps), at the maximum of emission (660 nm for H₂TPP and 625 nm for H₂OEP). The red dashed lines are included to guide the reader's eye to the spectral shift over time.

These bands can be assigned to Q_y(0,0) and Q_y(0,1) transitions, respectively, based on their mirror image symmetry with respect to the absorption band (Figure 3-1) [129]. On the contrary, the red most band (655 nm and 625 nm for H₂TPP and H₂OEP, respectively), which corresponds to the Q_x(0,0) emission band exhibits a long lifetime, which is ~ 10 ns, as previously reported [139].

Figure 3-4 shows the Decay Associated Spectra (DAS) extracted by a Singular Value Decomposition (SVD). For both samples, the orange and red DAS, associated with two fast relaxations, are very similar in shape with three broad maxima ascribed to the Q_y(1,0), Q_y(0,0), and Q_y(0,1) emission. These broad maxima are a signature of the decay of these bands on with biphasic relaxation process. In the blue side, the Soret emission of the H₂TPP appears to exhibit a positive feature in the 80 fs DAS (red) component, but not the longer component (orange), which is expected since its lifetime should be <100 fs. In the case of the

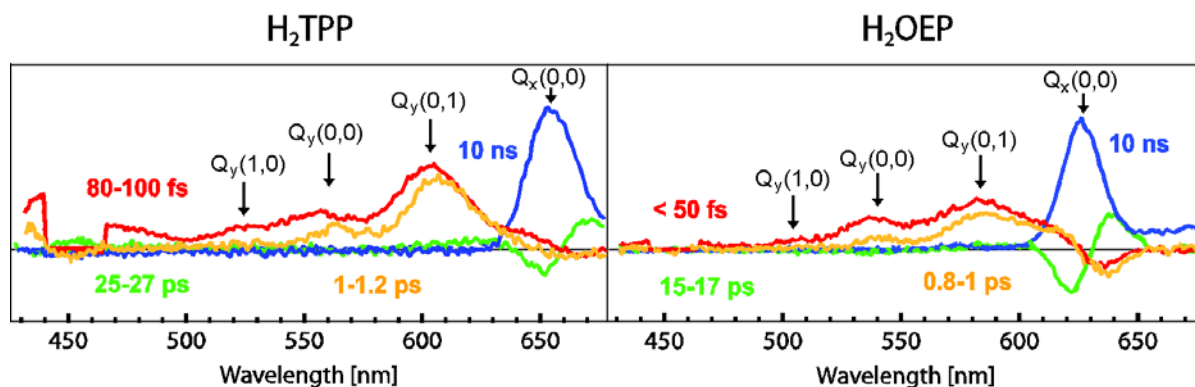


Figure 3-4 Decay Associated Spectra (DAS) of the time-resolved fluorescence of H₂TPP (right) and H₂OEP (left) upon excitation.

H₂OEP we cannot resolve the Soret emission region since it is partially covered by the Raman response of the toluene. By close inspection of the transient spectra in Figure 3-3 in the Q_x(0,0) region (the dashed red lines are for eye guidance), a bathochromic shift is clear in the first 500 fs. This shift can be also seen in the DAS spectra of the first two components, signified by the second derivative like shape in the region above 630 nm for H₂TPP and 600 nm for H₂OEP. This second derivative shape is more apparent in the case of the H₂OEP compared to the H₂TPP.

The lack of negative features in the DAS spectra in the region of the Q_x band show that the Q_x emission appears within the IRF, and there is no rise in the signal. Although by inspection of the transients in Figure 3-3, the transient of the Q_x emission bands (red trace) appear to be rising in a slower manner than the others, it does not show any rise in the DAS. Such a rise can be accounted for by considering the red shift of the bands over the first 500 fs. In Figure 3-5 we present a simulation of the decay of the Q_x(0,0) emission band of H₂TPP over time, considering a multi-exponential scheme using the timescales obtained from the data convoluted with the IRF. The first simulation (a) takes only the relaxation into account, while the other two (a and b) take into consideration the spectral shift (red shift) and narrowing of the band over time. All of the variables used are obtained from the data analysis of the real data. A transient from each model is taken at the center of the emission band between -100 fs and 2 ps, and plotted in Figure 3-5 (bottom) for comparison. The transients taken from the simulations with spectral shift, show a slower rise compared to the blue one, which can be misinterpreted as a rise of the band. When analyzing single traces, such spectral shifts will not be observed and the slow rise can be easily mistaken by other processes.

The DAS of the 26 (16) ps and 10 ns components show the subsequent picosecond dynamics of the lowest S₁^x state. The 26 (16) ps component for H₂TPP (H₂OEP), describes a concomitant narrowing and blue-shift of the Q_x(0,0) band. Indeed, its spectral profile resembles a mix of first and second derivative of the latter ns-band, which is a typical signature of shift and cooling processes combined [126, 144]. The longer 10-ns DAS component represents the subsequent decay of the excited S₁^x to the triplet state as described by Baskin et al. [126].

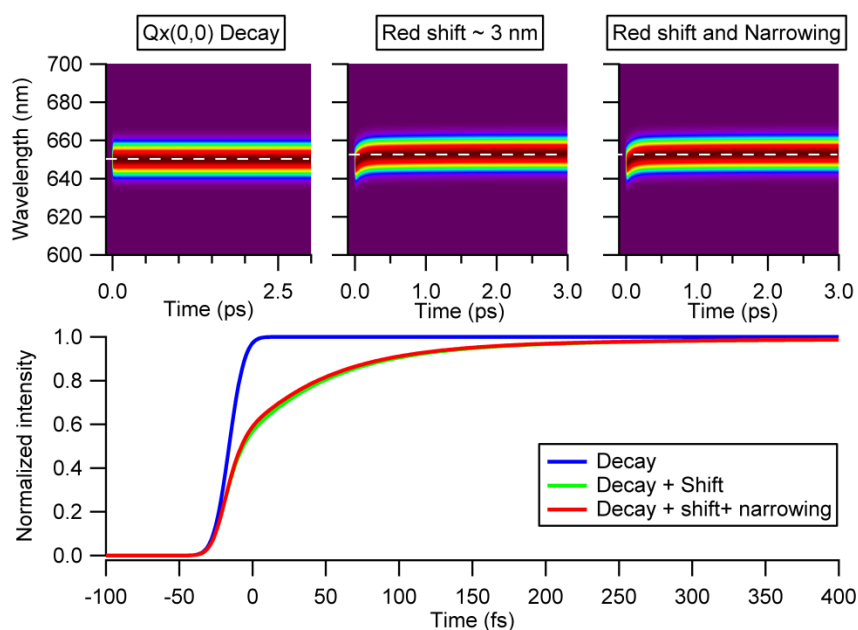


Figure 3-5 Simulation of the $Q_x(0,0)$ emission band over time. a) Pure decay with three exponential decays. b) Considering the 3 nm red shift observed in the FU transients. c) Considering the red shift and the band narrowing. d) Transients from each simulation is taken and compared.

The weak bands that are present on the blue side of the $Q_y(0,0)$ bands (black arrows) at 527 nm and 508 nm for H_2TPP and H_2OEP , respectively. They decay on a comparable timescale as the Q_y bands and can be observed in the DAS presented in Figure 3-4. For H_2TPP the energy splitting between the vibrational levels in the Q_y bands are in the range of 1300 cm^{-1} and the fluorescence around 527 nm can be assigned to the first Frank-Condon active vibrational mode in the Q_y state to the zeroth vibrational mode in the ground state, $Q_y(1,0)$. The same can be concluded for the 508 nm band of the H_2OEP .

3.3.2 Transient absorption measurements

Time-wavelength plots of difference transient absorption ΔA are presented in Figure 3-6 a and Figure 3-7 a, for H_2TPP and H_2OEP , respectively. The plots are split in two, the first part presenting the time delay between -100 fs till 3 ps and the other part spans from 4 ps till 25 ps. The transient absorption difference spectra obtained for both samples upon photoexcitation show a series of troughs embedded on a relatively broad excited state absorption positive signal. The spectral window of these measurements ranges between 430 nm and 677 nm covering the Q bands absorption bands and leaving the Soret band out of observation window. The troughs in the spectra can be identified as the ground state bleach (GSB) of the four Q bands. These features are typical of free base porphyrins, and have been reported in various studies [128]. The transients do not recover within our measurement window of 25 ps, which are in accordance with the long lifetime of the Q_x state $> 10\text{ ns}$ [126, 145]. The ground state bleach (GSB) signals all relax and behave in a common way, but the ESA signal has different relaxation dynamics depending on the wavelength denoted by the 2

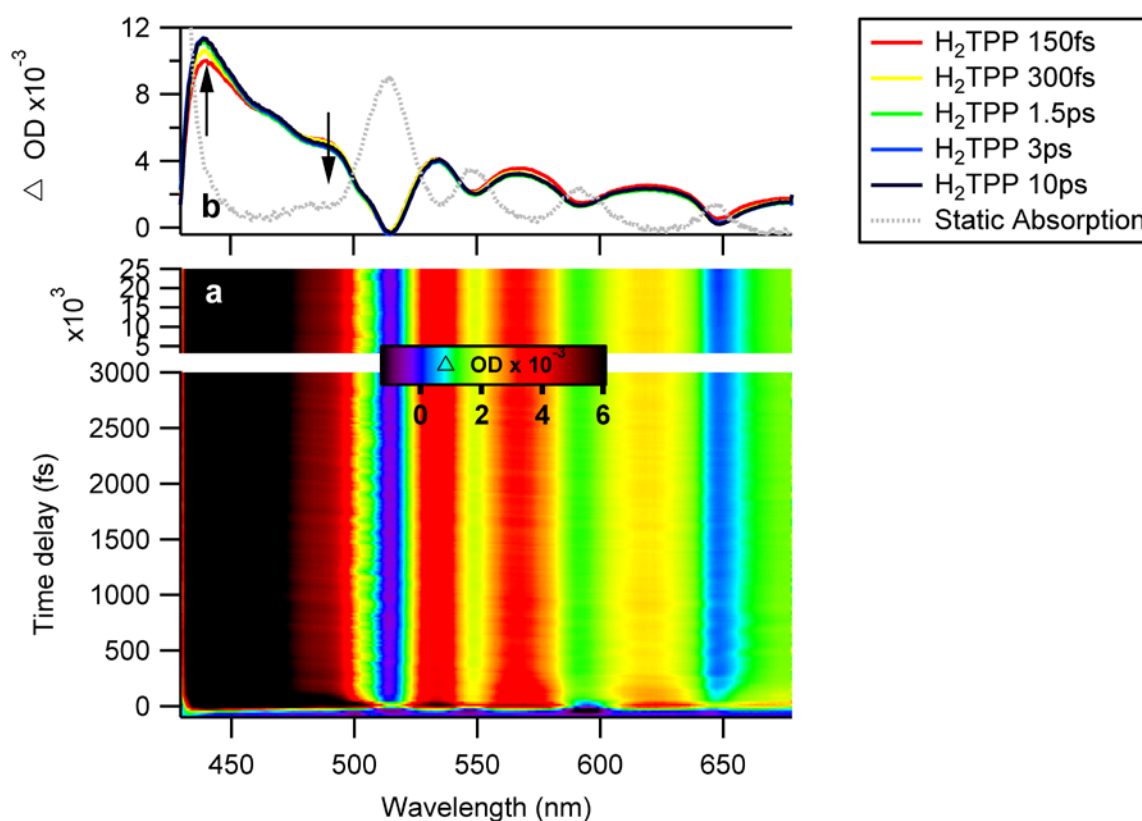


Figure 3-6 Difference spectra at specific time delays of H₂TPP in Toluene (top panel) and its transient absorption in the femto/picosecond regime upon 505 nm excitation (bottom panel). The first 3 ps are shown with a linear scale while the following 20 ps are shown separately.

arrows pointing to growth and decay of the signal. A global fit analysis of the data reveals a multiphasic relaxation dynamics. Along with the electronic and vibrational relaxation, high and low frequency oscillations appear in the traces over the whole probe spectral window. The intensity of the oscillations varies between the GSB and ESA which we discuss later in details.

Table 1 Relaxation timescales for both H₂TPP and H₂OEP

	H₂TPP	H₂OEP
T1	93 ± 6 fs	40 ± 8 fs
T2	1.6 ± 0.8 ps	930 ± 100 fs
T3	26 ± 5 ps	15 ± 3 ps
T4	Set to 10 ns	Set to 10 ns

In the case of H₂TPP the data presented in Figure 3-6, a total of four exponential decay functions are needed to get a satisfactory fit of the data, all convoluted with instrumental response function IRF. Three timescales of 93 fs ± 6 fs, 1.6 ps ± 0.8 ps, 26 ps ± 5 ps were found by a free fit of the transients while leaving the long lifetime of 10 ns fixed through the whole procedure. The 10 ns timescale was fixed since the Q_x lifetime in both samples ranges between 10 and 15 ns [128, 129], which exceed our time window by orders of magnitude.

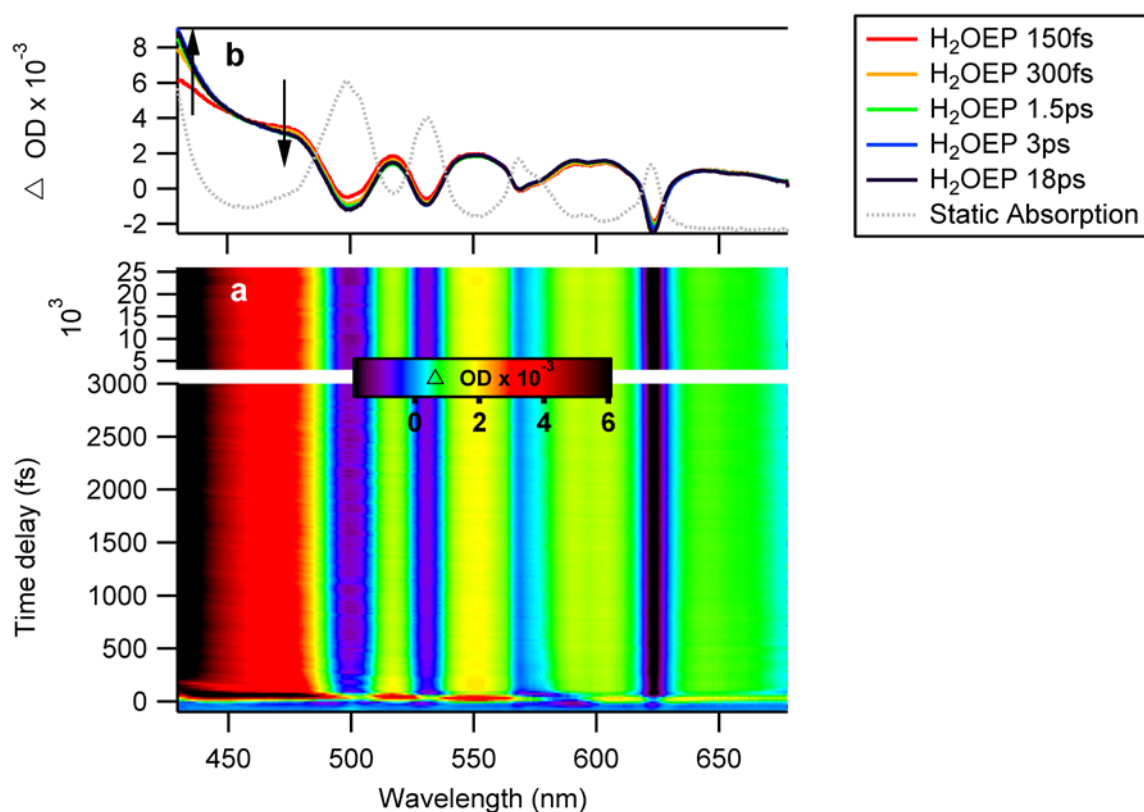


Figure 3-7 Difference spectra at specific time delays of H₂OEP in Toluene (top panel) and transient absorption in the femto/picosecond regime upon 505 nm excitation (bottom panel). The first 3 ps are shown with a linear scale while the following 22 ps are shown separately.

The error of the 26 ps decay time is high since our maximum probe time window is only 25 ps and few data points were taken between 3 ps and 25 ps, since we are interested in the early time scales. Comparable to the fluorescence data, a blue shift is also observed in the transient absorption data of H₂TPP. The inset in Figure 3-6 b, show the evolution of the bleach overtime. The timescales are presented in Table 1 and the interpretation is in the discussion.

In the case of H₂OEP presented in Figure 3-7, very similar spectral behavior is observed with shorter relaxation processes. Since the absorption bands are stronger and sharper than the ones of the H₂TPP, the GSB of the Q_x(0,0) overcomes the ESA signal and reaches a negative value of about -2 mOD. A satisfactory fit consisted of four exponential decay functions convoluted with the same IRF as H₂TPP, since both measurements were performed under the same conditions. The timescales extracted in this case were a slightly shorter than the ones of H₂TPP, 40 fs ± 8 fs, 930 fs ± 100 fs, and 15 ps ± 3 ps, and 10 ns (Table 1). The 10 ns decay time was fixed during the fit process for the same reasons mentioned earlier. Comparable to the H₂TPP, the ESA exhibits 2 different behaviors for the regions above and below 450 nm. The same blue shift observed earlier is also present.

3.4 Discussion

In a common electronic cascading relaxation, the depopulation of high energy states feeding lower energy ones is reflected into the concomitant decay of emission at short wavelengths and rise at longer ones. Considering the case of Q_y feeding Q_x state, we expect that the Q_x emission should be rising on the same time scale as the Q_y decay. Therefore a negative feature is expected in the $Q_x(0,0)$ region of the short time DAS component. The absence of a significant negative feature specifically shows that other pathways in parallel to the sequential cascading might be present. The Q_y bands show bi-exponential decay, the fastest of which is being shared with the Soret emission (red traces Figure 3-4). This is evidence of multiple branching occurring already at an early stage in the Soret region, which likely contains more than one electronic transition simultaneously populating the S_{1x} and S_{1y} .

In the next chapter, we discuss the coherent wave packet dynamics observed in these systems, and we present that in the time resolved fluorescence spectra we could observe wavelength dependent wave packets specific for each Q band. In the H_2TPP for example, we observe a vibrational frequency of 190 cm^{-1} in the region of the Q_x emission, while only low frequency modes were observed in the Q_y regions ($> 630\text{ nm}$). Similar results were found in the case of H_2OEP . These coherent wavepackets are generated as a consequence of the impulsive IC from the Soret band to the Q bands. To generate such WPs in the Q bands upon $B \rightarrow S_1$ IC, that means that the IC process must be faster than half the vibrational period of the triggered mode in order to generate a coherent superposition of vibrational states. Overall, the presence of WP dynamics with different frequencies in the Q_x and Q_y bands confirms that different electronic states S_{1x} and S_{1y} are populated in parallel with different IC.

Nevertheless, Q_x emission (static and time resolved) is also observed when exciting within the Q_y or Soret bands [129]. Therefore, the IC process from the Soret is populating both S_{1x} and S_{1y} states in a parallel fashion, and then the S_{y1} relaxes through IC to the S_{1x} . This also must be accompanied by a negative feature in the DAS at the $Q_x(0,0)$ region. The absence of significant negative contribution, even for the $S_{1y} \rightarrow S_{1x}$ IC, can be explained by the competing vibrational relaxation of the Q_y band that is feeding the long living Q_x state, represented by the 650-nm (630-nm) emission band of H_2TPP (H_2OEP), in accordance with the literature [126, 129]. Note that the fastest exponential decay is shared with the Soret emission (red traces, covering the 420 to 680 nm region). Due to all of these different pathways, the strong early spectral shift, and their convolution with the IRF we could not distinguish between the different pathways and extract their timescales, but we could resolve the Soret lifetime, and it was measured to be 80 fs for H_2TPP and <40 fs for H_2OEP . The H_2TPP Soret lifetime is in accordance with the earlier reported lifetime of $68\text{ fs} \pm 15\text{ fs}$. To resolve the $S_{1y} \rightarrow S_{1x}$ IC process we use the ultrafast TA data in the next part [130].

The energy splitting between the Q_x and Q_y corresponding to 2750 cm^{-1} , which is close to twice the frequency of the vibrational modes in the Q_y (1230 cm^{-1}) and Q_x (1460 cm^{-1}) excited state, which correspond to the C=C stretch mode in the pyrrole rings. This energy splitting shows quasi-degeneracy of vibrational levels of Q_x and Q_y which enhances the coupling between them, leading to ultrafast IC from $S_{1y} \rightarrow S_{1x}$. In earlier studies [126], the

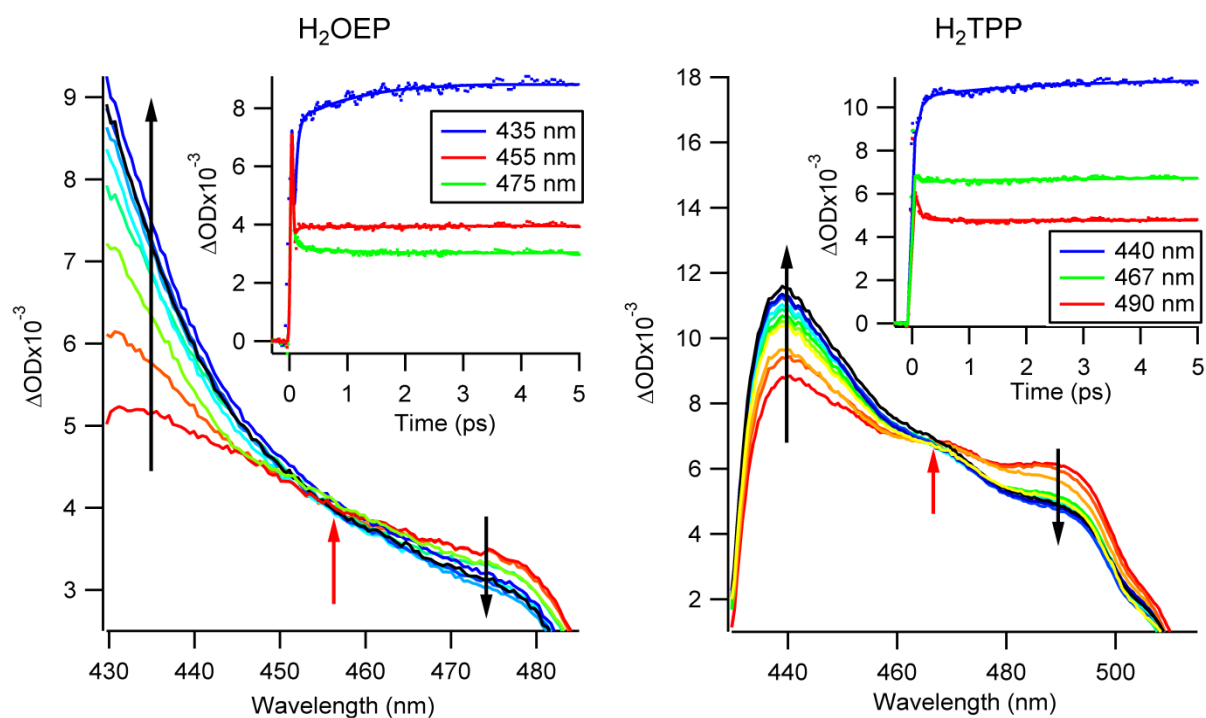


Figure 3-8 Difference spectra evolution of the ESA region between 380 nm and 520 nm of both H₂TPP and H₂OEP upon 505 nm excitation, with the black arrows showing different behavior depending on the spectral position. The red arrow points to an isosbestic point.

IC process in H₂TPP was estimated to be < 100 fs, due to the limited time resolution. For example, in the case of porphyrin derivatives with only 2 phenyl substituents on opposite meso positions and methyl or ethyl groups in all β positions, this time scale was estimated to be 90 fs [125]. On the other side, in case of H₂P, where no substituents are attached to the macrocycle, the timescale was reported to be 150 fs [128]. Therefore, the IC from $S_{1y} \rightarrow S_{1x}$ timescale might vary strongly between H₂TPP and H₂OEP.

In TA spectra, we can extract information about the excited states through stimulated emission or excited state absorption, and the recovery of the ground state bleach. Since the absorption of the Q bands is quite weak due to their forbidden nature, the ESA signal dominates the whole spectral range. Therefore, the best way is to monitor the ESA which will contain information excited states and their dynamics. In the blue side of the transient spectra, only contribution from the ESA exists without the contribution of the bleach. And since we excite the Q_y band (505 nm), we definitely do not have any SE from the Soret band. By investigating the ESA behavior in this region we can draw conclusions about the ultrafast electronic relaxation involving the Q bands. Two distinct behaviors are observed; the signal exhibits a rise in one region contemporary with decay in the other, creating an isosbestic point in the center, as shown in Figure 3-8, for H₂TPP and H₂OEP respectively. In the inset, we present kinetic traces at the 3 wavelengths indicated by the arrows.

In the case of the H₂TPP, the traces at 440 nm and 490 nm show a clear rise and decay, respectively. By globally fitting these traces with a three exponential decay functions, we extract timescales of 93 fs, 1.4 ps, and 26 ps. A very similar behavior is observed in the case

of H₂OEP, yielding the time scales of 40 fs, 930 fs, and 15 ps. This behavior can be explained by the fact the Q_y depopulation is coupled to the population growth of the quasi-degenerate vibrational levels of the Q_x manifold. We attribute the 90 fs/ 40 fs timescale to the S_y¹ → S_x¹ IC for H₂TPP and H₂OEP, respectively. However, the fluorescence transients presented in Figure 3-3 show that the fluorescence of the Q_y bands is not fully relaxed within the first couple of ps. Therefore, we should think about reverse IC process from S_y¹ ← S_x¹, which keeps both Q_x and Q_y populated as long as they are in equilibrium [129]. In such a case the fluorescence decay of the Q_x band is probed via measuring the emission decay of the Q_y bands [129], which interprets the lack of rise of the Q_x emission band in the transient spectra.

The 1.4 ps was assigned in earlier reports [126, 129] to intramolecular vibrational energy redistribution (IVR) and the 26 ps component was attributed to vibrational cooling of the Q_x state, relaxing the vibrational energy by coupling to solvent molecules. These cooling dynamics are signified by a blue shift of the difference spectra with time, comparable to the results obtained by Holten et al. on ZnTPP [131]. This blue shift is identical to the one of the fluorescence discussed earlier. Comparable assignment can be given to the H₂OEP time scales, with 900 fs and 15 ps for IVR and VR, respectively. This assignment of the IVR and VR to these decay timescales is further supported by making use of the superiority of the broadband detection of both experiments over monochromatic detection schemes, probing the change in the spectral weight of the emission and absorption over time.

The temperature dependence of the stationary Q_x(0,0) fluorescence maximum, reported in Figure 3-2 for H₂TPP and H₂OEP in toluene, allows us to follow in real time quantitatively the temperature evolution of the porphyrin after photoexcitation. This temperature effect needs to be considered with cautious since when performing the temperature dependence of the static fluorescence, the solvent and the solute are heated, leading to two opposing effects; the weakening of the solute/solvent interaction leading to a blue shift and solute temperature increase leading to a red shift [131]. Therefore these numbers are only considered for qualitative estimation of the temperature. Figure 3-9 shows the first spectral moment (average position M1) of the Q_x(0,0) band fluorescence, and as inferred by Figure 3-2.

Such a hypsochromic shift of the Q_x emission band results also from a temperature effect: the position of the fluorescence spectrum of porphyrins is sensitive to temperature. Indeed, such a blue shift was already observed in TA and FU measurements of metal and free-base porphyrins by Holten et al. [131]. They attributed it to vibrationally induced reduction of the energy gap by anharmonic expansion of the porphyrin ring when the temperature of the latter is increased; excluding solvation effects and conformational changes by comparing the results to gas phase ones. Such an important shift is expected through internal vibrational redistribution (IVR) of the large excess energy deposited upon excitation within the Soret band [146]. Accordingly, the hypsochromic shift corresponds to recovery of the initial porphyrin size as it cools down by coupling to the solvent.

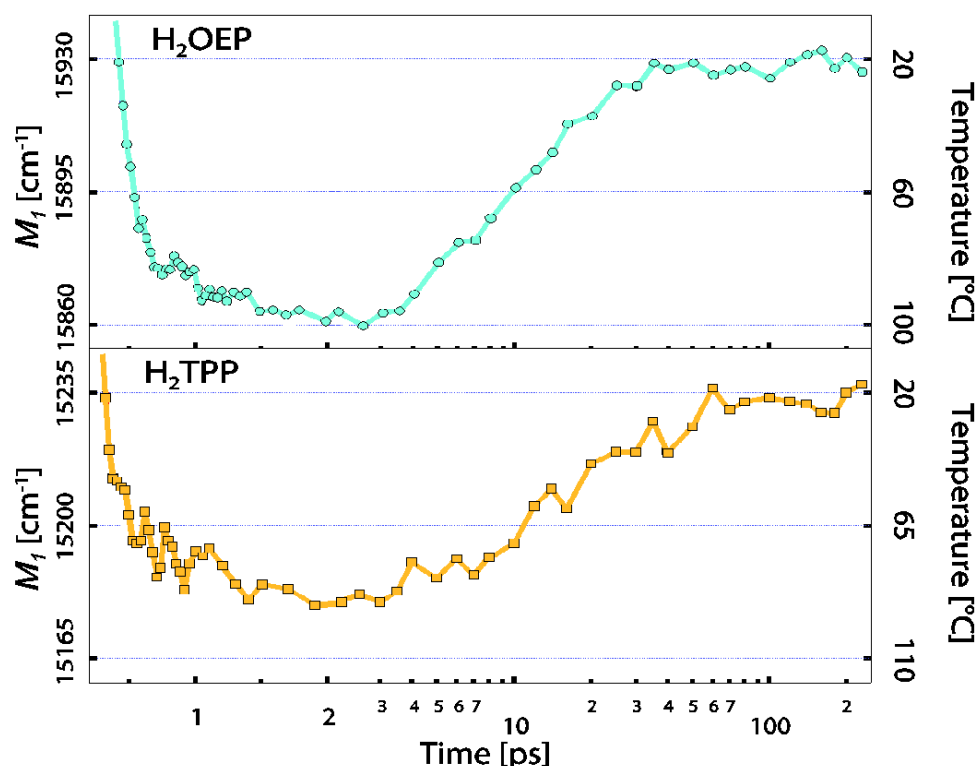


Figure 3-9 First spectral moment of the $Q_x(0,0)$ emission band from H_2OEP (top) and H_2TPP (bottom), upon excitation in the linear regime (light blue and orange) and in the saturation regime (dark blue and red). In the first 2 ps M_1 is plotted in a linear scale while a logarithmic scale is used from 2 to 200 ps.

The presence of emission on the blue side (Q_y emission) decaying on the same timescale does not allow an accurate measurement of the expansion time, but we can conclude an upper limit of ~ 1 ps. The energy of the $Q_x(0,0)$ electronic transition being directly related to the size L of the aromatic ring as L^{-2} , the relative energy shift gives direct access to the relative change in size of the porphyrin [131]: the amplitude of the shift here reported (~ 70 cm^{-1} for H_2OEP and ~ 52 cm^{-1} for H_2TPP) corresponds to an expansion of $\sim 0.45\%$ of the size of the cold porphyrin. The difference in cooling times (~ 26 ps for tetraphenyl and ~ 16 ps for octaethyl peripheral group) suggests an important role of the substituents in this process. The presence of phenyl groups at the periphery probably reduces significantly the number of solvent molecules in direct contact with the porphyrin macrocycle, decreasing the heat transfer efficiency.

The M_1 of the GSB around the $Q_x(0,0)$ band in the transient absorption data is shown in Figure 3-10. The M_1 dynamics of both H_2TPP and H_2OEP are consistent with the fluorescence data, showing a primary fast red shift upon photoexcitation, followed by a slow blue shift. Since the excess energy deposited by 505 nm excitation is smaller compared to the 400 nm excitation in the fluorescence case, the amplitude of the shifts is reasonably smaller (~ 40 cm^{-1} for H_2OEP and ~ 22 cm^{-1} for H_2TPP) but maintain comparable dynamics. By fitting with multi-exponential decay functions, the dynamics of the M_1 can be expressed by 3 exponential decay functions only, the red shift signified by a 60/45 fs and 1.8/1.6 ps components and the blue shift by 11/9.3 ps component for H_2TPP and H_2OEP , respectively.

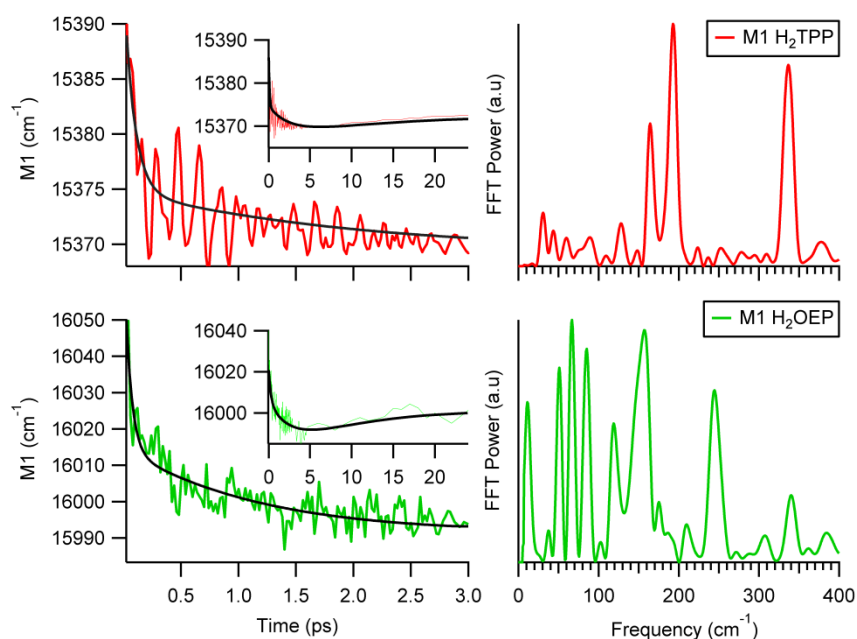


Figure 3-10 First moment of the $Q_x(0,0)$ of both H_2TPP and H_2OEP , showing a primary blue shift on two time scales followed by a slow red shift. Both moments are fit with bi-exponential functions, and the corresponding FFT of the residual of each trace is presented on the right side. The FFT show multiple modes contributing to the energy degradation.

Interestingly, the M1 traces of both samples show oscillations that are triggered by the impulsive heating. The Fourier transforms of the residual of the fit (black traces left panel) and presented in Figure 3-10 (right panels). These vibrational modes are discussed in details in the next chapter, which are mostly due to out-of-plane vibrations by comparison with various theoretical studies [147, 148].

Typically, visible or UV excitation promotes the molecules to a high vibrational level of the electronic excited state. The excess vibrational energy is then redistributed among all other vibrational modes anharmonic coupling. The IVR process is iso-energetic and independent of the solvent, and it has been shown that its timescale varies vastly depending on the molecular system under investigation, from ps to tens of fs [146, 149-152]. By examining the vibrational modes resolved by the FFT of the M1, we expect the conversion of the high frequency modes to lower frequency modes. Therefore, the frequency modes involved in the vibrational relaxation obtained from the FT of the M1 should have a longer lifetime for the high frequency modes compared to the low frequency modes [24, 25]. From the bandwidth of the each mode, the corresponding vibrational dephasing time can be obtained. In Table 2, we present all the vibrational modes resolved in the FT of the residual of the M1, and as expected the low frequency modes show about twice the lifetime of the high frequency modes.

Such dramatic shifts (to the red and then followed by the blue) of the absorption and fluorescence spectra upon photoexcitation can be connected to the vibronic coupling between the Soret and the Q bands [153]. By di-cation of the porphyrins or attachment of bulky substituents, the porphyrins macrocycle gets distorted leading to changes in the absorption and fluorescence spectra. Studies over such systems have been extensively performed and

reported: red shift of the absorption bands, larger Stokes shift, broader and less structured fluorescence spectrum, and reduced fluorescence yield [128, 140, 154]. Since the vibrational modes observed are mainly out-of-plane modes, i.e. distorting the planar geometry of the porphyrins, we know for a fact that the vibrationally excited porphyrins are changing their planarity affecting the vibronic coupling, which in turn appears as spectral shift due to the reduced energy gap.

Table 2 Mode lifetimes of H₂TPP and H₂OEP obtained from the First moment of the Q_x(0,0) absorption band

H ₂ TPP modes (cm ⁻¹)	Mode lifetime (ps)	H ₂ OEP modes (cm ⁻¹)	Mode lifetime (ps)
31	4.1	37	4.5
43	4.76	51	5.2
60	3.7	66	4.7
88	2.2	85	3.6
127	3	118	2.8
164	3.08	156	1.4
192	2.7	209	2.4
--	--	244	2
--	--	308	2.2
336	2.2	340	2.1

For a long time, it was argued that the IVR and VC are temporally well separated processes, the former happening on sub-ps timescale while the later happening on ps timescale [149]. The work of Baskin et al. [126] proposed that IVR in the Q_x of H₂TPP occurs on a timescale ranging between 100-200 fs, preceded by the sequential relaxation from the Soret → S_{1y} → S_{1x} band through IC processes. Considering the ultrafast M1 dynamics seen in fluorescence and absorption experiments, the IVR process shows faster dynamics than reported earlier and points to being initiated earlier to the sequential relaxation. The ultrafast timescale of 60/45 fs of both samples distinctly imply IVR process starting earlier than any electronic relaxation. This can be explained by an impulsive vibrational relaxation on the range of multiple oscillations of the fastest vibrational modes available in free-base porphyrins, on the range of 1500 cm⁻¹ (22 fs). This interpretation can be also supported by the instantaneous appearance of the mirror image fluorescence within the instrumental response time as shown in Figure 3-3. In other words, the molecule is acting as one damped oscillator, distributing the energy over the entire collection of vibrational modes regardless of the electronic population. Such impulsive IVR has been observed earlier in various systems such as ruthenium and Iron complexes [155] and in organic molecules (UV dyes) [146].

3.5 Summary

We performed both time resolved fluorescence up-conversion (400 nm excitation) and transient absorption spectroscopy (505 nm excitation) experiments on both H₂TPP and H₂OEP. The only difference between the two systems lies in the decay of the Soret emission, shortened by a factor of ~3 in H₂OEP. This can be explained by an enhanced vibronic

coupling induced by the OE substituents, also hinted by the broader Soret band. We show that a pulse limited IC from $S_2 \rightarrow S_1$ feeding both S_{1x} and S_{1y} simultaneously, followed by $S_{1y} \rightarrow S_{1x}$ IC. This conclusion was reached due to the lack of population rise in the lower states peaks (Qx bands). Furthermore, impulsive IVR process estimated by ~ 50 fs followed by a slower timescale of ~ 1 ps was observed, and a cooling recovery of the molecules by vibrational relaxation through vibration dissipation to the solvent molecules on the timescale of 25/16 ps.

Wave-packet dynamics in free-base porphyrins

4.1 Introduction

Despite the fact that equivalent vibrational information could be obtained using both frequency and time domain techniques, short lived transient species (sub picosecond) and low frequency vibrations in the THz region ($<200\text{ cm}^{-1}$) could only be accessed by ultrafast time domain techniques [18, 156]. Femtosecond time resolved spectroscopy reveals a wealth of information about electronic and vibrational dynamics and coherences in molecular systems, simultaneously. Ultrafast laser pulses shorter than the vibrational period of the molecule (typically on the order of picoseconds to femtoseconds) are spectrally broad enough to simultaneously excite a vibrational manifold preparing a wave-packet (WP) in the ground and/or excited state. As a result, one could trace the real time motion of the nuclei of the molecule through the time evolution of vibrationally coherent state [156]. These WPs can be observed by several techniques, such as time-resolved Transient Absorption (TA) and Fluorescence Up-conversion (FU) spectroscopy. Also the phase of the vibration is preserved in the case of time resolved techniques, facilitating the differentiation between processes happening in the ground state from the ones happening in the excited state [16, 157]. In this work we utilize the ultrafast TA and FU techniques, available in our laboratories, to study the energy relaxation of photo-excited free base porphyrins through intermolecular and intramolecular vibrational coupling of various vibrational modes in free-base tetraphenylporphyrin (H_2TPP) and octaethyl-porphyrin (H_2OEP), presented in Figure 4-1.

The introduction of bulky substituents [158], addition of a central metal ion [159], or dication (H_2P^{2+}) [147] can lead to the distortion of the planarity of porphyrins. Non-planar distortion (static or dynamic) of the macrocycle perturbs the chemical and photochemical properties of the porphyrins (electronic structure, redox potential, and absorption and fluorescence spectra). Skeletal mode frequencies of the porphyrins shift as a result of distortion induced alterations in the ring structure and electronic structure. Several Raman studies have been conducted monitoring the porphyrin distortions by following the shifts of the skeletal mode frequencies [160-162]. In planar porphyrins only in-plane (IP) modes are observed, because of the resonant π - π^* electronic transitions are polarized in the porphyrin plane, while distorted porphyrins show out-of-plane (OOP) intensity modes in the RR [160]. Coupling between the forbidden OOP modes and the allowed IP modes induce RR intensity [147, 160]. The work of Andrzej et al. [160] concluded that the major contributors to the OOP distortions can be accounted for by the linear combination of the low frequency modes below 200 cm^{-1} , especially the doming, waving, ruffling and saddling modes.

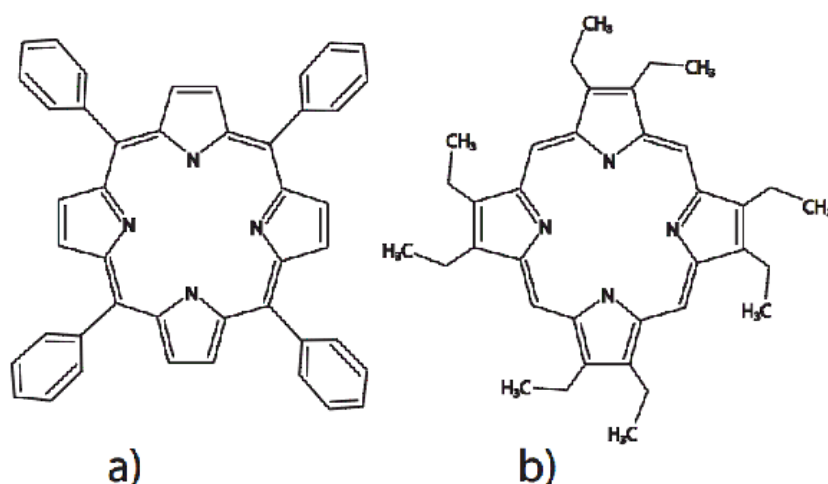


Figure 4-1 Molecular structure of a) free base tetraphenyl-porphyrin and b) free base octaethyl-porphyrin.

As a consequence of the sub-40 fs pulses used in the TA experiment and sub-70 fs pulses in fluorescence up-conversion experiment carried out in our laboratories, coherent vibrational modes between 30 and 400 cm^{-1} are triggered and observed in both samples. Low frequency modes (30-200 cm^{-1}) associated with IP and OOP modes of the porphyrins are identified experimentally for the first time in both samples and assigned to non-Condon vibrational modes. At least 10 different modes are observed for each sample, some are reported for the first time experimentally and some were observed earlier in resonant Raman (RR) studies confirming the validity of our experiment. Reporting these low frequency modes in real time spectroscopy is very important for further understanding of the porphyrin vibrational and electronic dynamics as well as intramolecular vibrational redistribution. We classify each of them to the state they originate from (excited or ground state) using the phase and amplitude of the oscillation. The dephasing time of these modes is comparable of the intramolecular vibrational energy redistribution timescale of around 2-5 ps, showing the importance of these modes in distributing the deposited energy.

Extracting of this information from the TA data is only possible by careful data analysis procedure. Here we discuss briefly three different techniques used to separate the electronic and relaxation dynamics from the vibrational frequencies. Such that the vibrational frequencies can be treated separately using Fourier transformation, leading to information about the mode intensity and phase.

4.2 Experimental section

The TA and FU setups used for these experiments are described in the previous chapter. Briefly, in the TA experiments we used excitation pulses at 505 nm with pulse duration of ~ 35 fs and a white light continuum to probe the dynamics. On the other side, in the case of FU, pulses centred at 400 nm with duration of ~ 70 fs were used to excite the samples. The

luminescence, collected in forward-scattering geometry, was up-converted in a 250-mm thick β -barium borate (BBO) crystal by mixing with an 800 nm gate pulse.

In an attempt to measure the oscillatory patterns generated by WP dynamics in the excited or ground state, steps of 15 fs time delay were used for the first 3 ps of the TA experiments. Since our excitation pulse is in the range of 50 fs, the maximum frequency mode we could trigger is about 800 cm^{-1} and we are interested in the low frequency modes, the 15 fs step is a compromise between the measurement time and the step size. An average of 200 scans were performed for each sample and averaged before any data manipulation.

4.3 Data analysis

Performing TA or FU experiments with short excitation pulses, can lead to generation of coherent vibrational wavepackets (WP) in the case where the excitation pulse is shorter than the vibrational dephasing time and the electronic relaxation. A transition probability change induced by molecular vibrations is observed in modulation of the fluorescence or absorption over time.

Therefore, experimental signals contain both electronic and vibrational relaxation processes, as well as vibrational coherences in case of generation of WP. When exciting in resonance conditions, the dominant component will be population decay which is represented generally by a sum of exponential decay functions. The amplitude of the vibrational coherences in the signal is about 2 orders of magnitude smaller relaxation dynamics. Therefore, the relaxation dynamics must be removed in order to reveal the vibrational coherences. Since we are interested in the frequency range from 30 cm^{-1} to 400 cm^{-1} (oscillations periods between 1 ps and 100 fs) with damping factors of 2-3 ps, special precautions must be taken into account during this procedure. Accordingly, three different methods were used to extract these oscillations in order to check the validity of the frequency modes extracted.

The first is the maximum entropy method [163]. The non-oscillatory signal was fit with multi-exponential functions convoluted by the IRF, disregarding the number of exponentials used and their correspondence to real relaxation dynamics. The residual of individual transient fits contains the coherent oscillations of interested.

The second method is based on SVD technique, where a multi-exponential fit of the kinetic vector basis obtained from the SVD of the time-wavelength plot is performed. Only the data between 80 fs and 3 ps are included in the fit to avoid any contribution of the coherent spike due to pump-probe temporal overlap. Using the DAS for each decay time extracted (minimal number of times), a new time-wavelength surface is constructed containing only the slow electronic dynamics. The difference between the reconstructed and original data yields the oscillatory signal.

A third method based on low and high frequency filters applied to the individual transients in order to extract the oscillatory signal without any exponential fit. Since our IRF is longer than 50 fs and our sampling is 15 fs, we know for a fact that any oscillation shorter than 50 fs cannot be attributed to any vibrational or electronic coherence. Therefore the traces were

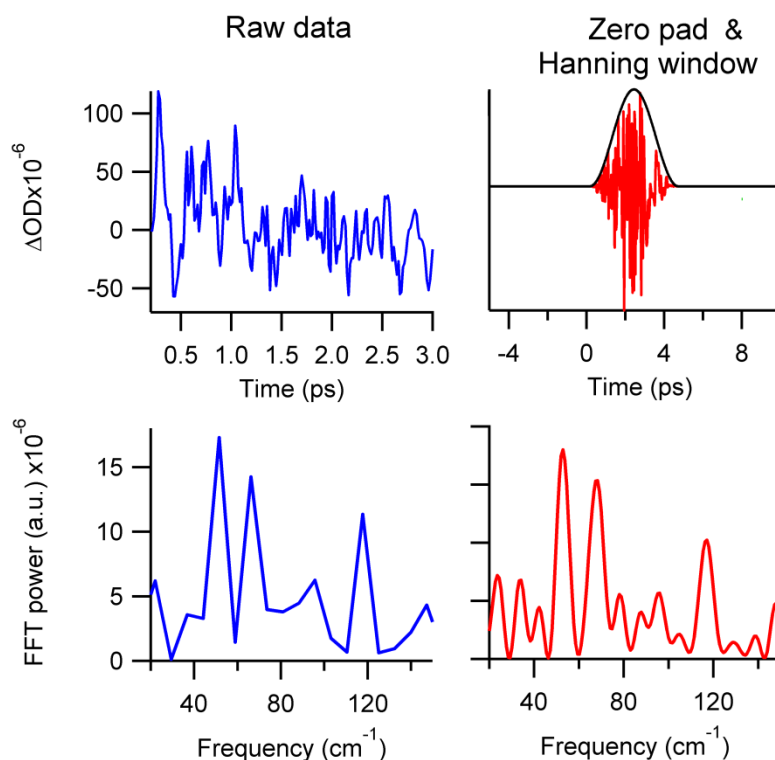


Figure 4-2 Raw data are the extracted oscillations from a transient at 522 nm of H₂OEP showing the first 3 ps and its Fourier transform. The zero padding procedure and the application of a Hanning window are presented as well showing strong enhancement of the frequency resolution.

smoothed by averaging over 50 fs period, eliminating any modes that will appear higher than 470 cm⁻¹. To eliminate the non-oscillatory contributions, smoothed traces, by averaging a window of 2 ps which correspond to frequencies we cannot differentiate from the exponential decays due to our time window, are subtracted from the original traces.

In the three techniques, the Fourier transforms of the traces were compared to verify the modes that are present, avoiding any fake modes resulting from errors in the analysis process. These traces contain information about the coherences that result from the superposition of various vibrational states coupled to electronic excitation. Due to dephasing mechanisms and sample inhomogeneity, the oscillations damps within the first 2-3 ps.

The traces containing only the oscillatory signal are multiplied by a Hanning window and zero padded in preparation to perform a Fourier transform. Applying a Hanning window (a Gaussian can do the same) is important before performing Fourier analysis to avoid the appearance of a sinc function overlapped the frequency data, that can be mistaken to real frequency modes. Zero padding is a standard method used to increase the resolution of a Fourier analysis. By adding zeros around the traces, the number of sampling points increases but do not interfere with the integrity of the data. As a consequence, when performing a FFT of a zero padded time trace additional points will be available in the frequency trace, i.e. higher FFT resolution. It is important not to confuse the frequency resolution with the FFT resolution. The zero padding cannot increase the frequency resolution since it directly

depends on the delay time window, which in our case corresponds to 11 cm^{-1} . The FFT resolution can be increased by the zero padding, which adds more points in the frequency traces. The effect of these procedures is introduced in Figure 4-2 showing the resolution change between the FFT of the raw data and the zero padded data.

By performing FFT of every trace, a 2d plot of probe wavelength vs frequency is created showing the frequency intensity dependent of the probe wavelength. Taking advantage of the complex nature of Fourier transform, the phase of each frequency can be calculated by the angle of the complex number. Thanks to the broad probe spectral window detection, we can calculate probe wavelength dependence initial phases of the molecular vibrations. This information can help identify if the WP motion is on the excited or ground state [16, 20]. Finally, information about the dephasing time including effects of inhomogeneous broadening can be extracted from the Fourier power line width.

Since we are performing Fourier transformation to extract not only the frequency of the oscillation but also the phase, it is very important to set all the transients to start at time zero. As an example, errors in the GVD corrections of 20 fs will affect minimally the low frequency modes of 33 cm^{-1} (1ps oscillation) by shift the phase by about 0.02π , while frequency modes of 400 cm^{-1} (80 fs) will have a phase shift of $\pi/4$. For that reason, the phases of low frequency modes were extracted and could be trusted, in contrast with phase of modes higher than 300 cm^{-1} that should be considered with caution.

In order to assess the quality of the data, and the integrity of the calculated oscillations, the data analysis procedure was performed over different scans of the data set. A comparison between the data analysis of the first 10 scans, last 10 scans, and the full average of the 200 scans is performed. They all show the same resolved frequencies which mean that the vibrational modes resolved are real. Moreover, the frequencies resolved are in great agreement with previously predicted modes and some reported experimentally by Raman spectroscopy.

4.4 Results

4.4.1 Ultrafast fluorescence studies

Similar to the FU experiments discussed in the earlier chapter, these measurements were performed with ~ 70 fs pulses centered at 400 nm exciting the Soret band of the porphyrins. Here the sampling (time points) is higher such that vibrational wave-packets can be observed. Figure 4-3 displays the time dependent fluorescence traces up to 3 ps showing the fluorescence signal decay of the Q bands and an oscillatory component due to molecular vibrations. The kinetic traces are well reproduced using 2 damped cosine functions in addition to 3 exponential decays. We obtained two frequencies of $36 \pm 4 \text{ cm}^{-1}$ ($T = 930$ fs) and $80 \pm 5 \text{ cm}^{-1}$ ($T = 420$ fs) in the Q_y region, and two higher frequencies of 193 and 170 cm^{-1} ($T \sim 170$ fs) for H_2TPP and one of 130 cm^{-1} ($T = 260$ fs) for H_2OEP in the Q_x region. Figure 4-3 (right panels) shows a Fourier transform analysis of traces at 3 characteristic wavelengths, confirming these values. The damping factors obtained varies from 0.3 to 0.5 ps

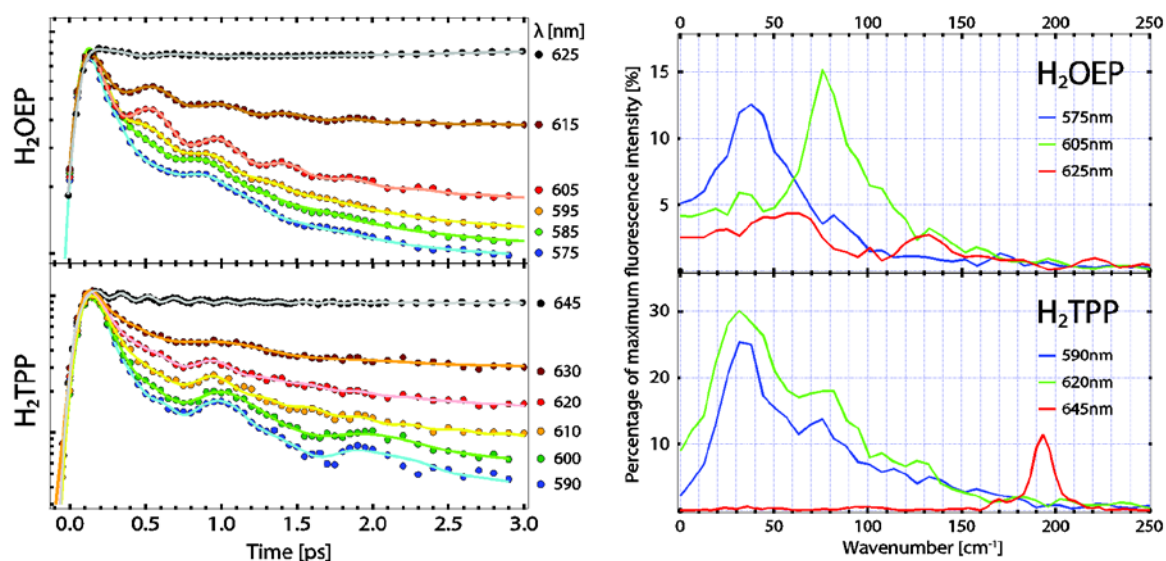


Figure 4-3 (Right panel) Normalized fluorescence kinetic trace of H₂OEP (top) and H₂TPP (bottom), at the detection wavelengths indicated in the legend, integrated over 5 nm, along with their fit, including 3 exponential decays and 2 cosines. A logarithmic intensity scale was chosen since the oscillations are superimposed with a fast decay. (Left panel) Fourier Transform spectra of the oscillations pattern in the kinetic traces at 575 (blue), 605 (green) and 625 nm (red) for H₂OEP (top) and at 590 (blue), 620 (green) and 645 nm (red) for H₂TPP (bottom).

for the lowest frequencies and is ~ 1 ps for higher ones. Very recently, a similar observation have been reported by Joo et al. where they resolved identical nuclear WP frequencies [164].

Remarkably, the frequencies involved in the oscillation strongly depend on the probed wavelength. A clear difference in frequencies between the emission of the Q_x and Q_y can be observed, which show that different WPs exist in each state. The fact that the Soret band is exclusively excited; the WPs observed in the Q bands can only be triggered by ultrafast (impulsive) IC process from S \rightarrow Q. Such IC must be fast enough (faster than the vibrational period) to generate such a coherent superposition of vibrational states on the lower electronic states. This observation can be of great importance since it provides information on the relaxation processes and vibronic coupling.

Such information can only be extracted by FU experiments due to the high temporal resolution and direct probing of the excited state dynamics of each state independently without any signal contamination as in other techniques (such as excited state absorption and ground state bleach in TA experiments). Nonetheless, TA experiments exciting at the Q_y band are performed, in order to trigger WPs in the Q states independent of the S \rightarrow Q IC limitation. We will be able to excite and resolve the WPs more efficiently as a result of the short excitation pulses used and the high signal to noise ratio.

4.4.2 Transient absorption studies

A transition probability change induced by molecular vibrations is observed in the form of oscillations in the time-dependent difference absorption transients. In figures 4 and 5, we

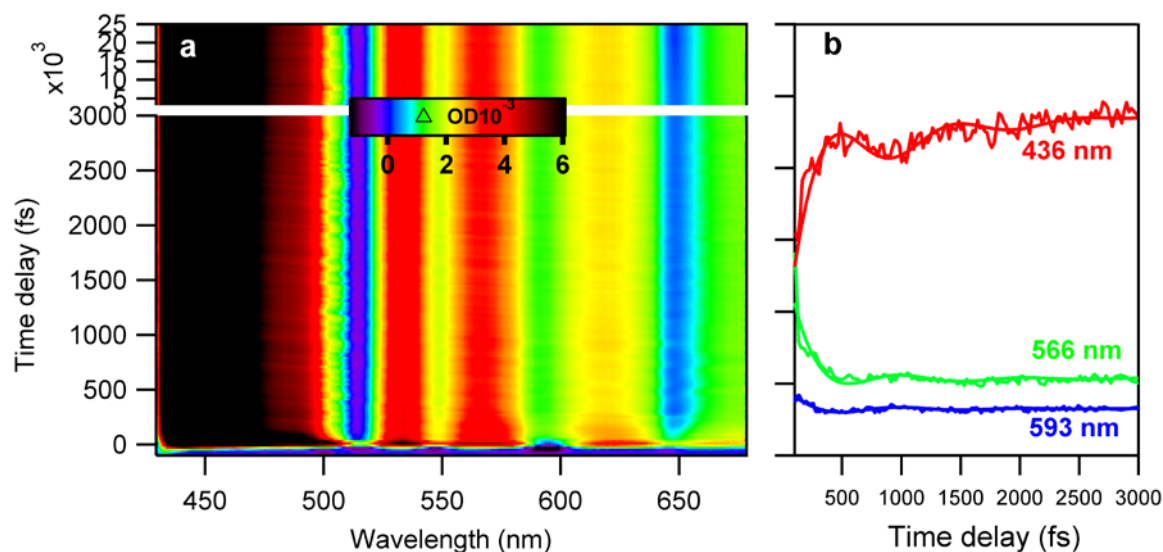


Figure 4-5 a) Wavelength-time plot of H₂TPP, first 3 ps are shown with a linear scale while the following 22 ps are shown separately. **b)** In order to show the main oscillation of 33 cm⁻¹, selected normalized kinetic traces at 436, 566 and 593 nm (right panel, dotted) and their fit (smoothed line) are represented for the first 3 ps.

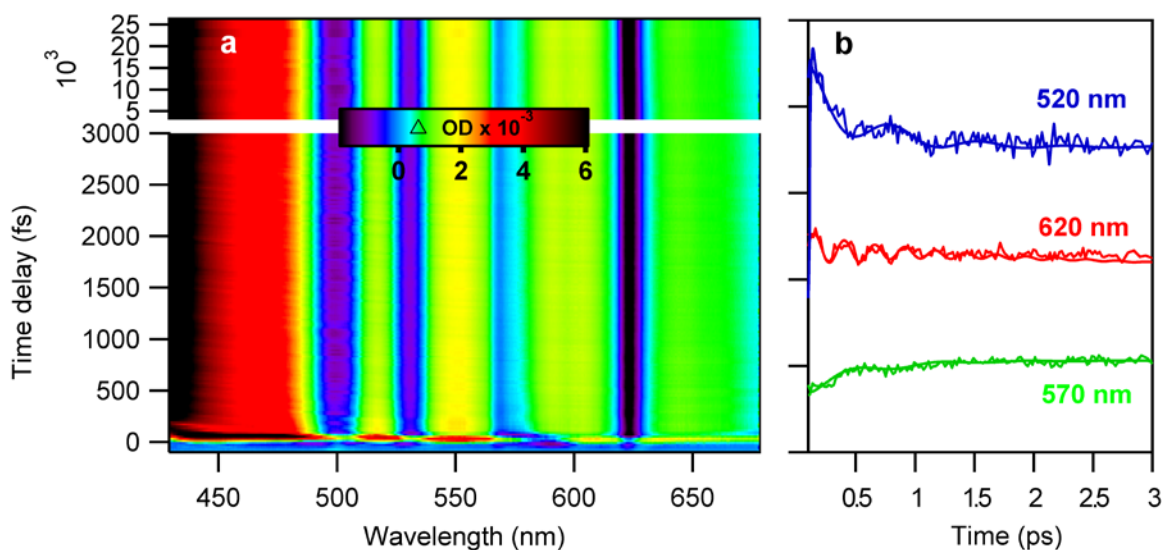


Figure 4-5 a) Wavelength-time plot of H₂OEP, first 3 ps are shown with a linear scale while the following 22 ps are shown separately. **b)** In order to show the oscillations of 47 and 129 cm⁻¹, selected kinetic traces at 520, 570 and 620 nm (right panel, dotted) and their fit (smoothed line) are represented for the first 3 ps.

present the TA data measured under the conditions mentioned earlier averaged over ~200 scans. The data is presented in the form of a wavelength-time plot covering the spectral range between 420 nm and 670 nm covering the Q bands of the porphyrins. In these plots, one could notice some oscillation overlapped with relaxation decay. In the right panels of these plots, transients at different wavelength are presented with a multi-exponential decay fit summed with a damped sine function to represent the oscillations. Such a fit can represent the relaxation processes and one single vibrational mode. In the case of H₂TPP, a 33 cm⁻¹ frequency mode is easily fit with high damping time. While in the case of H₂OEP, a low

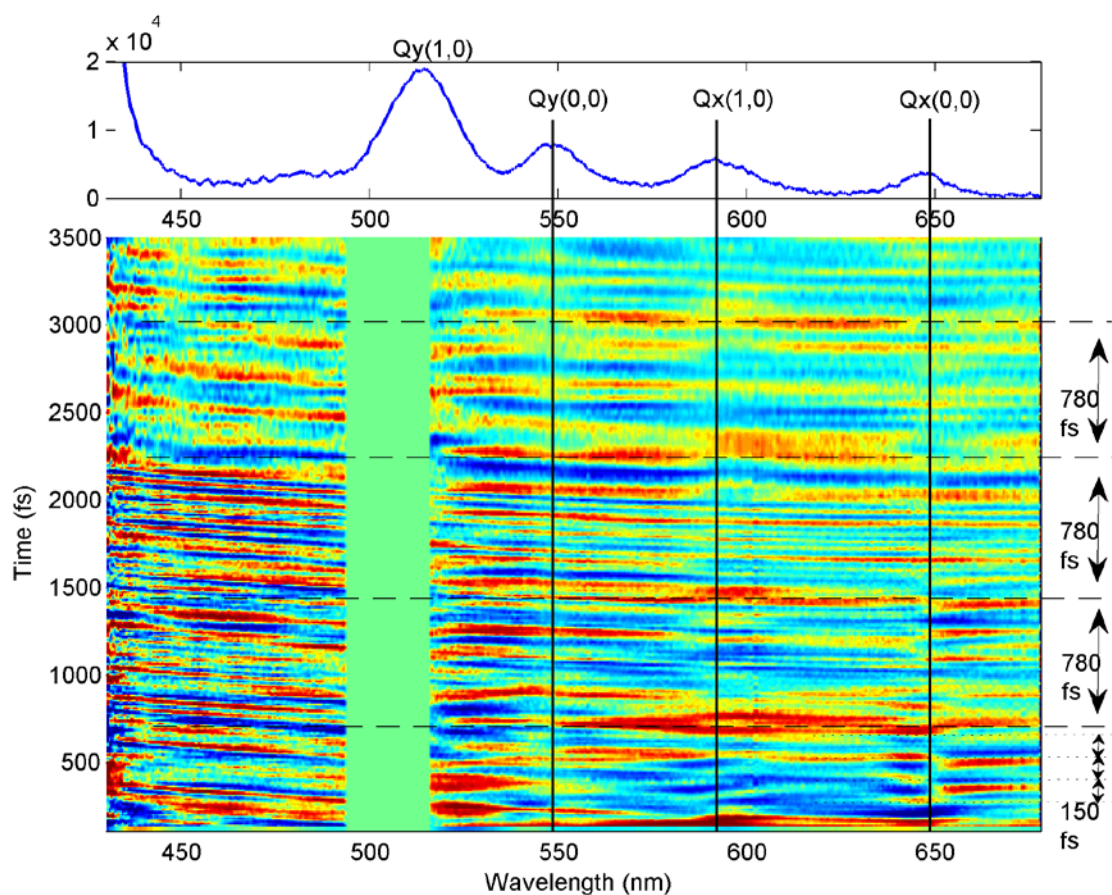


Figure 4-6 Residual of the difference between the H₂TPP transient data and the reconstructed surface. Oscillations can be observed with different frequencies, for example a 150 fs oscillation can be observed around 650 nm, and another one of 780 fs all over the spectrum. The static absorption spectrum of the H₂TPP is presented in the top panel for comparison.

frequency mode of 47 cm^{-1} is observed at 520 nm and 570 nm, while at 620 nm a 129 cm^{-1} mode is dominant. By investigating in details the fit, one can easily see that higher frequency oscillations can be observed. Therefore, such fitting with sine functions cannot represent the data. For a better understanding the vibronic coupling mechanisms, a deeper analysis must be performed to resolve the vibrational modes frequencies and probe-wavelength dependent amplitudes.

The three different approaches proposed in the earlier section to extract the non-oscillatory part of the signal were investigated. The three methods yielded very similar results; therefore the presented data in this section are all residual of the subtraction between the probe-wavelength/delay-time surface and reconstructed surface from the SVD analysis. Due to the pump scattering on the CCD, the region around 500 nm is set to zero to avoid artifacts and confusion of random oscillations that are not caused by the molecular vibrations.

To resolve low frequency modes, removing the slow electronic and vibrational dynamics is an important step. Figure 4-7 is the residual of the difference between the H₂TPP transient data and the reconstructed surface using SVD analysis. Oscillations all over the 2D surface

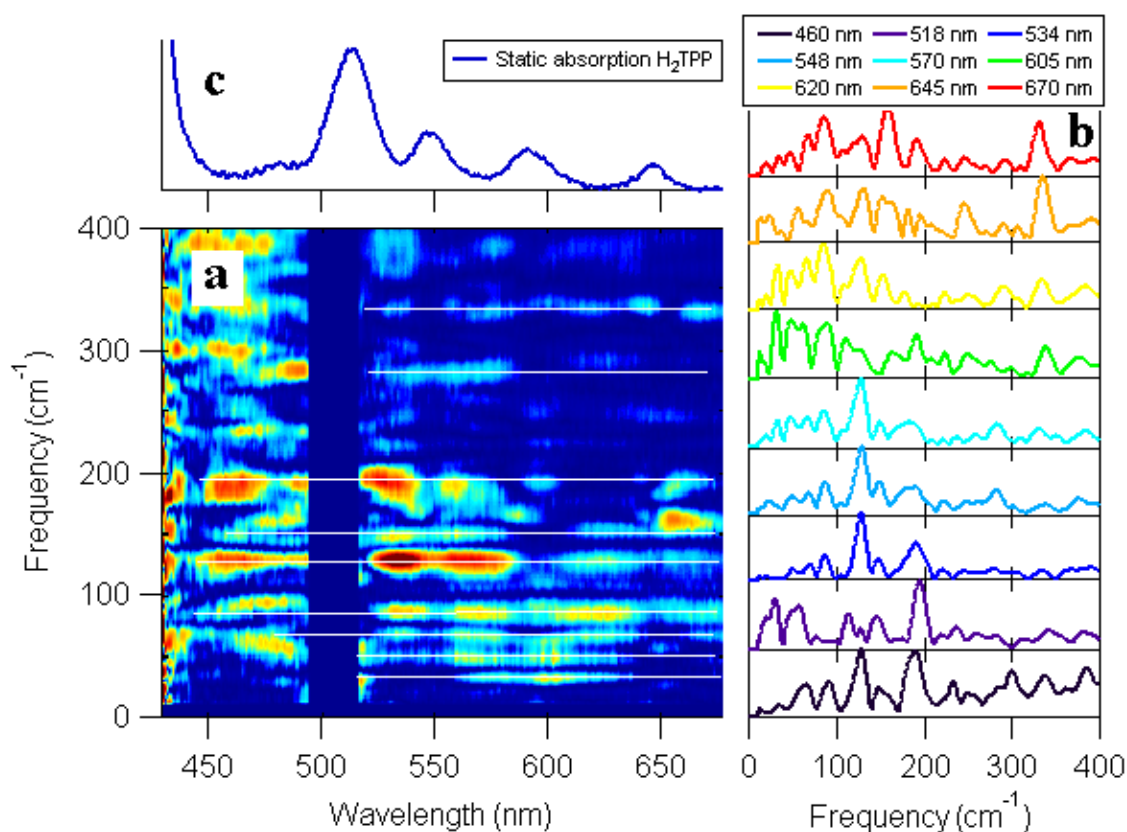


Figure 4-7 a) Two dimensional plot of Fourier transform spectra of the TA signal of H₂TPP. b) Static absorption spectrum of H₂TPP. c) FT spectra of chosen wavelengths.

can be observed, with various frequencies and amplitudes. A 780 fs oscillation can be easily observed in the residual over the whole spectral range corresponding to a frequency of 42 cm⁻¹. Another strong oscillation is observed with 150 fs oscillation in the first 500 fs corresponding to 222 cm⁻¹.

The oscillations possess a clear spectral dependent phase. This can be observed in the clear case of the 150 fs oscillations, which shows a flip of half-wavelength between the oscillations above and below 650 nm. The same is also observed at 580 nm and 550 nm. This is no coincidence, since the phase flip coincide with the peaks of the absorption spectrum. The significance of such an observation is discussed later.

Since these oscillations are overlapped in time and wavelength, it is hard (nearly impossible) to extract all the frequencies just by normal fitting. By using a FT, the data will be transformed into frequency where it will be easier to separate individual contributing frequencies. Furthermore, due to the complex nature of FT, the phase of each frequency mode can be extract. Therefore, FT of the residual is computed for each individual wavelength independently. The FT is performed over the data ranging between 80 fs and 3 ps in order to avoid artifacts caused by the coherent spike due to the pump-probe interaction at time zero. The resolution of the FT spectra is determined by the width of the delay window measured yielding to ± 6 cm⁻¹.

Figure 4-7 shows the two dimensional Fourier amplitude as a function of molecular vibrational frequency and probe wavelength for H₂TPP. FT spectra at specific wavelengths are presented in Figure 4-7b showing a number of strong peaks appearing at different wavelength. Ten different modes are clearly visible and recurrent in most of the spectral regions; 336 cm⁻¹, 280 cm⁻¹, 190 cm⁻¹, 168 cm⁻¹, 149 cm⁻¹, 128 cm⁻¹, 87 cm⁻¹, 69 cm⁻¹, 49 cm⁻¹, and 33 cm⁻¹. Due to the limited frequency resolution, the frequency of the modes might appear slightly different depending on the wavelength. Some of these modes have been reported in previous TA and FU measurements or in resonance Raman (RR) experiments [147, 165]. There are some modes that were not reported earlier in experiments but have been predicted by theory [166, 167] as presented in Table 3.

Table 3 Vibrational modes comparison between Fluorescence, Transient Absorption, Resonance Raman, and theoretical prediction and their assignments, for H₂TPP are presented.

TA	FU	Exp. [147]	Theo.	Sym (D2h)	Assignment	G/Ex state
33	36		28	A _g (OOP)	ph torsion	E
49			48	A _g (OOP)	ph torsion	E
69			73	A _g (OOP)		E/G
87	80		86	B _{1g} (IP)	ph torsion	E
128		126	122	E _g (IP)	γ(Cm-Φ)	E
149		144	131/183	A _g (OOP)	δ(pyr trans)	E/G
168	170	166	170	B _{1g} (IP)	δ(pyr trans)	E
190	193	199	195	A _g (OOP)	Ph	E
280			289	B _{1g} (OOP)	Ph wag	E/G
336		336	339	A _g (OOP)	ν(pyr trans)	E

The amplitude of the oscillations seems to have strong wavelength dependence. By comparing the static absorption in Figure 4-7c and the Fourier plane in Figure 4-7a, one could notice that the amplitude of the oscillation is at minimum in the regions of the absorption peaks and increase in between. The regions in between the absorption peaks are where the ESA is dominant in the TA measurements. The vibrational modes typically show a phase change of π in between ESA and GSB process, which can lead to cancellation of the mode in case these two regions are overlapping and equally strong, which is the case here. Further investigation of the individual modes is presented in the next part and the spectral dependent amplitude and phase will be discussed.

Similar data analysis is performed on the H₂OEP data and is presented in Figure 4-8. Due to the sharper absorption peaks of H₂OEP, the amplitude of the oscillation show a stronger wavelength dependence as clearly seen in Figure 4-8a. The amplitude is mainly dominated by the regions in between the absorption bands, similar to the H₂TPP case. Twelve different vibrational modes are resolved; 340 cm⁻¹, 311 cm⁻¹, 240 cm⁻¹, 213 cm⁻¹, 194 cm⁻¹, 148 cm⁻¹, 118 cm⁻¹, 84 cm⁻¹, 84 cm⁻¹, 65 cm⁻¹, 52 cm⁻¹ and 37 cm⁻¹ all summarized in Table 4. The high frequency modes above 200 cm⁻¹ have been reported earlier in RR experiments, single site electronic spectroscopy, while the low frequency modes are only reported in theoretical work [148, 168, 169].

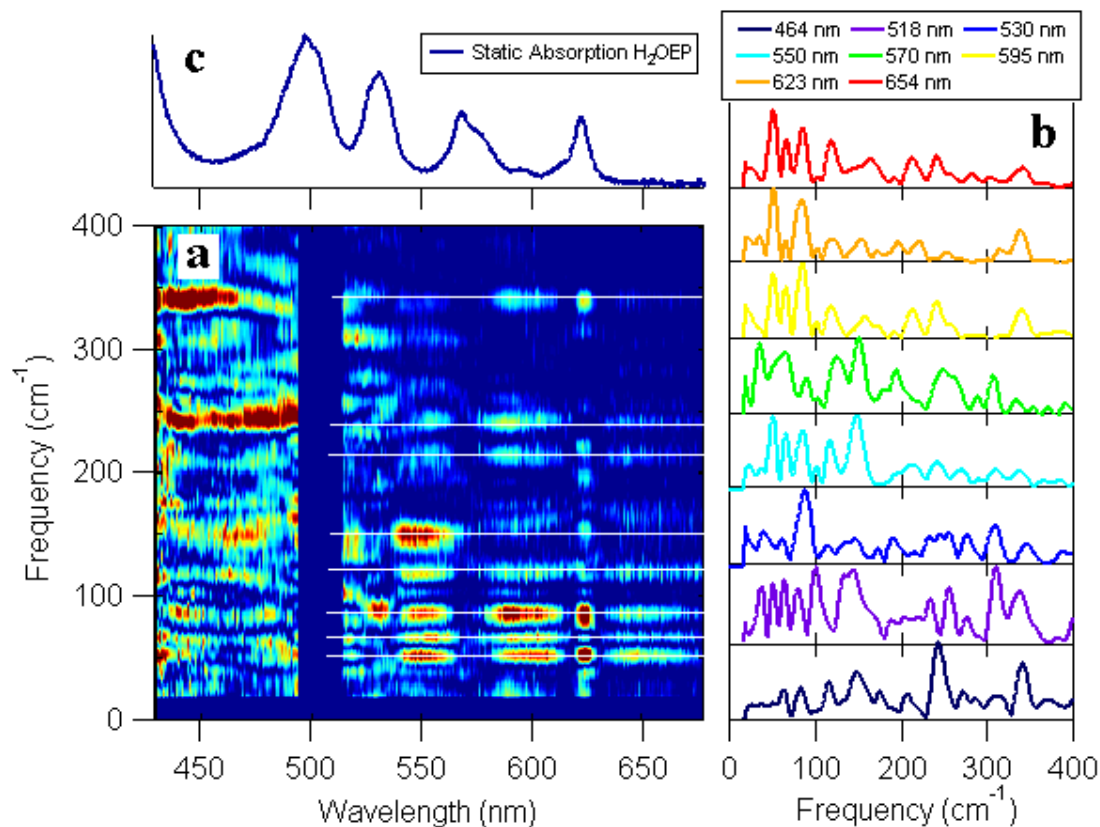


Figure 4-8 a) Two dimensional plot of Fourier transform spectra of the TA signal of H₂OEP. b) Static absorption spectrum of H₂OP. c) FT spectra of chosen wavelengths.

In contrast with H₂TPP, the amplitude seems to have a maximum in the spectral region of the Q_x(0,0). In the other Q band, the oscillation is mainly back to minimum as in the former case of H₂TPP. This can be explained by the strong and sharp absorption band of the Q_x(0,0) that overcomes the ESA and appears as a negative feature in the difference spectra. Therefore, considering that the GSB contains stronger signal than the ESA; the modes in that region will not cancel out and appear on their own with a π phase difference compared to the phase of the modes in the ESA region. The spectral dependence amplitude and phase of the modes is discussed later on.

Table 4 Vibrational modes comparison between Fluorescence, Transient Absorption, Resonance Raman, and theoretical prediction and their assignments, for H₂OEP are presented.

TA	FU	Exp.[169]	Theor.[160, 168]	Sym. (D2h)	Assignment [168]	G/Ex state
37	36		36	B _{1u} (OOP)	(pry translation)	E/G
52			53	A _u (OOP)	Ethyle rock	G
65			62	B _{1u} (OOP)	Ethyle rock	E/G
84	80		88/90	B _{2g} (OOP)	(pry deformation), ethyle rock	E
118	130	129	130	A _g (IP)	(pry deformation)	E/G

148			139/155	B _{2g} (OOP)	Ethyle rock	E/G
194		199	192	B _{2u} (IP)	$\gamma(\text{CH}_3)$	E
213		209	216	A _{1g} (IP)	$\gamma(\text{CH}_3)$	E
240		247	238	B _{1u} (IP)	(pry breath), CH ₂ wag	E
311		315	316	A _g (IP)	(Pyr swivel), $\gamma(\text{CH}_2)$	E/G
340		336	341	B _{2u} (IP)	$\gamma(\text{CH}_2)$	E

4.5 Vibrational modes assignment

The coherent oscillations observed in the transient data will be discussed and assigned based on the initial phase and the oscillation spectral intensity dependence. In Figure 4-11 and Figure 4-12, the phase (dotted lines) and normalized spectral dependent amplitude (solid lines) of each mode is presented for both H₂TPP and H₂OEP, respectively. A wavelength region between 510 and 670 nm is presented, covering the Q bands region of both samples, consequently resolving the oscillations in both the GSB/SE and ESA regions simultaneously, thanks to the broadband detection. In some cases, the phase was unwrapped to obtain a continuous phase change over the whole spectral range.

The main difference between the Condon and non-Condon type WP is the conservation of the oscillator strength, as it is not conserved in the non-Condon type WP. Therefore, the total signal intensity of a non-Condon mode associated with the Q excited state must be modulated, while Condon type modes will show inhibited modes (sum down to zero in an ideal case). Therefore, the integrated signal intensity ($\text{ISI} = \int \Delta A(\lambda) d\lambda$) can be used to distinguish between the two WP types. Figure 4-9 and Figure 4-10 show the ISI and the corresponding FFT of both H₂TPP and H₂OEP, respectively. These figures show clear beating between various oscillatory modes in the time plots confirming that the oscillations caused by non-Condon type WP motion intensify upon integration instead of suppression. The Fourier analysis of the integrated transients reveals which modes are intensified compared to other modes that are suppressed, and the classification of the WP type can be done based on that.

Although the three ISI transients of H₂TPP display different oscillatory features in the time domain, the FFT spectra show qualitatively similar results. All the low frequency modes are present and enhanced compared to the FFT of the single transients. Therefore, the vibrational modes of 33 cm⁻¹, 49 cm⁻¹, 69 cm⁻¹, 87 cm⁻¹, 128 cm⁻¹, and 149 cm⁻¹ can be assigned to non-Condon type WP. This result is expected, since the Q bands are vibronic bands and their profile fit perfectly with the non-Condon type WP model presented earlier. These modes vary their intensity between the Q_x ISI and the full probe ISI, depending on the corresponding spectral amplitude dependence. The 33 cm⁻¹ mode is intensified in the Q_x(1,0) since it appears mostly around that region while it is very weak elsewhere. Therefore, it seems to be reduced in the broad ISI spectrum compared to the modes that are stronger and are present over the whole probe window such as the 128 cm⁻¹ one.

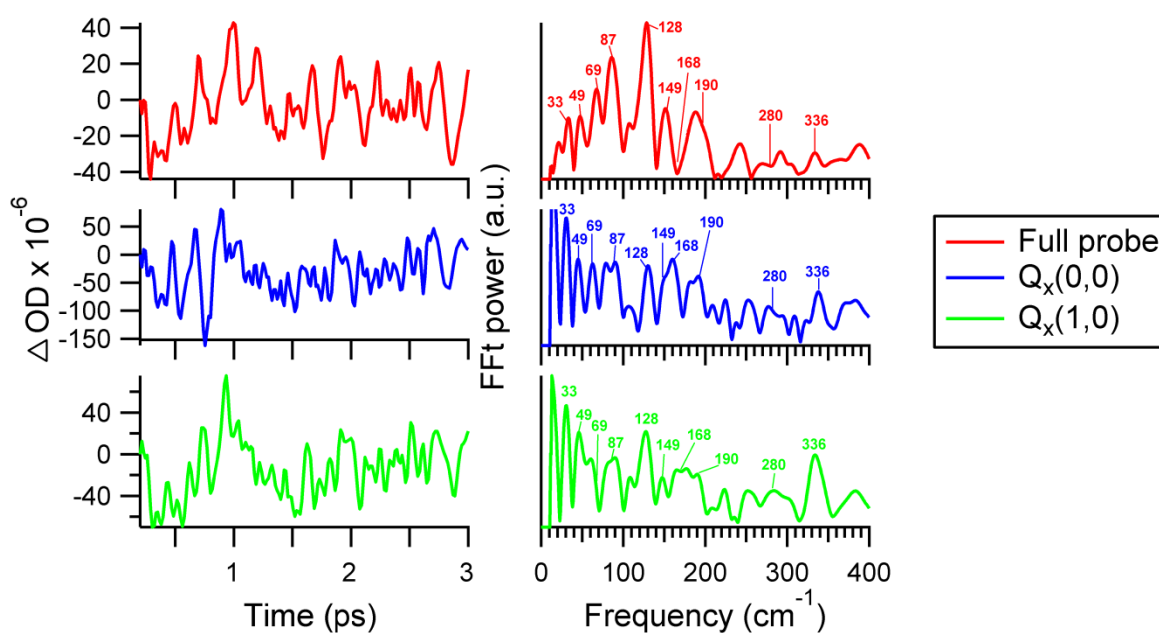


Figure 4-9 Integrated single intensity (right) and their corresponding FFT (left) of H_2TPP over the spectral windows 515 nm to 670 nm (Red), the $Q_x(0,0)$ band 625 nm to 670 nm (blue), and $Q_x(1,0)$ band 570 nm to 625 nm.

The modes 168 cm^{-1} , 190 cm^{-1} and 336 cm^{-1} , appear in the different FFT spectra with varied intensities. The main issue with the high frequency modes is the probe dependent phase drifts due to errors in the GVD correction that can lead to cancellation of the modes in the integrated signals, even if the modes belong to a non-Condon type WP. Therefore, for the high frequency modes, it would be more insightful looking at the ISI of narrow bands, such as the ISI of the Q_x bands, to minimize the uncertainty. The three modes 168 cm^{-1} , 190 cm^{-1} and 336 cm^{-1} appear clearly in the ISI of both Q_x bands, which is a sign of their relation to a non-Condon type WP.

The 280 cm^{-1} mode is completely diminished in all the FFT spectra. In order to decide if this mode diminishes due to its nature as a Condon WP, we investigate its presence in the narrow band ISI mentioned above, and its probe dependent amplitude. In Figure 4-11, the amplitude of this mode shows a reasonable intensity in the region below 600 nm and a phase that decrease rapidly, while a minute amplitude around the $Q_x(0,0)$ region but with a flat phase. In both regions the ISI show no reasonable intensity, but to conclude that it belongs to a Condon type WP we check the spectral dependent amplitude of the mode. The amplitude of the mode show a zeroth order shape resembling the one presented in Figure 4-13. Therefore this mode can be assigned to non-Condon WP as well since the zeroth order appear only in the case of non-Condon WP to compensate for the varying transition dipole.

Similar to the H_2TPP , integration of the signal intensity is performed and presented in Figure 4-10. Strong oscillations appear showing the co-existence of various modes, signified by the FFT power spectrum. All the low frequency modes appear distinctly in the FFT; 37 cm^{-1} , 52 cm^{-1} , 65 cm^{-1} , 84 cm^{-1} , 118 cm^{-1} , 148 cm^{-1} , 213 cm^{-1} , 240 cm^{-1} and 311 cm^{-1} . And so these modes are categorized as non-Condon modes. Here, the phase is much sharper

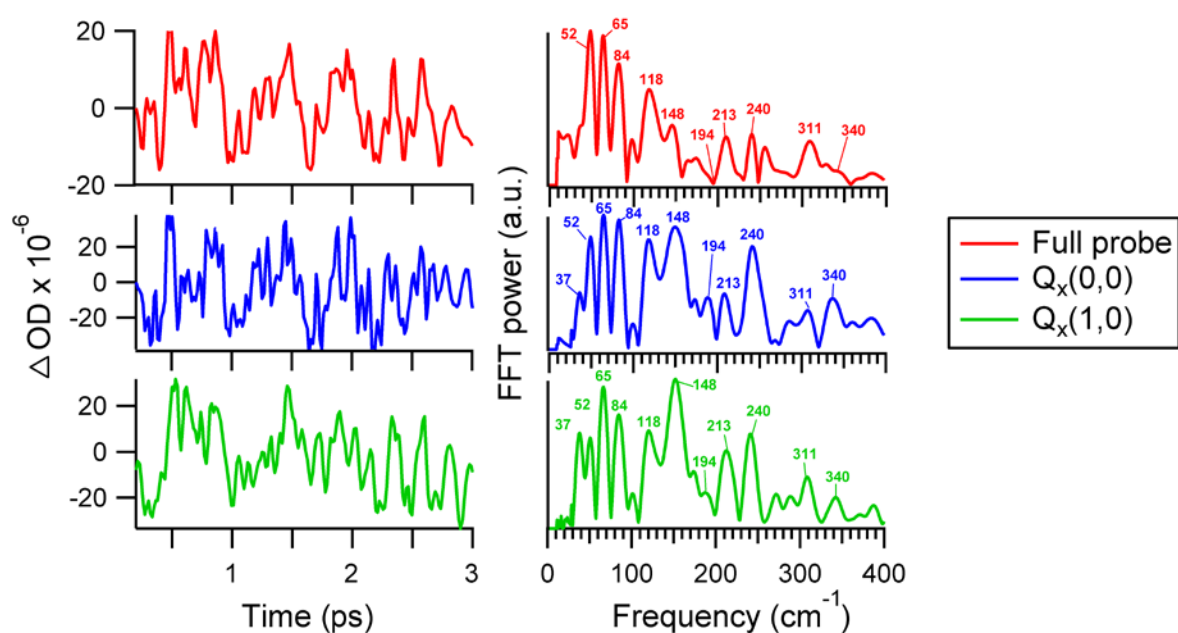


Figure 4-10 Integrated single intensity (right) and their corresponding FFT (left) of H₂OEP over the spectral windows 500 nm to 670 nm (Red), the Q_x(0,0) band 600 nm to 645 nm (blue), and Q_x(1,0) band 550 nm to 594 nm.

compared to the H₂TPP case, due to the sharper Q bands and stronger vibronic coupling between the Q and S states leading to more pronounced changes in the phase. The 194 cm⁻¹ and 340 cm⁻¹ modes are not present in the FFT of the total Q band ISI. Since both modes are very weak and appear mostly around the Q_x(0,0) band, the integration around 620 nm – 650 nm was performed where both modes are observed. The wavelength dependent phase around the Q_x(0,0) band presented in Figure 4-12 shows a flat phase with $\pm \pi$ jumps and spectral dependent amplitude resembles a second order derivative of the difference spectra. Thus these two modes are also considered to be of the non-Condon type.

All of the vibrational modes appearing in both samples were characterized of being a result of a non-Condon WP, which is in agreement with the fact that the Q bands are originally forbidden states and come to existence due to the vibronic mixing with the B state. This goes beyond the scope of the Condon approximation and as a consequence cannot be modeled by a Condon type WP motion. All the results of both samples are summarized in Table 3 and Table 4 for H₂TPP and H₂OEP, respectively.

After confirming the modes as of non-Condon type, we will use the phase to assign the modes to identify the WP in motion on the ground state ($0, \pm \pi/2$) or the excited state PES ($0, \pm \pi$), or a mixture between the two. The phase in both samples is showing a fairly flat behavior with phase jumps of π , consistent with the dominant non-Condon type WPs. In both samples, the phase is most consistent in the Q_x(0,0) region due to being the strongest GSB/SE signal compared to the ESA signal.

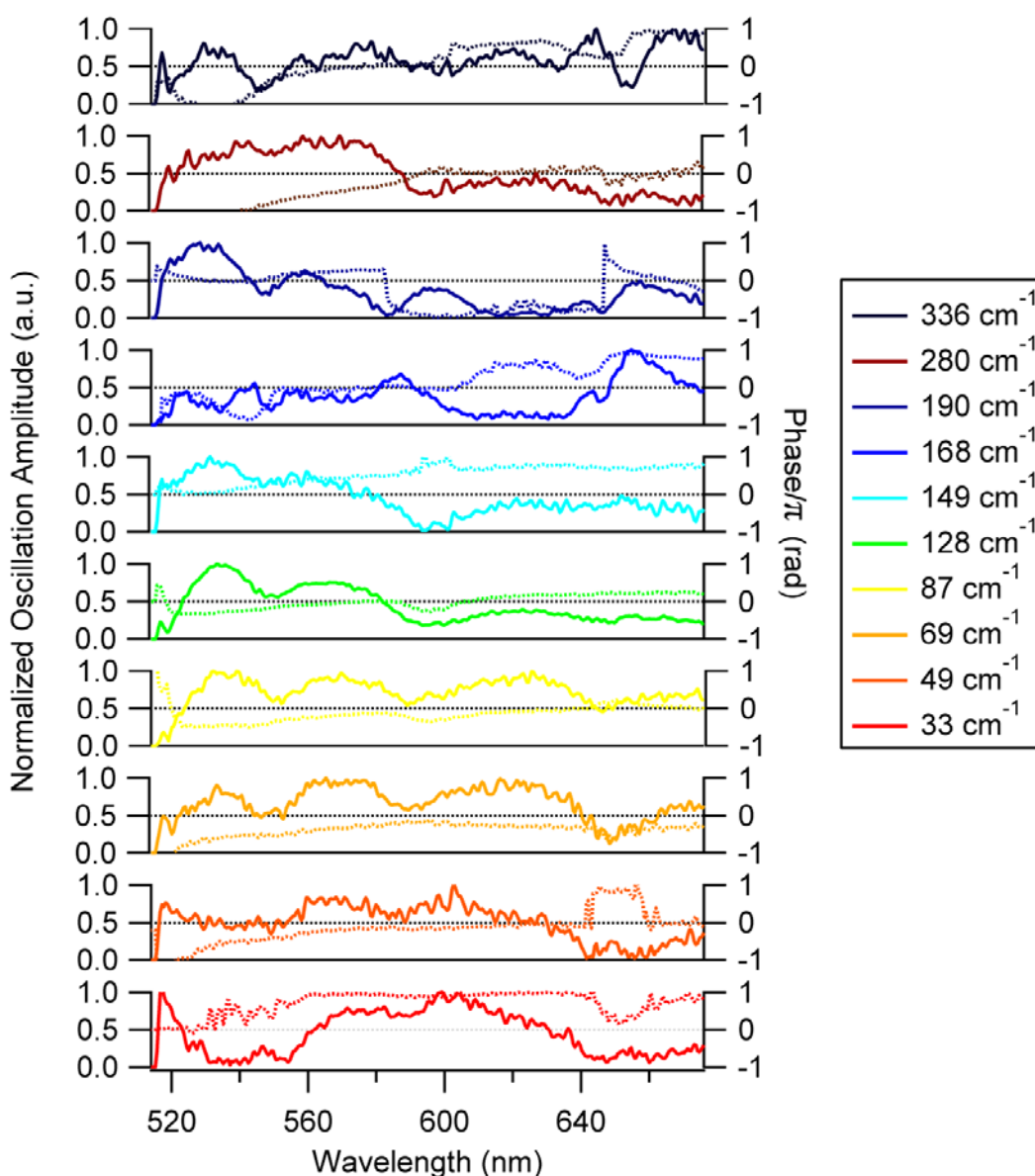


Figure 4-11 Wavelength dependence of the phase (dotted lines) and the amplitude (solid lines) of the oscillations in the transient signal of H_2TPP . Legend shows the corresponding frequency of the oscillations.

Starting with the H_2TPP presented in Figure 4-11, the lowest vibration mode of 33 cm^{-1} show a stable initial phase across the ESA regions of the probe, and phase flip to zero in the GSB region of the $Q_x(0,0)$. On the blue side of the spectrum, the phase changes also to 0 which can be contributed to GSB of the Q_y bands. In the region of the $Q_x(1,0)$ GSB, no π difference is observed due to the dominant ESA. Therefore, the WP generating this 33 cm^{-1} mode is considered to be on the excited state PES. The 49 cm^{-1} mode is very similar to the earlier one, where it shows a π phase change between the GSB (π) and ESA (0) regions. Hence it originates due to a WP motion on the excited state PES.

The 69 cm^{-1} vibrational mode shows no π phase change in the whole spectral range, instead it varies between $-\pi/5$ and $-3\pi/4$. This behavior is evidence to the presence of two WPs on

both the excited and ground state PES. The modes 87 cm^{-1} and 128 cm^{-1} , are very similar, showing a phase oscillation around zero over the whole probe window, which is consistent with a WP oscillating on the excited state PES. The 149 cm^{-1} is a product of a WP on both the ground and excited state PESs since the phase is around 0.9π and changes to 0.5π and zero in the blue region. The modes 168 cm^{-1} and 190 cm^{-1} show only phases varying strictly between 0 and $\pm\pi$, which correspond to a WP motion on the excited state. The 280 cm^{-1} mode show a phase constant of zero, and change in the blue side; therefore, we can assign it to WP mixture. Finally, the 336 cm^{-1} mode show phase change between 0 and $\pm\pi$, which lead to the assignment to a WP on the excited state.

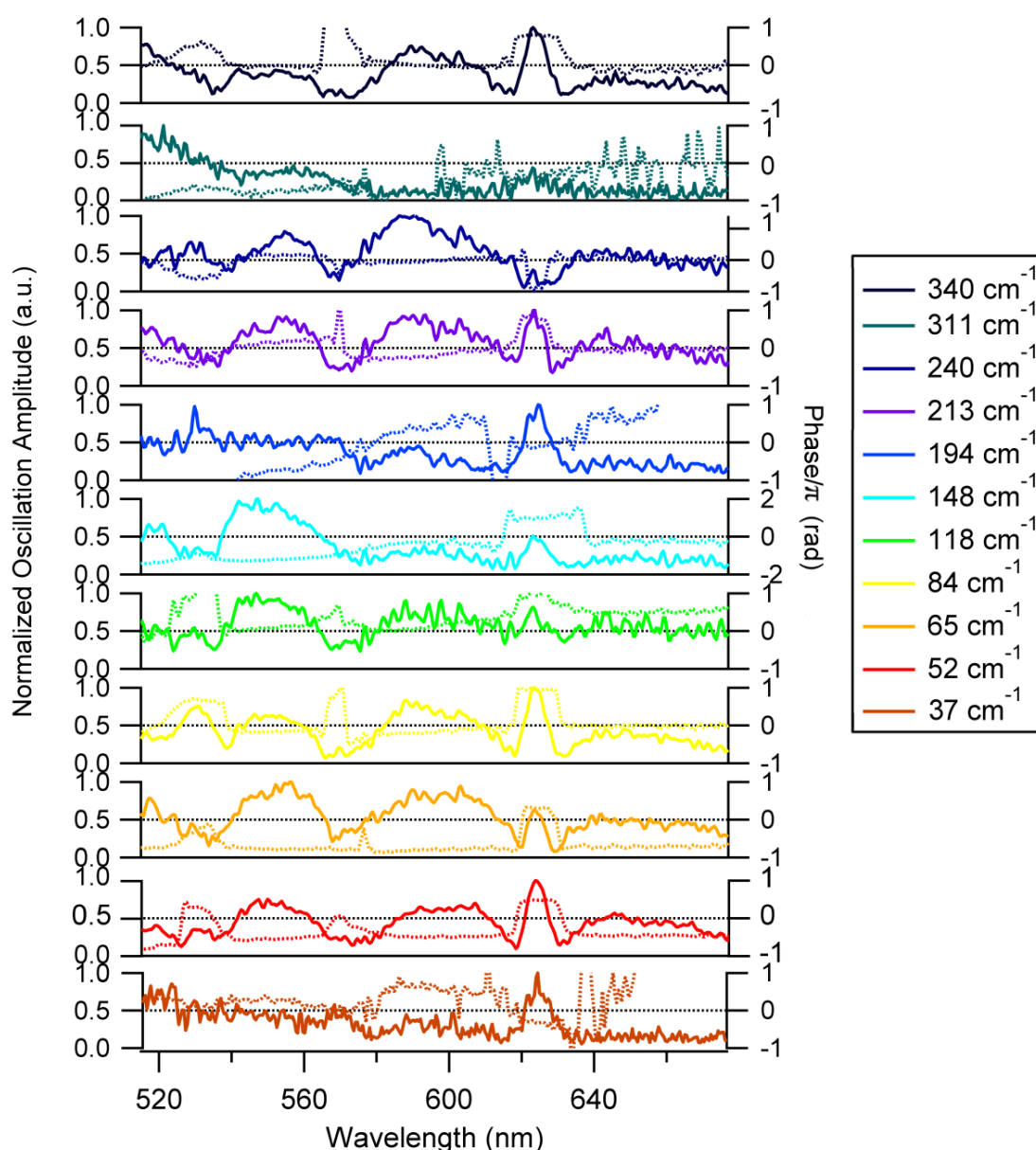


Figure 4-12 Wavelength dependence of the phase (dotted lines) and the amplitude (solid lines) of the oscillations in the transient signal of H₂OEP. Legend shows the corresponding frequency of the oscillations.

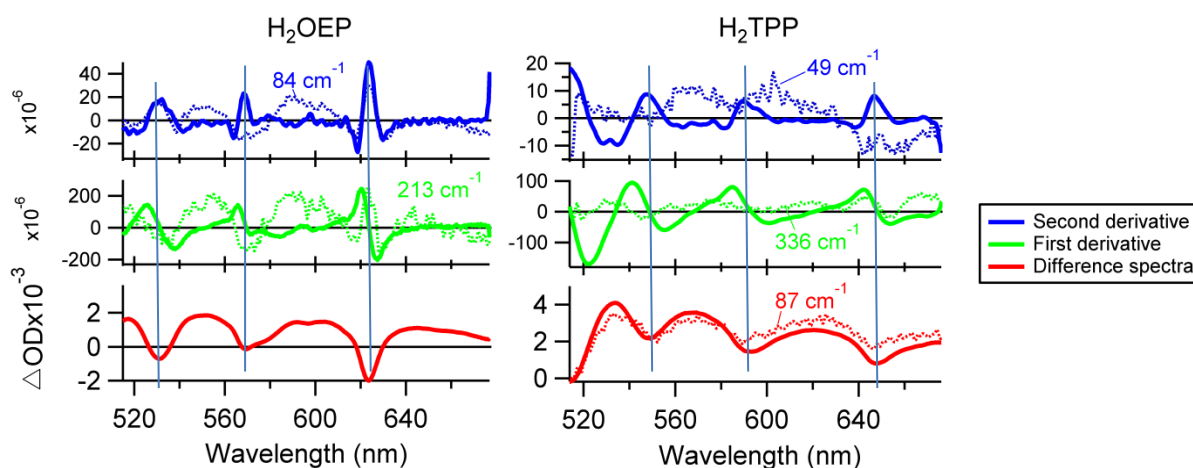


Figure 4-13 Bottom spectrum is the difference absorption spectrum (red solid) at 1 ps time delay of H₂OEP, with its first (green solid) and second derivatives (blue solid). Wavelength depend amplitude of some modes are presented (dotted lines) for comparison.

In H₂OEP, the phase change is much sharper and cleaner, as observed in Figure 4-12. Using the same reasoning, the assignment of the involved WPs depending on the phase was carried out. The most dominant modes are found related to an excited state WPs. The results are summarized in Table 4.

Finally, the spectral dependent amplitude of the modes is employed to classify the WPs into subgroups of potential minimum displacement, PES curvature change, and a mixture of both. Considering the negligible Stokes shift of 5 and 7 meV in H₂TPP and H₂OEP, respectively, the excited state PES could be considered positioned just above the ground state PES. Therefore the WP dynamics will be mostly dominated by a breathing of the WP on the excited state PES. The spectral dependent amplitude of each mode can be compared to zeroth, first and second derivative of the involved processes to assign whether each specific modes belongs to a breathing WP or not. A vibrational mode caused by a WP on the excited state PES getting narrower and broader (breathing) will have a spectral-dependent amplitude which is given by a mixture of the second and zeroth order derivative of the relevant transition. In Figure 4-13 we present the zeroth, first, and second derivative of the difference spectrum of H₂OEP and H₂TPP, respectively, at 500 fs averaged around 300 fs to 700 fs to eliminate spectral changes due to oscillations.

In the case of H₂OEP, the spectral dependent phase and amplitude are much sharper than the H₂TPP case. Most of the H₂OEP modes presented in Figure 4-12 resemble the second derivative of the difference spectrum as can be seen in Figure 4-13. A comparison between the second derivative and the 84 cm⁻¹ modes shows a great resemblance between the two. In the region of the GSB of the Q_x(0,0), the two spectra match perfectly, while in the ESA regions the oscillation amplitude resembles more the difference absorption spectrum. Other modes such as 52 cm⁻¹, 65 cm⁻¹ and 340 cm⁻¹ show very similar behavior to the 84 cm⁻¹ mode. These modes are definitely caused by breathing of the WP on the excited state PES. The fact that the amplitude does not match the second order perfectly and is made of a

mixture between the zeroth and second order derivatives is explained by the fact that these WPs are non-Condon WP. Therefore, they contain the second order to account for the WP breathing, and the zeroth order for the change in transition dipole moment.

Other modes such as 37 cm^{-1} and 194 cm^{-1} show reasonable amplitudes around the $Q_x(0,0)$ region with a peak resembling the second order derivative, therefore these are also considered to be caused by a breathing WP. The 148 cm^{-1} mode show a second order derivative resemblance in the $Q_x(0,0)$ region as well as zeroth order resemblance in the $515\text{ nm} - 560\text{ nm}$ region, leading to the same assignment.

Upon first impression the modes of 118 cm^{-1} and 213 cm^{-1} appear to be closer looking to the first derivative. In Figure 4-13, the 213 cm^{-1} mode is compared with the first order, showing that the $Q_x(0,0)$ band is shifted away from the first derivative, and the peak is more alike to the second derivative although it is slightly less symmetric. Finally, the 311 cm^{-1} mode show a general zeroth order behavior with a small peak at 622 nm and 530 nm matching those of the second derivative at the $Q_x(0,0)$ and $Q_y(0,0)$ respectively. Therefore, as expected all the modes belong to breathing WPs on the excited state PES.

For the H_2TPP , the bands are less sharp and the signal is mostly dominated by the ESA which makes it harder to visualize the similarity between the energy dependent vibrational amplitude and the derivatives. Figure 4-13 show the first and second derivative of the difference spectrum at 500 fs averaged around 400 fs to eliminate the effects of the vibrations.

The spectral amplitude of 69 cm^{-1} and 87 cm^{-1} show a nearly identical shape as the difference absorption spectrum, as seen for mode 87 cm^{-1} . Modes such as the 129 cm^{-1} and 149 cm^{-1} have comparable features to the difference absorption spectrum showing the same local maxima and minima in the regions of the GSB and ESA. The lowest frequency modes are weak and show a shape that does not resemble any of the derivatives, but upon close investigations, these modes show a very weak peak at around 650 nm (blue line in Figure 4-13) resembling the second derivative, while in the region between 560 nm and 640 nm show a shape resembling the zeroth order derivative. Therefore all these modes can be assigned to a breathing WP.

The $Q_x(0,0)$ region of the 336 cm^{-1} mode display a feature that can be compared to the first derivative, while the rest of the spectrum show a fairly flat amplitude. This can be a hint of an oscillating WP. The rest of the modes show slight resemblance to the zeroth order or second order derivatives, but with no clear features to give a clear assignment. Lastly, the dominant WP dynamics is the breathing as in the case of H_2OEP , which is expected due to the small stokes shift and the harmonicity of the bands.

4.6 Discussion

Using femtosecond coherent spectroscopy (FCS) to study the dynamics of metallo-porphyrins in hemoproteins, Champion et al. reported low frequency modes of $\sim 40\text{ cm}^{-1}$ and $\sim 80\text{ cm}^{-1}$.

In these experiments the doming mode ($\sim 40\text{ cm}^{-1}$) is well characterized and used as a benchmark of ligand photolysis, the origin of the 80 cm^{-1} mode is supposed to be a combination of haem doming with other out-of-plane low frequency modes [148, 165, 170-172]. These modes have high dephasing time ($\approx 2\text{ ps}$); similar to the ones observed here (Table 3).

When the metal center in metalloporphyrins is removed and replaced by two hydrogen atoms on the opposing nitrogen atoms, the symmetry of the molecule is reduced from D_{4h} to D_{2h} . This symmetry reduction leads to the splitting of the electronic excitations into x and y polarized components. As a consequence vibrations of A_{1g} and B_{1g} symmetry have A_g , and A_{2g} and B_{2g} symmetry have B_{1g} symmetry for free base porphyrins [147, 167]. Depending on the symmetry of the vibrational mode, various mechanisms can come into play. The molecular symmetry is preserved in the case of fully symmetric modes A_{1g} , which might belong to the FC type and/or HT coupling. While non-symmetric modes, such as B_{1g} and B_{2g} , destroy the molecular symmetry leading to further reduction of the symmetry to C_{2v} inducing HT and JT couplings [147, 160]. The JT coupling can induce static and/or dynamic distortions on the total molecular geometry. In the case of H_2TPP and H_2OEP , the JT coupling might induce static distortions to the molecular geometry, but since the molecules including their substituents are still highly symmetric, these distortions will be mostly due to dynamic changes upon photoexcitation [147, 173]. And finally, a change in the mode frequencies can be expected upon replacement of the metal ion with 2 protons, mostly in the low frequency region since the metal center reduce the IP bending frequencies [160]. This accounts for the discrepancies between the modes resolved in here and the calculated frequency modes for metal porphyrins.

The modes reported in this study cover the ideal frequency region ($30 - 400\text{ cm}^{-1}$) that sheds light of the IP and OOP modes that have not been accessed experimentally earlier in Raman studies. The lowest frequency modes observed in the H_2OEP data (37 cm^{-1} , 52 cm^{-1} , 65 cm^{-1} , and 84 cm^{-1}) are in good agreement with predicted OOP modes in the work of Andrzej et al. (36 cm^{-1} , 53 cm^{-1} , 62 cm^{-1} , and 88 cm^{-1}) which are assigned to Saddling, Ruffling, Doming, and Waving-x, respectively [160]. The OOP 90 cm^{-1} mode is not resolved in these measurements due to the limited frequency resolution. These frequency modes belong to A_u , B_{1u} , and B_{2g} under the D_{2h} molecular symmetry, which are all distorting the molecular geometry and breaking the symmetry. In centrosymmetric molecules such as porphyrins, the ungerade modes are exclusive to IR active modes which are not Raman active, but these OOP modes come into play by coupling onto the IP electronic excitation hence inducing Resonant Raman intensity. The rest of the modes are mixed between IP and OOP modes with variety of symmetries.

Based on the work of Prendergast et al. [174], the changes in the core size or the geometrical distortions of the porphyrins can impact the vibrational frequencies. In their work they showed linear relations in between the ruffling and doming effects caused by the variations of the metal center of the frequency of the modes, especially the asymmetric modes. This can be applied to free base porphyrins as well. When changing from Ethyl substituents to the bulkier

Phenyl substituents we expect changes in the geometry that will shift the frequencies. This can be seen from the vibrational modes tabulated in Table 3 and Table 4. The lowest frequency modes in the H₂TPP are supposed to be related to OOP modes as the ones of H₂OEP, but they are shifted slightly. The H₂OEP show better agreement with free base porphyrin with attachment H₂P, which is expected since the geometry is closer to the H₂P than it is to H₂TPP.

In addition to the static distortion caused by the bulky substituents and the static/dynamic distortion induced by the normal modes, dynamic activation of the OOP modes in the resonance Raman spectra can be induced by the proton tunneling [147]. The tautomerization of the protons involves the tunneling of the hydrogen atoms across the four nitrogen atoms, where they can stabilize in the Cis or Trans conformation. It has been studied theoretically [175] and experimentally [176-178], where the hydrogen transfer involves the transition between trans-cis-trans conversion, with the cis being the intermediate (metastable state) and its involvement as a transition state. These states and the transition state belong to different point symmetry groups: in the trans conformation (most stable), the molecule belongs to the D_{2h} symmetry group, while for the cis state and transition state, the symmetry is reduced to C_{2v} and C_s [175]. The mixing of IP and OOP modes is now possible under both symmetries D_{2h} and C_{2v}/C_s, leading to having all modes becoming Raman active [147]. In the work of Butenhoff et al. [176], the barrier height was estimated for the porphyrin with the inner hydrogens on adjacent nitrogens has an energy of 1670-1960 cm⁻¹ above the energy of the isomer with hydrogens on opposite nitrogens. Therefore such a process can easily be triggered by the excess vibrational energy, and it can be related directly to the modes observed.

Concerning the WPs observed in the FU experiments, the fact that they were generated after an IC process and has distinct frequencies in Q_x and Q_y fluorescence, show that these WPs are generated from different IC processes. Otherwise, if they originated from the same IC process, they should share the same frequency. This backs up the branching in the Soret relaxation dynamics proposed in the earlier chapter. Moreover, in the TA data we observed several vibrational modes; the FU data show a limited number of modes. This shows that a limited number of modes are playing a significant role in the B → Q_x/Q_y IC process, indicating that the IC dynamics is localized in one dominant mode [164].

4.7 Summary

In this chapter we dealt with resolving vibrational WPs in free base porphyrins (H₂TPP and H₂OEP) using fluorescence up-conversion and transient absorption spectroscopy. Using the FU data we manage to observe WPs generated by impulsive IC process happening between the Soret and the Q bands in a non-sequential way, leading to the confirmation of the branching mechanism. From the TA data we managed to observe multiple vibrational frequencies covering the whole spectral range. Using SVD and DAS analysis the oscillations were extracted from the transients and Fourier transformed. Information about the spectral dependent phase and amplitude were extracted. Vibrational frequencies between 30 cm⁻¹ and

400 cm^{-1} were resolved, which are mostly related to out-of-plane vibrational modes that impact directly the vibronic coupling of the Soret and Q bands.

Excited state relaxation dynamics of triply fused diporphyrins

5.1 I. Introduction

Highly π -conjugated organic systems such as triply fused porphyrin tapes are receiving considerable attention because they incorporate ease of synthesis with tunable chemical structure that can be tailored for various applications [179]. Pioneered by Osuka et al. [180], these tapes are two dimensional extensions of porphyrins with direct covalent linkages between constituent porphyrin units (meso-meso, β - β , β - β), in the case of conjugating only 2 moieties they are called triply fused diporphyrins (3DP). Compared to single-porphyrins, these 3DP's possess a very broad absorption spectrum covering the whole visible spectral region spanning from 400 nm reaching to the NIR (up to 1200 nm) as presented in Figure 1. It is common for organic molecules possessing electronic absorption bands in the NIR to have a very short excited state life time, due to the exponential increase of the excited state deactivation rate as the energy gap between the electronic HOMO-LUMO decreases [181, 182]. Nonetheless, investigation of the effect induced by varying either the metal center or the substituents at the meso-like positions shows a broad range of relaxation times: from ultrafast relaxation of 4.5 ps up to μ s lived triplet states lifetime [183-186]. The tunability of the excited state dynamics and spectral features of 3DPs make them very interesting for a wide range of applications such as molecular electronics that demands fast and high charge delocalization [187, 188]. On the contrary, reverse saturable absorbers (RSA) in the NIR [184, 185], NIR sensing [189], and NIR sensitizers require long lived ($> \mu$ s) excited state and high ISC yields [190-192].

Despite the variety of possible applications of 3DP's only a handful of studies have been carried out to understand their excited state relaxation dynamics. Initial studies by Osuka et al. on Zn-3DP with hexaaryl peripheral substituents at the meso-like position, demonstrated that the ultrafast excited state relaxation had a lifetime of 4.5 ps for Zn-3DP with no triplet yield. They also showed that the longer tapes, the faster the dynamics are, as fast as 0.3 ps in the case of 6 conjugated moieties [183]. Based on these observations, the ultrafast internal conversion was explained in terms of the energy gap law [181, 182]. Anderson et al. investigated the influence of incorporating heavy atoms at the terminal peripheries instead of aryl substituents, where they achieved ISC from $S_1 \rightarrow T_1$ and triplet lifetime variation depending on the nature of the heavy atom used; iodo ($\tau = 52$ ns, $\Phi_{ISC} = 0.2$), bromine ($\tau = 280$ ns, $\Phi_{ISC} = 0.12$), and (triisopropylsilyl) alkynyl ($\tau = 177 \mu$ s, $\Phi_{ISC} =$ extremely small) [184]. Further studies were performed on extensively deuterated Zn-3DP that demonstrated no effect on the fluorescence quantum yield. Based on these observations, a conclusion was drawn that the ultrafast internal conversion is not simply a consequence of the energy gap law, suggesting that a specific deactivation pathway is active via an accessible intersection of

the S_1 and S_0 potential energy surfaces [185]. The effect of the metal chelate in combination with the periphery substituents was investigated by Schmidt and co-workers by studying the ultrafast relaxation dynamics of Zinc and Palladium 3DP's with butyl-end-capped terminal periphery [186]. The Zn-3DP displayed relaxation with 13.5 ps lifetime while the Pd-3DP show longer singlet lifetime of 18 ps and weak $S_1 \rightarrow T_1$ ISC with a triplet lifetime of 1.7 ns. Zn-3DP shows variation in the excited state lifetime upon varying the substituents at the terminal position, despite the similar chemical structure and nearly identical absorption spectrum; the authors suggest that the energy gap law alone does not explain the ultrafast excited state relaxation. Indeed for the Pd-3DP, the short triplet lifetime was explained by reverse $T_1 \rightarrow S_0$ ISC due to the high spin-orbit coupling caused by presence of the heavy atom in the center [186]. Therefore, to fully understand the photophysical properties and the processes contributing in the relaxation dynamics further investigation must be done.

Understanding the photophysical behavior of 3DP's and learning how to adapt them in order to achieve one specific relaxation pathway dominating over the others, opens the door to custom tailoring 3DP's for particular application. For example, photochemical upconversion (PUC) via Triplet-Triplet annihilation is one of the domains that can make use of such NIR sensitizers [186, 190, 191]. PUC is used in solar cells to harvest the unabsorbed part of the solar spectrum with energy lower than the band-gap, increasing the conversion efficiencies by about one third [193, 194]. An ideal sensitizer for PUC should to have high absorption cross section in the NIR, high $S_1 \rightarrow T_1$ ISC yield, and long lived triplet state [191, 194, 195]. RSA in the NIR are also subject to comparable properties but also require that their excited state's absorption cross section be higher than the one of the ground state. 3DP's can be good candidates as sensitizers for PUC and dyes for RSA if their behavior was tuned to match the requirements.

Selective photoexcitation of either bands II or III allowed us to investigate the electronic energy relaxation process of the each state via ultrafast transient absorption spectroscopy. To the best of our knowledge, this the first ultrafast time resolved study of H2-3DP which can therefore serve as benchmark for the other samples and further studies. Our results on Zn-3DP support the presence of a conical intersection, previously proposed in literature [185], while in comparison, the results on Pt-3DP shed light on the role of the metal center on the energy relaxation process. Interestingly, Pt-3DP shows an extremely high ISC rate and long triplet lifetime that are much longer than any other 3DP's so far studied [179, 184-186]. It is therefore of great importance in photochemical up-conversion systems as well as in broadband RSA in the NIR.

5.2 Material and methods

5.2.1 The setup

The measurements were performed on two different set-ups. The set-up used to excite the Q band manifold state (pump at 800 nm) is a 1 kHz, 600 mW regenerative amplifier producing pulses centered at 800 nm with 15 nm FWHM with pulse duration of 120 fs. The pulses are

split by a beam splitter into two parts, 98% as excitation pulses, and rest is used to spectrally broaden the pulse by tight focusing onto a 5 mm thick CaF₂ crystal, generating a spectrum spanning between from the UV to the IR [196]. Both pump and probe are focused and overlapped spatially into spots of ~ 80 and ~ 55 μm diameters, respectively. The delay of the pump with respect to the probe pulses is controlled by a motorized Newport translation stage that results in a time accuracy of ± 7.5 fs. The relative polarization of the beams was set to the magic angle to avoid rotational effects [197, 198]. A phase locked optical chopper (Thorlabs) is set in the path of the pump pulse to create a pulse train at half frequency of the probe pulses. After passing through the sample, the probe beam is focused into an 80 μm input slit of a Triax 190 spectrometer using a 300 grooves/mm blazed for 550 nm wavelength grating. A 1024 pixel CMOS array is set at the exit of the spectrograph to detect the light at a 1 KHz repetition rate. Such conformation allows for a probing window from 340 to 750 nm with a spectral resolution of 1.7 nm.

For the Soret band excitation (pump at 560 nm), the output of a 20 KHz, 12 W regenerative amplifier is used to pump a commercial Non-collinear Optical Parametric Amplifier NOPA [199] (TOPAS White) delivering an output power of ~ 400 mw at 560 nm with pulse duration of about 40 fs. A fluence of ≈ 0.3 $\text{mJ}\cdot\text{cm}^{-2}$ is used for the three samples, which was found to be in the middle of the linear regime. The probe pulse is a broadband white light pulse generated by spectral broadening on a 5 mm CaF₂ crystal, same as explained previously. The same procedure as before is repeated on this setup by focusing and overlapping both the pump and probe, and sending the probe beam to a 0.25 m imaging spectrograph (Chromex 250is) using a multimode fiber.

5.2.2 Sample preparation

The samples were prepared under inert gas environment, by flowing Argon (Ar) in a portable glove box. The three samples (free base, Zinc, and platinum 3DP) were dissolved in deoxygenated toluene and bubbled with argon for 20 minutes. The concentrations were adjusted to obtain acceptable differential optical density in the pump-probe measurements but still have reasonably low concentrations (to avoid clustering). Concentrations of 18 μM , 30 μM and 26 μM , where used of H₂-3DP, Zn-3DP, and Pt-3DP, respectively. The samples were handled in air tight containers with an opening to put a slight overpressure of Argon gas to avoid any leaks during measurements. A 0.2 mm thick flow cell is used to circulate the sample so that every measurement is performed on a fresh spot. Static spectra were recorded before and after every measurement to check for any damaging or photoproducts photo-damage and no differences could be seen.

5.2.3 Data treatment

The probe pulses used are temporally chirped since they pass through a filter and a wave plate to set the desired power and magic angle conditions. Therefore the first step of data analysis is the Group Velocity Dispersion correction. Global fitting is done by choosing various kinetic traces at various wavelengths; the traces are fit with a sum of exponential decays convoluted with Instrumental Response Function (IRF). A global fit of the Singular

Value Decomposition (SVD) is used to generate Decay Associated Spectra (DAS) helping us understand the different contributions of different components in the spectra [200, 201].

5.3 Results

5.3.1 Steady state spectroscopy

Comparing the static absorption spectra of the samples we synthesized, with samples from literature gives insight on the expected photophysical behavior. Figure 1 shows the static UV-Vis-NIR absorption spectrum of the three different types of 3DP's that we synthesized, varying only their center (Pt, Zn, and Free-base), with a Pt-based mono-porphyrin. The strong excitonic coupling between the adjacent porphyrin units in the 3DP induces splitting of the Soret band into two bands I (y-axis) and II (x-axis) [179, 183, 202-204]. The efficient π conjugation along the x axis lifts the cancellation of the transition dipole in the single porphyrins and stabilizes the LUMO, leading to a significant increase of the Q-bands amplitude as well as a substantial shift to the NIR (zone III). The Q-band shift and intensity enhancement could be well observed in the case of the 3DP's in contrast with the Pt mono porphyrins. The absorption spectrum of Zn-3DP is nearly identical to the one of H2-3DP, while the Pt-3DP is strongly blue shifted. A comparable blue shift was reported by Schmidt et al. for the Pd-3DP compared to Zn-3DP. This phenomenon, common in porphyrins with a metal center having unoccupied d orbitals, results from the significant metal $d\pi$ to porphyrin π^* orbital interaction, causing an increase in the energy gap and illustrated by a blue shift. Enhanced absorption between the bands I and II arises from located charge transfer (CT) states with moderate oscillator strength. These CT states are solely localized over the macrocycle and have to be distinguished from the ring-metal charge transfer or back [183, 205].

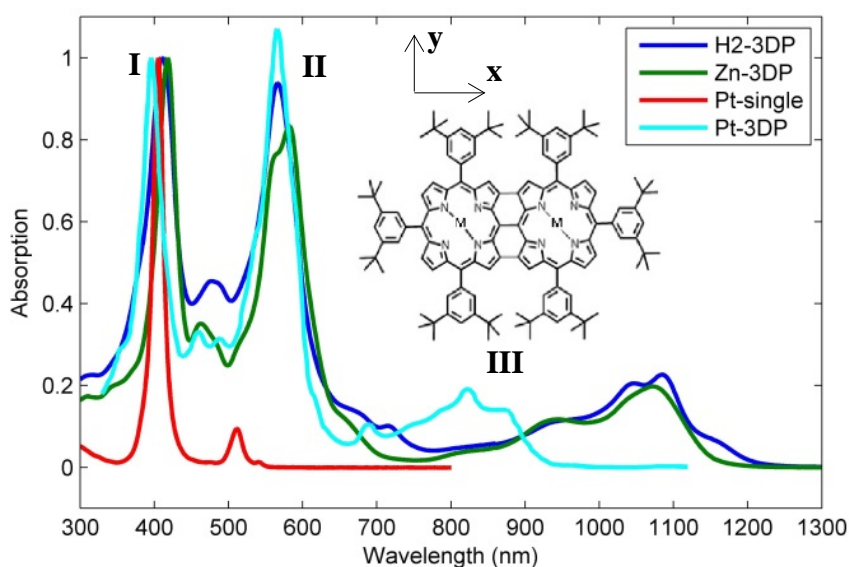


Figure 5-1 Normalized absorption spectra of H2-3DP (blue), Zn-3DP (green), Pt-3DP (light blue), and Pt-single (red) in Toluene. The bands were numbered by I for soret band, II for the split of the soret, and III for Q-bands.

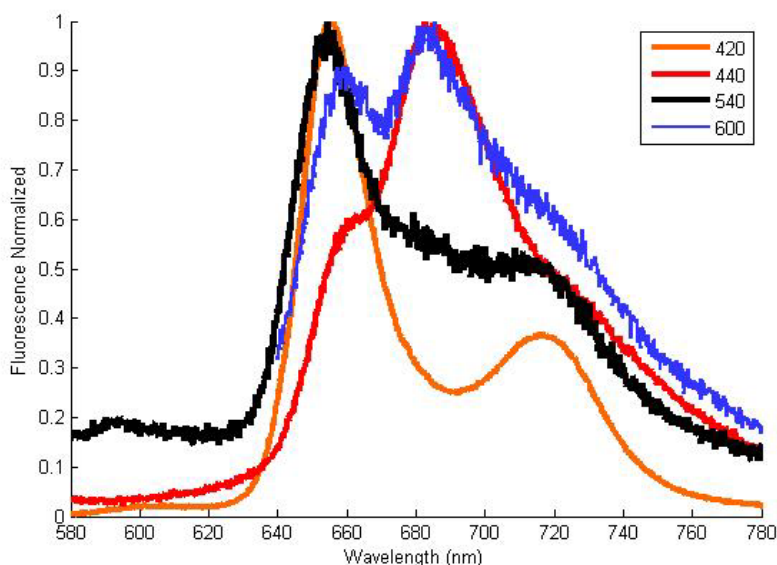


Figure 5-2 Static fluorescence spectra of H2-3DP upon different excitation wavelength, showing excitation wavelength dependence.

Fluorescence spectroscopy is a great way to study the Soret relaxation, especially with time-resolved fluorescence up-conversion spectroscopy. But, first, static fluorescence spectra in the region of the Soret emission are performed. We observed changes in the fluorescence spectrum of the Soret emission (600 – 800 nm) upon varying the excitation wavelength between 400 nm and 560 nm (Figure 5-2). These changes are related to mono porphyrin contaminants that have a Soret absorption band around 420 nm and Q bands between 500 and 600 nm. As we have shown previously, upon photoexcitation of the Soret band of a free base porphyrin, the energy is transferred almost instantaneously (<100 fs) through IC to the Q bands, and fluorescence of the Q bands is seen with life times of 1-2 ps from both Q_y and Q_x , 10-20 ps, and 1-12 ns time scale from the Q_x band [206, 207].

The emission spectrum of the Q_x bands of the monomer coincides spectrally with the emission spectra from the Soret band of the dimer in the 600 to 800 nm region. While the fluorescence quantum yield of the Soret band of the 3DP's is expected to be very low ($\Phi_f \approx 10^{-5}$), the yield of the single Q bands of mono porphyrins is 2 orders of magnitude higher. Therefore even for tiny amount of monomer contaminants (less than 1%), the fluorescence spectra will be a mixture of both at some excitation wavelength. At 420 nm excitation, the dominant emission resembles the emission of H₂OEP and H₂TPP [207]. On the contrary, at 440 nm excitation wavelength the dominating emission spectrum is of the H2-3DP and very little contribution of the mono porphyrins, which is expected since the absorptivity of the monomers at 440 is negligible. Finally at 540 and 600 where both absorb, the low energy side of the Soret of the dimer and the Q_x of the monomers, a contribution of both is observed.

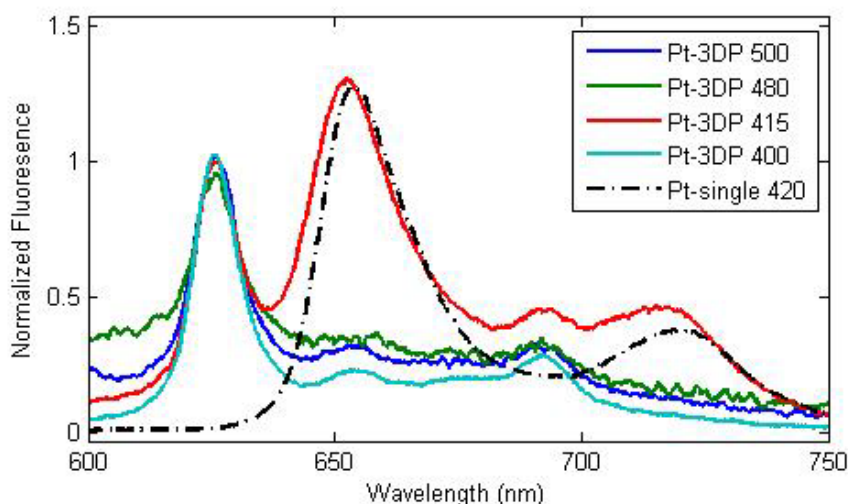


Figure 5-3 Static fluorescence spectra of Pt-3DP upon different excitation wavelength compared to Pt-single porphyrin at 420 nm excitation.

Equivalent to the case of H2-3DP, the Zn-3DP and Pt-3DP show variation in the fluorescence for different excitation. In the case of Zn-3DP, at excitation wavelength of 410, 420 and 500, and 550, the dominant emission spectrum is of the monomers since their emission is around 640 nm and is two orders of magnitude higher than the S2 fluorescence of the triply fused porphyrins. While at excitation wavelengths between 450 and 500 nm, the fluorescence spectrum of the Soret state of the Zn-3DP dominates with a very low quantum yield ($\Phi_f \leq 10^{-6}$) [206, 208]. Finally, in the case of Pt-3DP (Figure 5-3), comparison between fluorescence of the Q bands of the single porphyrins and the Pt-3DP shows that the main bands of emission of the S2 are centered at 625 and 693 nm. The fluorescence spectrum at 415 nm excitation is mainly dominated by single porphyrins, while a combination of both is appearing at other excitation wavelengths.

Such contamination due to the leftover monomers prohibits the ability to perform a “clean” fluorescence up-conversion experiment to study the soret relaxation dynamics in real time. Such measurements were performed and reported to have contaminated signals that might be misleading since the two signals overlap temporally and spectrally [183]. Therefore such experiments were not performed, and we used only transient absorption spectroscopy to study the relaxation dynamics.

5.3.2 Free base triply fused diporphyrins (H2-3DP):

Figure 5-4 A shows transient absorption (TA) spectra at different time delay obtained upon 560 nm photoexcitation of H2-3DP in deoxygenated toluene. At first glance, one can notice two strong negative peaks at 410 nm (I) and 560 nm (II) appearing instantaneously upon photo-excitation, that are attributed to the Ground State Bleach (GSB) of the split Soret bands. Compared to the static absorption spectrum the initial bleach at 100 fs appears red shifted by 8 nm, and shifts to the blue at later times, as shown in Figure 5-4 A. A similar behavior was reported earlier for Zn-3DPs [186] and metalloporphyrins [209] and was explained by non-radiative vibrational relaxation of the hot Q band, as it will be discussed

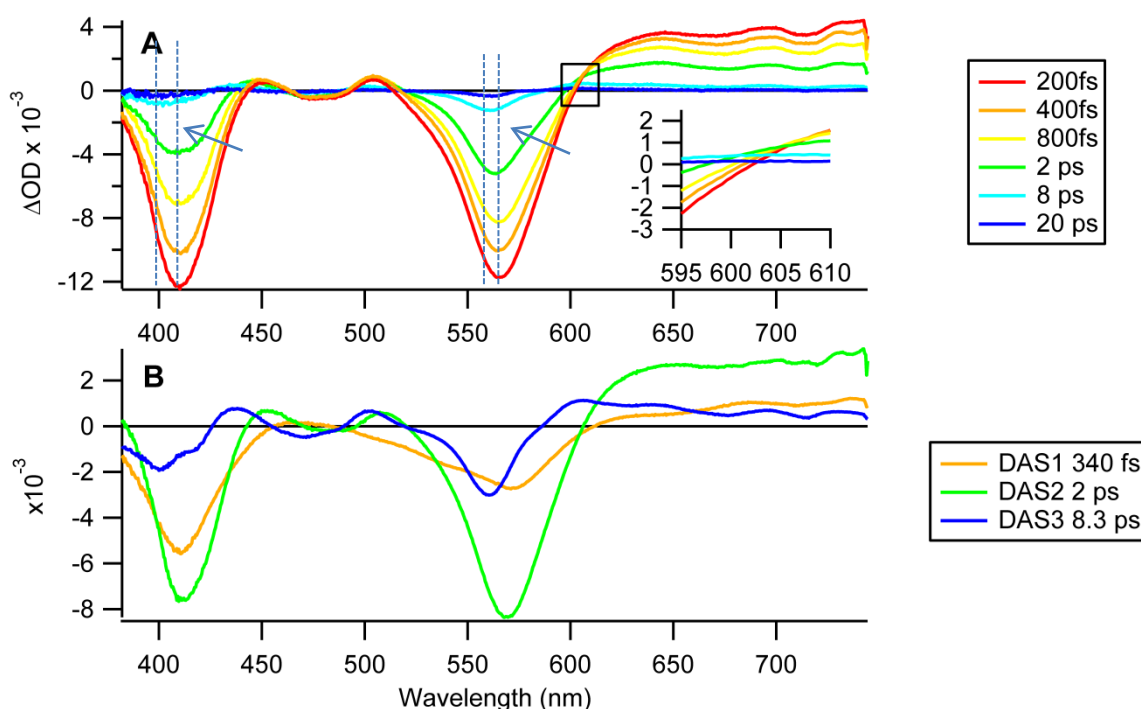


Figure 5-4 (A) Transient absorption spectra at selected time delay of H2-3DP upon 560 nm photoexcitation. (B) DAS of the timescales retrieved by a singular value decomposition analysis. The arrow and the dashed lines show the amount of blue shift happening over time.

later. A broad positive feature appears for wavelengths above 600 nm that is assigned to Excited State Absorption (ESA). Being usually broad and featureless, we conclude that this ESA is nearly canceled in the region between bands I and II by the GSB of the CT bands, analogous to transient spectra reported by Osuka et al. for Zn-3DP [183-186, 210].

Using both SVD and a global fit (GF); we extract a minimum of three exponential components: $340 \text{ fs} \pm 15 \text{ fs}$, $2 \text{ ps} \pm 32 \text{ fs}$, and $8.3 \text{ ps} \pm 190 \text{ fs}$ that fit well the kinetic traces (Figure 5-5). The resulting DAS is presented in Figure 5-4 B. The 340 fs component displays broad negative features in the regions of the GSB and a positive signal $> 600 \text{ nm}$; these features show a general decay of the signal signifying relaxation of the hot molecules. Upon photoexcitation of the S_2 , electronic excitation as well as excess vibrational energy is deposited in the system that needs to relax. A relaxation through internal conversion from $S_2 \rightarrow S_1$ is expected to happen in the range of 100 – 300 fs as proposed by Osuka et al. [183]. Therefore, the 340 fs component is assigned to a mixture of the IC from the Soret S_2 to a S_1 state and vibrational relaxation in the Q band. Our resolution does not allow us to distinguish between the two processes.

If the DAS has a shape that resembles that first derivative of the static absorption, then it displays a shift in the bands, while just negative or positive peaks resembles growth or decay of the signal. In the 2 ps components, band I shows a non-symmetric shape and goes to zero around 390 nm unlike the other decay components, as well as a strong red shift of its minimum. This can be explained by a negative band overlapped with its first derivative. While the

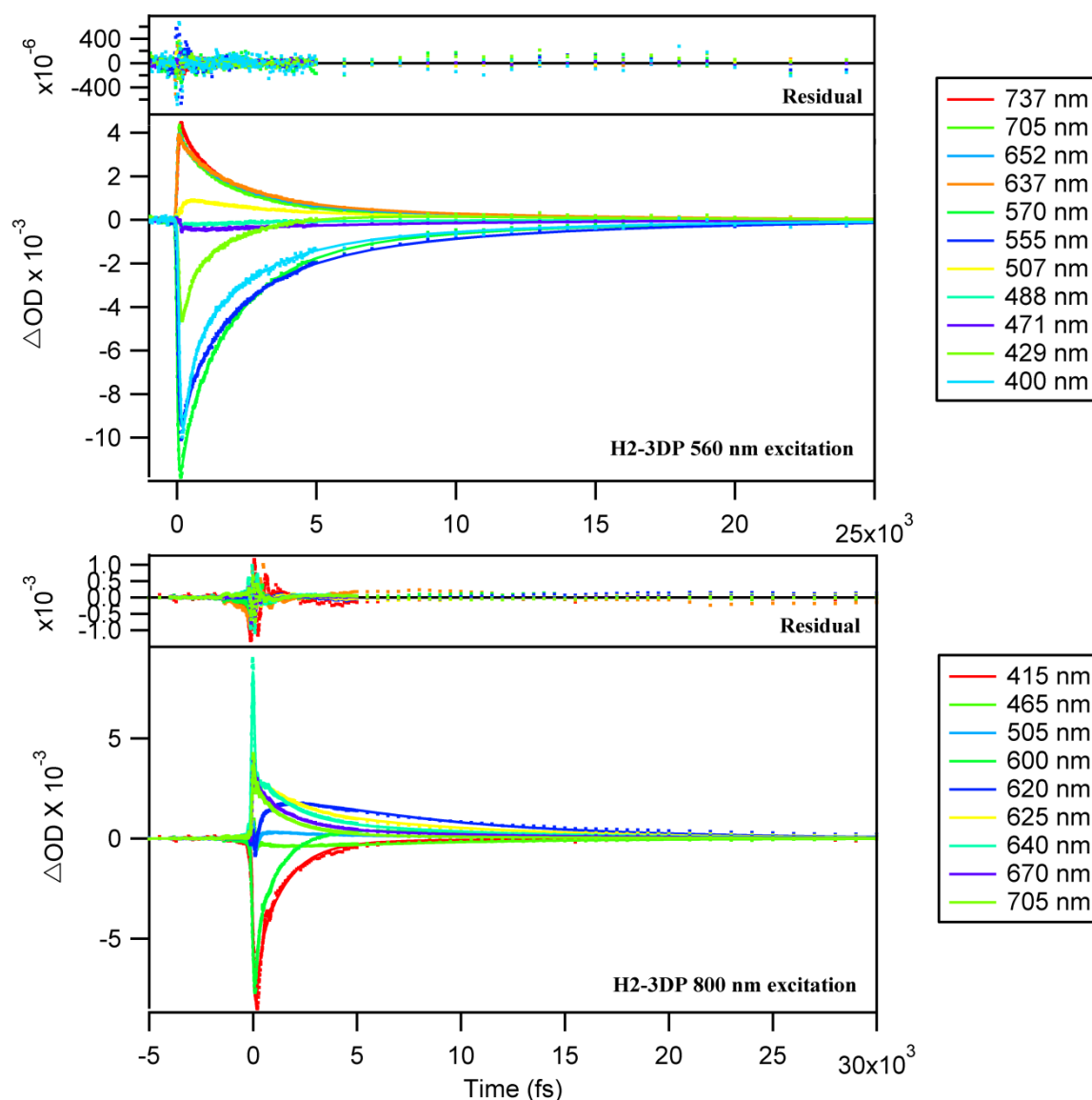


Figure 5-5 Global fitting of the H2-3DP transients upon 560 nm and 800 nm excitation pulses with the residual of the fit.

dominant feature is the fast relaxation process signified by the negative features in the bleach region and positive features in the ESA regions.

Comparable DAS component is presented later in the case of Zn-3DP with more prominent shift features on both bands (I and II) due to the increase of lifetime of the vibrational relaxation from 2 to 4.3 ps. Upon femtosecond excitation, the molecule is set in a high vibrational level of the S_1 state leading to lower energy ESA from the $S_n \leftarrow S_1$ which is illustrated by the initially red shifted transient spectrum. This hot band relaxes to lower vibrational levels of the S_1 leading to a larger energy gap $S_n \leftarrow S_1$ indicated by a blue shift of the transient spectrum. This process is most pronounced at the band edges due the abrupt change in signal intensity of the GSB in the regions between 400-430 nm and 560-600 nm. It is similar to the blue shift reported by Schmidt et al. in the 570-590 nm [186] and assigned to vibrational relaxation. Such a blue shift was also reported for single porphyrins by Holten et

al. [209] with a lifetime of < 10 ps; the shift was assigned to vibrationally excited S_1 state and excluded any participation of the solvent nor conformational effects. As a result the 2 ps timescale is assigned to vibrational relaxation within the S_1 state.

The 8 ps component is characterized by a GSB that better corresponds to the static absorption spectrum with the addition of a positive ESA signal, representative of the relaxation to the ground state. Alternatively, fluorescence lifetimes measured in comparable systems, such as Zn-3DPs, yielded nanosecond lifetimes [185], which shows that the most dominant relaxation pathway is non-radiative relaxation to S_0 . Therefore the most probable deactivation pathway will be through non-radiative relaxation via $S_1 \rightarrow S_0$ IC with 8 ps lifetime.

The treatment of the data for 800 nm photoexcitation results in comparable timescales (bottom panel of Figure 5-5); $130 \text{ fs} \pm 10 \text{ fs}$, $1.4 \text{ ps} \pm 35 \text{ fs}$ and $8.4 \pm 0.2 \text{ ps}$. The 1.4 ps and 8.4 ps are comparable to the ones observed with Soret excitation which confirms our assignment of the relaxation pathways and timescales. The ultrashort timescales of 130 fs and 340 fs differ from each other, and this could be given by the fact that IVR is the only process happening in the case of the Q band excitation, while both IVR and $S_2 \rightarrow S_1$ IC process are coexisting in the case of Soret excitation [183]. A difference in the vibrational relaxation timescale is also observed by a change between 1.4 ps to 2 ps, which could be attributed to excess vibrational energy deposited in the case of 560 nm compared to 800 nm excitation, which would facilitate the IVR process.

5.3.3 Zn-Zn triply fused diporphyrins (Zn-3DP):

Figure 5-6A shows TA spectra at different time delays upon photoexcitation. Comparable to the H2-3DP, a momentary GSB appears at the bands I and II, and a broad ESA band in the region above 600 nm and between the band II and III. As before, the CT states between the bands I and II do not show reasonable GSB and is explained by an overlapping ESA. Note that the blue shift in the transient spectra is more prominent than in the H2-3DP case.

Three timescales are extracted from the GF of the data, i.e. 370 fs, 4.3 ps and 8.3 ps, which are comparable to the timescales observed earlier for the H2-3DP and in the literature [183]. The shortest time decay of 370 fs is associated to fast IC from the S_2 to S_1 and to VR, the 4.3 ps is assigned to non-radiative relaxation from an excited vibrational level within the Q band manifold to the low vibrational states in the S_1 state, and the 8.3 ps timescale is the $S_1 \rightarrow S_0$ IC. The three timescales are associated to three DAS that resemble the DAS in Figure 5-4 B for H2-3DP. The correspondence with H2-3DP indicates that the main relaxation pathway did not change. The 4.3 ps component shows pronounced features of the shift at 580-640 nm and 400-450 nm and resembles by the derivative-like shape of the absorption peaks, overlapped with the negative and positive peaks in the regions of the GSB and ESA, respectively. The feature reflecting the shift in the DAS2 of Zn-3DP is more pronounced than that of H2-3DP owing to the increase of the vibrational relaxation timescale from 2 ps to 4.3 ps. This could be explained by the free H-N bond in the H2-3DP and more flexible molecular core, which can

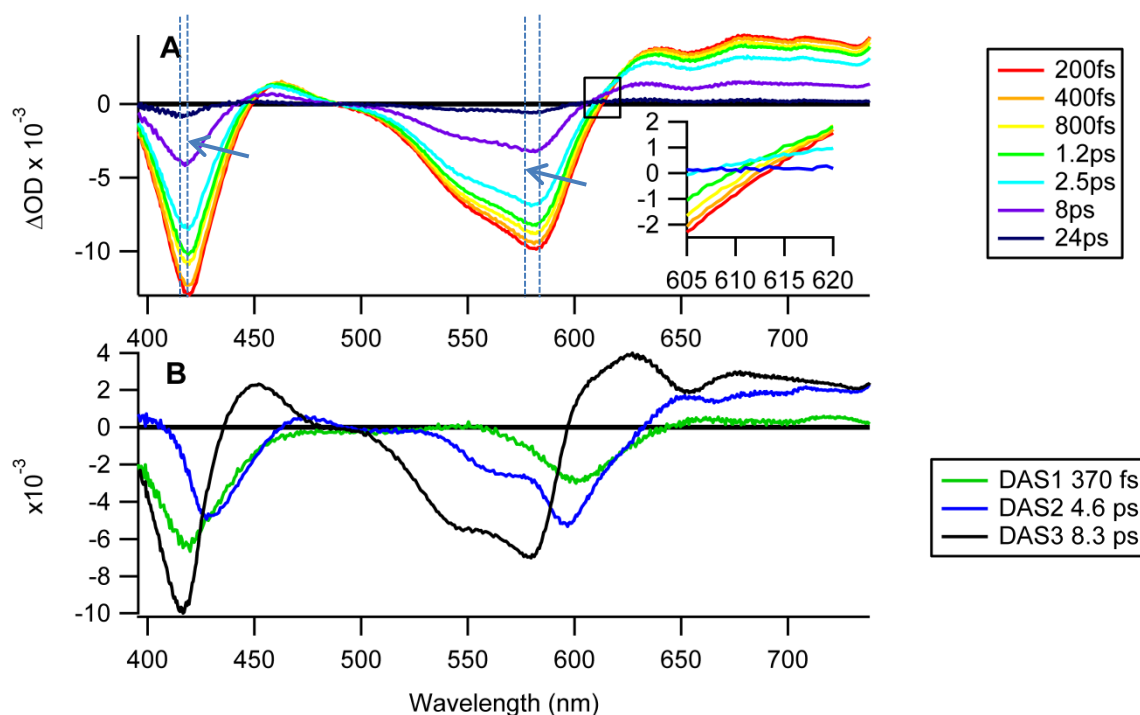


Figure 5-6 (A) Transient absorption spectra at selected time delay of Zn-3DP upon 560 nm photoexcitation. (B) DAS of the timescales retrieved by a singular value decomposition analysis. The arrow and the dashed lines show the amount of blue shift happening over time.

dissipate the extra vibrational energy faster compared to the reasonably more rigid molecular core of Zn-3DP.

Previously, various groups reported comparable dynamics with a small percentage (2%) of a non-recovering signal, which was attributed either to the excited state dynamics of a monoporphyrin contaminant in their sample [183], or to a very small triplet yield [186]. Despite a minute percentage of contamination by monomeric Zn-porphyrins, the TA measurements at 560 nm excitation are not affected because of the low absorption coefficient of the Q_x band of the monomers and reasonably low laser fluence used to excite the sample. Indeed, our transients show full recovery of the GSB over the whole spectrum. Therefore the 2% signal of non-recovering signal reported earlier is not due to an ISC to a triplet state and is most probably due to contamination of mono Zn porphyrins. TA measurements upon 800 nm photoexcitation are in agreement with the 560 nm excitation, giving comparable timescales: 106 ± 15 fs, 3.6 ± 0.3 ps, and 8.2 ± 0.4 ps. The 3.6 ps and 8.2 ps are comparable to the timescales reported for the Soret excitation, which supports the assignment of these timescales. The ultrashort timescales of 106 fs and 370 fs, as well as 3.6 ps and 4.3 ps differ from each other, for the same reasons mentioned earlier in the case of H2-3DP, the excess vibrational energy deposited in the case of 560 nm excitation.

5.3.4 Pt-Pt triply fused diporphyrins (Pt-3DP):

Figure 5-7 shows, an instantaneous GSB in the region of bands I and II, and a broad ESA band above 600 nm. In contrast to Zn and H2 3DP's, the Pt-3DP difference signal persists

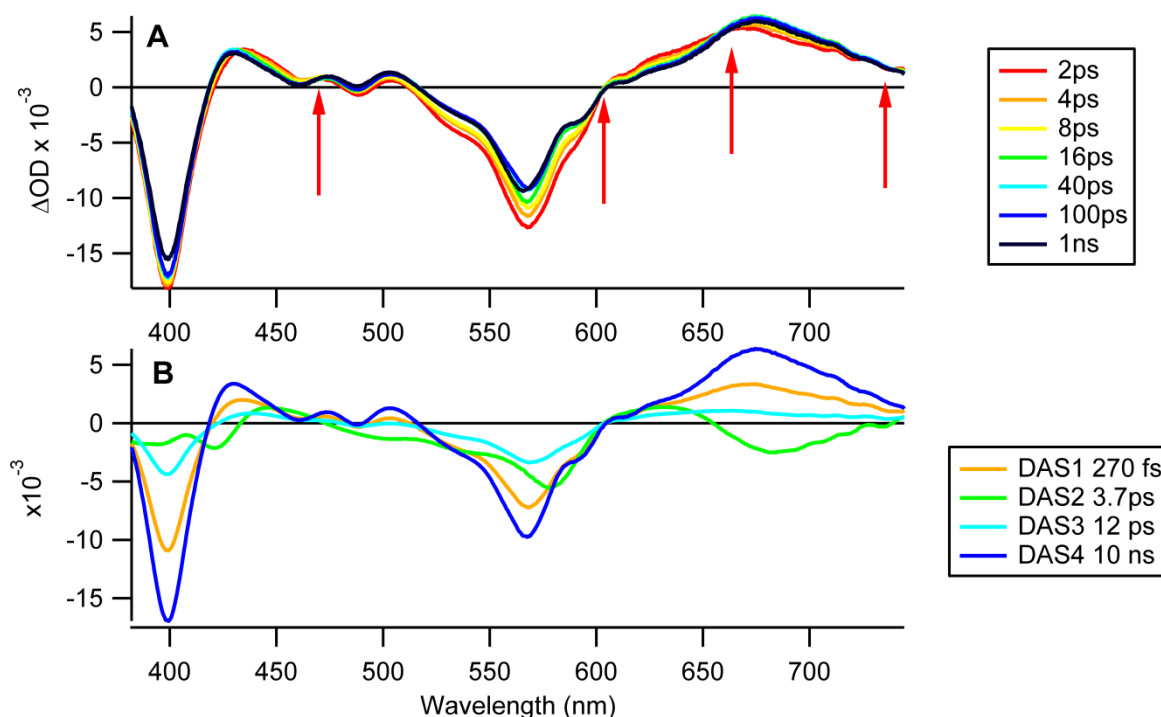


Figure 5-7 (A) Transient absorption spectra at selected time delay of Pt-3DP upon 560 nm photoexcitation. (B) DAS of the timescales retrieved by a singular value decomposition analysis.

after 1 ns over the whole spectrum, show no spectral shifts, and have different characteristics. The spectrum of the long-lived signal is different from the static absorption spectrum, and isosbestic points appear in the transient spectra (red arrows in Figure 5-7), manifesting the presence of a new species. Considering the most dominant pathway of the lowest singlet state is through non-radiative deactivation, as reported earlier and in the literature, it is safe to guess that life time of the lowest singlet state will be in the range of ps. Therefore, since the long-lived signal cannot be associated to a long-lived singlet state and the spectrum is different from the static absorption, this long lived signal can only be assigned to a triplet state. Using the static absorption spectrum and knowing the percentage of molecules excited in the transient absorption measurement, the scaled static absorption spectrum is subtracted from the transient at 1 ns, obtaining the excited state absorption spectrum of triplet $T_1 \rightarrow T_n$ (Figure 5-8). The triplet spectra calculated are qualitatively similar in both experiments, showing similar number of peaks at similar energies. A Φ_{ISC} yield of ≈ 0.7 is estimated by comparing the non-recovering signal with the initial bleach upon photo excitation.

By SVD analysis and global fitting, four exponential decays are required to represent the data; $270 \text{ fs} \pm 10 \text{ fs}$, $3.7 \text{ ps} \pm 30 \text{ fs}$, $12 \text{ ps} \pm 1 \text{ ps}$, and 10 ns . The 270 fs component in Figure 5-7 B shows negative features in the regions of the GSB and positive feature in the region of the ESA very comparable to the shape of the transient spectrum at 270 fs, are representative of a general relaxation of the whole spectrum with no spectral shifts or changes. Therefore, the short timescale of 270 fs is assigned to VR and IC from the S_2 to the S_1 manifold, as observed previously and in other comparable systems [183]. The features of the 3.7 ps component are vastly different from the 2 ps and 4 ps components observed earlier,

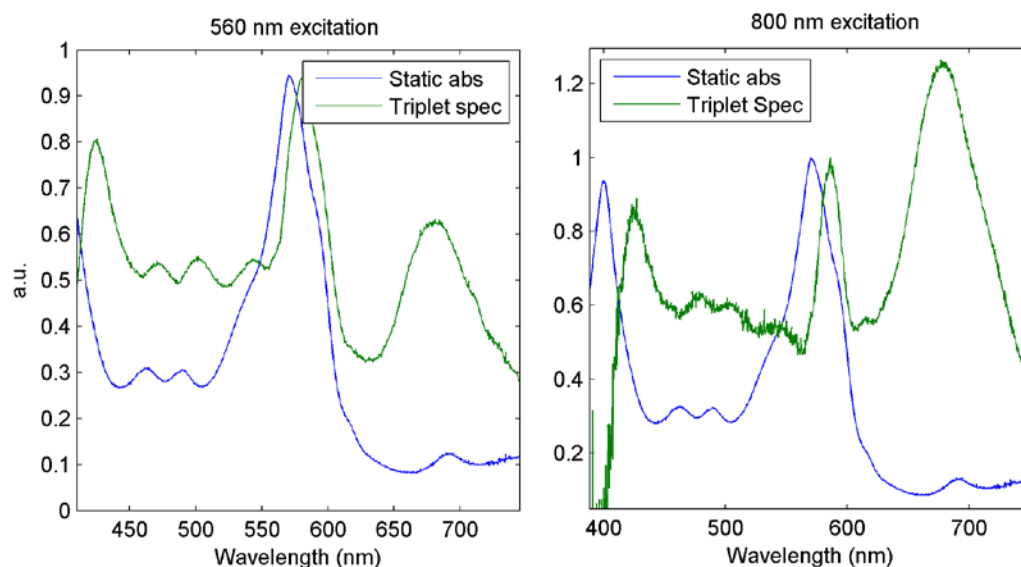


Figure 5-8 The excited state absorption of the triplet state spectrum calculated from the transient spectra, for both 560 nm and 800 nm excitation. The triplet spectrum is qualitatively similar, showing the same number of bands at the identical frequencies in both experiments.

in the case of H2-3DP and Zn-3DP. Here, this component shows a rise in the 650-750 nm region and decay in the 600-650 nm, as well as a shift in the GSB in respect to static absorption bands at 400 and 570 nm. Although a spectral shift appears in the DAS, the difference spectra in Figure 5-7 A show no shift at all, as it was clear in the earlier cases. Instead, isosbestic points appear at different points in the probe spectral region; the isosbestic point at 610 nm clearly show no spectral shift caused by cooling dynamics. As a consequence, the 3.7 ps can be assigned to a transition between two species, instead of the vibrational cooling. Therefore the 3.7 timescale can be confidently assigned to the ISC process from $S_1 \rightarrow T_1$.

The amplitude of DAS3 is very weak and has been multiplied by 10 to be visible in comparison with the others. Due to the non-unit ISC yield, it is expected that a small percentage of the molecules will relax through other pathways. Considering the assignment of the 3.7 ps timescale to ISC and the estimated yield of 0.7-0.75, the $S_1 \rightarrow S_0$ IC timescale can be estimated using the following rate equation.

$$\tau_{IC} = \frac{\tau_{S1}}{1 - \phi} \approx 12 - 14 \text{ ps}$$

Considering the spectral features and small amplitude of DAS3, and the fact that it matches the estimate of 12 -14 ps for IC, it is safe to assign the 12 ps component to $S_1 \rightarrow S_0$ IC. The singlet S_1 state is minimally affected by the vibrational relaxation since it is depleted much faster than the vibrational relaxation timescale. Comparable results for Pt mono-porphyrins were reported by Kobayashi et al. in a comparative study of monomeric Zn, Pt, and Pd porphyrins [211].

The long-lived signal appears to persist over the experimental delay limit (1 ns), presented as the DAS4. Due to the limitation of the delay limit, resolving the long time scale was not possible since it is much longer than a couple of ns. As a consequence, a 10 ns timescale was fixed while analyzing the data to obtain a satisfactory fit. Therefore DAS4 represents the triplet T_1 relaxation.

Measurements performed at 800 nm excitation wavelength, while exciting the Q band manifold only, yielded comparable timescales and spectra for the singlet relaxation and triplet formation; 115 ± 6 fs, 4.1 ± 0.5 ps, 11.8 ± 1.1 ps, 10 ns. The fact that the triplet state is equally populated by both Soret and Q band excitation excludes any possibility of a bypass of the S_1 state directly populating the triplet state. The 4.1 ps and 11.8 ps are similar to the timescales observed earlier, and confirm our assignments of the timescales to specific processes. Due to the same reason mentioned above, the triplet lifetime was fit with a fixed 10 ns timescale. Static absorption and fluorescence spectroscopy measurements were performed before and after every TA measurement to make sure that no photochemical products were produced, ensuring that the reminiscent signal is due to the long lived state and not a photoproduct. Moreover, a reminiscent transient signal identical to the transient signal at 1 ns, is found to appear before time zero in the case of low flow rates of the sample while exciting at 800 nm and probing at 1 kHz rate. Such an effect can only be explained by a very long lived triplet state that can survive till the next pump pulse, therefore with a lifetime in the millisecond range. Since the decay of triplet state is exponential, the lifetime was estimated to be ≈ 1.3 ms using the method proposed in reference [212].

The ultrashort timescales of 115 fs and 270 fs differ from each other due to the same reasons discussed earlier in the case of Zn-3DP and H2-3DP. These timescales are comparably shorter than what was observed in the case of H2-3DP and Zn-3DP. The main factor that influences the $S_2 \rightarrow S_1$ IC timescale is the energy gap between S_2 and S_1 potential energy surfaces. As can be realized for the static absorption spectrum, the energy gap between S_2 and S_1 is smaller in the case of Pt-3DP compared to the other two 3DP samples. By invoking the energy gap law, a faster IC process is predicted. Additionally, the overlap between the 2 bands provides a ladder for sequential relaxations between successive pairs of levels, facilitating the relaxation process.

Table 5 Summary of decay timescales obtained from the data analysis of H2-3DP, Zn-3DP, Pt-3DP for both excitation wavelengths of 560 nm and 800 nm. The timescales are categorized by IC, VR, and ISC.

	λ_E (nm)	T1(fs)		T2(ps)		T3(ps)		T4(ns)	
H23DP	560	340	IC $S_2 \rightarrow S_1$ & VR	2	VR	8.3	IC $S_1 \rightarrow S_0$	-	} $T_1 \rightarrow S_0$
	800	130		1.4		8.4		-	
Zn-3DP	560	370		4.3	8.3	-			
	800	106		3.6	8.2	-			
Pt-3DP	560	270		3.7	12	> 10			
	800	115		4.1	11.8	> 10			

Such long lifetimes and high ISC yields are not surprising. Platinum mono-porphyrins are widely used as phosphorescent material in OLEDs due to their strong ISC rate from S_1 to T_1 . It was demonstrated by Ponterini et al. [213] that the S_1 lifetime of PtOEP in the gas phase is in the range of 1 ps with an extremely weak fluorescence yield, and that it has a triplet state with a lifetime > 50 ns (experimental limit). Other studies on PtOEP in various solvents or solid films reported triplet state lifetimes varying between 90 μ s and 100's of μ s with extremely high ISC yield, close to 100% [214, 215]. The enhancement of the ISC yield is attributed to the large spin-orbit coupling constant of the Pt atom [216, 217]. A similar behavior to PtOEP is witnessed by Pt-3DP, where high yield ultrafast ISC at 3.7 ps dominates the relaxation dynamics suppressing the IC process, leading to a very weak singlet $S_1 \rightarrow S_0$ relaxation signal and very high T_1 formation with long lifetime.

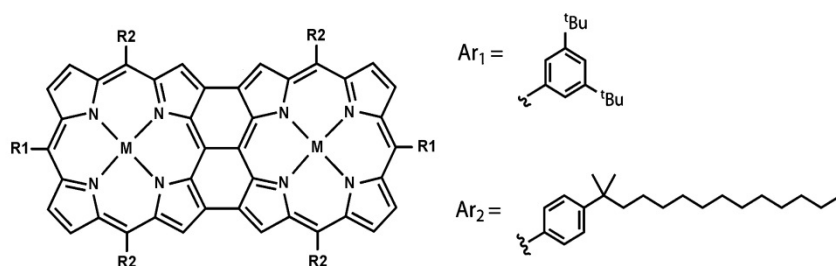
The timescale of S_1 due to IC is found to be slightly longer than that of Zn-3DP and H2-3DP. This could be due to the HOMO-LUMO energy gap that is larger in the case of Pt-3DP. Estimation of the non-radiative rate based on the energy gap law predicts $K_{IC}(Pt) = 1.76 \times 10^9 \text{ s}^{-1}$ and $K_{IC}(Zn) = 9.3 \times 10^9 \text{ s}^{-1}$, using the proportionality value $\alpha = 0.064 \text{ KJ}^{-1} \cdot \text{mol}$ and maximum possible decay rate $f_0 = 10^{13} \text{ s}^{-1}$ as used by Anderson et al. for Zn-3DP [185]. This estimate is about 45 times longer than the measured 12 ps for Pt-3DP and 12 times longer for the 8.3 ps of Zn-3DP. This demonstrates that the energy gap law is not sufficient to explain the energy deactivation in such systems due to the manifold of relaxation pathways [181, 218]. The timescales and processes observed in all three samples under both 560 and 800 nm excitation are all summarized in the table below showing what each timescale correspond to.

5.4 Discussion:

Using femtosecond pump-probe pulsed laser experimental setups, we measured the ultrafast transient absorption spectroscopy of the H2-3DP, Zn-3DP, and Pt-3DP. Two sets of measurements were performed on each sample, exciting the Q band manifold by 800 nm and the low energy side of the Soret band at 560 nm, comparing the different behavior of the relaxation dynamics. Lifetime and excited state behavior of H2-3DP and Zn-3DP are consistent with the literature [183, 186], while the Pt-3DP shows high ISC yield (0.7) and long lived triplet state.

Studying the excited state dynamics of the three samples (H2, Zn, and Pt -3DP) in comparison to other systems provides further insight into the various pathways of energy relaxation in 3DP's. Two main points should be discussed in order to understand the excited state dynamics of the 3DP's; the effect of the peripheral substituents, and the effect of the metal. The variation of the substituents has proven to be highly influential on the S_1 lifetime and the triplet state formation quantum yield [184, 185]. On the other hand, the impact of varying the metal center on the dynamics of the 3DP's has been argued to be of minor effect compared to the substituents [186]. Table 2 puts our results in comparison with the literature, indicating the metal centers used, the substituents and relaxation lifetimes.

	R1	R2	M	$\tau(S_1)$	$\tau(T_1)$	$\Phi(\text{ISC})$	solvent	Ref.
1	Ar1	Ar2	Zn (II)	4.5 ± 0.5 ps	-	-	Toluene	[183]
2	Ar1	Ar1	-	8.3 ± 0.4 ps	-	-	Toluene	This work
3	Ar1	Ar1	Zn (II)	8.3 ± 0.4 ps	-	-	Toluene	This work
4	Ar1	Ar1	Pt (II)	12 ps	1.3 ms	0.7	Toluene	This work
5	Bu	Ar1	Zn (II)	13.5 ± 0.7 ps	-	-	CHCl ₃	[186]
6	Br/I	Ar1	Pb (II)	<5 ns ^a	-	-	CHCl ₃ /pyridine	[184]
7	Bu	Ar1	Pd (II)	18 ± 1 ps	1.7 ± 0.3 ns	b	CHCl ₃	[186]
8	I	Ar1	Zn (II)	- ^a	52 ns	0.2	CHCl ₃ /pyridine	[184]
9	Br	Ar1	Zn (II)	- ^a	280 ns	0.12	CHCl ₃ /pyridine	[184]
10	C≡C-Si(^t Pr) ₃	Ar1	Zn (II)	- ^a	177 ± 25 μ s	b	CHCl ₃ /pyridine	[185]



^a singlet lifetimes were not reported due to the long pulses used.

^b Triplet yields were negligible.

Table 6 List of various 3DPs with various substituents and metal centers manifesting the lowest singlet and triplet lifetimes.

The sole use of aryl substituents on Zn porphyrin tapes displays extremely rapid relaxation with lifetime < 10 ps and no measurable ISC yield, as observed in our measurements and in the work of Osuka et al. [183]. In comparison, introducing bromine, iodine, alkynyl, or butyl-ended, caused lengthening of the singlet life time, and a small increase in the ISC yield (< 0.2) with triplet lifetimes ranging from nanoseconds to hundreds of microseconds [184, 185]. In the work of Osuka et al., the ultrafast $S_1 \rightarrow S_0$ transition through internal conversion was described by the energy gap law [183]. The energy gap law ($K_{\text{IC}} = f_0 \cdot f_v$) directly relates the total deactivation rate K_{IC} (radiative and non-radiative) to the Frank-Condon factor $f_v = e^{-\alpha \Delta E}$, and f_0 the maximum possible decay rate and α is the proportionality factor. Anderson et al. reported no change in the fluorescence quantum yield upon extensive deuteration of Zn-3DP's with various ligands, knowing that deuteration impacts directly the Frank-Condon factor by changing the stretch frequency of C-H (3000 cm⁻¹) to C-D (2200 cm⁻¹) generally reducing the deactivation processes rate [185, 219]. The authors concluded that the energy gap law is not sufficient to be used a sole explanation of the energy relaxation, and propose the presence of a conical intersection between the S_1 - S_0 potential energy surfaces that depend on the nature of the substituents. The deactivation pathway of the H2-3DP and Zn-3DP are identical, with $S_1 \rightarrow S_0$ IC in 8.3 ps timescale. A similar trend is observed in mono-porphyrins where the ultrashort behavior of free base porphyrin is very similar to that of Zn porphyrins [208, 217]. This is explained by the presence of closed (d^{10}) shell metal center, excluding any possible ring-to-metal charge transfer that can cause a fast relaxation pathway. This leads us to believe that the most dominant process of deactivation in the case of full d metal orbitals, is the conical intersection between the S_1 and S_0 potential energy curves as proposed by Anderson et al. [185].

Replacing Zn by Pt changes the dynamics drastically, i.e. very high ISC yields > 0.7 and extremely fast T_1 formation of < 3.7 ps, are observed. Although the Pt-3DP have a bigger S_1 - S_0 energy gap compared to the Zn or H2 3DP, the life time of S_1 is estimated to be comparable, which again cannot simply be explained by the energy gap law [181, 183, 220, 221]. The lifetime of the triplet state is in the millisecond range, longer than the achieved triplet lifetimes in 3DP's [183, 186]. Likewise, the platinum mono-porphyrins exhibit ultrafast relaxation of the singlet state < 1 ps with nearly 100% ISC yield and triplet lifetimes up to microseconds [213, 222].

Studies on butylated Pd-3DP in CHCl_3 /pyridine reported the presence of a short-lived triplet state < 2 ns with negligible quantum yield [186]. The short triplet state lifetime was explained by $T_1 \rightarrow S_0$ reverse ISC due to the high SOC caused by the palladium atom in the center; enhancement of $S_1 \rightarrow T_1$ as well as $T_1 \rightarrow S_0$ [186]. While measurements on halogenated Pb-3DP in CHCl_3 /pyridine, showed no triplet state and short deactivation time that was not estimated due to the long pulses used (5 ns) [184]. In the case of Pb mono-porphyrins, the Pb ion has full d and f shells and the HOMO is constructed from 7s and $6p_z$ orbitals of the Pb and the $2p_x$ and $2p_y$ of the nitrogen atoms. Because the ion radius of Pb(II) is larger than those of metal centers in other usual porphyrins, the Pb(II) is accommodated out of porphyrin plane by 1 Å [223]. A comparable structure is expected for the Pb-3DP molecule where the Pb ion will be accommodated out of plane, with comparable construction of the molecular orbital. Therefore the presence of the Pb will not alter the ISC rates due to two main reasons, the full d and f shell reducing its ability to present a CT intermediate facilitating the spin flip, and the reduced coupling of the Pb atom with the macrocycle due the Pb-N distance.

Systematic studies of ISC rates in metal complexes show that they do not comply with the heavy atom effect. In case of transition metals with unoccupied d orbitals, density of states, charge transfer states and structural parameters become key factors [224, 225]. In monomeric porphyrin for example, it has been proven that the metal center effect is not just a heavy atom effect, but it offers relaxation pathway through Ring-to-Metal charge transfer and back due to the unoccupied metal d-orbitals [217, 226-228]. This is also the case here, the ISC rates do not scale linearly with the SOC constants of the metals used ($\text{SOC}(\text{Pd}) < \text{SOC}(\text{Pt}) < \text{SOC}(\text{Pb})$). The metal center is also expected to impact the dynamics of the system due to the strong interaction between the metal and the π -electrons of the porphyrin excited state is a result of the large spin density localization on the nitrogen atoms predicted for HOMO and LUMO orbitals of 3DP's [229].

The excited state dynamics of 3DP's mimic any other metal complex. In the case of a full shell metal in the center, the metal has minor influence on the relaxation pathways as seen in Zn, Pb, compared to H2 monomeric and diporphyrin. On the contrary, in the presence of a transition metal, such as Cu, Ni, Pd, or Pt, the relaxation pathways are highly altered by additional background levels due to the unoccupied d orbitals in the ligand field of the porphyrin [208, 217, 226]. Therefore the relaxation dynamics of 3DPs is governed by far more complex approximation than the energy gap law, and it is not straight forward to use heavy atoms at certain position as an approach to increase the ISC yield. One should take into

account the offered alternative pathways for energy relaxation, density of states, and structural parameters, as pointed out in the case of Pb-3DP.

3DP's are highly desirable in different situations due to their high π conjugation and ease in changing their relaxation properties through variation of the metal center or peripheral ligands. Longer porphyrin arrays with fast relaxation times such Zn tapes possess metallic properties and could be used as metallic molecular wires or films [183, 204]. On the other side longer lifetimes and higher triplet yield formation as in the case of Pt-3DP are a clear advantage in numerous photovoltaic systems. The high ISC yield, long triplet lifetime, and high cross-section of Pt-3DP make it a perfect candidate as a NIR sensitizer for photochemical up-conversion via triplet-triplet annihilation [190, 191, 230, 231]. Broadband reverse saturable absorber (RSA) extending to NIR is also a suitable application for Pt-3DP due to its triplet state properties [184, 232].

5.4.1 Conclusion:

Relaxation dynamics were measured using ultrafast transient absorption experiments photoexciting the samples at 560 nm and 800 nm under comparable conditions. The relaxation dynamics were explained showing a fast relaxation from the Soret band to the Q bands within 500 fs, and different relaxation dynamics of the S_1 state depending on the metal used. The Zn-3DP and H2-3DP results confirm the presence of a potential energy surface crossing between S_1 and S_0 leading to ultrafast relaxation as proposed by Anderson et al. [185]. High ISC yield (> 0.7) and long lived triplet (milliseconds) state as recorded in the case of Pt-3DP shows the strong influence of the metal center on the relaxation dynamics. As a consequence our results illustrate the importance of the metal center in the ultrafast relaxation process.

References

References

1. Brixner, T., et al., *Phase-stabilized two-dimensional electronic spectroscopy*. Journal of Chemical Physics, 2004. **121**(9): p. 4221-4236.
2. Jonas, D.M., *Two-dimensional femtosecond spectroscopy*. Annual Review of Physical Chemistry, 2003. **54**: p. 425-463.
3. Robinson, J.S., et al., *The generation of intense, transform-limited laser pulses with tunable duration from 6 to 30 fs in a differentially pumped hollow fibre*. Applied Physics B, 2006. **85**(4): p. 525-529.
4. Wilson, M.W.B., et al., *Singlet Exciton Fission in Polycrystalline Pentacene: From Photophysics toward Devices*. Accounts of Chemical Research, 2013. **46**(6): p. 1330-1338.
5. Mukamel, S., *Principles of nonlinear optical spectroscopy*. 1995: Oxford University Press.
6. Mukamel, S. and R.F. Loring, *Nonlinear response function for time-domain and frequency-domain four-wave mixing*. Journal of the Optical Society of America B, 1986. **3**(4): p. 595-606.
7. A, N., et al., *Compact phase-stable design for single- and double-quantum two-dimensional electronic spectroscopy*. Opt. Lett., 2009. **34**: p. 3301.
8. N, C., et al., *Electronic double-quantum coherences and their impact on ultrafast spectroscopy: the example of β -carotene*. J. Phys. Chem. Lett., 2010. **1**: p. 3366.
9. Dobryakov, A.L., S.A. Kovalenko, and N.P. Ernsting, *Coherent and sequential contributions to femtosecond transient absorption spectra of a rhodamine dye in solution*. The Journal of Chemical Physics, 2005. **123**(4): p. 044502.
10. Yeazell, J.A. and T. Uzer, *The Physics and Chemistry of Wave Packets*. 2000: Wiley.
11. Zewail, A.H., *Coherence—a powerful concept in the studies of structures and dynamics*. Laser Physics, 1995. **5**(417): p. 3.
12. Baskin, J.S. and A.H. Zewail, *Freezing Atoms in Motion: Principles of Femtochemistry and Demonstration by Laser Stroboscopy*. Journal of Chemical Education, 2001. **78**(6): p. 737.
13. Bowman, R.M., M. Dantus, and A.H. Zewail, *Femtosecond transition-state spectroscopy of iodine: From strongly bound to repulsive surface dynamics*. Chemical Physics Letters, 1989. **161**(4–5): p. 297-302.
14. Pollard, W.T., S.Y. Lee, and R.A. Mathies, *Wave packet theory of dynamic absorption spectra in femtosecond pump–probe experiments*. The Journal of Chemical Physics, 1990. **92**(7): p. 4012-4029.
15. Perrin, M.H., M. Gouterman, and C.L. Perrin, *Vibronic Coupling. VI. Vibronic Borrowing in Cyclic Polyenes and Porphyrin*. The Journal of Chemical Physics, 1969. **50**(10): p. 4137-4150.
16. Kobayashi, T. and A. Yabushita, *Transition-state spectroscopy using ultrashort laser pulses*. The Chemical Record, 2011. **11**(2): p. 99-116.

References

17. Kano, H., T. Saito, and T. Kobayashi, *Dynamic Intensity Borrowing in Porphyrin J-Aggregates Revealed by Sub-5-fs Spectroscopy*. The Journal of Physical Chemistry B, 2001. **105**(2): p. 413-419.
18. Kano, H., T. Saito, and T. Kobayashi, *Observation of Herzberg–Teller-type Wave Packet Motion in Porphyrin J-Aggregates Studied by Sub-5-fs Spectroscopy*. The Journal of Physical Chemistry A, 2002. **106**(14): p. 3445-3453.
19. Kobayashi, T., Z. Wang, and T. Otsubo, *Classification of Dynamic Vibronic Couplings in Vibrational Real-Time Spectra of a Thiophene Derivative by Few-Cycle Pulses†*. The Journal of Physical Chemistry A, 2007. **111**(50): p. 12985-12994.
20. Kumar, A.T.N., et al., *Investigations of amplitude and phase excitation profiles in femtosecond coherence spectroscopy*. The Journal of Chemical Physics, 2001. **114**(2): p. 701-724.
21. Garraway, B.M. and K.A. Suominen, *Wave-packet dynamics: new physics and chemistry in femto-time*. Reports on Progress in Physics, 1995. **58**(4): p. 365.
22. Lin, S.H. and H. Eyring, *Study of the Franck-Condon and Herzberg-Teller Approximations*. Proceedings of the National Academy of Sciences, 1974. **71**(10): p. 3802-3804.
23. Kumar, A.T.N., et al., *Investigations of ultrafast nuclear response induced by resonant and nonresonant laser pulses*. The Journal of Chemical Physics, 2001. **114**(15): p. 6795-6815.
24. Ikuta, M., et al., *Phase analysis of vibrational wave packets in the ground and excited states in polydiacetylene*. Physical Review B, 2004. **70**(21): p. 214301.
25. Stannard, P.R. and W.M. Gelbart, *Intramolecular vibrational energy redistribution*. The Journal of Physical Chemistry, 1981. **85**(24): p. 3592-3599.
26. Owrutsky, J.C., D. Raftery, and R.M. Hochstrasser, *Vibrational Relaxation Dynamics in Solutions*. Annual Review of Physical Chemistry, 1994. **45**(1): p. 519-555.
27. Elles, C.G. and F.F. Crim, *CONNECTING CHEMICAL DYNAMICS IN GASES AND LIQUIDS*. Annual Review of Physical Chemistry, 2006. **57**(1): p. 273-302.
28. Felker, P.M. and A.H. Zewail, *Dynamics of intramolecular vibrational-energy redistribution (IVR). I. Coherence effects*. The Journal of Chemical Physics, 1985. **82**(7): p. 2961-2974.
29. Jean, J.M. and G.R. Fleming, *Competition between energy and phase relaxation in electronic curve crossing processes*. The Journal of Chemical Physics, 1995. **103**(6): p. 2092-2101.
30. Veen, R.M.v.d., *Ultrafast X-ray and Optical Spectroscopy of Binuclear Molecular Complexes*. 2010, ÉCOLE POLYTECHNIQUE FÉDÉRALE DE LAUSANNE (EPFL).
31. Higgins, J.R., *Sampling Theory in Fourier and Signal Analysis: Foundations*. 1996: Clarendon Press.
32. Smith, S.W., *The Scientist and Engineer's Guide to Digital Signal Processing*. 1997: California Technical Pub.
33. Wikipedia, *Nyquist-Shannon sampling theorem --- Wikipedia, The Free Encyclopedia*. 2015.

34. Bartholdi, E. and R.R. Ernst, *Fourier spectroscopy and the causality principle*. Journal of Magnetic Resonance (1969), 1973. **11**(1): p. 9-19.
35. L, L., C. G, and J. M, *Linear techniques of phase measurement by femtosecond spectral interferometry for applications in spectroscopy*. J. Opt. Soc. Am. B, 1995. **12**: p. 2467.
36. Dorrer, C. and M. Joffre, *Characterization of the spectral phase of ultrashort light pulses*. Comptes Rendus de l'Académie des Sciences - Series IV - Physics, 2001. **2**(10): p. 1415-1426.
37. G, D., et al., *Diffraction optics-based heterodyne-detected four-wave mixing signals of protein motion: from "protein quakes" to ligand escape for myoglobin*. Proc. Natl. Acad. Sci. USA, 2001. **98**: p. 6110.
38. AA, M., N. KA, and R. TA, *Optical heterodyne detection of laser-induced gratings*. Opt. Lett., 1998. **23**: p. 1319.
39. WP, D., P. MS, and W. DA, *Phase-locked heterodyne-detected stimulated photon-echo: a unique tool to study solute-solvent interactions*. Chem. Phys. Lett., 1995. **238**: p. 1.
40. WP, d.B., P. MS, and W. DA, *Heterodyne-detected stimulated photon echo: applications to optical dynamics in solution*. Chem. Phys., 1998. **233**: p. 287.
41. G, P., *Flash photolysis and spectroscopy: a new method for the study of free radical reactions*. Proc. R. Soc. Lond. A, 1950. **200**: p. 284.
42. G, P. and T. MR, *Nanosecond flash photolysis and absorption spectra of singlet excited states*. Nature, 1968. **220**: p. 1228.
43. S, M., T. Y, and H. P, *Coherent multidimensional optical spectroscopy*. Acc. Chem. Res., 2009. **42**: p. 1207.
44. M, W., et al., *Ultrafast two-dimensional terahertz spectroscopy of elementary excitations in solids*. New J. Phys., 2013. **15**: p. 025039.
45. W, K., et al., *Two-dimensional terahertz correlation spectra of electronic excitations in semiconductor quantum wells*. J. Phys. Chem. B, 2011. **115**: p. 5448.
46. YS, K., et al., *2D IR provides evidence for mobile water molecules in β -amyloid fibrils*. Proc. Natl. Acad. Sci. USA, 2009. **106**: p. 17751.
47. DE, R., et al., *Structural dynamics of a catalytic monolayer probed by ultrafast 2D IR vibrational echoes*. Science, 2011. **334**: p. 634.
48. V, V., S. R, and H. P, *Active phase stabilization in Fourier-transform two-dimensional infrared spectroscopy*. Opt. Lett., 2005. **30**: p. 2010.
49. JT, K., R. MR, and K. KJ, *Ultrafast α -like relaxation of a fragile glass-forming liquid measured using two-dimensional infrared spectroscopy*. Phys. Rev. Lett., 2012. **108**: p. 157401.
50. Selig, U., et al., *Inherently phase-stable coherent two-dimensional spectroscopy using only conventional optics*. Optics Letters, 2008. **33**(23): p. 2851-2853.
51. Brixner, T., I.V. Stiopkin, and G.R. Fleming, *Tunable two-dimensional femtosecond spectroscopy*. Optics Letters, 2004. **29**(8): p. 884-886.
52. Fuller, F.D., D.E. Wilcox, and J.P. Ogilvie, *Pulse shaping based two-dimensional electronic spectroscopy in a background free geometry*. Optics Express, 2014. **22**(1): p. 1018-1027.

References

53. JA, M., et al., *Two-color two-dimensional Fourier transform electronic spectroscopy with a pulse-shaper*. Opt. Express, 2008. **16**: p. 17420.
54. Fuller, F.D. and J.P. Ogilvie, *Experimental Implementations of Two-Dimensional Fourier Transform Electronic Spectroscopy*. Annual Review of Physical Chemistry, 2015. **66**(1): p. 667-690.
55. Zheng, H.B., et al., *Dispersion-free continuum two-dimensional electronic spectrometer*. Applied Optics, 2014. **53**(9): p. 1909-1917.
56. Al Haddad, A., et al., *Set-up for broadband Fourier-transform multidimensional electronic spectroscopy*. Optics Letters, 2015. **40**(3): p. 312-315.
57. CH, T., M. S, and W. TC, *Two-dimensional ultrafast Fourier transform spectroscopy in the deep ultraviolet*. Opt. Express, 2009. **17**: p. 18788.
58. N, K., et al., *Two-dimensional Fourier transform spectroscopy in the ultraviolet with sub-20 fs pump pulses and 250–720 nm supercontinuum probe*. New J. Phys., 2013. **15**: p. 085016.
59. U, S., et al., *Coherent two-dimensional ultraviolet spectroscopy in fully noncollinear geometry*. Opt. Lett., 2010. **35**: p. 4178.
60. JR, W., et al., *Solution conformation of 2-aminopurine dinucleotide determined by ultraviolet two-dimensional fluorescence spectroscopy*. New J. Phys., 2013. **15**: p. 025028.
61. BA, W. and M. AM, *Two-dimensional electronic spectroscopy in the ultraviolet wavelength range*. J. Phys. Chem. Lett., 2012. **3**: p. 2575.
62. BA, W., et al., *Toward two-dimensional photon echo spectroscopy with 200 nm laser pulses*. Opt. Express, 2013. **21**: p. 2118.
63. Hauri, C.P., et al., *Generation of intense, carrier-envelope phase-locked few-cycle laser pulses through filamentation*. Applied Physics B-Lasers and Optics, 2004. **79**(6): p. 673-677.
64. Zhang, T., et al., *Optical two-dimensional Fourier transform spectroscopy with active interferometric stabilization*. Optics Express, 2005. **13**(19): p. 7432-7441.
65. JD, H., C. Y, and J. DM, *Peak shapes in femtosecond 2D correlation spectroscopy*. Chem. Phys., 2001. **266**: p. 295.
66. ML, C., et al., *Ultrafast memory loss and energy redistribution in the hydrogen bond network of liquid H₂O*. Nature, 2005. **434**: p. 199.
67. T, B., et al., *Two-dimensional spectroscopy of electronic couplings in photosynthesis*. Nature, 2005. **434**: p. 625.
68. FD, F., et al., *Vibronic coherence in oxygenic photosynthesis*. Nat. Chem., 2014. **6**: p. 706.
69. E, C., et al., *Coherently wired light-harvesting in photosynthetic marine algae at ambient temperature*. Nature, 2010. **463**: p. 644.
70. Turner, D.B., et al., *Comparison of Electronic and Vibrational Coherence Measured by Two-Dimensional Electronic Spectroscopy*. The Journal of Physical Chemistry Letters, 2011. **2**(15): p. 1904-1911.
71. JD, H., F. AA, and J. DM, *Two-dimensional Fourier transform electronic spectroscopy*. J. Chem. Phys., 2001. **115**: p. 6606.

72. AD, B., et al., *A versatile ultrastable platform for optical multidimensional Fourier-transform spectroscopy*. Rev. Sci. Instrum., 2009. **80**: p. 073108.
73. Hybl, J.D., et al., *Two-dimensional electronic spectroscopy*. Chemical Physics Letters, 1998. **297**(3–4): p. 307-313.
74. Shim, S.-H. and M.T. Zanni, *How to turn your pump-probe instrument into a multidimensional spectrometer: 2D IR and Vis spectroscopies via pulse shaping*. Physical Chemistry Chemical Physics, 2009. **11**(5): p. 748-761.
75. Keusters, D., H.-S. Tan, and Warren, *Role of Pulse Phase and Direction in Two-Dimensional Optical Spectroscopy*. The Journal of Physical Chemistry A, 1999. **103**(49): p. 10369-10380.
76. SM, G., et al., *Heterodyne detection of the complete electric field of femtosecond four-wave mixing signals*. J. Opt. Soc. Am. B, 1998. **15**: p. 2338.
77. GD, G., D. G, and M. RJD, *Ultrafast heterodyne-detected transient-grating spectroscopy using diffractive optics*. J. Opt. Soc. Am. B, 1998. **15**: p. 1791.
78. JP, O., et al., *Dynamics of ligand escape in myoglobin: Q-band transient absorption and four-wave mixing studies*. J. Phys. Chem. B, 2002. **106**: p. 10460.
79. F, M., L. CN, and H. J, *Precise phasing of 2D-electronic spectra in a fully non-collinear phase-matching geometry*. Opt. Express, 2013. **21**: p. 15904.
80. AD, B., et al., *All-optical retrieval of the global phase for two-dimensional Fourier-transform spectroscopy*. Opt. Express, 2008. **16**: p. 18017.
81. EHG, B., G.-R. S, and H. P, *Phasing problem of heterodyne-detected two-dimensional infrared spectroscopy*. Opt. Lett., 2008. **33**: p. 2665.
82. L, L. and J. M, *Two-dimensional nonlinear optics using Fourier-transform spectral interferometry*. Opt. Lett., 1996. **21**: p. 564.
83. EM, G., et al., *Facile collection of two-dimensional electronic spectra using femtosecond pulse-shaping technology*. Opt. Express, 2007. **15**: p. 16681.
84. PF, T., et al., *Effects of chirp on two-dimensional Fourier transform electronic spectra*. Opt. Express, 2010. **18**: p. 11015.
85. ML, C., O. JP, and M. RJD, *Two-dimensional spectroscopy using diffractive optics based phased-locked photon echoes*. Chem. Phys. Lett., 2004. **386**: p. 184.
86. T, B., et al., *Phase-stabilized two-dimensional electronic spectroscopy*. J. Chem. Phys., 2004. **121**: p. 4221.
87. Prokhorenko, V.I., A.M. Nagy, and R.J.D. Miller, *Coherent control of the population transfer in complex solvated molecules at weak excitation. An experimental study*. The Journal of Chemical Physics, 2005. **122**(18): p. -.
88. Prokhorenko, V.I., A. Halpin, and R.J.D. Miller, *Coherently-controlled two-dimensional photon echo electronic spectroscopy*. Optics Express, 2009. **17**(12): p. 9764-9779.
89. IA, H., et al., *Two-dimensional electronic spectroscopy based on conventional optics and fast dual chopper data acquisition*. Rev. Sci. Instrum., 2014. **85**: p. 063103.
90. YZ, Z., et al., *Passively phase-stable, monolithic, all-reflective two-dimensional electronic spectroscopy based on a four-quadrant mirror*. Opt. Lett., 2013. **38**: p. 356.
91. JC, V., et al., *Coherently controlled ultrafast four-wave mixing spectroscopy*. J. Phys. Chem. A, 2007. **111**: p. 4873.

References

92. Shirakawa, A., I. Sakane, and T. Kobayashi, *Pulse-front-matched optical parametric amplification for sub-10-fs pulse generation tunable in the visible and near infrared*. Optics Letters, 1998. **23**(16): p. 1292-1294.
93. Cerullo, G., et al., *Sub-8-fs pulses from an ultrabroadband optical parametric amplifier in the visible*. Optics Letters, 1998. **23**(16): p. 1283-1285.
94. Shirakawa, A., et al., *Sub-5-fs visible pulse generation by pulse-front-matched noncollinear optical parametric amplification*. Applied Physics Letters, 1999. **74**(16): p. 2268-2270.
95. Ishii, N., et al., *Multimillijoule chirped parametric amplification of few-cycle pulses*. Optics Letters, 2005. **30**(5): p. 567-569.
96. Nisoli, M., S. De Silvestri, and O. Svelto, *Generation of high energy 10 fs pulses by a new pulse compression technique*. Applied Physics Letters, 1996. **68**(20): p. 2793-2795.
97. Sartania, S., et al., *Generation of 0.1-TW 5-fs optical pulses at a 1-kHz repetition rate*. Optics Letters, 1997. **22**(20): p. 1562-1564.
98. Pierre, A. and F.D. Louis, *The physics of attosecond light pulses*. Reports on Progress in Physics, 2004. **67**(6): p. 813.
99. Ganeev, R.A., et al., *High-order harmonic generation in fullerenes using few- and multi-cycle pulses of different wavelengths*. JOURNAL OF THE OPTICAL SOCIETY OF AMERICA B-OPTICAL PHYSICS, 2013. **30**: p. 7-12.
100. Durfee, C.G., et al., *Intense 8-fs pulse generation in the deep ultraviolet*. Optics Letters, 1999. **24**(10): p. 697-699.
101. Nagy, T. and P. Simon, *Generation of 200- μ J, sub-25-fs deep-UV pulses using a noble-gas-filled hollow fiber*. Optics Letters, 2009. **34**(15): p. 2300-2302.
102. Suda, A., et al., *Generation of sub-10-fs, 5-mJ-optical pulses using a hollow fiber with a pressure gradient*. Applied Physics Letters, 2005. **86**(11): p. 111116.
103. Nurhuda, M., et al., *Propagation dynamics of femtosecond laser pulses in a hollow fiber filled with argon: constant gas pressure versus differential gas pressure*. Journal of the Optical Society of America B, 2003. **20**(9): p. 2002-2011.
104. Zeek, E., et al., *Pulse compression by use of deformable mirrors*. Optics Letters, 1999. **24**(7): p. 493-495.
105. Baumert, T., et al., *Femtosecond pulse shaping by an evolutionary algorithm with feedback*. Applied Physics B, 1997. **65**(6): p. 779-782.
106. Beasley, D. and J. Heitkötter. *The Hitch-Hiker's Guide to Evolutionary Computation*. comp.ai.genetic [(FAQ)] 1999 April 1; Available from: <http://aiinfinance.com/gafaq.pdf>.
107. Holland, J.H., *Adaptation in Natural and Artificial Systems: An Introductory Analysis with Applications to Biology, Control and Artificial Intelligence*. 1992: MIT Press. 228.
108. Grefenstette, J.J., *Optimization of Control Parameters for Genetic Algorithms*. Systems, Man and Cybernetics, IEEE Transactions on, 1986. **16**(1): p. 122-128.
109. Trebino, R., *Frequency-Resolved Optical Gating: The Measurement of Ultrashort Laser Pulses*. Frequency-Resolved Optical Gating: The Measurement of Ultrashort Laser Pulses. 2002: Springer.

110. Sweetser, J.N., D.N. Fittinghoff, and R. Trebino, *Transient-grating frequency-resolved optical gating*. Optics Letters, 1997. **22**(8): p. 519-521.
111. Eichler, H.J., U. Klein, and D. Langhans, *Coherence time measurement of picosecond pulses by a light-induced grating method*. Applied physics, 1980. **21**(3): p. 215-219.
112. Tekavec, P.F., et al., *Effects of chirp on two-dimensional Fourier transform electronic spectra*. Optics Express, 2010. **18**(11): p. 11015-11024.
113. Jundt, C., et al., *Exciton dynamics in pentacene thin films studied by pump-probe spectroscopy*. Chemical Physics Letters, 1995. **241**(1-2): p. 84-88.
114. Gust, D., T.A. Moore, and A.L. Moore, *Solar Fuels via Artificial Photosynthesis*. Accounts of Chemical Research, 2009. **42**(12): p. 1890-1898.
115. Hasobe, T., *Supramolecular nanoarchitectures for light energy conversion*. Physical Chemistry Chemical Physics, 2010. **12**(1): p. 44-57.
116. Kalyanasundaram, K. and M. Graetzel, *Artificial photosynthesis: biomimetic approaches to solar energy conversion and storage*. Current Opinion in Biotechnology, 2010. **21**(3): p. 298-310.
117. Bram, O., et al., *Femtosecond UV Studies of the Electronic Relaxation Processes in Cytochrome c*. Journal of Physical Chemistry B, 2011. **115**(46): p. 13723-13730.
118. Bräm, O., et al., *Ultrafast UV and Visible Studies of the Electronic Relaxation Processes in Cytochrome C*. Journal of Physical Chemistry 2011(in press).
119. Shafizadeh, N., S. Sorgues, and B. Soep, *Observation of doubly ionised metalloporphyrins in the gas phase prepared by femtosecond ionisation*. Chemical Physics Letters, 2004. **391**(4-6): p. 380-384.
120. Sorgues, S., et al., *Femtosecond electronic relaxation of excited metalloporphyrins in the gas phase*. Journal of Chemical Physics, 2006. **124**(11): p. -.
121. Steiger, B., et al., *Femtosecond dynamics of dioxygen - Picket-fence cobalt porphyrins: Ultrafast release of O-2 and the nature of dative bonding*. Angewandte Chemie-International Edition, 2000. **39**(1): p. 257-+.
122. Gouterman, M., *Study of the Effects of Substitution on the Absorption Spectra of Porphin*. Journal of Chemical Physics, 1959. **30**(5): p. 1139-1161.
123. Gouterman, M., *Spectra of Porphyrins*. Journal of Molecular Spectroscopy, 1961. **6**(1): p. 138-&.
124. Gouterman, M., L.C. Snyder, and G.H. Wagniere, *Spectra of Porphyrins .2. 4 Orbital Model*. Journal of Molecular Spectroscopy, 1963. **11**(2): p. 108-&.
125. Akimoto, S., et al., *Excitation relaxation of zinc and free-base porphyrin probed by femtosecond fluorescence spectroscopy*. Chemical Physics Letters, 1999. **309**(3-4): p. 177-182.
126. Baskin, J.S., H.Z. Yu, and A.H. Zewail, *Ultrafast dynamics of Porphyrins in the condensed phase: I. Free base tetraphenylporphyrin*. Journal of Physical Chemistry A, 2002. **106**(42): p. 9837-9844.
127. Enescu, M., et al., *Femtosecond relaxation processes from upper excited states of tetrakis(N-methyl-4-pyridyl)porphyrins studied by transient absorption spectroscopy*. Physical Chemistry Chemical Physics, 2002. **4**(24): p. 6092-6099.

References

128. Marcelli, A., et al., *Excited-state absorption and ultrafast relaxation dynamics of porphyrin, diprotonated porphyrin, and tetraoxaporphyrin dication*. Journal of Physical Chemistry A, 2008. **112**(9): p. 1864-1872.
129. Bialkowski, B., et al., *The dynamics and origin of the unrelaxed fluorescence of free-base tetraphenylporphyrin*. Journal of Photochemistry and Photobiology a-Chemistry, 2012. **234**: p. 100-106.
130. Yeon, K.Y., D. Jeong, and S.K. Kim, *Intrinsic lifetimes of the Soret bands of the free-base tetraphenylporphine (H(2)TPP) and Cu(II)TPP in the condensed phase*. Chemical Communications, 2010. **46**(30): p. 5572-5574.
131. Rodriguez, J., C. Kirmaier, and D. Holten, *Time-Resolved and Static Optical-Properties of Vibrationally Excited Porphyrins*. Journal of Chemical Physics, 1991. **94**(9): p. 6020-6029.
132. Cannizzo, A., et al., *Femtosecond fluorescence upconversion setup with broadband detection in the ultraviolet*. Optics Letters, 2007. **32**(24): p. 3555-3557.
133. Zgrablic, G., et al., *Ultrafast excited state dynamics of the protonated Schiff base of all-trans retinal in solvents*. Biophysical Journal, 2005. **88**(4): p. 2779-2788.
134. Auböck, G., et al., *Femtosecond pump/supercontinuum-probe setup with 20 kHz repetition rate*. Review of Scientific Instruments, 2012. **83**(9): p. 093105.
135. Niu, Y.L., et al., *Theory of Excited State Decays and Optical Spectra: Application to Polyatomic Molecules*. Journal of Physical Chemistry A, 2010. **114**(30): p. 7817-7831.
136. Santoro, F., et al., *Effective method for the computation of optical spectra of large molecules at finite temperature including the Duschinsky and Herzberg-Teller effect: The Q(x) band of porphyrin as a case study*. Journal of Chemical Physics, 2008. **128**(22): p. -.
137. Diau, E.W.G., et al., *Tuning Spectral and Electrochemical Properties of Porphyrin-Sensitized Solar Cells*. Journal of Physical Chemistry C, 2010. **114**(27): p. 12018-12023.
138. Ohno, O., Y. Kaizu, and H. Kobayashi, *Delayed Fluorescence of Zinc Porphyrin in Polyvinyl-Alcohol) Film*. Bulletin of the Chemical Society of Japan, 1985. **58**(1): p. 62-64.
139. Ohno, O., Y. Kaizu, and H. Kobayashi, *Luminescence of Some Metalloporphins Including the Complexes of the Iiib Metal Group*. Journal of Chemical Physics, 1985. **82**(4): p. 1779-1787.
140. Chirvony, V.S., et al., *Comparative Study of the Photophysical Properties of Nonplanar Tetraphenylporphyrin and Octaethylporphyrin Diacids*. The Journal of Physical Chemistry B, 2000. **104**(42): p. 9909-9917.
141. Quimby, D.J. and F.R. Longo, *Luminescence Studies on Several Tetra-Arylporphins and Their Zinc Derivatives*. Journal of the American Chemical Society, 1975. **97**(18): p. 5111-5117.
142. Yu, H.Z., J.S. Baskin, and A.H. Zewail, *Ultrafast dynamics of porphyrins in the condensed phase: II. Zinc tetraphenylporphyrin*. Journal of Physical Chemistry A, 2002. **106**(42): p. 9845-9854.

143. Tripathy, U., et al., *Photophysics of Soret-excited tetrapyrroles in solution. I. Metalloporphyrins: MgTPP, ZnTPP, and CdTPP*. Journal of Physical Chemistry A, 2008. **112**(26): p. 5824-5833.
144. Rodriguez, J. and D. Holten, *Ultrafast Vibrational Dynamics of a Photoexcited Metalloporphyrin*. Journal of Chemical Physics, 1989. **91**(6): p. 3525-3531.
145. Mataga, N., et al., *Internal conversion and vibronic relaxation from higher excited electronic state of porphyrins: Femtosecond fluorescence dynamics studies*. Journal of Physical Chemistry B, 2000. **104**(17): p. 4001-4004.
146. Braem, O., et al., *A femtosecond fluorescence study of vibrational relaxation and cooling dynamics of UV dyes*. Physical Chemistry Chemical Physics, 2012. **14**(10): p. 3513-3519.
147. Saini, G.S.S., *Resonance Raman study of free-base tetraphenylporphine and its dication*. Spectrochimica Acta Part A: Molecular and Biomolecular Spectroscopy, 2006. **64**(4): p. 981-986.
148. Schlücker, S., et al., *Structural Investigations on Octaethylporphyrin Using Density Functional Theory and Polarization-Sensitive Resonance Coherent Anti-Stokes Raman Scattering Spectroscopy*. The Journal of Physical Chemistry A, 2001. **105**(41): p. 9482-9488.
149. Elsaesser, T. and W. Kaiser, *Vibrational and vibronic relaxation of large polyatomic molecules in liquids*. Annual review of physical chemistry, 1991. **42**(1): p. 83-107.
150. Foggi, P., et al., *Transient absorption and vibrational relaxation dynamics of the lowest excited singlet state of pyrene in solution*. The Journal of Physical Chemistry, 1995. **99**(19): p. 7439-7445.
151. Kovalenko, S.A., et al., *Cooling dynamics of an optically excited molecular probe in solution from femtosecond broadband transient absorption spectroscopy*. The Journal of Chemical Physics, 2001. **115**(7): p. 3256-3273.
152. Pigliucci, A., et al., *Investigation of the Influence of Solute–Solvent Interactions on the Vibrational Energy Relaxation Dynamics of Large Molecules in Liquids*. The Journal of Physical Chemistry A, 2007. **111**(28): p. 6135-6145.
153. Edwards, L., et al., *Porphyrins .17. Vapor Absorption Spectra and Redox Reactions - Tetraphenylporphins and Porphin*. Journal of Molecular Spectroscopy, 1971. **38**(1): p. 16-&.
154. Gentemann, S., et al., *Unusual picosecond $I(\pi, \pi^*)$ deactivation of ruffled nonplanar porphyrins*. Chemical Physics Letters, 1995. **245**(4–5): p. 441-447.
155. Bram, O., et al., *Polychromatic femtosecond fluorescence studies of metal-polypyridine complexes in solution*. Chemical Physics, 2012. **393**(1): p. 51-57.
156. Ishii, K., S. Takeuchi, and T. Tahara, *Pronounced Non-Condon Effect as the Origin of the Quantum Beat Observed in the Time-Resolved Absorption Signal from Excited-State cis-Stilbene*. The Journal of Physical Chemistry A, 2008. **112**(11): p. 2219-2227.
157. Dhar, L., J.A. Rogers, and K.A. Nelson, *Time-resolved vibrational spectroscopy in the impulsive limit*. Chemical Reviews, 1994. **94**(1): p. 157-193.
158. Jentzen, W., et al., *Ruffling in a Series of Nickel(II) meso-Tetrasubstituted Porphyrins as a Model for the Conserved Ruffling of the Heme of Cytochromes c*. Journal of the American Chemical Society, 1995. **117**(45): p. 11085-11097.

References

159. Sparks, L.D., et al., *Correlations between Raman frequencies and structure for planar and nonplanar metalloporphyrins*. Inorganic Chemistry, 1994. **33**(10): p. 2297-2302.
160. Jarzęcki, A.A. and T.G. Spiro, *Porphyrin Distortion from Resonance Raman Intensities of Out-of-Plane Modes: Computation and Modeling of N-Methylmesoporphyrin, a Ferrochelatase Transition State Analog*. The Journal of Physical Chemistry A, 2005. **109**(3): p. 421-430.
161. Czernuszewicz, R.S., X.Y. Li, and T.G. Spiro, *Nickel octaethylporphyrin ruffling dynamics from resonance Raman spectroscopy*. Journal of the American Chemical Society, 1989. **111**(18): p. 7024-7031.
162. Brennan, T.D., W.R. Scheidt, and J.A. Shelnutt, *New crystalline phase of (octaethylporphinato)nickel(II): effects of .pi.-.pi. interactions on molecular structure and resonance Raman spectra*. Journal of the American Chemical Society, 1988. **110**(12): p. 3919-3924.
163. Kumar, A.T.N., et al., *On the Rate Distribution Analysis of Kinetic Data Using the Maximum Entropy Method: Applications to Myoglobin Relaxation on the Nanosecond and Femtosecond Timescales*. The Journal of Physical Chemistry B, 2001. **105**(32): p. 7847-7856.
164. Kim, S.Y. and T. Joo, *Coherent Nuclear Wave Packets in Q States by Ultrafast Internal Conversions in Free Base Tetraphenylporphyrin*. The journal of physical chemistry letters, 2015. **6**(15): p. 2993-2998.
165. Ye, X., A. Demidov, and P.M. Champion, *Measurements of the Photodissociation Quantum Yields of MbNO and MbO2 and the Vibrational Relaxation of the Six-Coordinate Heme Species*. Journal of the American Chemical Society, 2002. **124**(20): p. 5914-5924.
166. Xu, J., et al., *Excited state structural dynamics and Herzberg–Teller coupling of tetraphenylporphine explored via resonance Raman spectroscopy and density functional theory calculation*. Spectrochimica Acta Part A: Molecular and Biomolecular Spectroscopy, 2010. **75**(5): p. 1381-1387.
167. Minaev, B., et al., *Density functional theory study of vibronic structure of the first absorption Qx band in free-base porphin*. Spectrochimica Acta Part A: Molecular and Biomolecular Spectroscopy, 2006. **65**(2): p. 308-323.
168. Yin, J., et al., *Photodecay dynamics of octaethylporphine in the condensed phase explored via resonance Raman spectroscopy and density functional theory calculation*. Spectrochimica Acta Part A: Molecular and Biomolecular Spectroscopy, 2011. **78**(5): p. 1416-1423.
169. Singh, A. and L.W. Johnson, *Single site electronic spectroscopy of free base octaethylporphyrin, octaethylchlorin and their diacids in n-octane at 298 K and 7 K*. Spectrochimica Acta Part A: Molecular and Biomolecular Spectroscopy, 2006. **64**(3): p. 761-770.
170. Champion, P.M., et al., *Rapid timescale processes and the role of electronic surface coupling in the photolysis of diatomic ligands from heme proteins*. Faraday Discussions, 2004. **127**(0): p. 123-135.
171. Gruia, F., et al., *Investigations of Vibrational Coherence in the Low-Frequency Region of Ferric Heme Proteins*. Biophysical Journal, 2008. **94**(6): p. 2252-2268.

172. Gruia, F., et al., *Low Frequency Spectral Density of Ferrous Heme: Perturbations Induced by Axial Ligation and Protein Insertion*. *Biophysical Journal*, 2007. **93**(12): p. 4404-4413.
173. Schweitzer-Stenner, R., et al., *Raman dispersion spectroscopy on the highly saddled nickel(II)-octaethyltetraphenylporphyrin reveals the symmetry of nonplanar distortions and the vibronic coupling strength of normal modes*. *The Journal of Chemical Physics*, 1997. **107**(6): p. 1794-1815.
174. Prendergast, K. and T.G. Spiro, *Core expansion, ruffling, and doming effects on metalloporphyrin vibrational frequencies*. *Journal of the American Chemical Society*, 1992. **114**(10): p. 3793-3801.
175. Maity, D.K., R.L. Bell, and T.N. Truong, *Mechanism and Quantum Mechanical Tunneling Effects on Inner Hydrogen Atom Transfer in Free Base Porphyrin: A Direct ab Initio Dynamics Study*. *Journal of the American Chemical Society*, 2000. **122**(5): p. 897-906.
176. Butenhoff, T.J. and C.B. Moore, *Hydrogen atom tunneling in the thermal tautomerism of porphine imbedded in a n-hexane matrix*. *Journal of the American Chemical Society*, 1988. **110**(25): p. 8336-8341.
177. Limbach, H.H., et al., *Proton-transfer kinetics in solids: tautomerism in free base porphines by nitrogen-15 CPMAS NMR*. *Journal of the American Chemical Society*, 1984. **106**(14): p. 4059-4060.
178. Limbach, H.H., J. Hennig, and J. Stulz, *IR-spectroscopic study of isotope effects on the NH/ND-stretching bands of meso-tetraphenylporphine and vibrational hydrogen tunneling*. *The Journal of Chemical Physics*, 1983. **78**(9): p. 5432-5436.
179. Kim, D. and A. Osuka, *Photophysical Properties of Directly Linked Linear Porphyrin Arrays*. *The Journal of Physical Chemistry A*, 2003. **107**(42): p. 8791-8816.
180. Tsuda, A., H. Furuta, and A. Osuka, *Completely Fused Diporphyrins and Triporphyrin*. *Angewandte Chemie International Edition*, 2000. **39**(14): p. 2549-2552.
181. Englman, R. and J. Jortner, *ENERGY GAP LAW FOR RADIATIONLESS TRANSITIONS IN LARGE MOLECULES*. *Molecular Physics*, 1970. **18**(2): p. 145-&.
182. Caspar, J.V. and T.J. Meyer, *Application of the energy gap law to nonradiative, excited-state decay*. *The Journal of Physical Chemistry*, 1983. **87**(6): p. 952-957.
183. Cho, H.S., et al., *Photophysical Properties of Porphyrin Tapes*. *Journal of the American Chemical Society*, 2002. **124**(49): p. 14642-14654.
184. McEwan, K.J., et al., *Reverse Saturable Absorption in the Near-Infrared by Fused Porphyrin Dimers*. *Advanced Materials*, 2004. **16**(21): p. 1933-1935.
185. Frampton, M.J., et al., *Synthesis and near-infrared luminescence of a deuterated conjugated porphyrin dimer for probing the mechanism of non-radiative deactivation*. *Organic & Biomolecular Chemistry*, 2007. **5**(7): p. 1056-1061.
186. Roberts, D.A., et al., *Synthesis and Ultrafast Excited-State Dynamics of Zinc and Palladium Triply Fused Diporphyrins*. *Journal of Physical Chemistry A*, 2012. **116**(30): p. 7898-7905.
187. Cornil, J., et al., *Interchain Interactions in Organic π -Conjugated Materials: Impact on Electronic Structure, Optical Response, and Charge Transport*. *Advanced Materials*, 2001. **13**(14): p. 1053-1067.

References

188. Ikeda, T., N. Aratani, and A. Osuka, *Synthesis of Extremely π -Extended Porphyrin Tapes from Hybrid meso-meso Linked Porphyrin Arrays: An Approach Towards the Conjugation Length*. Chemistry – An Asian Journal, 2009. **4**(8): p. 1248-1256.
189. Diev, V.V., et al., *Fused Pyrene–Diporphyrins: Shifting Near-Infrared Absorption to 1.5 μm and Beyond*. Angewandte Chemie, 2010. **122**(32): p. 5655-5658.
190. Cheng, Y.Y., et al., *Kinetic Analysis of Photochemical Upconversion by Triplet–Triplet Annihilation: Beyond Any Spin Statistical Limit*. The Journal of Physical Chemistry Letters, 2010. **1**(12): p. 1795-1799.
191. Cheng, Y.Y., et al., *On the efficiency limit of triplet-triplet annihilation for photochemical upconversion*. Physical Chemistry Chemical Physics, 2010. **12**(1): p. 66-71.
192. Partee, J., et al., *Delayed Fluorescence and Triplet-Triplet Annihilation in π -Conjugated Polymers*. Physical Review Letters, 1999. **82**(18): p. 3673-3676.
193. Schulze, T.F., et al., *Efficiency Enhancement of Organic and Thin-Film Silicon Solar Cells with Photochemical Upconversion*. The Journal of Physical Chemistry C, 2012. **116**(43): p. 22794-22801.
194. Nattestad, A., et al., *Dye-Sensitized Solar Cell with Integrated Triplet–Triplet Annihilation Upconversion System*. The Journal of Physical Chemistry Letters, 2013. **4**(12): p. 2073-2078.
195. Zhao, J., S. Ji, and H. Guo, *Triplet-triplet annihilation based upconversion: from triplet sensitizers and triplet acceptors to upconversion quantum yields*. RSC Advances, 2011. **1**(6): p. 937-950.
196. Johnson, P.J.M., V.I. Prokhorenko, and R.J.D. Miller, *Stable UV to IR supercontinuum generation in calcium fluoride with conserved circular polarization states*. Optics Express, 2009. **17**(24): p. 21488-21496.
197. Gruebele, M. and A.H. Zewail, *Femtosecond wave packet spectroscopy: Coherences, the potential, and structural determination*. The Journal of Chemical Physics, 1993. **98**(2): p. 883-902.
198. Sebastian, S., et al., *Generalized magic angle for time-resolved spectroscopy with laser pulses of arbitrary ellipticity*. Journal of Physics B: Atomic, Molecular and Optical Physics, 2014. **47**(12): p. 124014.
199. Huber, R., et al., *Noncollinear optical parametric amplifiers with output parameters improved by the application of a white light continuum generated in CaF₂*. Optics Communications, 2001. **194**(4–6): p. 443-448.
200. van Stokkum, I.H.M., D.S. Larsen, and R. van Grondelle, *Global and target analysis of time-resolved spectra (vol 1658, pg 82, 2004)*. Biochimica Et Biophysica Acta-Bioenergetics, 2004. **1658**(3): p. 262-262.
201. DeSa, R.J. and I.B.C. Matheson, *A practical approach to interpretation of singular value decomposition results*. Numerical Computer Methods, Pt E, 2004. **384**: p. 1-8.
202. Kasha, M., *ENERGY TRANSFER MECHANISMS AND MOLECULAR EXCITON MODEL FOR MOLECULAR AGGREGATES*. Radiation Research, 1963. **20**(1): p. 55-&.
203. Kasha, M., H.R. Rawls, and A. El-Bayoumi, *The exciton model in molecular spectroscopy*. Pure and Applied Chemistry, 1965. **11**(3-4): p. 371-392.

204. Yamaguchi, Y., *Time-dependent density functional calculations of fully π -conjugated zinc oligoporphyrins*. The Journal of Chemical Physics, 2002. **117**(21): p. 9688-9694.
205. Pedersen, T.G., et al., *Theoretical study of conjugated porphyrin polymers*. Thin Solid Films, 2005. **477**(1–2): p. 182-186.
206. Akimoto, S., et al., *Excitation relaxation of zinc and free-base porphyrin probed by femtosecond fluorescence spectroscopy*. Chemical Physics Letters, 1999. **309**(3–4): p. 177-182.
207. Baskin, J.S., H.-Z. Yu, and A.H. Zewail, *Ultrafast Dynamics of Porphyrins in the Condensed Phase: I. Free Base Tetraphenylporphyrin \dagger* . The Journal of Physical Chemistry A, 2002. **106**(42): p. 9837-9844.
208. Yu, H.-Z., J.S. Baskin, and A.H. Zewail, *Ultrafast Dynamics of Porphyrins in the Condensed Phase: II. Zinc Tetraphenylporphyrin \dagger* . The Journal of Physical Chemistry A, 2002. **106**(42): p. 9845-9854.
209. Rodriguez, J., C. Kirmaier, and D. Holten, *Time-resolved and static optical properties of vibrationally excited porphyrins*. The Journal of Chemical Physics, 1991. **94**(9): p. 6020-6029.
210. Kim, P., et al., *Excited-state energy relaxation dynamics of triply linked Zn(ii) porphyrin arrays*. Chemical Communications, 2011. **47**(15): p. 4433-4435.
211. Kobayashi, T., K.D. Straub, and P.M. Rentzepis, *ENERGY RELAXATION MECHANISM IN Ni(II), Pd(II), Pt(II) and Zn(II) PORPHYRINS*. Photochemistry and Photobiology, 1979. **29**(5): p. 925-931.
212. Benoist D'azy, O., R. López-Delgado, and A. Tramer, *No fluorescence decay from low-lying electronic states excited into single vibronic levels with synchrotron radiation*. Chemical Physics, 1975. **9**(3): p. 327-338.
213. Ponterini, G., et al., *Comparison of radiationless decay processes in osmium and platinum porphyrins*. Journal of the American Chemical Society, 1983. **105**(14): p. 4639-4645.
214. Bansal, A.K., et al., *Absorption and emission spectroscopic characterization of platinum-octaethyl-porphyrin (PtOEP)*. Chemical Physics, 2006. **330**(1–2): p. 118-129.
215. Baldo, M.A., et al., *Highly efficient phosphorescent emission from organic electroluminescent devices*. Nature, 1998. **395**(6698): p. 151-154.
216. Ha-Thi, M.-H., et al., *An Efficient Indirect Mechanism for the Ultrafast Intersystem Crossing in Copper Porphyrins*. The Journal of Physical Chemistry A, 2013. **117**(34): p. 8111-8118.
217. Sorgues, S., et al., *Femtosecond electronic relaxation of excited metalloporphyrins in the gas phase*. Journal of Chemical Physics, 2006. **124**(11).
218. Fidler, H., M. Rini, and E.T.J. Nibbering, *The Role of Large Conformational Changes in Efficient Ultrafast Internal Conversion: Deviations from the Energy Gap Law*. Journal of the American Chemical Society, 2004. **126**(12): p. 3789-3794.
219. Dosche, C., et al., *Deuteration effects on the vibronic structure of the fluorescence spectra and the internal conversion rates of triangular [4]phenylene*. Physical Chemistry Chemical Physics, 2004. **6**(24): p. 5476-5483.

References

220. Doffek, C., et al., *Breakdown of the Energy Gap Law in Molecular Lanthanoid Luminescence: The Smallest Energy Gap Is Not Universally Relevant for Nonradiative Deactivation*. Inorganic Chemistry, 2014. **53**(7): p. 3263-3265.
221. Freed, K.F., *Radiationless transitions in molecules*. Accounts of Chemical Research, 1978. **11**(2): p. 74-80.
222. Kim, D., et al., *Comparative photophysics of platinum(II) and platinum(IV) porphyrins*. Journal of the American Chemical Society, 1984. **106**(14): p. 4015-4017.
223. Yamaki, T. and K. Nobusada, *Theoretical Study of Metal–Ligand Bonds in Pb(II) Porphyrins*. The Journal of Physical Chemistry A, 2003. **107**(13): p. 2351-2355.
224. Cannizzo, A., et al., *Femtosecond Fluorescence and Intersystem Crossing in Rhenium(I) Carbonyl–Bipyridine Complexes*. Journal of the American Chemical Society, 2008. **130**(28): p. 8967-8974.
225. Chergui, M., *On the interplay between charge, spin and structural dynamics in transition metal complexes*. Dalton Transactions, 2012. **41**(42): p. 13022-13029.
226. Rodriguez, J. and D. Holten, *Ultrafast vibrational dynamics of a photoexcited metalloporphyrin*. The Journal of Chemical Physics, 1989. **91**(6): p. 3525-3531.
227. Rodriguez, J., C. Kirmaier, and D. Holten, *Optical properties of metalloporphyrin excited states*. Journal of the American Chemical Society, 1989. **111**(17): p. 6500-6506.
228. Yu, H.Z., et al., *Femtosecond dynamics of metalloporphyrins: electron transfer and energy redistribution*. Chemical Physics Letters, 1998. **293**(1–2): p. 1-8.
229. Cho, S., et al., *Electron delocalization in various triply linked zinc(ii) porphyrin arrays: role of antiaromatic junctions between aromatic porphyrins*. Physical Chemistry Chemical Physics, 2011. **13**(36): p. 16175-16181.
230. Monguzzi, A., et al., *Upconversion-induced fluorescence in multicomponent systems: Steady-state excitation power threshold*. Physical Review B, 2008. **78**(19): p. 195112.
231. Singh-Rachford, T.N., et al., *Supramolecular-Chromophore-Sensitized Near-Infrared-to-Visible Photon Upconversion*. Journal of the American Chemical Society, 2010. **132**(40): p. 14203-14211.
232. Zhang, B., et al., *Extending the Bandwidth of Reverse Saturable Absorption in Platinum Complexes Using Two-Photon-Initiated Excited-State Absorption*. ACS Applied Materials & Interfaces, 2013. **5**(3): p. 565-572.

Published work

Set-up for broadband Fourier-transform multidimensional electronic spectroscopy

A. Al Haddad, A. Chauvet, J. Ojeda, C. Arrell, F. van Mourik, G. Auböck, and M. Chergui*

Laboratoire de Spectroscopie Ultrarapide, École Polytechnique Fédérale de Lausanne, ISIC-FSB, CH-1015 Lausanne, Switzerland

*Corresponding author: majed.chergui@epfl.ch

Received September 29, 2014; revised December 5, 2014; accepted December 5, 2014;
posted December 8, 2014 (Doc. ID 223961); published January 20, 2015

We present a compact passively phase-stabilized ultra-broadband 2D Fourier transform setup. A gas (argon)-filled hollow core fiber pumped by an amplified Ti:Al₂O₃ laser is used as a light source providing spectral range spanning from 420 to 900 nm. Sub-10-fs pulses were obtained using a deformable mirror-based pulse shaper. We probe the nonlinear response of Rhodamine 101 using 90 nm bandwidth and resolve vibrational coherences of 150 fs period in the ground state. © 2015 Optical Society of America

OCIS codes: (260.0260) Physical optics; (300.6300) Spectroscopy, Fourier transforms; (300.6530) Spectroscopy, ultrafast; (320.7110) Ultrafast nonlinear optics.

<http://dx.doi.org/10.1364/OL.40.000312>

Coherent multidimensional spectroscopy is an analogue of two-dimensional (2D) NMR and is a powerful technique to resolve couplings between different chromophores [1–3]. Optical 2D spectroscopy evolved over years from using limited wavelength ranges accessible using stable oscillators [4] and infrared sources [5,6], into the visible regime using optical parametric amplifiers (OPA) [7,8], and more recently, the ultraviolet (UV) [9–11]. These experiments had in common the use of noncollinear OPA (NOPA) systems to generate the excitation pulses that are limited in bandwidth to several tens of nanometers. Studying complex systems requires addressing several electronic states simultaneously, and this often requires large spectral bandwidth spanning tens to hundreds of nanometers not accessible by NOPAs. The recent advancement of light sources generating continua in inert gases [12,13] allows for the realization of ultra-broadband 2D setups [14]. Here we present a compact passively phase-stabilized 2D setup using only conventional optics in a boxcar geometry that can perform measurements using near Fourier-limit ultra-broadband pulses in the visible range as well as in the UV with minimal modifications.

A cryogenically cooled Ti:Al₂O₃ regenerative amplifier tunable from 3 to 15 kHz provides 800-nm, sub-50-fs pulses of 1–3 mJ. The laser output is used to pump a 1.1-m long 260- μ m diameter hollow core fiber (Imperial Consultants) filled with 3 bars differential pressure of argon. A pressure gradient along the fiber is produced by pumping the fiber entrance with a scroll pump, achieving a base pressure of $\approx 5 \times 10^{-1}$ mbar while at the fiber exit 3 bar of argon is applied. This pressure gradient allows the decreasing intensity profile along the fiber to be matched with and increase gas pressure, thus allowing a higher transmission before plasma formation in the gas produces instabilities in the output.

Part of the laser output (≈ 0.5 mJ) is coupled into the fiber using a 75-cm concave mirror, causing self-phase modulation and spectral broadening due to high intensity coupling through a confined mode. By tuning the coupled intensity, pressure, and the pulse duration, the generated

continuum can span from 420 to 900 nm (Fig. 1), while pumping the fiber with the second harmonic of the laser gives us access to the 360–450-nm spectral range [15]. The advantages of the hollow core fiber, compared to conventionally used NOPA, resides in a flatter spectrum over a large spectral range, a TEM₀₀ spatial mode, and high output intensity simplifying the use of pulse shapers. In comparison to the light continuum generated by filamentation in a gas cell, the output of the hollow-core fiber has higher inherent pointing stability and is spectrally smoother output [12,13,16]. Furthermore, the ability to differentially pump hollow core fibers increases transmission for a set broadening as compared to a filament.

A home-built deformable mirror (DM) based pulse shaper is used to compress the output of the fiber to near Fourier-limit pulses using the geometry (Fig. 2(b)) proposed by Vdovin et al. [17]. A 3.3-cm-long DM (OKO tech) is positioned in the Fourier plane of a folded 4 f zero dispersion stretcher. The stretcher consists of a 300 grooves/mm grating blazed for 550 nm and a 27 cm focal

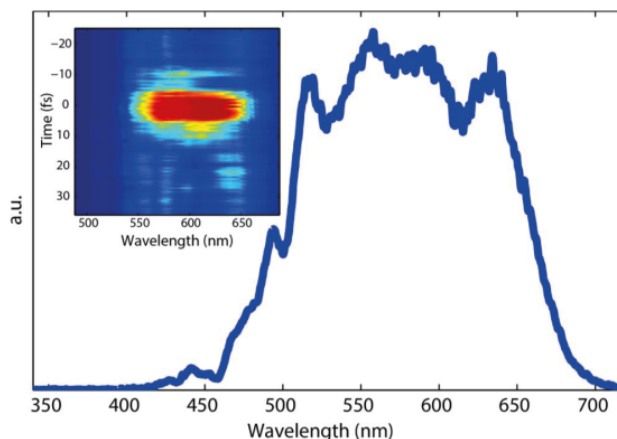


Fig. 1. Accessible spectrum of the hollow core fiber pumped 0.5-mJ, 55-fs pulses centered at 790 nm. (b) shows a TG-FROG autocorrelation trace of the selected spectrum from 480 to 685 nm with a flat spectral phase.

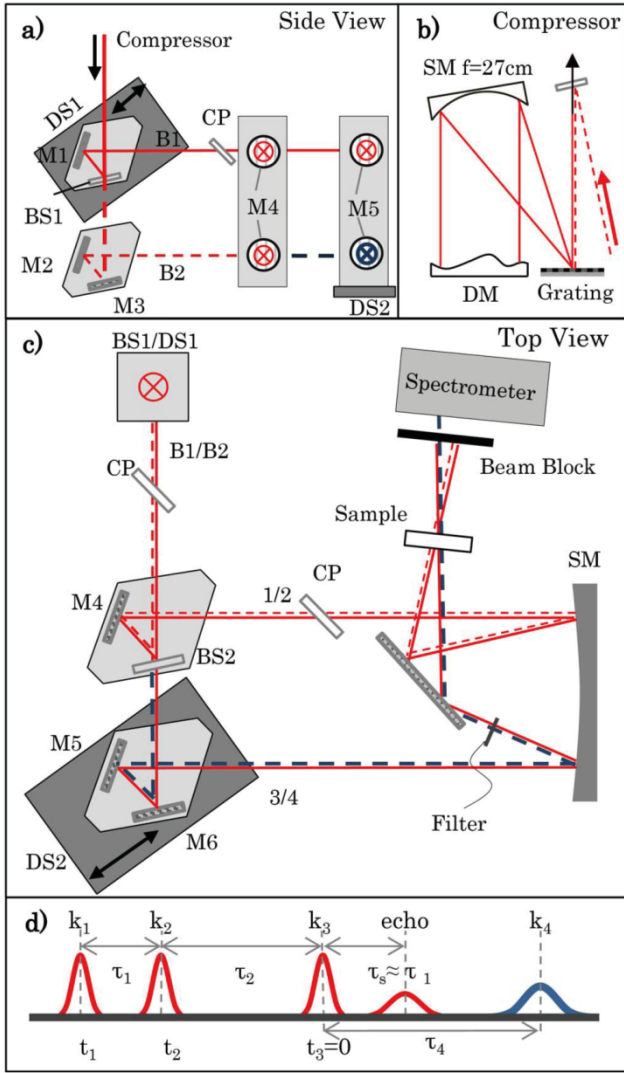


Fig. 2. Schematic drawing of the setup. (a) Side view showing the metallic holders and the spitting of the pulses. (b) Pulse shaper schematic showing the grating, deformable mirror DM, and a 27 cm spherical mirror SM. (c) Top view of the setup showing the stages and the path of the 4 (black) beams through the sample and into the spectrometer. (d) Generated pulse sequence.

length mirror allowing to fill the whole DM surface with a spectral range of about 300 nm visible light. After spectral recombination, the beam is sent downward toward the optical table into BS1 splitting it into two identical parts (beam 1/2 and 3/4) as shown in Fig. 2(a). A delay stage DS1 is used to move BS1 and M1 at 45° angle (along the vector direction in Fig. 2) with respect to the incoming beam creating a path difference between the beam pairs B1 and B2. Another set of metallic BSs (BS2) are used to split B1 and B2 into 4 identical beams, such that we can use the first three as excitation pulses (red) and the fourth as a local oscillator (black) as shown in Fig. 2(c). Mirrors M4 and M6 are mounted on DS2 moving at 45° angle creating the time difference between the pulse pairs 1/2 and 3/4. Glass plates of the same thickness as the BS are added in the path of the beams reflected off the BS to compensate for the delay due to its

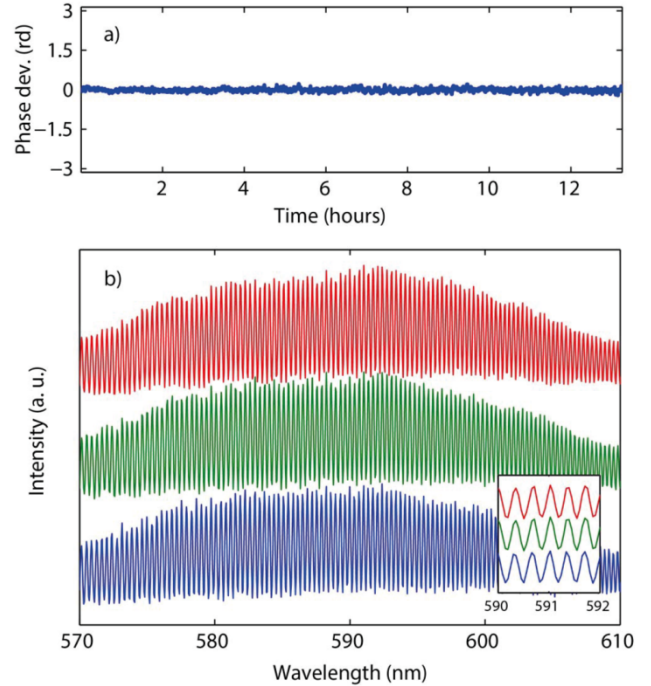


Fig. 3. Phase stability measurements. (a) Phase deviation calculated from the spectral interference between third-order nonlinear signal generated by a thin glass plate and the local oscillator was recorded every second over 12 h. (b) Cuts from different 2D spectra take over multiple 2D scans (6 h apart) showing stability of the fringes and reproducibility of the general shape.

substrate, and more importantly for the dispersion, which is crucial for broadband pulses. The compensation plates (CP) are set at a specific angle adjusted to minimize the spectral phase difference between the three beams, which is measured by spectral interferometry.

In order to create the desired pulse sequence [Fig. 2(d)], combination of movement of DS1 and DS2 is needed. A standard spherical mirror ($f = 40$ cm) focuses the four beams onto the sample via a folding mirror and with a focal spot of 80 μm in diameter. The spectral interferograms of pulses 1 and 2 for different positions of DS 2 and pulses 1 and 3 for different positions of DS1 are sent via a single-mode fiber to a 0.5-m imaging spectrograph and a cooled 400 \times 1600 CCD camera. The FFT analysis of the interferograms gives a direct relationship between time delay and motor position.

With the boxcar geometry used, the generated photon echo is emitted in the same direction as beam 4, due to the phase matching condition $k_s = -k_1 + k_2 + k_3$. A 2-mm-thick variable density filter is placed in the path of the local oscillator to attenuate its intensity, and to delay it by about $\tau_4 = 3.2$ ps. As seen in Fig. 3, the resulting interference fringes are well resolved. The filter is positioned between the spherical mirror and the sample to displace the focal spot on the sample, thus avoiding overlap with pulses 1 to 3, while the beam remains parallel to its original path. This is required to prevent the local oscillator from containing any undesired pump-probe signals [7].

Optimum pulse compression at the sample position is obtained using the standard MATLAB genetic-algorithm

optimization method to control the actuators of the DM [18,19]. The genetic algorithm uses the spectrally resolved second-harmonic (SH) signal generated by a 10- μm BBO placed at the sample position as a feedback. A 10- μm -thick BBO allows the doubling of a relatively broad pulse of up to 100 nm in bandwidth, but not enough for broader pulses due to phase matching conditions. The efficiency of the SH signal is highly dependent on the phase matching angle, leading to a very high efficiency in the center of the spectrum and relatively low on the edges. This will lead to a good optimization for the center of the spectrum while leaving the wings poorly optimized. To overcome this limitation, the SH signal is spectrally resolved and multiplied by a wavelength dependent digital filter function (inverse of the phase match curve) before integration in order to optimize for all doubled frequencies with equal weight. The pulses are then characterized using transient grating frequency-resolved optical gating (TG-FROG) performed in the 2D setup by focusing three beams onto a 0.1-mm microscope slide and recording the TG signal. Traces were analyzed using FROG version 3.2.4 (Femtisoft Technologies) to calculate the phase and pulse duration. For a 120-nm pulse centered around 590 nm, we obtain durations of 9 fs full width half-maximum (FWHM), while the expected Fourier limit is 5 fs (Fig. 1 inset).

For determining a complete four-wave mixing signal for a specific population time T , both delays are used to scan the time difference between pulses 1 and 2 by steps of 0.2 fs between the signal field and the local oscillator recording spectral interferograms at every step. High interferometric phase stability is required since the signal phase depends directly on the timing of arrival of the three excitation pulses. Additionally, the fringe pattern also depends on the local oscillator phase as shown in the following relationship [7]:

$$\varphi_{si} = \varphi_{LO} - \varphi_s = \varphi_{LO} - i\omega_0(-t_1 + t_2 + t_3): \quad (1)$$

The geometry of our setup uses the same technique as Selig et al. [8] where pulses are paired such that no individual pulse hits an individual mirror. As shown in Fig. 2, mirrors and BS2 for beam pairs 1/3, and 2/4 are mounted on the same metallic holders. Any path variation of beams 1 or 2 causing a change in their arrival time Δt_1 or Δt_2 , will cause an opposite variation to its pair 3 or 4, respectively, changing the arrival time by $-\Delta t_1$ or $-\Delta t_2$. Therefore, the total phase variation of the four beams cancels out:

$$\omega_0(\Delta t_1 - \Delta t_3 + \Delta t_2 - \Delta t_4) = 0; \quad (2)$$

and the recorded spectral fringes are stable except from negligible air drifts that may affect the beams independently. To enhance the phase stability, the geometry used to split the beams and introducing delays at the same time makes the set-up very compact with minimal optical components. The absolute time and phase between the local oscillator and the signal are adjusted by comparing the sum of the absorptive 2D data along the probe axis with the pump-probe (PP) data (projection slice theorem) recorded on the same actual setup [2]. Automated

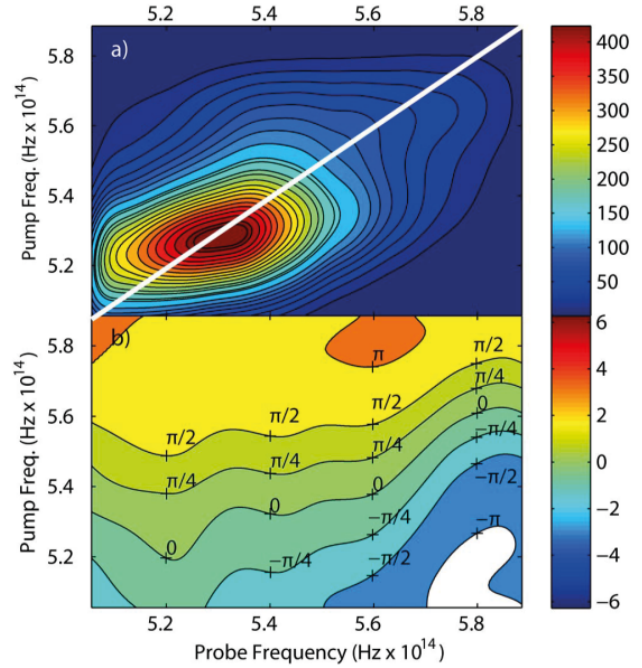


Fig. 4. (a) Absolute 2D spectrum of Rhodamine 101 at 100 fs showing the diagonal peaks. (b) Contour plot of the phase showing a stable phase along the diagonal peaks.

beam shutters are set in the path of the three pump beams and used to remove scattering terms [7].

In order to assess the stability of the setup, a photon echo signal is generated by placing a 100- μm glass plate in the sample position and setting the coherence and population time to zero. Spectral interference between the nonlinear signal and LO is recorded every second for more than 13 h. The mean phase deviation was calculated using inverse Fourier transform. Figure 3(a) shows that over the 13 h of measurements, we obtain a shot-to-shot (0.2 s accumulation per shot) stability of $\lambda/60$ at 540 nm, while there was no noticeable long-term drift. This long-term stability allows for the systematic phasing correction of the 2D data spectra taken over multiple hours.

To test the accuracy of the setup, 2D measurements were performed on a test system, Rhodamine 101 in ethanol in a 0.1-mm flow cell, which has been intensely studied previously and is known to exhibit vibrational coherences that could be triggered with such short pulses [19,20]. Pulses with 90-nm bandwidth centered at 550 nm were compressed to 7 fs and used for excitation to perform 2D measurements, as well as transient absorption measurements. Interferograms were taken at a specific time delay from every 2D scan and compared to each other. The phase was highly stable even though the stages were repeatedly moving for hours as shown in Fig. 3(b). An example of a 2D spectrum at 100-fs population time is shown in Fig. 4(a). The signal is a positive peak along the diagonal axis caused by ground state bleach, with a pronounced elongation indicative of spectral inhomogeneity. Analysis of the 2D spectra and integrating over a 10 nm window around the peak (570 nm) shows an oscillation of 150-fs period decaying within the first picosecond (Fig. 5). The same oscillations were also observed in the pump-probe measurements performed

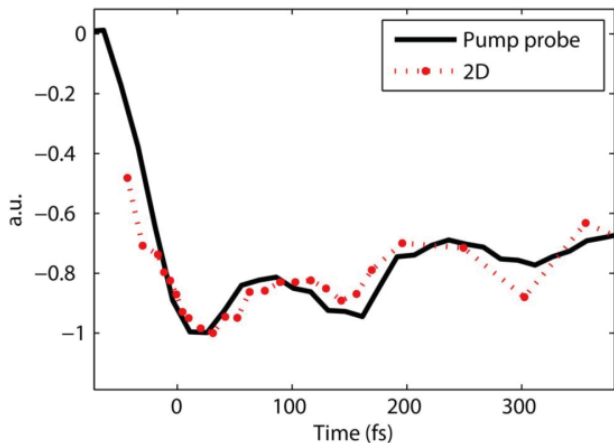


Fig. 5. Oscillations detected in the pump probe data and 2D spectra showing 150 fs period.

on the 2D setup and on an independent setup using sub-30-fs pump pulses centered around 580 nm (Fig. 5) [20].

In summary, a hollow core fiber was used to generate an ultra-broadband pulse for a passively phase-stabilized 2D visible spectroscopy using all conventional optics. Pulses were compressed to near Fourier limit using a deformable mirror based pulse shaper yielding 7-fs FWHM pulses. Short- and long-term phase stability was achieved allowing for measurements over long time periods.

This work was supported by the Swiss NSF via the NCCR: MUST as well by the FP7 Marie Curie COFUND.

References

1. S. Mukamel, *Annu. Rev. Phys. Chem.* 51, 691 (2000).
2. D. M. Jonas, *Annu. Rev. Phys. Chem.* 54, 425 (2003).
3. M. Cho, *Chem. Rev.* 108, 1331 (2008).
4. J. D. Hybl, A. W. Albrecht, S. M. Gallagher Faeder, and D. M. Jonas, *Chem. Phys. Lett.* 297, 307 (1998).
5. P. Hamm, M. Lim, and R. M. Hochstrasser, *J. Phys. Chem. B* 102, 6123 (1998).
6. S. Woutersen and P. Hamm, *J. Phys. Chem. B* 104, 11316 (2000).
7. T. Brixner, T. Mancal, I. V. Stiopkin, and G. R. Fleming, *J. Chem. Phys.* 121, 4221 (2004).
8. U. Selig, F. Langhojer, F. Dimler, T. Lohrig, C. Schwarz, B. Giesecking, and T. Brixner, *Opt. Lett.* 33, 2851 (2008).
9. U. Selig, C. F. Schleussner, M. Foerster, F. Langhojer, P. Nuernberger, and T. Brixner, *Opt. Lett.* 35, 4178 (2010).
10. G. Auböck, C. Consani, F. van Mourik, and M. Chergui, *Opt. Lett.* 37, 2337 (2012).
11. B. A. West and A. M. Moran, *J. Phys. Chem. Lett.* 3, 2575 (2012).
12. C. P. Hauri, W. Kornelis, F. W. Helbing, A. Heinrich, A. Couairon, A. Mysyrowicz, J. Biegert, and U. Keller, *Appl. Phys. B* 79, 673 (2004).
13. J. S. Robinson, C. A. Haworth, H. Teng, R. A. Smith, J. P. Marangos, and J. W. G. Tisch, *Appl. Phys. B Lasers Opt.* 85, 525 (2006).
14. H. B. Zheng, J. R. Caram, P. D. Dahlberg, B. S. Rolczynski, S. Viswanathan, D. S. Dolzhenkov, A. Khadivi, D. V. Talapin, and G. S. Engel, *Appl. Opt.* 53, 1909 (2014).
15. J. Liu, K. Okamura, Y. Kida, T. Teramoto, and T. Kobayashi, *Opt. Express* 18, 20645 (2010).
16. J. Kasparian, P. Béjot, J.-P. Wolf, and J. M. Dudley, *Opt. Express* 17, 12070 (2009).
17. E. Zeek, K. Maginnis, S. Backus, U. Russek, M. Murnane, G. Mourou, H. Kapteyn, and G. Vdovin, *Opt. Lett.* 24, 493 (1999).
18. T. Baumert, T. Brixner, V. Seyfried, M. Strehle, and G. Gerber, *Appl Phys B* 65, 779 (1997).
19. D. Beasley and J. Heitkötter, *The Hitch-Hiker's Guide to Evolutionary Computation*, <http://aiinfinance.com/gafaq.pdf>.
20. G. Auböck, C. Consani, R. Monni, A. Cannizzo, F. van Mourik, and M. Chergui, *Rev. Sci. Instrum.* 83, 093105 (2012).



Cite this: *Phys. Chem. Chem. Phys.*, 2015, 17, 2143

Photo-induced dynamics of the heme centers in cytochrome bc_1 †

Adrien A. P. Chauvet,^a André Al Haddad,^a Wei-Chun Kao,^b Frank van Mourik,^a Carola Hunte^b and Majed Chergui*^a

The ultrafast response of cytochrome bc_1 is investigated for the first time, *via* transient absorption spectroscopy. The distinct redox potentials of both c_1 - and b -hemes allow for a clear differentiation of their respective signals. We find that while the c_1 -heme photo-product exhibits the characteristics of a 5-coordinated species, the b -hemes presumably undergo photo-oxidation at a remarkably high quantum yield. The c_1 -heme iron–ligand recombination time is 5.4 ps, in agreement with previous reports on homologous cytochromes. The suggested photo-oxidized state of the b -hemes has a life-time of 6.8 ps. From this short life-time we infer that the electron acceptor must be within van der Waals contact with the heme, which points to the fact that the axial histidine residue is the electron acceptor. The different heme-responses illustrate the flexibility of the c_1 -heme ligation in contrast to the more rigid b -heme binding, as well as the higher electronic reactivity of the b -hemes within the bc_1 complex. This study also demonstrates the remarkable connection between the heme local environment and its dynamics and, therefore, biological function.

Received 31st October 2014,
Accepted 27th November 2014

DOI: 10.1039/c4cp04805a

www.rsc.org/pccp

Introduction

The cytochrome (cyt) bc_1 complex is a key player in mitochondrial and bacterial respiratory chains.¹ It is the main actor in the proton motive Q cycle as it catalyzes the two-electron oxidation of a quinol and the one-electron reduction of a c -type cytochrome and a quinone while conjugating this electron transfer to the formation of a proton gradient across the membrane.^{2–4} The generated potential gradient serves as the driving force to the ATP synthesis, the universal energy transporter in living organisms.¹ The cyt bc_1 complex is a dimer whose monomer comprises four key elements that are directly involved in the electronic pathway (Fig. 1): (1) the heme c_1 is located near the intermembrane-space side of the membrane; it is situated near the cyt c docking interface and serves as an electron donor for the reduction of cyt c ;^{2,5–7} (2) the Rieske iron–sulfur cluster mediates electron transfer between the quinol at the Q_o site and the heme c_1 *via* a series of conformational changes;¹ (3) and (4) the hemes b_L and b_H that mediate electron transfer between the two quinone binding sites, Q_o and Q_i sites.² Depending on the reaction stage, the three iron centers of the hemes are found in either their ferric (Fe(III)) or ferrous forms

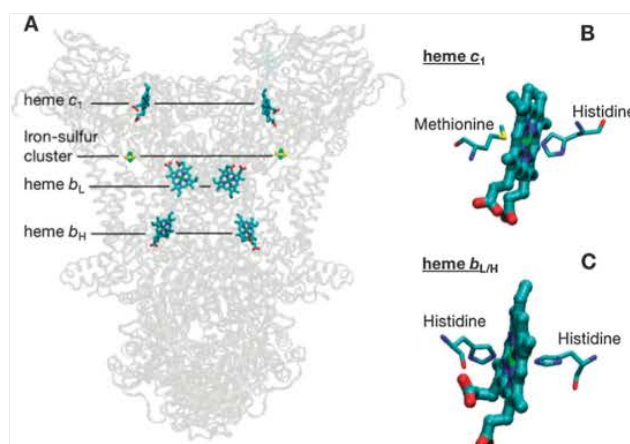


Fig. 1 (A) Structure of the bc_1 complex 7 with the protein backbone being shaded for clear visualization of the key actors in the proton-coupled-electron mechanisms. Structure of the heme- c_1 (B) and of the heme- b (C) with their axial amino acid ligands.

(Fe(II)) and are all characterized by a 6-coordinated (6-c) low-spin state, therefore minimizing the reorganization energy required to undergo the electron transfer.⁸

Crystallographic data reveal that the c_1 -heme is covalently attached *via* the vinyl groups to two cysteine residues and has both methionine (Met) and histidine (His) residues as axial ligands (Fig. 1). The b -hemes however are not covalently attached to polypeptides and have two His residues as axial ligands.⁹

^a Ecole Polytechnique Fédérale de Lausanne (EPFL), Laboratoire de Spectroscopie Ultrarapide, ISIC, Faculté des Sciences de Base, Station 6, 1015 Lausanne, Switzerland. E-mail: majed.chergui@epfl.ch; Tel: +41-21-693-0457

^b Albert-Ludwigs-Universität Freiburg, BIOSS Centre for Biological Signalling Studies, Institute for Biochemistry and Biology, Stefan-Meier-Str. 17, 79104 Freiburg, Germany

† Electronic supplementary information (ESI) available. See DOI: 10.1039/c4cp04805a

Such differences in the structural environment confer to each heme-type their particular redox properties and specific functions.¹⁰ The origins of the overall catalytic functions of the bc_1 complex remain however unknown. In this view, ultrafast spectroscopy is able to give access to the early mechanisms and local structural and electronic modifications that confer the heme-protein its overall functions. The ultrafast behaviors, and more specifically, the relaxation of photo-excited hemes, have indeed been the object of an intense study since the late 1980s.^{11,12} For example, the hemes in *cyt c* and *cyt b₅*, which are structurally comparable to the *c₁*- and *b*-hemes of the bc_1 complex, respectively,^{13,14} are known to dissociate from their axial ligand within femtoseconds as a response to light absorption.^{14–16} While the early steps of the heme photo-cycle still raise questions, it is generally accepted that photo-excitation of the heme is followed by an electron transfer (ET) to the iron d-orbitals,¹⁶ which in turn is believed to trigger the ligand dissociation in ferrous complexes. This photo-dissociation seems to be a universal feature in *cyt*'s¹⁷ but its relation to the overall functionality of the protein is unclear.

There is no previous study of the *cyt bc₁* complex in the femto-picosecond regime, most probably due to the quantity and purity of the sample required for such measurements. We therefore aim to complete our knowledge by presenting the first such study here. By means of ultrafast transient pump-probe spectroscopy, we bring to light the short-lived local electronic and nuclear modifications that are behind physiological processes and confer to the bc_1 complex its overall functionalities.

Most studies on *cyt*'s focus on the Soret band region (≈ 430 nm) for both, excitation and detection, as it is the most intense absorption band. In this work we focus on the weaker *a*-band around 550–570 nm. The pump is tuned at 523 nm in order to indifferently excite via the *b*-bands both heme-types while in their ferrous states (see Fig. 1). The reason for probing the *a*-bands rather than the Soret band is that in the presence of multiple heme-types, the Soret band region in the bc_1 complex is spectrally congested, while the *a*-band region allows a clear distinction between the *b*- and *c*-hemes.¹⁸ Furthermore, the *a*-bands are sensitive to changes in the electronic states and coordination of the hemes.¹⁹ Besides being spectrally distinguishable, each heme type has a particular redox potential that is conferred by their specific environment:¹⁰ while the heme *b_L* and *b_H* have a redox potential of -90 mV and 50 mV, respectively, the heme *c₁* has a redox potential of 230 mV.²⁰ These specificities will allow us to selectively change the reduction state of certain hemes, which in turn brings a clear distinction between the photo-induced mechanisms of each heme-type.

Materials and methods

The laser

The 800 nm output of a 1 kHz regenerative amplifier is used to pump a home-made visible non-collinear optical parametric amplifier (NOPA, see ref. 21 for a detailed description) producing the 523 nm pump pulses with a full-width-half-maximum

of 8 nm and a time duration of ≈ 50 fs. A small fraction of the regenerative amplifier output is focused onto a 5 mm thick CaF_2 crystal to provide a wide visible probe. The pump and probe pulses are focused onto spots of ≈ 80 and ≈ 55 mm in diameter, respectively, at the sample position by means of reflective optics in order to avoid degradation of the instrument response function. The resulting pump-probe cross-correlation is about 150 fs. The polarization of the pump and probe beam is set at the magic angle. After passing through the sample, the probe beam is focused onto the 160 mm input slit of the Triax 190 spectrometer, while using 300 grooves per mm and 550 nm blaze wavelength grating it is focused onto a 1024 pixel CMOS array. Such conformation allows for a probing window from 340 to 750 nm with a spectral resolution of 2.5 nm.

Sample handling

As an alternative to the common spinning cell with its moving parts and to the peristaltic pumping that necessitates large sample volumes, we use a home-made closed-loop flow-cell that requires a total sample volume of only ≈ 250 nL;²² a volume therefore comparable to that of the spinning cell with the advantage of having a steady window at the laser focus. The flow is generated using a turbisc micro-pump from the Swiss Center for Electronics and Microtechnology (CSEM)²³ and bubbles are removed from the circuit via a decantation chamber. The pump and probe pulses are focused onto a square quartz silica capillary of 0.5 mm path-length and a 0.1 mm thick window. While connected to both, the decantation chamber and the capillary, the pump generates a flow of ≈ 0.1 mL s^{-1} that was sufficient to refresh the sample for each laser shot at a 1 kHz repetition rate. Due to the small amount of sample, the oxidation state of the hemes as well as the possible degradation of the complexes were verified by recording their steady-state absorption using the probe beam. Each absorption spectrum consisted of an average of 40 consecutive images while flowing the solution. Note that by passing through the capillary, the probe beam contains an additional broad and featureless scattering signal. Consequently any adjustments of the beam path will confer each spectrum with a small, but specific background as shown in Fig. 2 while comparing the red and green curves.

The bc_1 complexes

The sample is prepared as described in ref. 24. Corresponding to a differential (reduced-oxidized) *c*-heme absorption of ≈ 0.16 OD for the *a*-band through the 0.5 mm path length capillary (Fig. 2) and assuming the differential extinction coefficient of 18.8 mM $^{-1}$ cm $^{-1}$,²⁵ the concentration of bc_1 monomer was about 170 nM. The fluence of the excitation pulses was kept low in order to avoid multiple excitation of a single complex. From the comparison between the *c₁*- and *b*-heme contribution to the steady state absorption and to the transient signal (as discussed later, Fig. 8A and B), only $\approx 5\%$ and $\approx 3\%$ of the reduced *c₁*- and *b*-heme, respectively, are involved in the major ps-long signal. The absorption of the reduced *c*-heme band was virtually identical before (addition of dithionite) and after the experiment (after oxidation of the

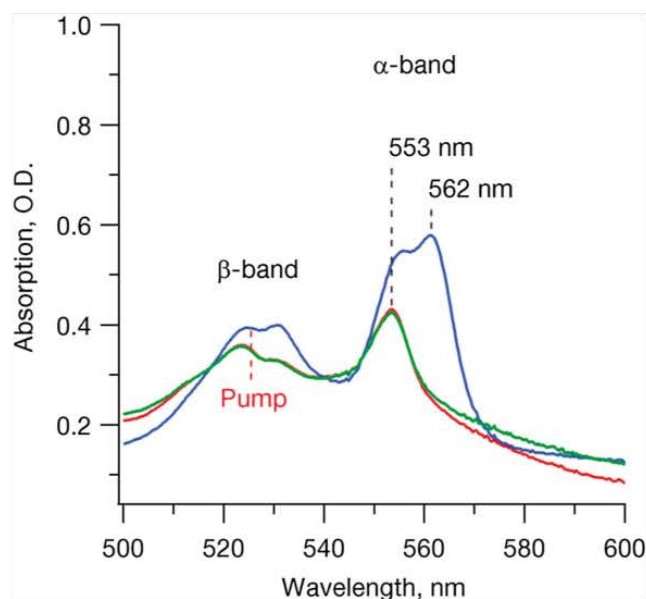


Fig. 2 Static absorption spectrum of the sequential reduction and oxidation of the cyt bc_1 dimer complex: at the beginning of the experiment, after pre-reduction by ubiquinol and before (red) and right after (blue) the addition of dithionite, and at the end, after oxidation of the complexes by oxygen (green). The 523 nm excitation pump is indicated as reference.

b-hemes), which confirms the stability of the complexes over the course of the experiment.

Data treatment

Since the probe pulses are temporally chirped by some hundreds of fs, a Group Velocity Dispersion (GVD) correction is performed in post data acquisition analysis. From the corrected data, several kinetics are extracted at wavelengths corresponding to the major transient features. This set of kinetic traces is globally fitted as a sum of exponential decays. The same exponential components are then used to fit the Eigen-kinetics that results from a Singular Value Decomposition (SVD) of the data-set.²⁶ Along with the Eigen-spectra, the corresponding Decay Associated Spectra (DAS) are generated, which will be presented later.

Results

Due to its low redox potential, the addition of dithionite to the cyt bc_1 solution effectively reduces all the c-hemes while, in our preparation, it only reduces about 70% of the b-hemes as shown in Fig. 2. Note that in dilute samples, dithionite effectively reduces all hemes. This estimate results from the fit of the absorption spectrum, described later (Fig. 8A). This partial reduction of the b-hemes is attributed to the presence of oxygen in solution as well as the high protein concentration (B 170 nM of cyt bc_1 monomer; see ESI † for calculations). Partial reduction of the b-hemes pool could raise questions concerning the presence of different reduction states of the bc_1 complex (1, 2, 3 or 4 reduced b-heme per dimer). Indeed, the reduction state of one heme affects its local environment²⁷ and

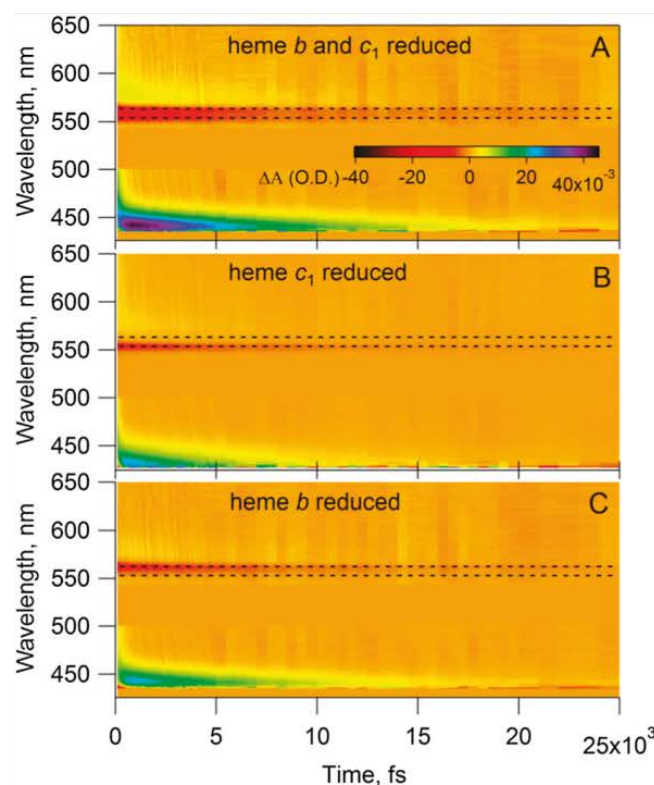


Fig. 3 (A) Transient data taken right after addition of dithionite, while both b- and c_1 -hemes are reduced. (B) Transient data taken after oxidation of the b-hemes by oxygen, while the c_1 -hemes are left reduced. (C) Difference (A-B) corresponding solely to the signal of the ferrous b-heme, as discussed in the text. The scattering region around the 523 nm excitation is set to zero. The horizontal dotted lines represent an eye-guide at 553 and 562 nm.

could influence other nearby hemes as in the case of the tightly packed chlorophylls within the photosynthetic reaction centers.²⁸

It was however shown via Raman studies that heme c_1 is structurally isolated from the b-hemes, and that the local environment of ferrous heme b_H is unaffected by the redox state of heme b_L .²⁹ Consequently we can assume that the partial reduction of the complexes, as opposed to a complete reduction, does not affect the individual behaviours of the hemes. The pump wavelength at 523 nm excites equally the b-band of both ferrous b- and c_1 -hemes. The resulting time-wavelength plot of the signal is shown in Fig. 3A. The response of both heme-types is seen by their respective bleach signals at 553 and 562 nm (horizontal dotted lines), as well as part of the mixed Soret-band signal from both heme c_1 and b at wavelengths below 470 nm. From the expected bi-phasic Soret-band signal, as monitored for cyt $c^{17,19}$ and cyt b_5 ,¹⁴ only the positive lobe is observed. The resolution of the anticipated negative lobe is hindered due to the high optical density of the sample. Over the course of the experiment, the successive scans were marked by the oxidation of the b-hemes resulting in the loss of their corresponding signal at B 562 nm. Since the data do not show any long lived signal (4 ns), we confirm that the oxidation of the b-hemes is not induced by the excitation pulses. If it were the case, we would expect the first scans to be characterized by a non-decaying

transient signal representative of the photochemical processes leading to the oxidation of the b-hemes. The later oxidation is consequently solely ascribed to the oxidative properties of dissolved oxygen molecules. Thus we take advantage of the properties of oxygen to fully oxidize the b-hemes while keeping intact the ferrous state of the c₁-heme. The resulting transient signal (Fig. 3B) as well as the final absorption spectrum (Fig. 2) show clearly that only the 553 nm signal persists, corresponding solely to the ferrous c₁-hemes. It is important to note that, while only the c₁-hemes are reduced, the absence of a sharp feature at around 562 nm confirms that the ferric state of the b-hemes is unresponsive to light excitation and that the yield of photo-reduction, if any, is negligible while exciting the heme's b-bands (523 nm). Indeed, changes in the electronic state of the heme iron center are not expected while exciting above 400 nm.³⁰ It is also necessary to mention that further (post-experiment) addition of dithionite partially recovers the ferrous state of the b-hemes (data not shown), which proves that the b-hemes remains functional. The absorbance of the c₁-heme a-band remains virtually identical before and after the experiment, as shown in Fig. 2; and the subsequent data analysis of the c₁-heme alone gives, within the error margin of the fit, the same spectral features and exponential decay values prior to the first addition of dithionite and after full oxidation of the b-hemes by oxygen (as shown in the ESI †). The temporal and spectral correspondence of the transient signal proves that the c₁-hemes remain functional. We therefore conclude that neither dithionite, nor the presence of oxygen affects the protein complex and that its functionality remains intact in the course of the experiment.

Since the selective oxidation of the b-hemes is done via solvated atmospheric oxygen molecules, the bc₁ concentration remains identical before and after oxidation of the b-hemes and direct comparison of the two sets of data is therefore possible (Fig. 3A and B). This would not have been possible without some renormalization of the data, had we proceeded via successive reductions by adding solutions of ascorbate and then dithionite. Thus, the difference spectrum (A–B) corresponds to the signal associated with the ferrous b-hemes alone, as shown in Fig. 3C. One can see that the resulting data set (Fig. 3C) lacks any sharp features or any bleach signal that would be specific of the 553 nm band of the ferrous c₁-heme a-band, which consequently, validates the data handling. To better illustrate the results of such a treatment of the data sets as well as the spectral evolution of each heme type, we present in Fig. 4A, B and C, the transient spectra recorded at selected time delays, corresponding to the two-dimensional data of Fig. 3A, B and C, respectively. Note that we do not differentiate between hemes b_L and b_H since dithionite and oxygen are able to reduce and oxidize both, respectively. Moreover, even if heme b_L has a distinct split a-band, it only appears as a shoulder at 554 nm in yeast bc₁ complexes¹⁸ with a differential extinction coefficient (reduced–oxidized) that is ~ 10 times weaker compared to that of the combined 562 nm band of both b-hemes. Since the present signal-to-noise ratio does not allow for the detection of such low signals, we refer to data set (B) and to the

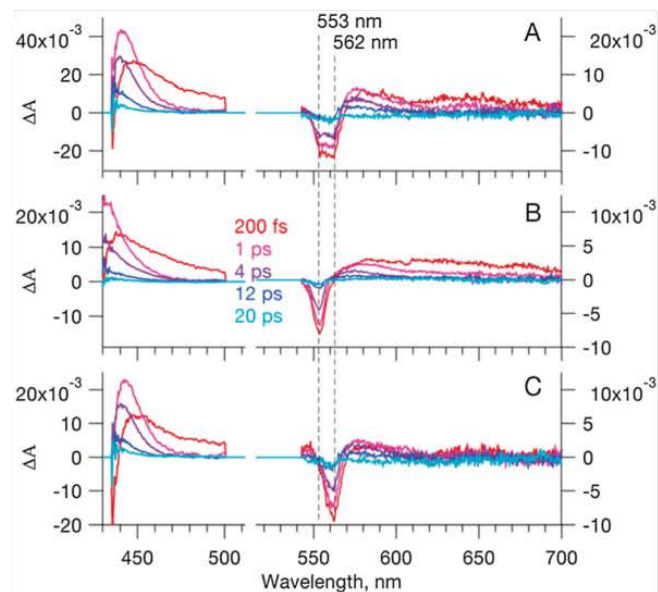


Fig. 4 (A) Spectra at selected time delays while both b- and c₁-hemes are reduced. (B) Spectra at selected time delays while only the c₁-hemes are left reduced. (C) Difference (A–B) corresponding solely to the signal of the ferrous b-heme, as discussed in the text. Note that the vertical scales below and above 515 nm differ by a factor of two.

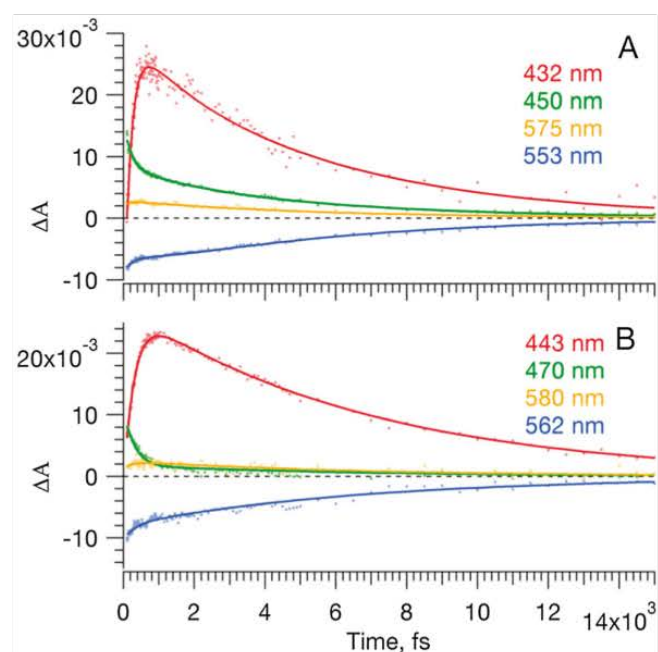


Fig. 5 Kinetics traces of the hemes c₁ (A) and b (B), respectively, at selected wavelengths and their global fit with a satisfactory minimum of three and two exponential decay components respectively.

difference data set (C) in Fig. 3 and 4 as representative of the overall c₁- and b-heme population, respectively.

From these data sets, Fig. 5 shows the globally fitted kinetic traces taken at selected wavelengths corresponding to the major spectral features. Satisfactory fits result in a minimum of three and two exponential decay components for the c₁- and

Table 1 Exponential decay components resulting from the global fit presented in Fig. 5

	Heme c_1	Heme b
t_1	190 fs	300 fs
t_2	1.6 ps	—
t_3	5.4 ps	6.8 ps

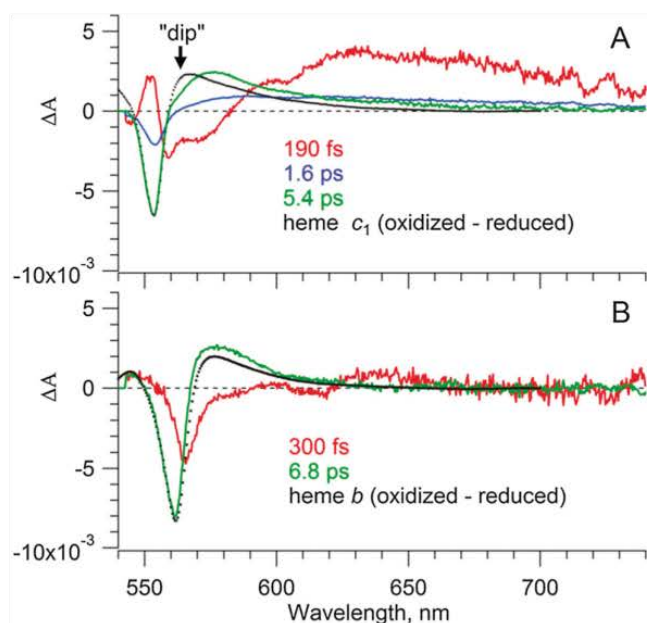


Fig. 6 Decay Associated Difference Spectra of the a -band spectral region corresponding to the c_1 -hemes (A) and to the b -hemes (B). The oxidized minus reduced spectrum of each heme, normalized at the maximum bleach amplitude, is superimposed as reference only (black dotted line). The arrow points to a spectral feature that is specific of the photo-dissociated heme, as discussed in the text.

b -hemes, respectively. The values of the decay constants used for the fits are given in Table 1. These exponential decay components agree with the components resulting from the Singular Value Decomposition (SVD) of the transient time-wavelength plots (Fig. 3). The generated Decay Associated Difference Spectra (DADS) are presented in Fig. 6. Because of the high protein concentration, the Soret band could not be monitored entirely. On the other hand, since the spectral changes in the a -band region are better fingerprints of the redox and coordination state of the hemes, we will focus on the spectral region from 540 to 750 nm.

Discussion

Heme c_1

Because this work is the first ultrafast study on cyt bc_1 , we base our analysis of heme c_1 in the bc_1 complex by comparing it with the cyt c whose heme and heme-environment are known to be structurally similar.¹³ Because of its correspondence with the cyt c signals, the 190 fs component is associated with an “intramolecular vibrational energy redistribution resulting in an equilibrated hot ground-state heme and possibly with a tail

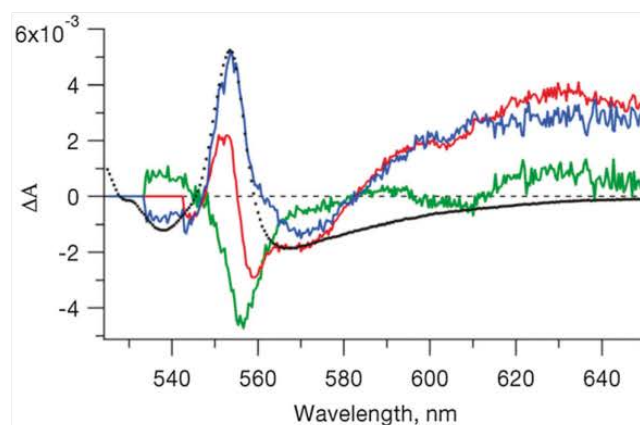


Fig. 7 The adjusted 300 fs Decay Associated Difference Spectra (DADS) of the b -heme signal (green) are subtracted from the 190 fs DADS of the c_1 -hemes (red). The resulting difference spectrum (blue) is superimposed with the 5.4 ps DADS of the (reduced-oxidized) heme c_1 (black dots) used for comparison only.

of the electronic relaxation”,³¹ while the 1.6 ps components are mostly ascribed to an “intermolecular vibrational energy transfer from the hot heme to the surroundings”.³¹ We would like to emphasize that these components cannot be representative of a single specific mechanism as the cooling processes are non-exponential.^{32,33} Indeed, both of these components show a broad positive amplitude to the red of the a -band static absorption that is typical for the heme Excited State Absorption (ESA). It has been argued in the case of cyt c and met-myoglobin that this ESA partially stems from a pulse-limited electron and back electron transfer between the porphyrin macrocycle and the d_z antibonding orbital of the iron.^{11,15,16}

In light of the subsequent b -heme spectral analysis, we can infer that part of the 540 to 580 nm region of the 190 fs DADS could also consist of a sharp Stimulated Emission (SE) similar to the 300 fs DADS component monitored for the b -heme (Fig. 6B). In order to differentiate the other concomitant processes from this expected SE, we subtract, from the c_1 -heme’s 190 fs DADS, the expected SE contribution by using the b -heme’s 300 fs DADS that is blue-shifted by 9 nm (Fig. 7, green curve). This shift is supposed to account for the difference in absorption and expected SE between the c_1 - and b -hemes. Note that such straightforward subtraction is valid as long as the extinction coefficients, overall reactivity and emission Stokes-shift of both heme-types are similar. Variation of $\pm 50\%$ in the subtracted SE amplitude however does not significantly affect the overall shape of the resulting difference spectrum. The blue curve in Fig. 7 shows the resulting difference spectrum, which resembles that of the (reduced-oxidized) heme c_1 , slightly red shifted by 0.5 nm. Because the band resembles that of the ferrous heme c_1 and is positive, it corresponds to the formation of a 6-c reduced species (decrease of an initial bleach signal). The small shift also suggests that it is a hot state. The features above 560 nm are ascribed to a broad ESA signal (positive featureless band), which decays in 190 fs (decay of an initially positive signal). A similar short-lived ESA signal (~ 500 fs) has been reported for different myoglobin (Mb) samples and has been

specifically assigned to the resulting charge transfer (CT) state (from the porphyrin ring to its metal center) that triggers ligand dissociation.^{34,35} Correspondingly, we conclude that the short-lived broad ESA monitored for the heme c_1 is also indicative of the heme's CT state.

Since the SE, ESA and the formation of a 6-c ferrous c -heme are concomitant, we suggest that an initially excited c -heme, having lost its reduced 6-c character via an impulsive CT from the heme macrocycle to the metal center,¹⁶ gives rise to the SE and ESA, and relaxes within 190 fs into its hot ground state through a non-dissociative pathway.

The bleach of the 1.6 ps DADS is slightly broader and red-shifted compared to the static c_1 -heme a-band. Since it is representative of the cooling of a hot 6-c species, it could be ascribed to the non-dissociative relaxation channel as proposed in the case of cyt c .^{15,19} Note that the 190 fs and 1.6 ps DADS only illustrate a mixture of the different non-exponential cooling mechanisms. Consequently, our assignment of particular processes to specific DADS features is approximative.

The 5.4 ps DADS, corresponding to the longest lived signal, is comparable to any transient spectrum taken after completion of the electronic and vibrational relaxation (from λ_B 2 to 10 ps). It is for example comparable to the different transient absorption spectra reported for cyt c .^{15,19} Following similar analysis, we can distinguish in the 5.4 ps DADS, the bleach of the c -heme a-bands from the absorption spectrum of the photo-product, characterized by the broader ESA. While superimposed with the c -heme (oxidized–reduced) spectrum, as shown in Fig. 6A, the photo-product exhibits clearly a broad red-shifted absorption that extends beyond 700 nm. The same contrast is present in cyt c while comparing its oxidized spectrum (Fig. 2 of ref. 30) with the corresponding generated photo-product spectrum,¹⁹ i.e. the cyt c photo-product's absorption spectrum is broader and red-shifted. Similarly, the cyt c photo-product represented in Fig. 6 of ref. 15 shows exactly the same features, including even the small "dip" at λ_B 555 nm. This "dip" is also present in our spectrum and is represented by the oxidized minus reduced heme c spectrum being above the 5.4 ps DADS near 560–565 nm (arrow in Fig. 6A). It was concluded that the generated cyt c photo-product corresponds to the photo-dissociated heme¹⁹ based on the similarity of its transient signal to the 5-coordinated (5-c) MP-8 spectrum that is structurally analogous to the 5-c cyt c . Assuming that the broad and red-shifted spectrum, with respect to the oxidized species, along with the "dip" on the red-side of the a-band are signatures of the 5-c photo-product, we conclude that the c_1 -hemes in the bc_1 complex also undergo photo-dissociation of one of their axial ligands.

The life time matches the 5–7 ps reported for the photo-cycle of a variety of 6-c hemes proteins, including cyt c .^{11,15,17,19} All these reports are unanimous in assigning this time constant to the rebinding of the photo-dissociated ligand. It should be mentioned that the 5.4 ps DADS might not be entirely free from other processes as vibrational cooling has previously been monitored with a life-time of λ_B 4.6 ps.³⁶ However, since the position and width of the transient bleach is identical to that of the static a-band absorption, any contribution to the 5.4 ps DADS from vibrational

cooling has to be minimal. Based on the correspondence of the overall monitored spectral features and life times with the literature, we conclude that the 5.4 ps component most probably corresponds to the rebinding of the photo-dissociated heme. As in cyt c , we suggest the dissociation of the Met residue.^{15,37}

Heme b

The corresponding data set could be satisfactorily fitted with only two exponential decays, which points to the fact that cooling dynamics differ from those monitored for the c_1 -hemes. The 300 fs DADS are in fact singular as they do not show any significant positive signal expected from the ESA. It is however characterized by a sharp bleach to the red of the a-band, and is of similar width. This feature is particular to the expected SE from the excited a-band of the 6-c ferrous heme, therefore associated with a non-dissociative relaxation pathway. The absence of the ESA signal in the b -heme's 300 fs DADS indicates that CT states, similar to the ones discussed in the case of the hemes c_1 , are not generated. Consequently we do not expect the axial ligands of the b -hemes to dissociate.

The absence of a component similar to the 1.6 ps monitored for the heme c_1 as well as for cyt c indicates that the relaxation of the excited b -hemes, which do not contribute to the longer 6.8 ps signal, occurs mainly within the first 300 fs. This ultrafast relaxation to the ground state is conferred to the b -heme by its environment.

As a matter of fact, the longer 6.8 ps DADS component (Fig. 6B) compares remarkably well to the oxidized minus reduced static spectrum of the b -hemes (ascorbate–dithionite). The small extra positive λ_B 580 nm signal present in the 6.8 ps DADS might probably result from a small fraction of hot photo-product with corresponding cooling life-time. However since the width and bleach position are identical and we can expect that vibrational cooling, if any, has a negligible contribution to the 6.8 ps DADS. The spectral features of the positive red-wing differ from those of the previous c_1 -heme (5.4 ps DADS of Fig. 6A); namely, a shifted red-wing, while compared to its corresponding oxidized minus reduced static spectrum; a broad positive ESA signal that extends beyond 700 nm; and the "dip" to the red of the alpha band. By assuming that these "discrepancies" are a signature of the 5-c state of the hemes, their absence in the 6.8 ps DADS are also indicative that the b -heme behaves differently compared to the c_1 -heme, and most probably does not photo-dissociate with its axial ligand. Together with its particular spectral features that mimic the oxidized minus reduced spectrum, we propose that the b -hemes undergo photo-oxidation. Photo-oxidation in cyt is well-known but typically implies the formation of a photo-induced electron acceptor. For example the tetra-heme cytochrome (THC) oxidizes as a result of the light-induced oxidation of nearby reaction centers.³⁸ Similarly, the cyt P450-BM3 oxidizes after photo-excitation of its covalently attached ruthenium complex.³⁹ The suggested b -heme's photo-oxidation differs as it results from direct excitation of the heme. In this respect, photo-oxidation by means of visible-light excitation is unusual among cyt's³⁰ and it requires further evaluation.

The different binding environments of the c_1 - and b -hemes (Fig. 1) may explain their different behaviours, because these

environmental differences confer to each heme a particular spectrum and redox potential.^{9,10} Cyt b_5 , structurally homologous to the b-hemes in cyt bc_1 ,¹³ is known to behave similar to cyt c .³⁰ However the difference in the Raman signal between the cyt b_5 and the b-hemes in cyt bc_1 ¹³ shows that we can also expect a different behavior for the b-heme with respect to cyt b_5 and cyt c . Hereafter, we present different arguments supporting the possibility of photo-oxidation of the b-hemes in cyt bc_1 :

(1) Stronger physical constraints are exerted by the protein backbone onto the b-heme, resulting in the loss of planarity of the b_L heme.⁴⁰ The higher protein constraint that is exerted on the hemes certainly stiffens the His-heme-His ligation and impedes the possible dissociation of these axial ligands. Since photo-dissociation is hindered, other processes are expected to prevail.

(2) Similar photo-oxidation reactions have been reported for both cyt c and cyt b_5 with excitation below 400 nm. Yet the yield was judged negligible when exciting above 400 nm.³⁰ The same study shows however that the photo-oxidation cross section of cyt b_5 is about 18 times higher than that of cyt c which, by analogy, shows that the b-heme is much more prone to photo-oxidation than the c_1 -heme.

(3) Photo-oxidation mechanisms were previously used to interpret signals from the 6-c heme-based oxygen sensor Dos excited with a B 30 fs, 563 nm low energy pulse,⁴¹ therefore similar to our B 50 fs, 523 nm pulse. The corresponding signals were long-lived (4 ns) and contributed only to 4–8% but, keeping in mind that the protein complexes are different, this study indicates that photo-oxidation is feasible while exciting the heme's Q-bands.

(4) The photo-oxidation properties of the THC are commonly used in light-induced electron transfer reactions.^{38,42} The transient study of these THCs are however limited to the micro-seconds to minutes time range. Nevertheless, we note that the photo-oxidation reactions involve primarily the THC's low potential c-type hemes that have redox properties corresponding to those of the b-hemes in the bc_1 complex.

(5) Interestingly, it was shown that oxidation of the b-heme by oxygen in cyt bc_1 happens without the need for a ligand dissociation.⁴³ It consequently presupposes that the electron transfer occurs via molecular intermediates rather than by direct contact with the iron center that would necessitate dissociation of the His ligand. Our results indeed coincide with the fact that electron transfer can be readily initiated from the b-heme without the need for close contact with an external electron acceptor such as quinones or molecular oxygen.

(6) It was also reported that the axial histidylimidazole ligands of the b_L heme have a distinct ionic character,⁴⁰ which would favour electron transfer processes. This electronegative character of at least one of the two His ligands was explained by the presence of nearby arginine residues.

(7) When compared to the compilation of the optimal rate-distances from Moser et al.⁴⁴ we see that an electron tunnelling life-time of 6.8 ps would correspond to donor-acceptor distances smaller than 6 Å. Such short distances match with the His being the electron acceptor as it lies at an average minimal distance of 2.0 Å from the heme's iron center (according to the crystallographic data, PDB-file 3CX5⁷).

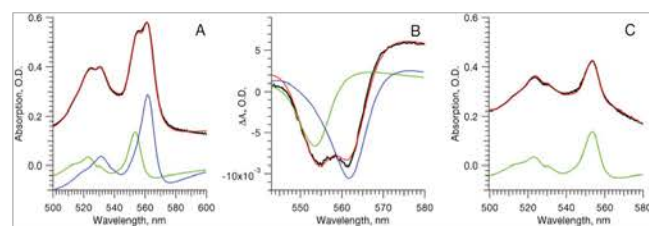


Fig. 8 The black curves represent (A) the static absorption spectrum after addition of dithionite, (B) the DADS corresponding to the longest ps component resulting from the combined analysis of the b- and c_1 -heme transient signals (see ESI †); while both are reduced and (C) the static absorption spectrum after full oxidation of the b-hemes via oxygen. Superimposed are the fits (red) and their components: the (reduced-oxidized) heme c_1 (green) and heme b (blue) spectrum. The background-component used in each fit, not shown here for clarity, is described in the ESI. †

(8) Finally, it is known that His residues actively participate in charge transfer processes and more specifically it was demonstrated that they can serve as electron acceptors.⁴⁵

In light of these arguments, we infer that the 6.8 ps DADS correspond to the photo-oxidation of the b-hemes. Furthermore we expect heme b_L to predominantly contribute to our signal with the His residue playing the role of the electron acceptor.

Quantum yield

The goal of this section is to evaluate the reactivity of each heme-type, i.e. the photo-dissociation and the photo-oxidation of the heme c_1 and b, respectively. In order to do so, we deconvoluted both the initial absorption spectrum (after addition of dithionite, Fig. 8A) and the 5.4 ps DADS (generated from the first data set after addition of dithionite, Fig. 8B) in terms of the c_1 - and b-hemes's (reduced-oxidized) spectrum. From the comparison of each heme's relative contributions to both spectra, we see that B 5% and B 4% of the c_1 - and b-hemes, respectively, contributed to the signal as described in Table 2. Alternatively, deconvolution of the final absorption spectrum (after oxidation of the b-hemes, Fig. 8C) gives the same c_1 -hemes contribution as did the initial absorption spectrum (Fig. 8A). The conservation of the c_1 -heme's absorption amplitude during the experiment proves that its ferrous state was not affected by oxygen. The fitting results are given in Table 2, while the details of the fitting procedure and calculations are to be found in the ESI. †

Considering the fit of Fig. 8B, weighing the coefficients obtained for each heme type by its extinction coefficient, i.e. 18.8 and 28.5 $\text{mM}^{-1} \text{cm}^{-1}$ for the c_1 - and b-hemes, respectively,²⁵ and taking into account that we can only expect signal from the B 70% offerrous b-hemes, it results that the reactivity of the

Table 2 Amplitude of the heme c_1 and b components resulting from the fitting of each plot in Fig. 8

	Fig. 8A	Fig. 8B	Fig. 8C
Heme c_1 ^a	$A_{\text{heme } c} = 3.88$	$0.189 = A_{\text{heme } c} \times 4.9\%$	3.93
Heme b ^a	$A_{\text{heme } b} = 2.8$	$0.103 = A_{\text{heme } b} \times 3.7\%$	—

^a (Reduced-oxidized) spectrum amplitude.

b-hemes is ~50% that of the c-hemes (assuming that we are equally exciting both heme-types).

If we assume that the photo-dissociation quantum yield of the c₁-heme in cyt bc₁ is comparable to ~0.8 in cyt c,¹⁹ because of their correspondence in structure, transient spectra and exponential decays, then the photo-oxidation quantum yield of the b-hemes is expected to exceed 0.4. This is to our knowledge, the highest reported photo-oxidation quantum yield for cytochromes, while the hemes are directly excited by visible light. The physiological consequences of such high reactivity are discussed subsequently.

Mechanistic consequences

The b-heme's high electronic reactivity makes perfect sense in light of cyt bc₁ being efficient in fulfilling its role in the Q-cycle: in order to mediate the reduction and oxidization of the ubiquinone and ubiquinol, respectively. The b-hemes have to efficiently "process" the electrons, which demand them to easily lose or gain electrons. Similar electronic-reactivity would in fact be counterproductive in soluble cytochromes as they would less efficiently keep their electrons from being scavenged by other solutes. In purified reaction centers, it was in fact shown that the electrons result from charge separation, while at the periphery of the complex could readily be "lost" to the solution.^{46–48} The hydrophilic environment of the bc₁ core on the other hand preserves the b-hemes from the unwanted solvated electron carrier and their high electronic reactivity is then an advantage.

The fact that efficient electron migration is initiated via visible light also indicates that the protein might behave differently under dark and light conditions. We can further speculate that the overall catalytic efficiency of cyt bc₁ is light-dependent. We can then contemplate the protein complex as an active element in phototherapy for example.⁴⁹ It is also of interest to compare the light-responses of the bc₁ complex with that of its photosynthetic homologue, the cyt b₆f.⁵⁰ Being an essential component of the photosynthetic electron transport chain and being therefore exposed to direct sun-light, the foreseen specificity of the heme responses to light excitation could affect the photosynthetic Q-cycle.

In contrast to the high electronic reactivity of the b-hemes, the high photo-dissociation quantum yield of the c₁-hemes can be understood as being an efficient "heat sink" that protects the reduced state of the heme against light excitations. The fact that the ferrous state of heme c₁ is stable and protected implies the need for a change in the local environment in order for the electron to proceed from heme c₁ to the cyt c. Such conformational changes could readily be induced by the motions of the adjacent Rieske iron-sulfur complex.¹ Speculations put aside, it is remarkable that, even though the b-hemes in cyt bc₁ and in other cyt b have similar ligation to their protein backbone; specific structural constraints and amino-acid arrangements result in clearly different responses, and therefore functions. While cytochromes were known to serve only as electron carriers, this study demonstrates that with the appropriate environment, light-induced charge separation can readily be initiated within single heme structures. This singular behaviour consequently

illustrates the importance of the local heme-bonding and the structural environment in initiating larger chemical reactions.

Conclusion

This study reveals the clear differences between the b and c₁-hemes behaviours within the bc₁ protein complex: while the c₁-hemes undergo photo-dissociation of their axial ligand as a result of ultrafast laser excitation, the b-hemes most likely undergo photo-oxidation with a high (~0.4) quantum yield that is beyond all expectations. The recombination of the photo-dissociated ligand with the c₁-heme occurs in 5.4 ps, which is comparable to the values reported for a large range of cytochromes.¹⁷ The efficient photo-oxidation of the b-heme is presumably linked to the stronger physical constraints exerted by the protein backbone onto the b-heme.⁴⁰ We suggest that these constraints hinder the flexibility of the adjacent His residues, and along with the induced ionic character of these same His ligands⁴⁰ favor the electron transfer process. The subsequent charge recombination takes place in 6.8 ps, in agreement with the electron residing on the axial His residue. It is to keep in mind that not all ferrous c₁- and b-hemes take part in these photo-reactions, and that, while the remaining excited c₁-hemes exhibit relaxation mechanisms that are mainly illustrated by broad ESA signals, the cooling-down of the remaining excited b-hemes does not show any significant ESA. Besides pointing to the fact that the c₁- and b-hemes behave and therefore function differently, these spectral differences call for further studies such as time-resolved fluorescence measurements¹⁶ in order to evaluate the nature of these non-dissociative and non-oxidizing pathways. We confirm that the ferric form of b-heme types in the bc₁ complex is electronically inert under our excitation regime, i.e. it does not undergo photo-reduction to any discernible extent. Finally, the high efficiency of the heme photo-oxidation clearly illustrates the high electronic reactivity of the ferrous b-hemes, which can be linked to their high efficiency in mediating the catalysis of ubiquinones and ubiquinols within the cell membrane.

Acknowledgements

This project has been funded by the Swiss NSF via the NCCR:MUST, by the FP7 Marie Curie COFUND, by the Excellence Initiative of the German Federal and State Governments (EXC 294, BIOSS) and by the Deutsche Forschungsgemeinschaft (RTG 1976) to C.H.

Notes and references

- 1 E. A. Berry, M. Guergova-Kuras, L. Huang and A. R. Crofts, *Annu. Rev. Biochem.*, 2000, 69, 1005–1075.
- 2 A. R. Crofts, *Biochim. Biophys. Acta, Gen. Subj.*, 2004, 1655, 77–92.
- 3 B. L. Trumpower, *Microbiol. Rev.*, 1990, 54, 101–129.
- 4 C. Hunte, S. R. N. Solmaz, H. Palsdottir and T. Wenz, *Results Probl. Cell Differ.*, 2007, 45, 253–278.
- 5 C. Lange and C. Hunte, *Proc. Natl. Acad. Sci. U. S. A.*, 2002, 99, 2800–2805.

- 6 R. Pietras, M. Sarewicz and A. Osyczka, *J. Phys. Chem. B*, 2014, 118, 6634–6643.
- 7 S. R. N. Solmaz and C. Hunte, *J. Biol. Chem.*, 2008, 283, 17542–17549.
- 8 F. A. Walker, *Chem. Rev.*, 2004, 104, 589–615.
- 9 S. E. J. Bowman and K. L. Bren, *Nat. Prod. Rep.*, 2008, 25, 1118–1130.
- 10 W. A. Cramer and D. B. Knaff, *Energy Transduction in Biological Membranes, a Textbook of Bioenergetics* Springer-Verlag, New York, 1990.
- 11 C. Consani, G. Aubeck, O. Bräm, F. van Mourik and M. Chergui, *J. Chem. Phys.*, 2014, 140, 025103.
- 12 M. Chergui, in *Comprehensive Biophysics* ed. E. H. Egelman, Oxford: Academic Press, 2012, vol. 1, pp. 398–424.
- 13 D. D. Hobbs, A. Kriauciunas, S. Giiner, D. B. Knaff and M. R. Ondrias, *Biochim. Biophys. Acta, Gen. Subj.*, 1990, 1018, 47–54.
- 14 K. A. Jongeward, D. Magde, D. J. Taube and T. G. Traylor, *J. Biol. Chem.*, 1988, 263, 6027–6030.
- 15 C. Consani, O. Bräm, F. van Mourik, A. Cannizzo and M. Chergui, *Chem. Phys.*, 2012, 396, 108–115.
- 16 O. Bräm, C. Consani, A. Cannizzo and M. Chergui, *J. Phys. Chem. B*, 2011, 115, 13723–13730.
- 17 M. H. Vos, A. Battistoni, C. Lechauve, M. C. Marden, L. Kiger, A. Desbois, E. Pilet, E. de Rosny and U. Liebl, *Biochemistry*, 2008, 47, 5718–5723.
- 18 J. N. Siedow, S. Power, F. F. de la Rosa and G. Palmer, *J. Biol. Chem.*, 1978, 253, 2392–2399.
- 19 W. Wang, X. Ye, A. A. Demidov, F. Rosca, T. Sjodin, W. X. Cao, M. Sheeran and P. M. Champion, *J. Phys. Chem. B*, 2000, 104, 10789–10801.
- 20 C.-A. Yu, L. Yu and D. Xia, in *Encyclopedia of Biophysics* ed. G. C. K. Roberts, Springer & European Biophysical Societies' Association, 2013, pp. 2679–2684.
- 21 C. Consani, M. Preumont-Schwarz, A. ElNahas, C. Bressler, F. van Mourik, A. Cannizzo and M. Chergui, *Angew. Chem.*, 2009, 121, 7320–7323.
- 22 A. Chauvet, T. Tibiletti, S. Caffarri and M. Chergui, *Rev. Sci. Instrum.*, 2014, 85, 103118.
- 23 A. Lisibach, E. Casartelli and N. Schmid, ASME 2010 3rd Joint US-European Fluids Engineering Summer Meeting and 8th International Conference on Nanochannels, Microchannels, and Minichannels, Montreal, Quebec, Canada, 2010.
- 24 T. Wenz, P. Hellwig, F. MacMillan, B. Meunier and C. Hunte, *Biochemistry*, 2006, 45, 9042–9045.
- 25 W. H. Vanneste, *Biochim. Biophys. Acta*, 1966, 113, 175–178.
- 26 J. Helbing, L. Bonacina, R. Pietri, J. Bredenbeck, P. Hamm, F. van Mourik, F. Chaussard, A. Gonzalez-Gonzalez, M. Chergui, C. Ramos-Alvarez, C. Ruiz and J. Lopez-Garriga, *Biophys. J.*, 2004, 87, 1881–1891.
- 27 J. S. Valentine, R. P. Sheridan, L. C. Allen and P. C. Kahn, *Proc. Natl. Acad. Sci. U. S. A.*, 1979, 76, 1009–1013.
- 28 A. Chauvet, J. Sarrou, S. Lin, S. P. Romberger, J. H. Golbeck, S. Savikhin and K. E. Redding, *Photosynth. Res.*, 2013, 116, 1–9.
- 29 F. Gao, H. Qin, M. C. Simpson, J. A. Shelnett, D. B. Knaff and M. R. Ondrias, *Biochemistry*, 1996, 35, 12812–12819.
- 30 Y. Gu, P. Li, J. T. Sage and P. M. Champion, *J. Am. Chem. Soc.*, 1993, 115, 4993–5004.
- 31 M. Negregerie, S. Cianetti, M. H. Vos, J.-L. Martin and S. G. Kruglik, *J. Phys. Chem. B*, 2006, 110, 12766–12781.
- 32 E. R. Henry, W. A. Eaton and R. M. Hochstrasser, *Proc. Natl. Acad. Sci. U. S. A.*, 1986, 83, 8982–8986.
- 33 P. Li and P. M. Champion, *Biophys. J.*, 1994, 66, 430–436.
- 34 S. Ishizaka, T. Wada and N. Kitamura, *Photochem. Photobiol. Sci.*, 2009, 8, 562–566.
- 35 J. W. Petrich, C. Poyart and J. L. Martin, *Biochemistry*, 1988, 27, 4049–4060.
- 36 D. Löwenich, K. Kleinermanns, V. Karunakaran and S. A. Kovalenko, *Photochem. Photobiol.*, 2008, 84, 193–201.
- 37 S. Cianetti, M. Negregerie, M. H. Vos, J.-L. Martin and S. G. Kruglik, *J. Am. Chem. Soc.*, 2004, 126, 13932–13933.
- 38 M. Yoshida, K. Shimada and K. Matsuura, *Plant Cell Physiol.*, 1999, 40, 192–197.
- 39 M. E. Ener, Y.-T. Lee, J. R. Winkler, H. B. Gray and L. Cheruzel, *Proc. Natl. Acad. Sci. U. S. A.*, 2010, 107, 18783–18786.
- 40 C. Le Moigne, B. Schoepp, S. Othman, A. Vermeiglio and A. Desbois, *Biochemistry*, 1999, 38, 1066–1076.
- 41 U. Liebl, L. Bouzhir-Sima, L. Kiger, M. C. Marden, J.-C. Lambry, M. Negregerie and M. H. Vos, *Biochemistry*, 2003, 42, 6527–6535.
- 42 D. Garcia, P. Richaud, J. Breton and A. Vermeiglio, *Biochimie*, 1994, 76, 666–673.
- 43 L. Kiger, L. Tilleman, E. Geuens, D. Hoogewijs, C. Lechauve, L. Moens, S. Dewilde and M. C. Marden, *PLoS One*, 2011, 6, e20478.
- 44 C. C. Moser, J. M. Keske, K. Warnck, R. S. Farid and P. L. Dutton, *Nature*, 1992, 355, 796–802.
- 45 O. B. Morozova and A. V. Yurkovskaya, *Angew. Chem., Int. Ed.*, 2010, 49, 7996–7999.
- 46 A. Chauvet, N. Dashdorj, J. H. Golbeck, T. W. Johnson and S. Savikhin, *J. Phys. Chem. B*, 2012, 116, 3380–3386.
- 47 S. Savikhin, W. Xu, P. Martinsson, P. R. Chitnis and W. S. Struve, *Biochemistry*, 2001, 40, 9282–9290.
- 48 A. Diaz-Quintana, W. Leibl, H. Bottin and P. Setif, *Biochemistry*, 1998, 37, 3429–3439.
- 49 R. S. Dawe, *Br. J. Dermatol.*, 2003, 148, 626–637.
- 50 M. Schütz, M. Brugna, E. Lebrun, F. Baymann, R. Huber, K.-O. Stetter, G. Hauska, R. Toci, D. Lemesle-Meunier, P. Tron, C. Christian Schmidt and W. Nitschke, *J. Mol. Biol.*, 2000, 300, 663–675.

Tryptophan-to-heme electron transfer in ferrous myoglobins

Roberto Monni, André Al Haddad, Frank van Mourik, Gerald Auböck, and Majed Chergui

Laboratoire de Spectroscopie Ultrarapide, Institut de Sciences et Ingénierie Chimiques, École Polytechnique Fédérale de Lausanne, CH-1015 Lausanne, Switzerland

nne,

Edited by Harry B. Gray, California Institute of Technology, Pasadena, CA, and approved March 31, 2015 (received for review December 5, 2014)

It was recently demonstrated that in ferric myoglobins (Mb) the fluorescence quenching of the photoexcited tryptophan 14 (*Trp¹⁴) residue is in part due to an electron transfer to the heme porphyrin (porph), turning it to the ferrous state. However, the invariance of *Trp decay times in ferric and ferrous Mbs raises the question as to whether electron transfer may also be operative in the latter. Using UV pump/visible probe transient absorption, we show that this is indeed the case for deoxy-Mb. We observe that the reduction generates (with a yield of about 30%) a low-valence Fe^{II}-porphyrin π [Fe^{II}(porph^{•-})]⁻ anion radical, which we observe for the first time to our knowledge under physiological conditions. We suggest that the pathway for the electron transfer proceeds via the leucine 69 (Leu⁶⁹) and valine 68 (Val⁶⁸) residues. The results on ferric Mbs and the present ones highlight the generality of Trp¹⁴-porphyrin electron transfer in heme proteins.

electron transfer | heme proteins | tryptophan | picosecond | low valence heme

Electron transfer plays a fundamental role in many biological systems (1–3) ranging from photosynthetic proteins (4) to iron–sulfur (5), copper (6), and heme (7, 8) proteins. It was demonstrated that electron transfer can be used to produce from heme proteins in situ drugs with antimalarial activity (9) and it might have a role in protein folding (2). In general, electron transfer in proteins can occur over long distances (>10 Å) by hopping through different residues, thus reducing the time that would be needed for a single step tunneling from the donor to the acceptor (10–12). Aromatic amino acids and Tryptophan (Trp) in particular can act as a relay in such processes (13–19). Trp also acts as a phototriggered electron donor, e.g., in DNA repair by photolyase (16–18) and in cryptochromes (20, 21). When no obvious electron acceptors are present, excited Trp or (*Trp) still displays shorter lifetimes than its nanosecond decay times in solution (22, 23). This is due to its strong tendency to act as an electron donor, undergoing electron transfer toward the protein's backbone as in the case of apo-myoglobin mutants (24), small cyclic peptides (25), and human γ -D-crystallin (26). It is interesting to note that in wild-type horse heart (WT-HH) apo-myoglobin the fluorescence lifetime of the two *Trp residues was reported to be comparable to that in water (27), demonstrating the absence of deactivation mechanisms, either by energy or by electron transfer.

The protein visible absorption spectrum is dominated by their cofactors, e.g., heme or flavins, whereas the UV absorption in the region between 250 nm and 300 nm is mainly due to the three aromatic amino acids, Trp, tyrosine (Tyr), and phenylalanine (Phe) (28), with Trp having the highest molar extinction coefficient. The high sensitivity of Trp to the local environment and the possibility to correlate it with its fluorescence response (28) have led to its widespread use as a local natural probe of protein structure and dynamics in time-resolved fluorescence resonance energy transfer (FRET) studies, and it has emerged as the “spectroscopic ruler” in such studies (28–30). FRET is mediated by dipole–dipole coupling between a donor *Trp and an acceptor molecule, and its rate is inversely proportional to the sixth power of the distance between them and to the relative orientation of their dipoles.

Myoglobin (Mb) is a small heme protein composed of 150 residues (31) arranged in eight α -helices (from A to H) (SI Appendix Fig. S7), whose biological function is to store molecular oxygen in muscles of vertebrates (32). This is accomplished by its prosthetic group: a Fe–Protoporphyrin IX complex bound to the protein structure via the proximal histidine (His⁹³) (SI Appendix, Fig. S7). Both ferric and ferrous hemes tend to bind small diatomic molecules (e.g., O₂, CO, NO, and CN) at the Fe site. Mb has two Trp residues that are situated in the α -helix A: Trp⁷ toward the solvent and Trp¹⁴ within the protein and closer to the heme (SI Appendix, Fig. S7) (33). Previous time-resolved fluorescence studies on various Mb complexes have reported decay times (SI Appendix, Table S1) of 120 ps and 20 ps, for *Trp⁷ and *Trp¹⁴, respectively (34–38). These decay times appear invariant with respect to the ligand and the oxidation state of the iron ion in the heme. They were attributed to *Trp-to-porphyrin energy transfer via FRET over different donor–acceptor distances (37, 38) [the Trp⁷-Heme and Trp¹⁴-Heme center-to-center distances are 21.2 Å and 15.1 Å, respectively (33, 39) (SI Appendix Fig. S7)]. We recently showed, using ultrafast 2D-UV and visible transient absorption (TA) spectroscopy, that in the ferric myoglobins (MbCN and MbH₂O) the relaxation pathway of *Trp¹⁴ involves not only a *Trp-to-heme FRET but also an electron transfer from the *Trp to the heme (40) in a ratio of approximately 60–40%. One can expect that due to its ferric character, the heme is a strong electron acceptor in these cases, and indeed our study showed the formation of an Fe^{II} heme.

However, the invariance of *Trp decay times in ferric and ferrous Mbs (SI Appendix, Table S1) suggests that similar electron transfer processes may also occur in ferrous Mbs. In this event, questions arise as to (i) whether a formally Fe^I heme is formed, which has to date been observed only in cryo-radiolysis experiments (41, 42), or (ii) whether the electron localizes on the porphyrin ring or even on the ligand that binds to the Fe ion. Theoretical investigations have suggested that an iron porphyrin anion radical can be formed (43–45).

Significance

We demonstrate the occurrence of tryptophan (Trp) to heme electron transfer (ET) in ferrous myoglobins by ultrafast UV spectroscopy. The ET gives rise to the theoretically predicted, low-valence Fe(II)(porph^{•-}) anion radical, which we observe for the first time to our knowledge under physiological conditions. These results highlight the generality of Trp¹⁴-porphyrin electron transfer events in heme proteins and question the systematic use of Trp fluorescence in FRET studies of protein dynamics.

Author contributions: M.C. designed research; R.M., A.A.H., F.v.M., and G.A. performed research; R.M., G.A., and M.C. analyzed data; and R.M., G.A., and M.C. wrote the paper.

The authors declare no conflict of interest.

This article is a PNAS Direct Submission.

Freely available online through the PNAS open access option.

¹To whom correspondence should be addressed. Email: majed.chergui@epfl.ch.

This article contains supporting information online at www.pnas.org/lookup/suppl/doi:10.1073/pnas.1423186112/-/DCSupplemental.

$\text{Fe}^{\text{II}}(\text{porph}^{\ominus-})$ (42). The latter results suggest that the e_g and $d_{x^2-y^2}$ orbitals are close in energy, leading to the $\text{Fe}^{\text{II}}(\text{porph}^{\ominus-})$ when the system has the possibility to relax. Low-valent heme species, their nature, and relevance under physiological conditions were also investigated in theoretical studies (43–45), which also suggest formation of an $\text{Fe}^{\text{II}}(\text{porph}^{\ominus-})$.

The photoproducts of $^*\text{Trp}^{14}$ -to-heme electron transfer can be $\text{TrpH}^{\oplus+}$ or $^*\text{TrpH}^{\oplus+}$ and $\text{Fe}^{\text{II}}(\text{porph}^{\ominus-})$ or $^*\text{Fe}^{\text{II}}(\text{porph}^{\ominus-})$. Because the transient spectra at delay times >40 ps do not display any changes (except for a small vertical offset due to $^*\text{Trp}^7$ and $^*\text{Trp}^{14}$ ESA), it is safe to assume that the $\text{Fe}^{\text{II}}(\text{porph}^{\ominus-})$ product is generated. In the opposite case [generation of $^*\text{Fe}^{\text{II}}(\text{porph}^{\ominus-})$] different spectral features should have been present in the transient spectra, together with their evolution. Further, if $\text{TrpH}^{\oplus+}$ is generated, an ESA feature at 560 nm [absorption band of $\text{TrpH}^{\oplus+}$ (66)] should arise with the $^*\text{Trp}^{14}$ decay time; if instead $^*\text{TrpH}^{\oplus+}$ is generated, some transient features should appear somewhere in the probing region (note that no information is available on $^*\text{TrpH}^{\oplus+}$ absorption bands, but an ESA feature should at least show up in the probed region). However, despite this fact, the transient spectra do not display any ESA feature around 560 nm, suggesting that the molar extinction coefficient of the generated $\text{TrpH}^{\oplus+}$ (or $^*\text{TrpH}^{\oplus+}$) is too small to detect the produced species. This is in line with the results on MbCN and met-Mb, in which the Trp radical cation was not detected either in its ground or in its excited state (40). Of course, if the signals of the products in their excited state fall outside the region of our probe and/or they decay to their ground state on a timescale that is too fast to be measurable with our setup, these considerations are no longer valid.

To estimate the quantum yield (QY) for electron transfer, the deoxy-Mb static spectrum (SI Appendix, Fig. S1) has been rescaled to the GSB amplitude of the LL transient spectrum at 900 ps, allowing a rough estimate of the proportion of Mbs with a $\text{Fe}^{\text{II}}(\text{porph}^{\ominus-})$ heme. The obtained value was divided by the total amount of excited Trp^{14} residues (details are given in SI Appendix). We find that $\approx 30\%$ of photoexcited Trp^{14} s relax via electron transfer to the heme whereas the remaining ones relax via FRET. Because there are only these two parallel relaxation mechanisms, we can apply the relationship $\text{QY} = k_{\text{et}}/(\sum_i k_i)$ to obtain an estimate of the k_{et} leading to $k_{\text{et}} = 1/\tau_{\text{et}} = 1.7 \times 10^{-10} \text{ s}^{-1}$ ($\tau_{\text{et}} = 60$ ps). These values are similar to the ferric Mbs, where the QY was found to be $\approx 40\%$ (40), implying $k_{\text{et}} = 1/\tau_{\text{et}} = 3.3 \times 10^{-10} \text{ s}^{-1}$ ($\tau_{\text{et}} = 30$ ps). More insights into the $^*\text{Trp}^{14}$ -to-heme electron transfer reaction in ferrous Mbs could be obtained using Marcus theory (ref. 67 and SI Appendix, section SII.4). However, too many parameters are unknown in the present case, hindering a deeper analysis of the Marcus region in which this electron transfer occurs.

The reported absence of $^*\text{Trp}$ fluorescence quenching in apo-Mb (27) highlights the strong affinity of $^*\text{Trp}$ to undergo energy and electron transfer to the heme. Given the similarity in yields and timescales for ferric and ferrous Mbs, it seems that the $^*\text{Trp}$ -to-heme electron transfer is not determined by the oxidation state of the iron ion, and therefore the interaction between $^*\text{Trp}$ and the porphyrin is the main cause for $^*\text{Trp}$ deactivation and thus for electron transfer to occur. We thus predict that in the ferric case, the prime acceptor of the electron is the porphyrin, even if at a subsequent stage it develops an Fe^{I} center.

Zhong and coworkers investigated Trp fluorescence quenching in proteins by interresidue and interhelical electron transfer and identified carbonyl- and sulfur-containing residues as quenching groups (24). Although a glutamic acid residue is present in the vicinity of Trp^{14} in Mb, it is oriented toward the solvent, so we do not consider it playing a role. Rather, we believe that a possible

pathway for a single-step electron transfer from $^*\text{Trp}^{14}$ to the heme can involve Leu⁶⁹, which is in van der Waals contact with Trp^{14} and Val⁶⁸ (SI Appendix, Fig. S7).

Having identified a Trp^{14} -to-heme electron transfer in ferric (40) and now in the ferrous deoxy-Mb and given the fact that the Trp fluorescence lifetimes are invariant in all Mbs (SI Appendix, Table S1), we anticipate the process to also be present in ligated ferrous Mbs. Hemoglobin (Hb) has six Trp residues: one in each α -subunit ($\alpha 14$) and two in each β -subunit ($\beta 15$ and $\beta 37$). Quite remarkably, their fluorescence lifetimes (68, 69) are comparable to the Mb values in SI Appendix, Table S1. As a matter of fact, in deoxy-, oxy-, and carboxy-Hb, the Trp residues are at typical distances of 13–18 Å from a heme porphyrin, which is comparable to the Trp^{14} -heme distance of 15.1 Å in Mb. We predict that a Trp-to-heme electron transfer also occurs in hemoglobins.

An extreme case of Trp fluorescence quenching in heme proteins was found for ferrous and ferric cytochrome c (Cyt c) with, respectively, decay times of 350 fs and 770 fs (57, 58). Trp is at van der Waals distances of the porphyrin (3–5 Å; SI Appendix, Fig. S8) in Cyt c, but the Trp quenching was clearly identified as being due to FRET, at least to 85%. In this case the FRET may well be mediated by an exchange (Dexter) mechanism, in which the donor loses an electron from its excited state that is donated back to its ground state by the acceptor. In the light of these and the present results, it seems that electron transfer can compete with FRET only when the latter is less efficient (due to distance and orientation of the donor/acceptor dipoles) and/or when residues between the Trp and the porphyrin are present that can mediate it. In any case, more studies are needed to fully understand the competition between FRET and electron transfer in hemoproteins.

Conclusions

Femtosecond UV-visible transient absorption experiments were performed on deoxy-Mb for excitation wavelengths near 300 nm. They reveal the formation of a long-lived photoproduct, which results from a $^*\text{Trp}^{14}$ -to-heme electron transfer with a quantum yield of $\approx 30\%$. This species is an Fe^{II} -porphyrin π -anion radical that has a lifetime exceeding our measurement window of 1 ns. To our knowledge this is the first observation of such a low-valent heme complex under physiological conditions, although their existence and biological importance as intermediates in the production pathway of active species in cytochrome P450 (43) as well as for CO_2 reduction (44) were discussed earlier.

The similarity to our previous results on ferric Mbs (40) and the invariance of the $^*\text{Trp}$ lifetimes for all myoglobins suggests that the $^*\text{Trp}^{14}$ -to-heme electron transfer is likely operative in the ligated ferrous Mbs.

We propose a single-step tunneling pathway for the electron transfer that involves the Leu⁶⁹ and Val⁶⁸ residues that lower the tunneling energy. Finally, as previously stressed (40, 70), care is advised when using $^*\text{Trp}$ fluorescence as a spectroscopic ruler, assuming that its fluorescence decay is due to FRET. This is surely an important tool in studies of protein dynamics but more often than previously thought, parallel electron transfer pathways may also contribute to its quenching.

Associated Content

Sample preparation, optical setup details, power dependence, data analysis details, and extra figures are available in SI Appendix.

ACKNOWLEDGMENTS. We thank Dr. Cristina Consani for useful discussions. This work was supported by the Swiss National Science Foundation via the National Centre for Competence in Research: Molecular Ultrafast Science and Technology.

1. Gray HB, Winkler JR (1996) Electron transfer in proteins. *Annu Rev Biochem* 65: 537–561.

2. Pascher T, Chesick JP, Winkler JR, Gray HB (1996) Protein folding triggered by electron transfer. *Science* 271(5255):1558–1560.

3. Cordes M, Giese B (2009) Electron transfer in peptides and proteins. *Chem Soc Rev* 38(4):892–901.
4. Rochaix JD (2011) Regulation of photosynthetic electron transport. *Biochim Biophys Acta* 1807(3):375–383.
5. Johnson DC, Dean DR, Smith AD, Johnson MK (2005) Structure, function, and formation of biological iron-sulfur clusters. *Annu Rev Biochem* 74:247–281.
6. Farver O, Pecht I (2011) Electron transfer in blue copper proteins. *Coord Chem Rev* 255(7-8):757–773.
7. Mines GA, Pascher T, Lee SC, Winkler JR, Gray HB (1996) Cytochrome c folding triggered by electron transfer. *Chem Biol* 3(6):491–497.
8. Schichman SA, Meyer TE, Gray HB (1996) Kinetics of electron transfer in *Pseudomonas aeruginosa* cytochrome cd(1)-nitrite reductase. *Inorg Chim Acta* 243(1–2):25–31.
9. Robert A, Benoit-Vical F, Meunier B (2005) The key role of heme to trigger the antimalarial activity of trioxanes. *Coord Chem Rev* 249(17–18):1927–1936.
10. Gray HB, Malmström BG (1989) Long-range electron transfer in multisite metalloproteins. *Biochemistry* 28(19):7499–7505.
11. Shih C, et al. (2008) Tryptophan-accelerated electron flow through proteins. *Science* 320(5884):1760–1762.
12. Gray HB, Winkler JR (2005) Long-range electron transfer. *Proc Natl Acad Sci USA* 102(10):3534–3539.
13. Farver O, et al. (1996) Structure-function correlation of intramolecular electron transfer in wild type and single-site mutated azurins. *Chem Phys* 204(2–3):271–277.
14. Blanco-Rodríguez AM, et al. (2011) Phototriggering electron flow through Re(I)-modified *Pseudomonas aeruginosa* azurins. *Chemistry* 17(19):5350–5361.
15. Lancaster KM, et al. (2011) Electron transfer reactivity of type zero *Pseudomonas aeruginosa* azurin. *J Am Chem Soc* 133(13):4865–4873.
16. Aubert C, Mathis P, Eker APM, Brettel K (1999) Intraprotein electron transfer between tyrosine and tryptophan in DNA photolyase from *Anacystis nidulans*. *Proc Natl Acad Sci USA* 96(10):5423–5427.
17. Aubert C, Vos MH, Mathis P, Eker APM, Brettel K (2000) Intraprotein radical transfer during photoactivation of DNA photolyase. *Nature* 405(6786):586–590.
18. Byrdin M, et al. (2004) Intraprotein electron transfer and proton dynamics during photoactivation of DNA photolyase from *E. coli*: Review and new insights from an “inverse” deuterium isotope effect. *Biochim Biophys Acta* 1655(1–3):64–70.
19. Wang M, Gao J, Müller P, Giese B (2009) Electron transfer in peptides with cysteine and methionine as relay amino acids. *Angew Chem Int Ed Engl* 48(23):4232–4234.
20. Giovanni B, Byrdin M, Ahmad M, Brettel K (2003) Light-induced electron transfer in a cryptochrome blue-light photoreceptor. *Nat Struct Biol* 10(6):489–490.
21. Immeln D, Weigel A, Kotte T, Pérez Lustres JL (2012) Primary events in the blue light sensor plant cryptochrome: Intraprotein electron and proton transfer revealed by femtosecond spectroscopy. *J Am Chem Soc* 134(30):12536–12546.
22. Léonard J, Sharma D, Szafarowicz B, Torgasin K, Haacke S (2010) Formation dynamics and nature of tryptophan’s primary photoproduct in aqueous solution. *Phys Chem Chem Phys* 12(48):15744–15750.
23. Fleming GR, et al. (1978) Nonexponential fluorescence decay of aqueous tryptophan and two related peptides by picosecond spectroscopy. *Proc Natl Acad Sci USA* 75(10):4652–4656.
24. Qiu WH, et al. (2008) Ultrafast quenching of tryptophan fluorescence in proteins: Interresidue and intrahelical electron transfer. *Chem Phys* 350(1–3):154–164.
25. Pan CP, Barkley MD (2004) Conformational effects on tryptophan fluorescence in cyclic hexapeptides. *Biophys J* 86(6):3828–3835.
26. Chen J, Flaugh SL, Callis PR, King J (2006) Mechanism of the highly efficient quenching of tryptophan fluorescence in human gammaD-crystallin. *Biochemistry* 45(38):11552–11563.
27. Glandières JM, Twist C, Haouz A, Zentz C, Alpert B (2000) Resolved fluorescence of the two tryptophan residues in horse apomyoglobin. *Photochem Photobiol* 71(4):382–386.
28. Lakowicz JR (2006) *Principles of Fluorescence Spectroscopy* (Springer, New York), 3rd Ed, Chap 16.
29. Lakowicz JR (2006) *Principles of Fluorescence Spectroscopy* (Springer, New York), 3rd Ed, Chap 13.
30. Truong K, Ikura M (2001) The use of FRET imaging microscopy to detect protein-protein interactions and protein conformational changes in vivo. *Curr Opin Struct Biol* 11(5):573–578.
31. Hershleth HP, et al. (2007) Crystallographic and spectroscopic studies of peroxide-derived myoglobin compound II and occurrence of protonated FeIV O. *J Biol Chem* 282(32):23372–23386.
32. Ordway GA, Garry DJ (2004) Myoglobin: An essential hemoprotein in striated muscle. *J Exp Biol* 207(Pt 20):3441–3446.
33. Evans SV, Brayer GD (1988) Horse heart metmyoglobin. A 2.8-Å resolution three-dimensional structure determination. *J Biol Chem* 263(9):4263–4268.
34. Janes SM, Holtom G, Ascenzi P, Brunori M, Hochstrasser RM (1987) Fluorescence and energy transfer of tryptophans in *Aplysia* myoglobin. *Biophys J* 51(4):653–660.
35. Willis KJ, Szabo AG, Zuker M, Ridgeway JM, Alpert B (1990) Fluorescence decay kinetics of the tryptophyl residues of myoglobin: Effect of heme ligation and evidence for discrete lifetime components. *Biochemistry* 29(22):5270–5275.
36. Willis KJ, Szabo AG, Krajcarski DT (1991) Fluorescence decay kinetics of the tryptophyl residues of myoglobin single-crystals. *J Am Chem Soc* 113(6):2000–2002.
37. Hochstrasser RM, Negus DK (1984) Picosecond fluorescence decay of tryptophans in myoglobin. *Proc Natl Acad Sci USA* 81(14):4399–4403.
38. Stevens JA, et al. (2010) Ultrafast dynamics of resonance energy transfer in myoglobin: Probing local conformation fluctuations. *J Phys Chem B* 114(3):1498–1505.
39. Phillips SEV, Schoenborn BP (1981) Neutron diffraction reveals oxygen-histidine hydrogen bond in oxymyoglobin. *Nature* 292(5818):81–82.
40. Consani C, Auböck G, van Mourik F, Chergui M (2013) Ultrafast tryptophan-to-heme electron transfer in myoglobins revealed by UV 2D spectroscopy. *Science* 339(6127):1586–1589.
41. Davydov R, Osborne RL, Kim SH, Dawson JH, Hoffman BM (2008) EPR and ENDOR studies of cryoreduced compounds II of peroxidases and myoglobin. Proton-coupled electron transfer and protonation status of ferryl hemes. *Biochemistry* 47(18):5147–5155.
42. Davydov R, Hoffman BM (2008) EPR and ENDOR studies of Fe(II) hemoproteins reduced and oxidized at 77 K. *J Biol Inorg Chem* 13(3):357–369.
43. Porro CS, Kumar D, de Visser SP (2009) Electronic properties of pentacoordinated heme complexes in cytochrome P450 enzymes: Search for an Fe(II) oxidation state. *Phys Chem Chem Phys* 11(43):10219–10226.
44. Kis Z, Silaghi-Dumitrescu R (2010) The electronic structure of biologically relevant Fe(0) systems. *Int J Quantum Chem* 110(10):1848–1856.
45. Silaghi-Dumitrescu R, Makarov SV (2010) A computational analysis of electromerism in hemoprotein Fe(II) models. *J Biol Inorg Chem* 15(6):977–986.
46. Ye X, Demidov A, Champion PM (2002) Measurements of the photodissociation quantum yields of MbNO and MbO(2) and the vibrational relaxation of the six-coordinate heme species. *J Am Chem Soc* 124(20):5914–5924.
47. Kruglik SG, et al. (2010) Picosecond primary structural transition of the heme is retarded after nitric oxide binding to heme proteins. *Proc Natl Acad Sci USA* 107(31):13678–13683.
48. Petrich JW, et al. (1994) Ultrafast measurements of geminate recombination of NO with site-specific mutants of human myoglobin. *J Mol Biol* 238(3):437–444.
49. Tian WD, Sage JT, Srajer V, Champion PM (1992) Relaxation dynamics of myoglobin in solution. *Phys Rev Lett* 68(3):408–411.
50. Jackson TA, Lim M, Anfirud PA (1994) Complex nonexponential relaxation in myoglobin after photodissociation of MbCO - measurement and analysis from 2-Ps to 56-Mu-S. *Chem Phys* 180(2–3):131–140.
51. Lim M, Jackson TA, Anfirud PA (1997) Ultrafast rotation and trapping of carbon monoxide dissociated from myoglobin. *Nat Struct Biol* 4(3):209–214.
52. Kholodenko Y, Volk M, Gooding E, Hochstrasser RM (2000) Energy dissipation and relaxation processes in deoxy myoglobin after photoexcitation in the Soret region. *Chem Phys* 259(1):71–87.
53. Kadish KM, Larson G (1977) A study of the redox potentials and electron transfer rates of several naturally occurring and synthetic iron porphyrins in DMF. *Bioinorg Chem* 7(2):95–105.
54. De Silva C, Czarniecki K, Ryan MD (1999) Visible and resonance Raman spectra of low valent iron porphyrins. *Inorg Chim Acta* 287(1):21–26.
55. Kadish KM, van Caemelbecke E, Royal G (2000) *Electron transfer. The Porphyrin Handbook*, eds Kadish KM, Smith KM, Guilard R (Academic, Orlando, FL), Vol 8.
56. Consani C, Auböck G, Bräm O, van Mourik F, Chergui M (2014) A cascade through spin states in the ultrafast haem relaxation of met-myoglobin. *J Chem Phys* 140(2):025103.
57. Consani C, Bram O, van Mourik F, Cannizzo A, Chergui M (2012) Energy transfer and relaxation mechanisms in Cytochrome c. *Chem Phys* 396:108–115.
58. Bräm O, Consani C, Cannizzo A, Chergui M (2011) Femtosecond UV studies of the electronic relaxation processes in Cytochrome c. *J Phys Chem B* 115(46):13723–13730.
59. Peychalh G, Wilson GS (1971) Electrochemical studies of some porphyrin Ix derivatives in aprotic media. *Anal Chem* 43(4):550–556.
60. Cohen IA, Ostfeld D, Lichtenstein B (1972) Characterization of a d iron system. Tetraphenylporphineiron (II) anion. *J Am Chem Soc* 94(13):4522–4525.
61. Lexa D, Momentea M, Mispel J (1974) Characterization of reduction steps of Fe(III) porphyrins. *Biochim Biophys Acta* 338(1):151–163.
62. Yamaguchi K, Morishima I (1992) Low-valent iron porphyrins - Nmr evidence for pi-anion-radical character in 2-electron-reduced iron(III) meso-substituted or beta-pyrrole-substituted porphyrins. *Inorg Chem* 31(15):3216–3222.
63. Balducci G, Chottard G, Gueutin C, Lexa D, Saveant JM (1994) Electrochemistry of iron(II) porphyrins in the presence of carbon-monoxide - comparison with zinc porphyrins. *Inorg Chem* 33(9):1972–1978.
64. Donohoe RJ, Atamian M, Bocian DF (1987) Characterization of singly reduced iron(II) porphyrins. *J Am Chem Soc* 109(19):5593–5599.
65. Kadish KM, Bottomley LA (1977) Substituent effects on the formation constants of iron(III) and iron (II) tetraphenylporphyrin-pyridine complexes. *J Am Chem Soc* 99(7):2380–2382.
66. Bellina B, et al. (2011) Spectroscopic signatures of peptides containing tryptophan radical cations. *Angew Chem Int Ed Engl* 50(48):11430–11432.
67. Marcus RA (1956) On the theory of oxidation-reduction reactions involving electron transfer. 1. *J Chem Phys* 24(5):966–978.
68. Bucci E, Malak H, Fronticelli C, Gryczynski I, Lakowicz JR (1988) Resolution of the lifetimes and correlation times of the intrinsic tryptophan fluorescence of human hemoglobin solutions using 2 GHz frequency-domain fluorometry. *J Biol Chem* 263(15):6972–6977.
69. Szabo AG, Willis KJ, Krajcarski DT, Alpert B (1989) Fluorescence decay parameters of tryptophan in a homogeneous preparation of human-hemoglobin. *Chem Phys Lett* 163(6):565–570.
70. Winkler JR (2013) Chemistry. FRETting over the spectroscopic ruler. *Science* 339(6127):1530–1531.

Curriculum Vitae

Andre AL Haddad

Laboratory of Ultrafast Spectroscopy, (LSU)
Faculty of Basic Sciences, Institute of Chemical Sciences
and Engineering (ISIC)
École Polytechnique Fédérale de Lausanne (EPFL)
EPFL campus, CH H1 535, Station 6
CH-1015 Lausanne, SWITZERLAND

Mobile: +41-798338011
Phone: +41-216930456
E-mail: andre.alhaddad@epfl.ch

PhD Candidate

Born on Sep. 27th, 1987 (Beirut, Lebanon)

Education

- Mar 2011- present: **PhD in Photonics.**
 École Polytechnique Fédérale de Lausanne (Switzerland).
 Supervised by Prof. M. Chergui.
 Title: “Ultra-broadband Multi-Dimensional Electronic Spectroscopy of molecular systems”.
- Sep 2008- June 2010: **Master degree in LASER: Medical and Industrial Applications.**
 Lebanese University faculty of sciences II, Beirut, Lebanon.
- Sep 2005- July 2008: **Bachelor degree in Physics.**
 Lebanese University faculty of sciences II, Beirut, Lebanon.

Research Experience

March 2011- present: **PhD in Photonics.** Laboratory of Ultrafast Spectroscopy (LSU), École Polytechnique Fédérale de Lausanne (Switzerland).
Supervisor: Prof. M. Chergui.
Title: Ultra-broadband Multi-Dimensional Electronic Spectroscopy of molecular systems.

Research topic: The first part of the thesis has been devoted to the design and implementation of a Two Dimensional spectrometer that is capable of performing measurements in the visible spectral range and with minimal adjustments in the ultraviolet range. As light source, spectral broadening in argon filled hollow core fiber compressor is used to generate light continuum spanning from 420 to 1000 nm with enough energy per pulse to afford pulse compression. A home built deformable mirror based pulse compressor is used to compress the continuum to sub-10 fs very close to the pulse Fourier limit. Using such broad light source in the visible regime presented new challenges in maintaining high interferometric stability and extracting the absorptive information using phase correction. Time resolution of 14 fs is achieved enabling ultrafast electronic relaxation of multiple coupled excitations to be studied at the same time. Ultra-fast transient absorption can be performed on the same setup using the same pulses. Different samples are being studied with this setup starting from dyes such as Rhodamine 101, Iron-tris-bipyridine, free-base porphyrins, various types of di-porphyrins, and different biological systems such as Cytochrome C oxidase and myoglobin.

The second part of the thesis is dedicated to studying the ultrafast electronic relaxation and wave packet dynamics in free-base porphyrins. Ultrafast transient absorption measurements were performed using a 20 kHz pump probe setup using a NOPA to tune the wavelength of the pump in the visible range (40 fs), in parallel to measurements performed on a fluorescence up-conversion setup. All experiments lead to the resolution of wave

packet dynamics below 500 cm^{-1} within the emission and transient absorption, and confirm a reversible ultrafast internal conversion between Q_x and Q_y . Further investigation is done using the multi-dimensional setup to map out the relaxation pathways earlier than 30 fs.

Mar 2010- Aug 2010: **Internship.** Institut de Physique et Chimie des Matériaux de Strasbourg, University of Strasbourg (Strasbourg, France),
Supervisor: Dr. Alberto Barsella.
Title: Real Time Monitoring of Photo-Polymerization of a Film Using Off Axis Holography

Research topic: The aim of the project is to study the photo-polymerization of liquid films in real time using interferometric system allowing the measurement of changes in the surface and the index of refraction. Off-axis holographic technique was used with a He-Ne laser and a CCD (1600x1200 pixels); the image is numerically reconstructed. The reconstruction was done using MatLab by building the 3D image of the object by complex wave retrieval technique, after this a phase unwrapping algorithm was used to be able to visualize the 3D image. The real dimensions of the images were in micrometers and the precision was in sub wavelength (in the order of nanometers).

2009 - 2010: **Internship.** Laboratoire de Physique Appliqué (**LPA**), Groupe des Biomatériaux et des Matériaux Intelligents (**GBMI**) Lebanese University.
Supervisor: Prof. Mario Tahchi.

Research topics:

- Starting with the variation of the particle size and volume during photo-polymerization, we used the variation of the index of refraction of the solution to measure the scattering of the light in the solution. So a laser and three photo-detectors were used to measure the variation of light intensity.
- The aim of this project is to dispose plastics such as PET using a low cost and low power laser. Gas chromatography was used to understand the effect of the laser on the material. A model of the system was made on COMSOL multi-physics, where it simulated the Laser-Material interaction and the thermal diffusion in the material.
- Started with the electrical characteristics of conducting Poly-aniline polymer and Poly-aniline with polyvinyl alcohol. Then, fabricated PANI-PVA fibers by electro spinning, and tested there electrical characteristics. A simulation using COMSOL Multi-physics was done to simulate the electro spinning process and the transition of the PANI-PVA drop from one pole to the other tracing after it the fibers.

Skills

- Operation and maintenance of **amplified laser systems**.
- Characterization and tailoring and compression of optical laser pulses.
- Experience with nonlinear sources: **Optical Parametric Amplifiers** (homemade and commercial) and **hollow core fibers** for generating broadband optical pulses spanning from several tens of nm to 100s of nm.
- Experience in **generation and compression of broadband UV pulses** spanning between 260 - 340 nm.
- Experience in building **phase stabilized interferometric experiments** to be used in **holography and interferometry**.
- Experience in building **Optical coherence tomography and Off-axis digital holography setups**.
- 2D image reconstruction by homemade **phase retrieval algorithms**.
- Sample preparation and characterization for optical experiments.

- Experience in interfacing various electronic devices and get all synchronized with the laser trigger (CCD arrays, CMOS arrays, choppers) for performing **shot-to-shot experiments** at rep-rates of several KHz.

Scientific and programming packages: Matlab, Igor, LabView, LabWindows, COMSOL Multi-physics, Silvaco (simulation of CMOS fabrication and characterization), C and C++, HTML and ASP.

Graphics design: PhotoShop, 3D-Max (Medium), Dreamweaver.

Electronic circuit reparation and diagnostics (Technician in Laboratoire de Physique Applique 2008-2010).

Languages: **Arabic** (native), **English** (C2), Italian (B1), French (B1).

Teaching Experience

Mar 2011- May 2014: **Teaching Assistant**. École Polytechnique Fédérale de Lausanne (Switzerland).

- Ultrafast Phenomena (Physics Doctoral School) (3 consecutive years)
- General Physics I and II for Civil Engineering. (2 consecutive years)
- Nonlinear Spectroscopy (Photonics Doctoral School)

Conference and Meetings

- Black forest focus in soft matter 7: Multidimensional optical spectroscopy and imaging: temporal and spatial resolution at the cutting edge. 14-18 March 2012, Black Forest, Freiburg, Germany.
- Ultrafast Phenomena 8-13 July 2012 Lausanne Switzerland (Poster presentation).
- International conference on Coherent Multidimensional Spectroscopy 16-18 July 2012 Berlin, Germany (Poster presentation).
- Swiss chemical society Fall Meeting 6 Feb. 2013 Lausanne Switzerland (Poster presentation).
- Jyväskylä summer school 2013: Non-linear ultrafast spectroscopy, theory, 2DIR and 2D electronic spectroscopy.
- Molecular Ultrafast Science and Technology meetings Switzerland 2012 and 2013 (Poster presentation).
- International conference on Coherent Multidimensional Spectroscopy 13-16 July 2014 Eugene, Oregon, USA (Poster presentation).

Research Papers

- Andre Al Haddad, Adrien Chauvet, Jose Ojeda, Chris Arrell, Frank van Mourik, Gerald Auböck, Majed Chergui, “**A setup-up for broadband Fourier-Transform multidimensional electronic spectroscopy**”, **Optics Letters**, Vol. 40, Issue 3, pp. 312-315 (2015).
- Adrien Chauvet, Andre Al Haddad, Wei-Chun Kao, Frank van Mourik, Carola Hunte, Majed Chergui, “**Photo-induced dynamics of the heme centers in cytochrome bc_1** ”, *Phys. Chem. Chem. Phys.* 2015, **17**, 2143-2151.
- Roberto Monni, Andre Al Haddad, Gerald Aubock, Majed Chergui, “**Tryptophan-to-haem electron transfer in ferrous myoglobins**”, **PNAS** 2015, **112** (18), 5602-5606.

- Andre Al Haddad, Adrien Chauvet, Roberto Monni, Jesse Bergkamp, Jakob Grilj, Silvio Decurtins, Majed Chergui, “**Study of ultrafast relaxation dynamics in metal centered triply fused diporphyrins**”, *in preparation*.
- Andre Al Haddad, Adrien Chauvet, Olivier Bräm, Majed Chergui, “**Impulsive heating and vibrational relaxation in free-base porphyrins**”, *in preparation*.

References

Prof. Majed Chergui

Laboratory for Ultrafast Spectroscopy (LSU)
Faculty of Basic Sciences, (ISIC)
École Polytechnique Fédérale de Lausanne (EPFL)
EPFL campus, CH H1 625, Station 6
CH-1015 Lausanne, Switzerland.

E-mail: majed.chergui@epfl.ch
Phone: +41-216930365

Prof. Mario El TAHCHI

Laboratoire de Physique Appliqué (LPA)
Groupe des Biomatériaux et des Matériaux Intelligents (GBMI)
Lebanese University – Faculty of Sciences II
Department of Physics
Fanar – Maten BP 90656 , Lebanon.

E-mail: mtahchi@ul.edu.lb
Phone: +961 3 209 688

Dr. Frank Van Mourik

Laboratory for Ultrafast Spectroscopy (LSU)
Faculty of Basic Sciences, (ISIC)
École Polytechnique Fédérale de Lausanne (EPFL)
EPFL campus, CH H1 595, Station 6
CH-1015 Lausanne, Switzerland.

E-mail: frank.vanmourik@epfl.ch
Phone: +41-216930422